The Dissertation Committee for Ahmed Moustafa Hassan Certifies that this is the Approved Version of the Following Dissertation:

Improving Optical Access, Sampling Speed, and Resolution for *In Vivo* Multiphoton Microscopy

Committee:

Andrew K. Dunn, Supervisor

Kristen M. Harris

Thomas Milner

Hsin-Chih "Tim" Yeh

Improving Optical Access, Sampling Speed, and Resolution for *In Vivo* Multiphoton Microscopy

by

Ahmed Moustafa Hassan

Dissertation

Presented to the Faculty of the Graduate School of

The University of Texas at Austin

in Partial Fulfillment

of the Requirements

for the Degree of

Doctor of Philosophy

The University of Texas at Austin

May 2020

Dedication

With deep gratitude to my family, friends, and mentors.

Acknowledgements

First and foremost, I thank my advisor, Dr. Andrew K. Dunn, whose patience and guidance was instrumental in my academic and professional development. He has been a role model and a mentor, and continually inspires me to become a better thinker and engineer. I've made countless mistakes, but he's never criticized me and has chosen to educate and encourage me instead. I will always be thankful for his instruction, kindness, and respect. I am also extremely grateful for the periodic feedback and comments received from my dissertation committee – Dr. Tim Yeh, Dr. Thomas Milner, and Dr. Kristen Harris. Their input was invaluable towards pushing my research in a novel and impactful direction. This research was largely funded by the support of the National Institutes of Health, the National Science Foundation, and the American Heart Association, so I would like to acknowledge the socially responsible and scientifically literate sector of our population who support these agencies, as well as the more begrudging fraction who pay their taxes anyways. I send extra special thanks to Mr. William L. Robinson, Dr. and Mrs. Ashley J. Welch, Dr. Garrett D. Polhamus, Mr. Gregg Harris, and Mrs. Marilyn Harris for their scholastic support of my foray into multiphoton microscopy.

I would also like to thank my current and past mentors: Dr. Manfred Auer, Dr. Eva Nogales, Dr. Patricia Grob, Dr. Xiaorui Shi, Dr. Tom Hoffend, Dr. Sabrina Relaix, Dr. William Tivol, and Dr. Hong Zhou. Each are outstanding and accomplished individuals, and they have all been highly influential in the way that I think about and approach science and engineering.

Finally, I thank the entire Dunn Lab, particularly Dr. Shams Kazmi, Dr. Jeremy Jarrett, Dr. Andrew Fowler, Dr. Evan Perillo, Dr. David Miller, and Annie Zhou. And I would especially like to thank soon-to-be Dr. Shaun Engelmann. He is a consummate leader – he takes ownership, holds himself and others to a high standard, and demonstrates a deep curiosity and passion for his craft. I am continually inspired by his thoughtful and inquisitive mind, and he has made the Dunn Lab a pleasant and productive environment. I don't think I could have pushed through to the doctoral finish line if it wasn't for his contributions, good nature, and commiseration. Thank you all.

Abstract

Improving Optical Access, Sampling Speed, and Resolution for *In Vivo* Multiphoton Microscopy

Ahmed Moustafa Hassan, Ph.D.

The University of Texas at Austin, 2020

Supervisor: Andrew K. Dunn

Multiphoton microscopy is a powerful optical imaging modality renowned for its non-invasive nature and relatively affordable characteristics. In particular, it has found its niche in neuroimaging due to its ability to probe *in vivo* biological processes in scattering brain tissue approaching millimeter depths with cellular resolution. However, the brain is a large and complex organ, and in order to fully understand its heterogeneous architecture and associated functional roles, several distal regions must be imaged simultaneously. Moreover, due to the critical implications of organelle features in various macroscale processes, whole-brain imaging at subcellular resolution scales presents itself as one of the outstanding challenges faced by the neuroscientific community today. Primarily, this research aims to expand the depth, field-of-view, and temporal throughput of multiphoton microscopy to enable large volume imaging of microvasculature at greater acquisition speeds. To accomplish this, we combine multi-faceted efforts focused on the engineering and development of advanced multiphoton microscopy techniques and technologies. This includes the characterization of novel contrast agents, the optimization of scan system optics, and the integration of high-

repetition rate lasers with a resonant galvanometer. In addition, we develop a two-color imaging system capable of enhancing excitation efficiency, improving signal-to-background ratio, and further extending imaging depth. Finally, we present a novel application for two-color non-degenerate mode mixing to effectively circumvent the diffraction-limited nature of optical resolution and enable subcellular imaging. Collectively, these efforts advance the state-of-the art of multiphoton microscopy for routine cerebrovascular and neuroimaging.

Table of Contents

List of Tables

List of Figures

Figure 4.11: **Non-degenerate mode mixing improves the super-resolution capabilities of fluorescence emission difference microscopy.** (*A*) A comparison of degenerate (D-) and non-degenerate fluorescence emission difference (ND-FED) microscopy procedures with circular and vortex polarizations used for TEM_{00} and TEM_{01} modes, respectively. A single wavelength is selected for D-FED (λ_D = 1080 nm) and two wavelengths are selected for ND-FED (λ_1 = 900 nm, λ_2 = 1350 nm), which compound at $\lambda_3 = \lambda_D$. ND-FED employs one more initial transverse electromagnetic (TEM) mode than D-FED in the construction of the excitation and dark beams, which are independently convolved with a virtual object (FWHM = 250 nm) to generate excitation and dark images. Digital subtraction of a γ weighted dark image from the excitation image results in the super-resolution difference. TEM_{00} = circular, TEM_{01} = vortex. (*B*) D- and ND-FED excitation beam full-width at half-maxima (FWHM) are similar. (*C*) ND-FED dark beam null spots are much smaller, conferring a greater resolution enhancement. (*D*) Using the same γ factor (γ = 0.535), both D- and ND-FED result in sub-diffraction limited images, although only ND-FED manages to achieve the true size of the imaged object 185

Chapter 1: Background and Significance

The overall goal of this study is to expand the optical access and imaging resolution capabilities of multiphoton microscopy for routine, non-invasive neuroimaging. Multiphoton microscopy is inherently limited in its depth penetration capabilities, field of view, and temporal resolution [1–4]. Moreover, conventional multiphoton imaging resolution is fundamentally diffraction-limited due to the physical nature of light [5]. Despite these disadvantages, light microscopy has become a staple of bioimaging applications due to its non-invasive nature and relatively affordable categorization. In particular, multiphoton microscopy has found its niche in neuroimaging due to its ability to probe *in vivo* biological processes in scattering brain tissue at greater depths at high spatial resolutions [6–8]. However, the brain is a large and complex organ, and in order to fully understand its heterogeneous architecture and associated functional roles, several distal regions must be imaged simultaneously. Moreover, due to the critical implications of organelle features in various macroscale processes – such as the role dendritic spines play in long-term potentiation, memory, and learning [9–12] – whole-brain imaging with *subcellular* resolution presents itself as a one of the outstanding challenges faced by the neuroscientific community today [13]. A brute force approach to high-resolution, large field-of-view optical microscopy may involve scanning several smaller, overlapping regions at a small pixel size and tiling the individual 3D volumes together [14–16]. Unfortunately, many processes that unfold *in vivo* are highly transient [17–19], meaning that time-resolved studies which require image data from distinct localized regions at varying time points are unable to exploit these rather slow, conventional tiling methodologies. Furthermore, there are structural and functional processes that play out well beyond a ~1 mm beneath the pial surface that neuroscientific

investigators demand insight to [20–22], and tiling deeper into brain tissue cannot be accomplished without cortical tissue excavation [23–25] or sacrificing a specimen to harvest brain tissue slices [26,27]. Ultimately, these substantial limitations prevent the widespread adoption and research applications of multiphoton microscopy, and hinder its translation into clinical settings. Nevertheless, the physical limits of multiphoton microscopy's capabilities are rarely attained in practice, and it is our aim to rigorously explore these limits to identify regimes where multiphoton microscopy naturally excels (e.g. the near-infrared regime) and develop commensurate advanced imaging technologies to acquire large volumes of microvasculature at greater acquisition speeds. In addition, we detail a super-resolution two-color, mixed mode multiphoton microscopy technique that exploits non-degenerate excitation processes and mixed spatial modes to effectively overcome the diffraction-limited nature of optical resolution. Ultimately, this work will be used to develop a fully optimized super-resolution multiphoton imaging system with enhanced *in vivo* optical access to quantify chronic microvascular changes and visualize subcellular neurophysiological features.

Specifically, the goals and design of the overall project can be divided into the following categories. Our first study explores novel contrast agent properties and culminates in the development of an imaging system that enables multiphoton microscopy of cerebrovascular architecture over large (i.e. millimeter scale) three-dimensional volumes at high speeds. This involves extending imaging depth through an investigation of the multiphoton properties of polymer dots, which we demonstrate the usage of for deep imaging of cortical microvasculature. We also increase the field-of-view of multiphoton imaging by optimizing a microscopy system for maximum light throughput and diffraction-limited performance over large scan angles. Moreover, we improve sampling speed by integrating high-repetition rate (i.e. 80 MHz) ultrafast lasers

with a resonant scanning mirror and a high-speed data acquisition system to achieve high throughput volumetric imaging. We use this enhanced system to collect chronic, *in vivo*, large volume (> 1 mm^3) images of microvasculature and vectorize the resulting data to attain a better understanding of the underlying morphology's bulk longitudinal properties. As a follow-up to this vectorization, we present an in-depth effort to curate geometric strand information.

In a subsequent study, we describe the development of a two-color imaging system that can be used to improve fluorescent excitation efficiency, and evaluate novel applications including extended imaging depth and fluorophore excitation in inaccessible spectral regions. We also present a novel method for super-resolution non-degenerate multiphoton imaging using multiple independently tunable and synchronized ultrafast lasers. For this study, we perform exhaustive computational modeling to identify optimal spectral combinations, spatial modes, and compatible fluorophores. Finally, we delve into an experimental evaluation of various beam shaping technologies and full optical design of a non-degenerate mixed mode multiphoton super-resolution imaging system.

1.1 NON-FLUORESCENT *IN VIVO* IMAGING

Imaging the brain requires some mechanism to generate tissue contrast that may be either exogenous or intrinsic. Fluorescence microscopy encapsulates both of these paradigms; naturally occurring structures can produce an autofluorescent signal when excited at appropriate wavelengths, or external fluorophores can be localized and tagged to targets of interest for fluorescent signal generation. Non-fluorescent imaging modalities follow this same pattern, and this brief review focuses on four non-fluorescent modalities for brain or vascular imaging: magnetic resonance imaging (MRI), computed tomography (CT), positron emission tomography (PET), and ultrasound. Not covered are

other valid methods such as functional near-infrared spectroscopy (FNIRS) and less widely practiced methods such as magnetoencephalography and electroencephalography.

MRI is a relatively nascent modality, initially demonstrated in 1973 by Paul Lauterbur [28]. Since its inception, its popularity has exploded for clinical imaging. To provide images of the brain, MRI relies on no foreign contrast mechanism, and instead exploits the properties of hydrogen molecules in water and in lipids. From a clinical perspective, a few main features distinguish MRI – it is non-ionizing, volumetric, and capable of imaging the entire brain [29]. Due to neurovascular coupling, functional MRI can detect changes in cerebral blood flow to report on cognitive brain function. Broadly, MRI's primary shortcomings are its temporal throughput, with prolonged acquisition times (30 – 40 minutes for a typical clinical session, or 5 – 10 minutes per scan) and its incompatibility with metallic objects [29]. From a research perspective, MRI shines in its capability to provide functional or anatomical images of the entire brain, but lacks in its spatial resolution (1 x 1 x 2.5 mm) and exorbitant expense [30]. In fact, a single voxel in an MRI image can integrate the activity of thousands of neurons – restricting our understanding of the brain to larger anatomical regions (e.g. cerebral cortex) and structures (e.g. tumor) while obscuring any interpretation of microvasculature or brain activity at a cellular level.

CT, technically a non-fluorescent optical imaging technique, is a three-dimensional extension of x-ray planar radiography that can be used to image both dense (e.g. bone) and soft (e.g. brain) tissue. An X-ray tube is rotated relative to, and directed at, a specimen to generate a series of 2D images on the basis of X-ray and tissue interactions that can be back-projected into a 3D reconstruction. X-ray and tissue effects proceed through photoelectric interactions and Compton scattering, which describe tissue-specific attenuation and X-ray deflections respectively [29]. With a sufficient

number of X-rays and minimal Compton scattering, signal-to-noise ratio can be quite large, but contrast-to-noise ratio remains largely dependent on the differential contrast between separate tissue types. Thus, contrast-enhancing iodinated compounds must be injected intravenously in order to resolve cerebrovascular networks [31]. CT is a commonly used modality for cerebral scans, and is frequently used to understand traumatic brain injury, detect aneurysms, and image edemas. However, like MRI, CT is mainly relevant in clinical applications for its sizeable anatomical access. Although its spatial resolution is slightly better than MRI (125 μm in-plane resolution), CT still falls short of resolving individual neurons [32].

PET encapsulates a widely practiced form of nuclear medicine, an umbrella which also encompasses the nuclear analogs to planar X-ray/CT in planar scintigraphy/single photon emission computed tomography. PET is recognized for its considerable anatomical access, ability to visualize glucose metabolism and therefore functional information, and superb sensitivity [29]. Briefly, PET requires the injection of a positron emitting radiotracer, which leads to the formation of two γ-rays with identical energies upon electron-positron annihilation. Radiotracers for PET like ^{18}F-fluorodeoxyglucose (FDG) mimic biological molecules partially substituted by a radioactive atom, and become incorporated into cells after intravenous injection, then trapped [29]. The high glycolytic rate of tumor cells and seizure foci causes a disproportionate uptake and retention of FDG, making PET incredibly well suited for oncology and neuroimaging with respect to seizure activity [33]. More generally, this disproportionate uptake in highly metabolic regions allows PET to provide functional images of brain activation due to the coupling of blood flow and metabolism. Other radiotracers like ^{82}Rb are more specific to myocardial tissue and therefore more applicable to cardiology. Ultimately, the functional information captured by PET is derived from the activity of thousands of

neurons (1 – 2 mm spatial resolution) [34], which affect metabolic activity in aggregate. While this is a favorable characteristic with respect to systems neuroscience, PET is just as limited for fundamental single-cell studies as are MRI and CT. Another significant drawback of PET is its dependency on a cyclotron to generate radiotracers, which are so prohibitively expensive that only very well funded hospitals can procure them. Thus, the cost burden of PET is an enormous barrier towards its adoption as a biomedical or clinical research tool.

Finally, ultrasound is distinct from the aforementioned non-fluorescent techniques in that it uses a mechanical wave to generate structural and functional images. Similar to CT, the primary contrast mechanism in ultrasound is the differential properties of heterogeneous tissue layers, with each interface reflecting a small fraction of incident acoustic energy determined by the relative tissue-specific properties [29]. Reflected waves are returned to and detected by a piezoelectric transducer, and the timing of received signals is used to construct an image. Ultrasound is favorable for its low-cost nature, portability, and non-ionizing characteristics as well its ability to measure blood flow velocity without any requirement for strong magnetic fields. Moreover, flow measurements can be localized to individual vessels. Intravenous administration of microbubbles containing a fluorinated gas are commonly used to enhance vascular contrast, and are sufficiently sized (~6 – 7 μm) to traverse human capillaries [29]. Due to microbubbles' compressibility, they are able to strongly absorb energy from incoming acoustic waves, and return a strong echo to the piezoelectric transducer. Ultimately, ultrasound is superbly suited for high resolution vascular imaging deep into organs, but *in vivo* brain imaging is hindered by the inability of transmitted acoustic waves to penetrate the dense skull. There is moderate optimism that dynamic images of deep human brain microvessels can be recorded at lower frequencies (~1 MHz), although there are no

convincing demonstrations to date [35]. Moreover, ultrasound is unable to record images of neurons, neither dynamically nor statically, disregarding photoacoustic imaging. Moreover, its fairly limited resolution (50 – 500 μm) eliminates the possibility of using ultrasound as a research tool to investigate microvasculature [34].

Modality	Anatomical Access	Penetration Depth	Spatial Resolution
MRI	Excellent	Excellent	1 x 1 x 2.5 mm [30]
CT	Excellent	Excellent	~125 μm [32]
PET	Excellent	Excellent	1 – 2 mm [34]
Ultrasound	Moderate	Moderate	50 – 500 μm [34]
Fluorescence Microscopy	Poor	Poor	~250 – 915 nm

Table 1.1: **Common *in vivo* imaging techniques contrasted.** Anatomical access, penetration depth, and spatial resolution of non-fluorescent *in vivo* imaging modalities compared to fluorescence microscopy.

1.2 Fluorescence Microscopy for Neuroscience

Overall, the review on non-fluorescent imaging modalities in the previous section illustrates their inability to visualize microvasculature and neurons in spite of their moderate to excellent anatomical access and penetration depth. In particular, neurons remain an opaque target to the aforementioned imaging techniques due to their incompatibility with the modality-specific contrast agents and, more importantly, those modalities' poor spatial resolutions. In this section, we will shift our focus to single and multiphoton fluorescence microscopy and discuss how it can circumvent these challenges. Simply stated, fluorescence is a photophysical process where the energy of one or more absorbed photons incites an electron transition in a specific molecule, which

then results in the emission of electromagnetic radiation at a lower energy. The difference in absorbed and emitted energy is a quantitative measure referred to as a Stokes shift. Fluorescence is distinct from phosphorescence with respect to its temporal dynamics - fluorescence occurs on a faster nanosecond time-scale, whereas phosphorescent decay proceeds much more slowly.

The resolution of all microscopes, including fluorescent microscopes, is limited by diffraction and determined by the system's point spread function. To characterize a system's point spread function, one must image a point source, i.e. a sub-diffraction limited object approximating an impulse function, and isolate the profile at focus to obtain an Airy pattern. The appearance of the Airy disk is determined by wavelength (λ) and numerical aperture (NA), and 84% of its intensity is contained within the central lobe. Resolution, which refers to the minimum distance between two features that can be visualized, is then defined by the radius of that central lobe. It is known that the first zero point of the Airy pattern is coincident at ν = 3.832, which allows us to derive the following expression for optical resolution:

$$\nu = \frac{2\pi r_{airy} NA}{\lambda} = 3.832 \tag{1.1}$$

$$r_{airy} = \frac{1.22\lambda}{2NA} \tag{1.2}$$

Thus, one can expect a transverse resolution of ~215 – 425 nm in the visible spectrum using a 1.0 NA objective. For reference, the expected soma diameter of CA1 pyramidal cells in rat are 21 μm, and the diameter of basal dendrites in distal portions can range from 500 nm to 1 μm, meaning that fluorescence microscopy possesses ample resolution for neuroimaging [36] (**Table 1.2**). With respect to microvascular imaging, smaller human venules are a comfortable 2.5 μm and capillaries range from 5 to 10 μm, which

reflects the size of red blood cells (**Table 1.2**). Axial resolution is generally three- to five-fold greater than the transverse Airy radius, and the depth of focus, d, is determined by the axial intensity distribution and can be calculated by wavelength, refractive index (n), and numerical aperture:

$$d = \frac{\lambda\sqrt{n^2 - NA^2}}{NA^2} \tag{1.3}$$

The point spread function, or system impulse response, is an enormously useful metric as its Fourier transform is the optical transfer function, the magnitude of which is the modulation transfer function (MTF), which itself is an autocorrelation of the pupil function, all of which provide information about the spatial frequencies that can be passed through a system. The inverse Fourier transform of the point spread function also yields the lens pupil function. For conventional, one-photon microscopy (1PM), the convolution of the system's point spread function, $I(\boldsymbol{r}, t)$, with an object yields a resulting image, where $\boldsymbol{r} = (x, y)$ denotes the distance from the optical axis and t is time. In the case of non-linear multiphoton microscopy (MPM), the same principle applies, except the point spread function is given by $I(\boldsymbol{r}, t)^n$, where n describes the number of photons absorbed by the fluorescent target.

Neuronal Structures [36]				Vascular Structures [37]	
	Average Soma Diameter	Proximal Dendrite Diameter	Distal Dendrite Diameter	**Anatomical Structure (Human)**	**Individual Vessel Diameter**
CA1 Pyramidal Cell Basal Dendrites (Rat)	21 µm	1 µm	0.5 – 1 µm	**Aorta**	2.6 cm
				Greater Arteries	8 mm
				Arterial Branches	0.6 – 3 mm
Principal Cell of Globus Pallidus (Human)	33 µm	3 µm	0.3 – 0.5 µm	**Arterioles**	20 µm
				Capillaries	9 µm
				Venules	2.5 µm
Cerebellar Purkinje Cell (Guinea Pig)	25 µm	3 µm	0.8 – 2.2 µm	**Venous Branches**	1.5 – 7 mm
				Great Veins	1.6 cm
				Venae Cavae	3.2 cm

Table 1.2: **Average diameters of neural architecture.** Typical diameters of neuronal and vascular structures fall within the resolution limits of multiphoton fluorescence microscopy [36,37].

Fluorescence microscopy can provide anatomical, spectroscopic, or functional information. Anatomical, or structural imaging is the most readily understood of the three. By relying on intrinsic fluorescence or introducing highly specific fluorescent probes to a specimen for excitation with an appropriate laser source, one can map out the physical architecture of a region of interest. Spectroscopic imaging refers to specialized implementations of fluorescence microscopy that enable investigators to uncover the optical properties and/or composition of those structures. For example, early *in vivo* multiphoton spectroscopic studies of human dermis showed that reduced pyridine nucleotides, NAD(P)H, may strongly contribute to autofluorescence at 730 nm excitation, whereas flavoprotein was a more likely contributor at 960 nm excitation [38]. Functional imaging is less concerned with structural anatomy, and more directly refers to the

underlying function and behavior of certain anatomical regions.

In the context of fluorescence functional imaging of the brain, there are three primary categories of functional information we endeavor to procure: metabolic, hemodynamic, and neuronal. Metabolic imaging typically exploits weak endogenous fluorescent signals to trace cell activity before, during, and after critical events such as tissue development and differentiation. Common targets for metabolic imaging are nicotinamide and flavin adenine dinucleotides (NADH and FAD), which are broadly implicated in the progression and regulation of nearly every major metabolic pathway [39]. Hemodynamic characteristics of interest include blood flow or flux, blood volume or hematocrit, and blood oxygenation levels, each of which can be garnered with unique fluorescent techniques. For instance, intravenous injection of fluorescently-labeled red blood cells and video-rate imaging can be used to measure blood flow velocity [40]. Alternatively, successive line-scans of a vessel injected with fluorescent dye can be used to track the spatial evolution of dark (i.e. non-fluorescent) red blood cells in time to assess their flux [mm/sec] and linear density [mm^{-1}] to calculate flux [s^{-1}] [41]. With knowledge of that vessel's cross-sectional area, one can also infer hematocrit. Finally, fluorescence microscopy is an attractive tool for measuring intravenous dissolved oxygen concentration due to its non-invasive nature, especially when compared to present alternatives. The most common method of measuring pO_2 in biological samples is the Clark electrode. However, its tip must be inserted directly into the region of interest and three-dimensional approaches would thus be highly invasive, physiologically disruptive, and slow [42]. In contrast, electron paramagnetic resonance oximetry can produce three-dimensional interstitial and intravascular pO_2 maps non-invasively [43]. Problematically, its spatial resolution is limited to ~200 μm *in vivo* [43]. In principle, two-photon laser scanning microscopy (2P-LSM) and phosphorescence lifetime measurements could be

readily combined for deep, high-resolution oximetry. Oxygen is one of the best-known collisional quenchers, and specific oxygen concentrations affect phosphorescent yields and lifetimes to varying degrees [44]. Probes with controllable quenching parameters and defined bio-distributions can thus be delivered directly to regions of interest and serve as site-specific molecular oxygen sensors. However, phosphorescent probes are either largely uncharacterized for their two-photon spectra or exhibit weak two-photon absorption cross sections, meaning this work is still in its infancy [45]. Nevertheless, given the importance of oxygen consumption in dynamic *in vivo* processes and the rising adoption of multiphoton microscopy, the potential outlook of various molecular oxygen sensors for high-resolution non-invasive two-photon oximetry remains optimistic.

Our final category of interest for functional optical brain imaging of interest is neural. Structural neuroimaging is readily carried out using standard (e.g. green fluorescent protein; GFP) or slightly more exotic (e.g. tdTomato) genetically encoded contrast agents. However, the development of more sophisticated probes can now provide functionality beyond simply providing contrast, and can be used to monitor the activity of distinct neurons in brain tissue [46]. Indicators of neural activity rely on sensitivity to calcium ions (a proxy for action potentials), membrane potentials, or neurotransmitters [47]. In particular, genetically encoded calcium indicators (GECIs) have garnered attention and popularity within the neuroscience community, despite challenges related to rapid calcium dynamics and low peak calcium accumulations [48]. Advances in protein engineering, structure based-design, and mutagenesis has produced a family of ultrasensitive protein calcium sensors (GCaMP6) that vastly outperform other indicators in terms of both sensitivity and reliability [49–51]. These sensors can be used to visualize large groups of neurons in addition to smaller synaptic protrusions, and remain stable for months [52]. The GCaMP6 family will undoubtedly be used to answer

significant questions in neuroscientific research and recent work has even enabled *in vivo* functional imaging of the hippocampus at a ~1 mm depth in mice [53].

Altogether, when one considers the collective ability of fluorescence microscopy, which spans the anatomic, functional, and spectroscopic domains, it presents itself as a very attractive research tool. Moreover, we believe that the fact that fluorescence microscopy can be used to capture hemodynamics, neural signaling, and metabolic activity makes it a particularly adept tool for *in vivo* brain imaging and neuroscientific studies in particular. For instance, a single multiphoton microscope could sufficiently probe the coupling between synaptic reorganization and hemodynamic oxygen supplies, leading to a deeper understanding of oxygen delivery and consumption by dendritic spines at a high three-dimensional spatial resolution. Longitudinal structural imaging experiments can be used to trace dendritic spine turnover in peri-infarct regions of the brain after stroke or traumatic brain injury while genetically encoded calcium indicators can indirectly report on the activity levels of the associated neurons. A concomitant scan of a molecular oxygen sensor such as PtP-C343 can accompany these observations for a quantitative characterization of environmental oxygen and its association with neural microanatomy. Ultimately, the richness and breadth of information gained from a simple uni-modal system (multiphoton microscopy) can tap into a nuanced understanding of hypoxic and anoxic environment on spine disappearance and regrowth. Finally, we emphasize that fluorescent microscopy possesses the resolution required to carry out these studies at the single cell level, unlike MRI, CT, PET or the other non-fluorescent modalities assessed in the previous section.

1.3 Advantages and Variations of Multiphoton Microscopy

In this section we will further delineate between different categories of

multiphoton microscopy, but more fundamentally, we establish multiphoton microscopy's inherent advantage to one-photon microscopy (1PM) in its ability to probe *in vivo* biological processes at greater depths at high spatial resolutions. 1PM is a non-depth resolved technique, meaning that fluorescence is smeared along the optical axis. Thus, images recorded by upright or inverted epifluorescence microscopes will contain substantial background fluorescence from thick specimens. Confocal laser-scanning microscopy (LSM) enables optical sectioning by placing a spinning disk array of pinholes before the detector to reject out-of-focus light. Even in the case of confocal LSM, one-photon excitation is limited to visualization of superficial tissue layers due to the extensive scattering of shorter wavelength excitation sources. In contrast, multiphoton microscopy, an LSM technique where a diffraction-limited, focused beam is raster-scanned across a specimen [6], allows for inherent optical sectioning without a requirement for pinholes due to the highly improbable nature of two or more photons being simultaneously absorbed by the same fluorophore away from focus. To elaborate, "simultaneous" refers to the maximum possible time period Δt between photon absorption events in which their summed energy will incite an electronic transition, which can be determined by the Heisenberg uncertainty principle, where ΔE is the difference in photon energy and the electronic transition energy gap and h is Planck's constant.

$$\Delta t = \frac{h}{4\pi\Delta E} \tag{1.4}$$

Using this formula, typical multiphoton excitation events require sub-femtosecond absorption time differentials, which requires an unfathomably immense photon flux. Therefore, multiphoton microscopy relies on two key technologies to ensure sufficient photon density. First, high numerical aperture (NA) objectives are used to

tightly focus light into a condensed point spread function and ensure the spatial density of excitation power. Second, pulsed ultrafast lasers, typically on the femtosecond scale are used to ensure the temporal overlap of excitatory photons. Therefore, these ultrafast lasers are distinct from one-photon sources in that they feature high peak powers and pulse energies relative to their average powers. Given the integration of high NA objectives with ultrafast lasers, multiphoton excitation is then an inherently localized, nonlinear process where fluorescence is given by I^n and n denotes the number of photons absorbed.

A second advantage of multiphoton microscopy is the reduction of background autofluorescence. Single-photon absorption usually occurs in the visible spectrum (~380 – 740 nm) and a typical one-photon microscope is commonly equipped with a set of laser excitation sources at 405, 488, 561, and 647 nm. Since multiphoton excitation relies on more than one photon to produce the same excited state, its laser sources are substantially lower energy or longer wavelength, most commonly in the near-infrared region of the spectrum ($\geq$ 750 nm). Near-infrared (NIR) excitation of fluorescence contrast agents has a few critical advantages, particularly for *in vivo* biological imaging. Unwanted tissue autofluorescence, or excited light emanating from unintended structures, is markedly reduced by NIR light. For instance, 'green' autofluorescence of the skin and viscera severely limits signal-to-background-ratio under blue light but not NIR light [54]. Moreover, *ex vivo* autofluorescence of fixed tissues is quite problematic in the visible regime. Glutaraldehyde, an ubiquitous fixative used to preserve cellular structures by crosslinking protein functional groups, is an indiscriminant source of background with visible excitation, but indiscernible at longer wavelengths [55]. Overall, reduced NIR autofluorescence from intrinsic (e.g. dermis) or exogenous (e.g. fixative) agents allows signal from fluorescent contrast agents to be collected in the absence of excessive

background, producing multiphoton images with greater signal-to-background ratios relative to conventional fluorescence microscopy. Finally, longer multiphoton excitation wavelengths are less prone to scatter in biological tissue than visible single photon excitation wavelengths, which allows a greater fraction of excitation light to arrive to the focal plane.

Multiphoton microscopy itself is a broad term that collectively describes any fluorescence process produced by the absorption of two or more photons. In the remainder of this section we will differentiate between two- and three-photon microscopy as well as degenerate-, non-degenerate, and two-color multiphoton microscopy.

1.3.1 Two- and Three-Photon Microscopy

Both two- and three-photon microscopy are nonlinear process where fluorescent signal generation is given by I^n, where I is excitation intensity and n denotes the number of photons absorbed. However, two- photon microscopy remains limited in its maximum imaging depth relative to its higher order analogues by tissue scattering limits [56]. Three-photon excitation allows researchers to target fluorophores at longer wavelengths where absorption and tissue scattering events are minimized [46,56], thereby overcoming background limitations and improving depth penetration. Of course, three-photon microscopy is not without its drawbacks. For instance, few fluorophores have been characterized for their intrinsic three-photon properties, and fewer still have been engineered and optimized specifically for three-photon excitation. Moreover, given comparable two- and three-photon cross sections, three-photon excitation requires higher pulse energies, which can lead to phototoxic effects in biological samples. Even in fixed or non-living samples, high pulse energies can lead to heating, ablation, or even ionization. Nevertheless, suppressed out-of-plane fluorescence, reduced scattering, and

increased signal-to-background ratio (SBR) remain significant motivators for the increased utilization rate of three-photon microscopy.

To compare two- and three-photon (2P and 3P) microscopy SBR for deep, high resolution imaging in highly scattering biological tissue, we derive relative expressions using a set of equations laid out by Horton et al. (2013) [56]. If we first assume that imaging depth is significantly longer than the uniformly labeled specimen's effective attenuation length, and that attenuation length is significantly longer than the objective focal length, such that $z \gg l_e \gg f$ then the time-averaged two- and three-photon signal generated by a diffraction-limited Gaussian beam is:

$$\langle F(t)_{2P} \rangle = 8C_2 n_0 \frac{\langle P \rangle^2}{\pi \lambda_{ex}} e^{\frac{-2z}{l_e}} \tag{1.5}$$

$$\langle F(t)_{3P} \rangle = 3.5C_3 n_0 \frac{NA^2 \langle P \rangle^3}{\lambda_{ex}^3} e^{\frac{-3z}{l_e}} \tag{1.6}$$

where NA is objective numerical aperture, n_0 is refractive index, $\langle P \rangle$ is average power, λ_{ex} is excitation wavelength, and C_n are constants that capture fluorophore properties such as concentration and absorption cross section [56]. Meanwhile, background is dictated by the excitation order, n, time-average intensity, $\langle I \rangle$, and cross sectional beam area on the tissue surface, A:

$$B \propto \langle I \rangle^n A l_e = \frac{\langle P \rangle^n}{A^{n-1}} l_e \tag{1.7}$$

Thus, two- and three-photon background levels, are approximated by:

$$B_{2P} = C_{2P} \langle P \rangle^2 \frac{n_0^2 l_e}{\pi z^2 NA^2} \tag{1.8}$$

$$B_{3P} = C_{3P} \langle P \rangle^3 \frac{n_0^4 l_e}{\pi^2 z^4 NA^4} \tag{1.9}$$

We are then able to simply calculate SBR as a ratio using Equations 1.5 - 1.6 and

Equations 1.8 – 1.9.

$$SBR_{2P} \approx \frac{6(NA)^2 z^2}{\lambda_{ex} l_e} e^{\frac{-2z}{l_e}} \tag{1.10}$$

$$SBR_{3P} \approx \frac{14.7(NA)^6 z^4}{\lambda_{ex}^3 l_e} e^{\frac{-3z}{l_e}} \tag{1.11}$$

Using Equations 1.10 and 1.11, we compare two- and three-photon SBR at a 750 – 3750 μm imaging depth using 1.0 NA objective to show that three-photon SBR is significantly better at equivalent imaging wavelengths (**Figure 1.1**). Attenuation lengths were obtained from Wang et al. (2018) and were specific to *in vivo* imaging of mouse brain [57]. The substantial improvement in SBR conferred by three-photon microscopy provides ample motivation to specifically engineer fluorophores for enhanced three-photon absorption. When one considers that two- and three-photon SBR is more realistically compared at different excitation wavelengths since three-photon absorption requires a lower energy for a given fluorophore, the advantages of three-photon excitation become even more apparent. For instance, three-photon SBR at 1300 nm excitation at a ~3 mm imaging depth rivals expected two-photon SBR at 920 nm excitation at a ~1 mm imaging depth.

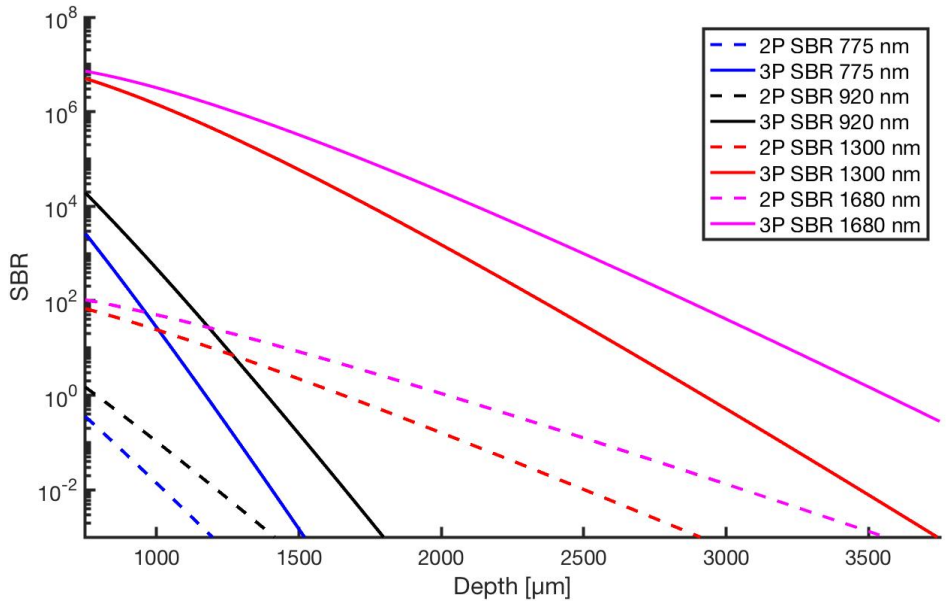

Figure 1.1: **Multiphoton signal-to-background ratio.** Two- (2P) versus three-photon (3P) signal-to-background ratio (SBR) from a 750 – 3750 μm *in vivo* imaging depth in mouse brain. Attenuation lengths: ~131 μm at 775 nm, ~155 μm at 920 nm, ~312 μm at 1300 nm, and ~383 μm at 1680 nm [57].

1.3.2 Two-color, Degenerate-, and Non-Degenerate Multiphoton Microscopy

Conventional, or degenerate, multiphoton microscopy (D-MPM) relies on the absorption of two or more spatiotemporally overlapped photons of identical energies to produce fluorescence [58]. Meanwhile, two-color imaging combines synchronized pulses from two lasers of different wavelengths (λ_1 and λ_2) to excite a fluorophore transition [59,60]. Provided the two pulses arrive at the same location at the same time, the energies of the photons compound at an intermediate excitation wavelength given by:

$$\lambda_3 = 2(\lambda_1^{-1} + \lambda_2^{-1})^{-1} \tag{1.12}$$

Notably, the total excitation of the combined beams is:

$$[I_1(\boldsymbol{r}, t-\tau) + I_2(\boldsymbol{r}, t)]^2 = I_1^2(\boldsymbol{r}, t-\tau) + I_2^2(\boldsymbol{r}, t) + 2I_1(\boldsymbol{r}, t-\tau)I_2(\boldsymbol{r}, t) \tag{1.13}$$

where **r** = (x,y) denotes the distance from the optical axis and τ refers to the temporal offset of the two beams [61]. $I_1^2(\boldsymbol{r}, t-\tau)$ and $I_2^2(\boldsymbol{r}, t)$ are the degenerate excitation

profiles (i.e. point spread function, or PSF) at λ_1 and λ_2 respectively, whereas $2I_1(\boldsymbol{r}, t-\tau)I_2(\boldsymbol{r}, t)$ dictates the non-degenerate PSF at λ_3. Existing literature has failed to distinguish between two-color multiphoton microscopy (2C-MPM) and non-degenerate multiphoton microscopy (ND-MPM), although there are significant distinctions that can be drawn. 2C-MPM yields the combined degenerate and non-degenerate excitation profiles, which typically results in a marked increase in fluorescence intensity [62] (**Figure 1.2**) and enables simultaneous multicolor imaging capabilities [63].

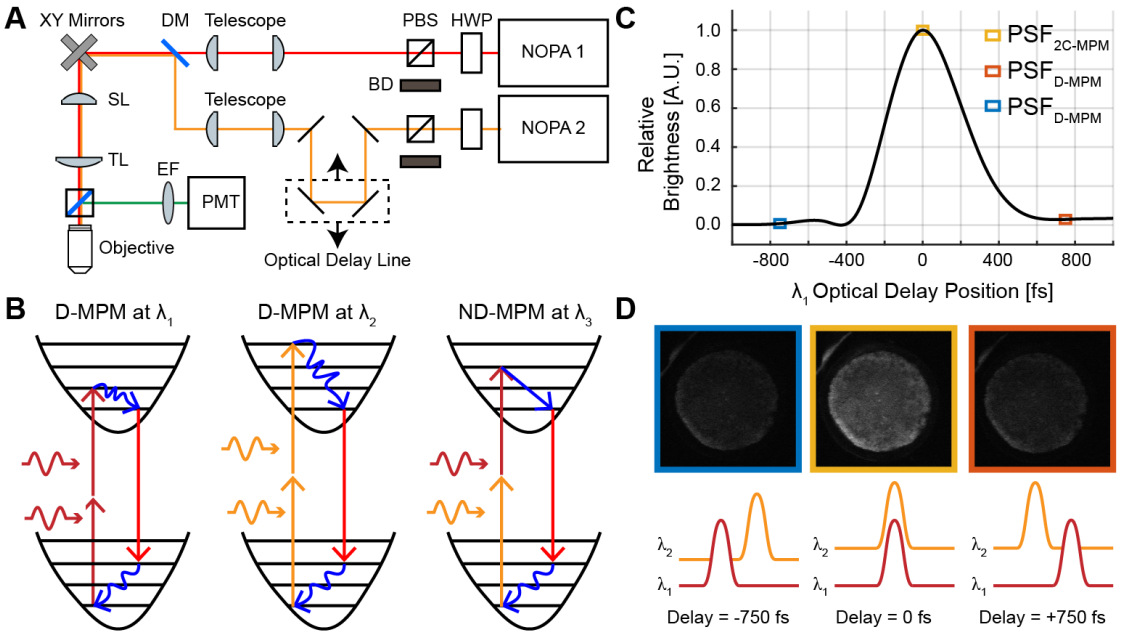

Figure 1.2: **Two-color multiphoton microscopy results in degenerate and non-degenerate excitation processes.** (*A*) A two-color multiphoton microscopy (2C-MPM) schematic; NOPA, noncollinear optical parametric amplifiers; HWP, half wave plate; PBS, polarizing beam splitter; BD, beam dump; DM, dichroic mirror; SL, scan lens; TL, tube lens; EF, emission filter; PMT, photomultiplier tube. (*B*) 2C-MPM can result in the degenerate absorption of photons with equal energies (D-MPM) and the non-degenerate absorption of photons with distinct energies (ND-MPM). (*C-D*) Temporal overlap of the co-aligned two-color beams results in a pronounced increase in brightness as non-degenerate excitation pathways become available.

Meanwhile, ND-MPM is an implementation of 2C-MPM where the target fluorophore's cross sections at λ_1 and λ_2 are negligible, resulting solely in the $2I_1(\boldsymbol{r}, t-\tau)I_2(\boldsymbol{r}, t)$ excitation profile at the virtual excitation wavelength λ_3 when $\tau \sim 0$ fs. Thus, ND-MPM as defined herein cannot achieve multicolor imaging effects, and while it may potentially achieve a fluorescent intensity greater than conventional D-MPM at equivalent wavelengths in certain cases, it will always produce a dimmer signal than collective 2C-MPM. Instead, ND-MPM is denoted by its own set of unique photophysical advantages, namely improved signal-to-background ratio [64] and improved spatial resolution for a given excitation wavelength (**Figure 1.3**). To compare D-, 2C-, and ND-MPM resolution we modeled circularly polarized beam profiles in the transverse *xy*-plane at wavelengths ranging from 650 to 2000 nm as they propagate through a 20x objective using water immersion (NA = 1.0; 20 mm bandwidth; $f_{\text{Tube Lens}}$ = 200 mm). Time-invariant matched mode mixing with no optical delay at $2I_1(\boldsymbol{r})I_2(\boldsymbol{r})$ was performed at all possible wavelength combinations to generate ND-MPM point spread functions and central line profiles were extracted. Gaussian fitting to the resulting line profiles and their corresponding full-width at half-maximum (FWHM) values were used to define resolution. D-, 2C-, and ND-MPM resolutions were directly compared at corresponding excitation wavelengths, λ_{ex}, where the D-λ_{ex} is the one color case, λ_D, and the 2C- and ND-λ_{ex} is λ_3. Since various combinations of λ_1 and λ_2 can result in identical λ_3 values, multiple 2C- and ND- data points are available at each discrete compound wavelength and direct comparisons were made at matching excitation wavelengths where $\lambda_D = \lambda_3$ for the 1C (D-MPM) and 2C (2C-MPM and ND-MPM) cases respectively. It is observed that the condition $\lambda_1 = \lambda_2$ results in identical transverse resolution for all MPM variants, as expected, whereas all other combinations where $\lambda_1 \neq \lambda_2$ results in a resolution enhancement for ND-MPM. Meanwhile, 2C excitation profiles, calculated according to

the combined PSFs $I_1^2(\mathbf{r}) + I_2^2(\mathbf{r}) + 2I_1(\mathbf{r})I_2(\mathbf{r})$, were shown to suffer degraded resolution for all wavelength combinations, except where $\lambda_1 = \lambda_2$ as in the case above. This entire process was repeated to assess axial resolution by modeling the beam profiles in the *xz*-plane and once again ND-MPM resolution was found to be most optimal while 2C-MPM resolution was poorest (**Figure 2(d)**). We emphasize that ND-MPM's inherent resolution enhancement capabilities are a novel discovery, made possible perhaps due to our distinction between 2C-MPM, which features non-negligible degenerate two photon absorption across sections, $\sigma_D^{(2)}(\lambda_1, \lambda_2)$, versus ND-MPM, where $\sigma_D^{(2)}(\lambda_1, \lambda_2) << \sigma_{ND}^{(2)}(\lambda_1, \lambda_2)$.

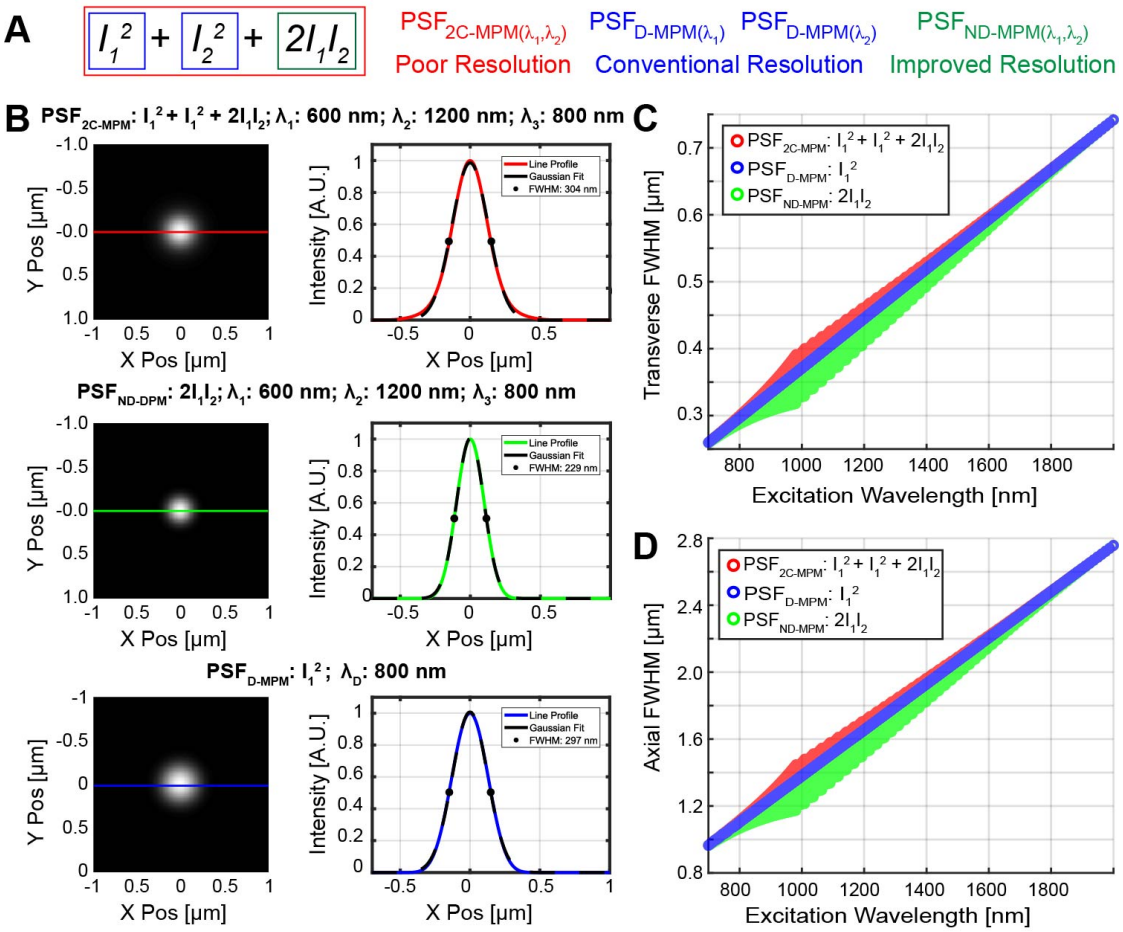

Figure 1.3: **Axial and transverse resolution comparisons of D-, 2C- and ND-MPM reveals that ND-MPM is inherently super-resolution.** (*A*) Two-color multiphoton microscopy (2C-MPM) results in a combined 2C point spread function, $\mathrm{PSF}_{\mathrm{2C-MPM}(\lambda_1,\lambda_2)}$, comprised of degenerate-, $\mathrm{PSF}_{\mathrm{D-MPM}(\lambda_1)}$ and $\mathrm{PSF}_{\mathrm{D-MPM}(\lambda_2)}$, and non-degenerate PSFs, $\mathrm{PSF}_{\mathrm{ND-MPM}(\lambda_3)}$. (B) Transverse cross section of a $\mathrm{PSF}_{\mathrm{2C-MPM}(\lambda_1=600\ \mathrm{nm},\ \lambda_2=1200\ \mathrm{nm})}$ and its constituent $\mathrm{PSF}_{\mathrm{ND-MPM}(\lambda_3=800\ \mathrm{nm})}$ compared to the matching $\mathrm{PSF}_{\mathrm{D-MPM}(\lambda_D=800\ \mathrm{nm})}$, where λ_D denotes the direct one-color, degenerate excitation wavelength and $\lambda_D = \lambda_3$. Solid lines denote intensity profile positions, plotted to the right with their Gaussian fits and full-width at half-maxima (FWHM). (C) A comparison of 2C-, D-, and ND-MPM resolution in the transverse and (D) axial dimensions.

Chapter 2: Tools for Large-Scale, Chronic Multiphoton Imaging of Cerebrovascular Architecture[1]

2.1 INTRODUCTION

The ideal neuroimaging modality maximizes optical access, sampling speed, and spatial resolution with excellent signal-to-noise ratio and high contrast [65]. Optical access describes the physical extent or volume over which data can be recorded, which is a product of both depth and field of view. Optical access is typically limited by optical aberrations and light scattering or attenuation [65]. Sampling speed refers to the rate at which these volumes can be recorded, and is directly constrained by the repetition rate of excitation sources [66], sample brightness [67], and the inertia of available instrumentation [65,66]. Finally, spatial resolution refers to the minimum spacing required by an imaging modality to differentiate two objects, and is dictated by a combination of physical characteristics (i.e. wavelength and numerical aperture), optical aberrations, and the number of pixels utilized in the construction of a digital image [68–70]. This chapter takes aim at improving optical access (i.e. imaging depth and field-of-view) and throughput for large-scale chronic vascular imaging, while maintaining sufficient resolution for the capture and co-registration of neuron structures.

---

[1] Portions of Chapter Two are based on prior publications. Ahmed Hassan conducted all experiments and independently wrote, "Hassan, A.M., Wu, X., Jarrett, J.W., Xu, S., Yu, J., Miller, D.R., Perillo, E.P., Liu, Y.L., Chiu, D.T., Yeh, H.C. and Dunn, A.K., 2019. Polymer dots enable deep in vivo multiphoton fluorescence imaging of microvasculature. *Biomedical optics express*, *10*(2), pp.584-599." He also performed all sample preparation and imaging experiments from, "Miller, D.R., Hassan, A.M., Jarrett, J.W., Medina, F.A., Perillo, E.P., Hagan, K., Kazmi, S.S., Clark, T.A., Sullender, C.T., Jones, T.A. and Zemelman, B.V., 2017. In vivo multiphoton imaging of a diverse array of fluorophores to investigate deep neurovascular structure. *Biomedical optics express*, *8*(7), pp.3470-3481."

2.2 Extending Multiphoton Imaging Depth

Multiphoton microscopy's ability to non-invasively provide depth-resolved images approaching millimeter depths has allowed it to emerge as a staple in neuroscientific investigations. However, layers of anatomy beyond a millimeter depth remain highly desirable imaging targets, and the optical properties that influence imaging depth must be fully understood to access layers beyond the rodent cortex. At the most fundamental level, scattering and absorption of both excitation and emission light restricts overall signal collection as well as the signal-to-background ratio of multiphoton images [71]. In certain cases, advanced surgical preparations such as polished skulls [72,73] or chronic cranial windows [74,75] can greatly reduce attenuation. In more extreme circumstances, embedded prisms [76,77] or gradient index lenses [78,79] can be used to bypass layers of anatomy entirely [65]. More recently however, several groups have exploited the decrease in light scattering with increasing wavelength to achieve imaging depths approaching 1.6 mm [80,81]. Moreover, three-photon excitation has been shown to reduce out-of-focus light to produce signal-to-background ratios that are orders of magnitude larger than conventional two-photon microscopy and thereby increase depth penetration [57,82–84]. These accomplishments are predicated on the development of high-power excitation sources at longer wavelengths and the availability of brighter, compatible fluorophores with large absorption cross sections and high quantum yields. Thus, characterizing the nonlinear properties and compatibility of existing contrast agents with longer-wavelength excitation sources is critical towards their adoption in multiphoton microscopy and evaluation for deep imaging applications [46]. In the following sections, we detail factors that influence and limit imaging depth and provide a thorough photophysical characterization of polymer dots, whose broad light absorption enables compatibility with multiple laser sources, allowing us to identify

ideal excitation wavelengths to minimize tissue scattering and water absorption for deep *in vivo* imaging.

2.2.1 Tissue Optical Properties

To collect signal deep within scattering medium, two basic factors must be considered. First, sufficient excitation light must be delivered to the focal plane of interest. Second, a sufficient number of fluorescent photons must be captured from the sample plane to maintain an appreciable signal-to-noise and signal-to-background ratio for image reconstruction. Excitation light is mainly reduced by a complement of scattering and absorption events in heterogeneous biological tissue, where total attenuation at a depth z is given by:

$$exp\left[-\left(\mu_a(\lambda) + \mu_s(\lambda)\right)z\right] \tag{2.1}$$

where μ_a and μ_s [cm^{-1}] are the bulk tissue absorption and scattering coefficients respectively. Absorption is both wavelength- and chromophore-dependent, and each constituent in tissue (e.g. hemoglobin or water molecules) has a unique absorption profile, most accurately captured by its molar extinction coefficient, ε' [$M^{-1}cm^{-1}$], such that the absorption coefficient with respect to any single chromophore in tissue with a concentration C is:

$$\mu_a(\lambda) = \varepsilon'(\lambda)C \tag{2.2}$$

In media with multiple species of chromophores, such as biological tissue, the total absorption coefficient is calculated by:

$$\mu_a(\lambda) = \sum_{i=1}^{N_{chromophores}} \varepsilon_i'(\lambda)C_i \tag{2.3}$$

and the mean free path of an excitation photon before absorption is $\frac{1}{\mu_a(\lambda)}$. To assess the attenuation of fluorescence traveling in the opposite direction, one can simply assume the

same tissue properties, only evaluated at the wavelength of the lower energy emitted light. Similarly, the scattering coefficient μ_s is determined by the medium's unique scattering cross section, which is a direct function of particle size and refractive index relative to the surrounding medium. There are many paradigms and probability density functions that describe scattering, and the appropriate model strongly depends on the size of the scattering particles relative to interrogation wavelength and the physical properties of the interface(s) in question (e.g. specular, diffuse, lambertian, etc.). Regardless of which scattering phase function is used, they generally assign a probability distribution to the direction of scattered light (i.e. scattering anisotropy) and the expected distance traveled between scattering effects. Since chromophore refractive indices' bearing on scattering probability depends on their relative difference with respect to their substrate, the more heterogeneous a tissue is, the greater the probability of a scattering event.

For brain tissue in particular, absorption is predominantly influenced by the presence of hemoglobin and water content. Typically, attenuation decreases with increasing wavelength although there are high absorption bands in water around ~1500 nm and ~1900 nm (**Figure 2.1**). Therefore, ideal biological imaging wavelengths present themselves around ~1300 nm and ~1700 nm, where photoattenuation is minimized [46]. In theory, one can compensate for attenuation with increased laser power, particularly with amplified fiber lasers, but this becomes quite risky for *in vivo* contexts due to water absorption. At excitation wavelengths where water absorption is greater, tissue heating becomes a salient concern due to its disruption of normal biological function and potential for acute damage in more extreme cases.

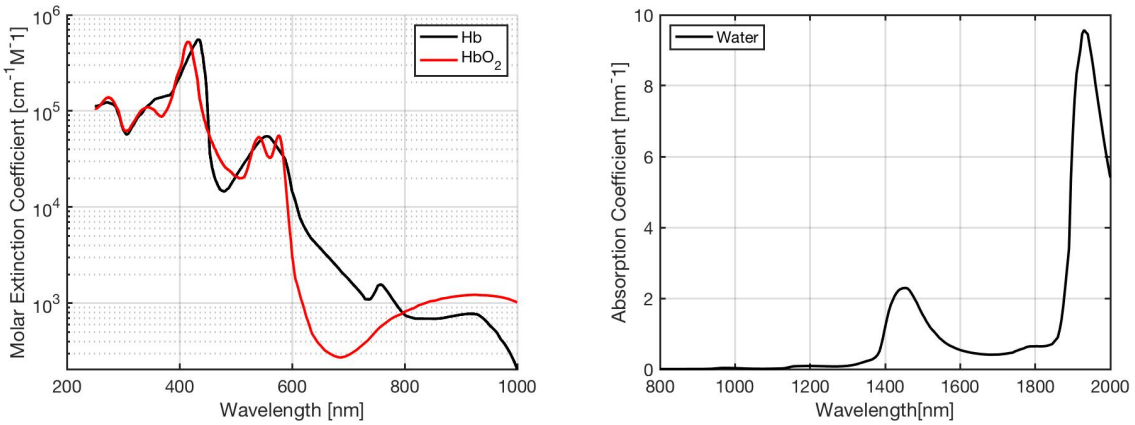

Figure 2.1: **Hemoglobin and water's effects on brain tissue absorption is wavelength dependent**. (*Left*) Molar extinction coefficient of oxygenated (HbO_2) and unoxygenated hemoglobin (Hb). (*Right*) Absorption coefficient of water.

2.2.2 Ultrafast Laser Sources and Deep Imaging

The laser source properties used for multiphoton imaging unquestionably affect imaging depth. Generally, one may describe a pulsed laser by its average power [W], pulse width full-width at half-maximum [fs], repetition rate [s^{-1}], and wavelength [nm]. Given this information, one is able to determine peak power, pulse energy, peak-to-peak time, and the number of photons per pulse. Excitation wavelength influences imaging depth in two ways: (1) absorption and scattering in the specimen of interest is wavelength-dependent, as discussed in the previous section, and (2) fluorophore absorption cross sections vary by wavelength. Excitation wavelengths less prone to scatter or absorption in tissue will ensure a greater fraction of excitation light arriving at the sample plane, while targeting a fluorescent probe at its peak multiphoton absorption cross section will yield a greater number of signal photons and help maximize signal-to-background ratio. As multichannel imaging experiments become more ubiquitous, a researcher is forced to either select a single excitation wavelength that produces a

reasonable compromise in terms of signal levels in all channels, or use several excitation wavelengths specific to each unique probe. This latter option is preferred, but requires either the availability of multiple excitation sources or a single tunable excitation source.

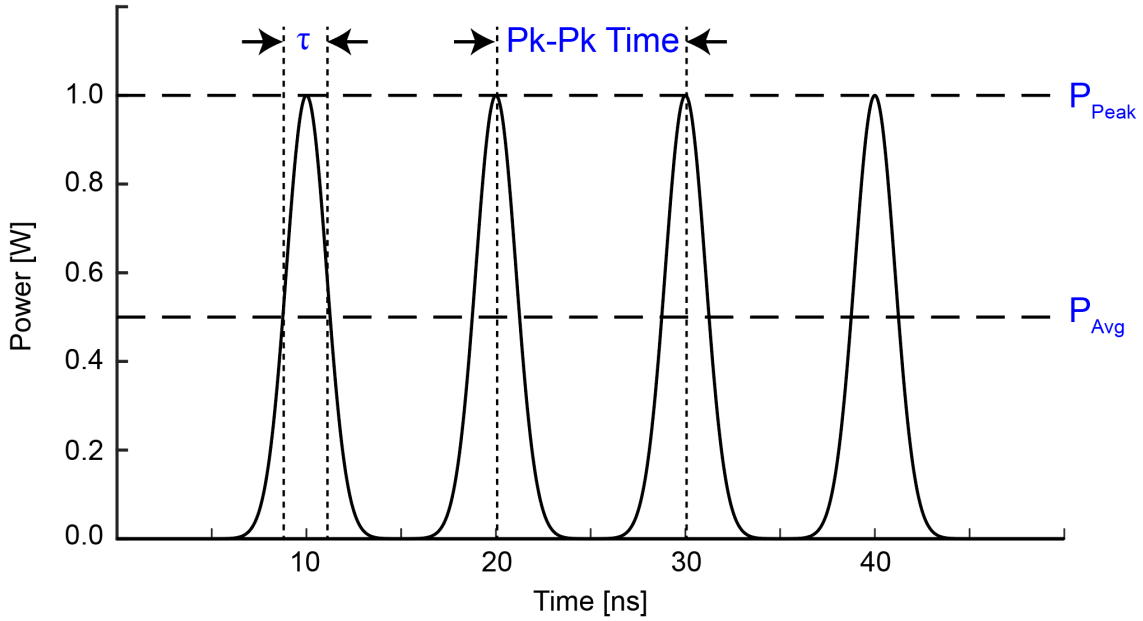

Figure 2.2: **Properties of pulsed ultrafast lasers**. Wavelength (not depicted), peak power (P_{Peak}), average power (P_{Avg}), peak-to-peak time (Pk-Pk Time), and pulse width (τ) are all important considerations with respect to imaging depth. Repetition rate, or the number of pulses per second can be inferred from peak-to-peak time. Average power and repetition rate collectively determine pulse energy. Typically, deep imaging setups require high average power and lower frequency repetition rates to ensure large pulse energies, along with the ability to compress pulses temporally to achieve high peak powers. Wavelength selection should be made with respect to both tissue and fluorophore properties.

In addition, a laser source's average power, repetition rate, and pulse duration collectively influence imaging depth in a strongly inter-related fashion. Ultimately, the goal is to increase photon flux in order to improve multiphoton excitation efficiency. This can be achieved in a number of ways, but it is important to avoid large average

powers that result in significant tissue heating or large peak powers that lead to acute damage like ionization or ablation. At the most fundamental level, average power and repetition rate collectively determine pulse energy. Given a fixed pulse energy, compression to reduce pulse duration will then maximize peak power and imaging depth. Compression can be achieved using prism pairs, diffraction gratings, or chirped dielectric mirrors. Assuming an excitation source is at a known repetition rate and pulse duration, increasing average power will indeed increase peak power, but at the cost of increased tissue heating as pulse energy increases concomitantly. Thus, deep imaging generally mandates a laser with high average power (several watts or greater, which can be attenuated to avoid tissue damage when needed) and smaller repetition rates ($\leq$ 1 MHz) to ensure high pulse energies, and the ability to perform temporal pulse compression to then maximize peak power. Moreover, a tunable excitation source is highly desirable in order to capitalize on intrinsic fluorophore properties, such as their *n*-photon power dependence and cross section profiles. Spectral and temporal pulse widths are inextricably linked through the time-bandwidth product. For fully compressed transform-limited pulses, the time-bandwidth product is minimized and its exact value depends on the pulse shape. For example, the smallest achievable time-bandwidth products are ~0.315 and ~0.44 for $sech^2$-shaped and Gaussian pulses, respectively [85]. Thus, broader spectral bandwidths, such as those observed from optical parametric amplifiers, benefit deep imaging by allowing for shorter pulse durations and ergo higher peak powers. This highlights an important distinction between typical single-photon or laser speckle excitation sources and multiphoton lasers. The former exhibit broad temporal pulse widths and are therefore spatially coherent, meaning that there is a fixed relationship at multiple spatial positions at any given time. In contrast, multiphoton excitation sources are temporally

coherent, meaning they have shorter pulse widths and a defined correlation between waves at fixed locations at different points in time.

When I first joined the Functional Optical Imaging Laboratory, available excitation sources included a tunable titanium-sapphire laser (Ti:S; λ_{ex} = 700 - 900 nm; repetition rate = 76 MHz) and an optical parametric amplifier (OPA; λ_{ex} = 1100 – 1400 nm; repetition rate = 511 KHz). Through the PhD work of Dr. Evan Perillo, a high power ytterbium fiber laser was developed (Yb-fiber; λ_{ex} = 1060 nm; repetition rate = 80 MHz), along with a Raman diamond laser (λ_{ex} = 1240 nm; repetition rate = 80 MHz). Each of these lasers had their own set of advantages and drawbacks. The Ti:S laser excelled at shallow, surface tissue two-photon imaging. However, its low pulse energies prohibited routine imaging depths beyond ~600 μm, and its limited tunability meant that the vast majority of fluorophores were incompatible for three-photon microscopy. The higher pulse energy OPA was ideal for deep imaging around ~1250 nm, but its average power quickly tapered off as it was tuned above or below this wavelength. In contrast, the fiber laser excelled for high average power imaging of fluorophores such as fluorescein and Texas Red, but its discrete spectral output at 1060 nm hampered its versatility. The development of the diamond laser was intended to shift 1060 nm excitation further out into the near infrared regime, and its synchronization with the Yb-fiber laser meant that they could be used jointly for two-color excitation. However, the diamond power output is quite limited (a few hundred milliwatts) and the meager Raman shift (<200 nm) is not only static, but less than ideal for two-color imaging which benefits from a wider wavelength discrepancy, and unworkable for non-degenerate imaging of most known fluorophores.

Thus, these excitation sources left significant gaps in our multiphoton imaging capabilities that were addressed by the Spirit-NOPA system. First, we required a laser

system that could encompass a broad tuning range spanning the visible and near infrared, which would serve useful for both two- and three-photon microscopy. Second, we sought a system with high average powers across this entire spectrum, unlike the former OPA. Third, we desired a lower frequency repetition rate and a broad spectral bandwidth to ensure high pulse energies and large peak powers. Fourth, it would be ideal if this laser system could accommodate two independently tunable and synchronized sources in order to perform two-color and non-degenerate multiphoton imaging. The solution to these four requirements was the Spirit-NOPA laser system; two iterations of which were explored in the lab.

The first iteration consisted of the Spirit laser pump (Spirit 1030-70, $\Delta\tau$ = 297 fs), a 70W fiber-based pump laser that is frequency doubled and used to pump two independently tunable non-collinear optical parametric amplifiers (NOPAs; **Figure 2.3**). A high-power resistant beam splitter is used to divide the pump laser output, which means that the NOPAs are synchronized, although their path lengths are not identical. The primary NOPA in the first iteration was a NOPA-VISIR (nicknamed "Batman"), with a signal tuning range from λ_{ex} = 650 – 950 nm and an idler tuning range from λ_{ex} = 1150 – 2500 nm. As the signal wavelength is shifted, the idler wavelength shifts concomitantly, and vice versa, as the lower frequency outputs of the signal (ω_s) and idler beam (ω_i) must sum to the higher frequency input of the pump laser, $\omega_p = \omega_s + \omega_i$, in the process of optical parametric generation. Therefore, the NOPA-VISIR can be used for two-color and non-degenerate imaging individually, but its outputs are not independently tunable. To allow for independent tuning, a second NOPA-IR (nicknamed "Robin") was integrated into the system, with a single output tuning range from λ_{ex} = 1200 – 1600 nm. The repetition rate of the entire set is orchestrated by the pump laser, which can be adjusted up to 4.3 MHz. In order to maintain deep imaging capabilities with the system,

we opted for a 1 MHz repetition rate. Seeing as the NOPA-VISIR would be used more frequently, 60 W of pump power or 60 μJ of pump energy were dedicated to this source. The remaining 10 W of pump power was diverted to the NOPA-IR, meaning that 10 μJ of pump energy is applied. Overall then, the first Spirit-NOPA laser system consisted of three outputs, two of which can be independently tuned, and all of which are vertically polarized.

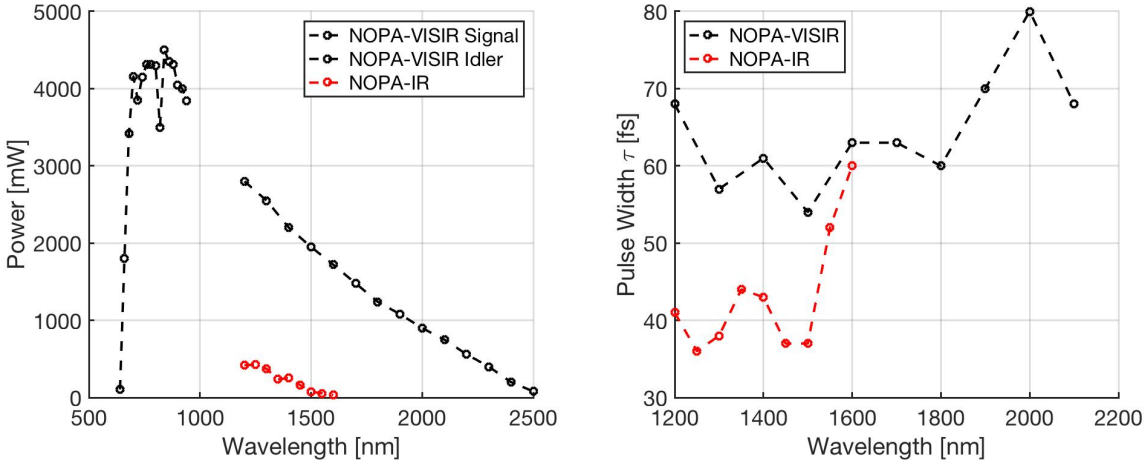

Figure 2.3: **Generation one of the Spirit laser system**. The system consists of two non-collinear optical parametric amplifiers (NOPA), one that emits in the visible (NOPA-VISIR signal) and near-infrared spectrum (NOPA-VISIR idler), and one that emits from 1200 – 1600 nm (NOPA-IR). (*Left*) Power as a function of wavelength is plotted for all three outputs. (*Right*) Pulse width as a function of wavelength is plotted for both idler outputs.

The second iteration of the Spirit laser system sought to replace the NOPA-IR with a more versatile NOPA-VISIR (**Figure 2.4**). To accommodate this change, the Spirit pump laser was now split evenly with 35 W sent to the original NOPA-VISIR (now nicknamed "Klay") and 35 W transmitted to the new laser (nicknamed "Steph"). Steph was mostly identical to Klay, with the exception of a redesigned, thicker second harmonic generation crystal, granting it slightly better conversion efficiency.

Surprisingly, Klay's properties were similar to Batman's despite the 25 W drop in pump power. This was an unexpected result, as pump conversion is believed to be a function of pulse energy, and the Spirit's repetition rate was maintained at 1 MHz. Ultimately, Steph and Klay teamed up to provide two major advantages over Batman and Robin. First, the replacement NOPA now featured outputs spanning 650 – 2500 nm, rather than just 1200 – 1600 nm. Second, the new system provides two independently tunable outputs in the near-infrared and two independently tunable outputs in the visible spectrum (four outputs in total), whereas the former system only allowed independent tunablity in the near-infrared with a single co-dependent visible line (three outputs in total).

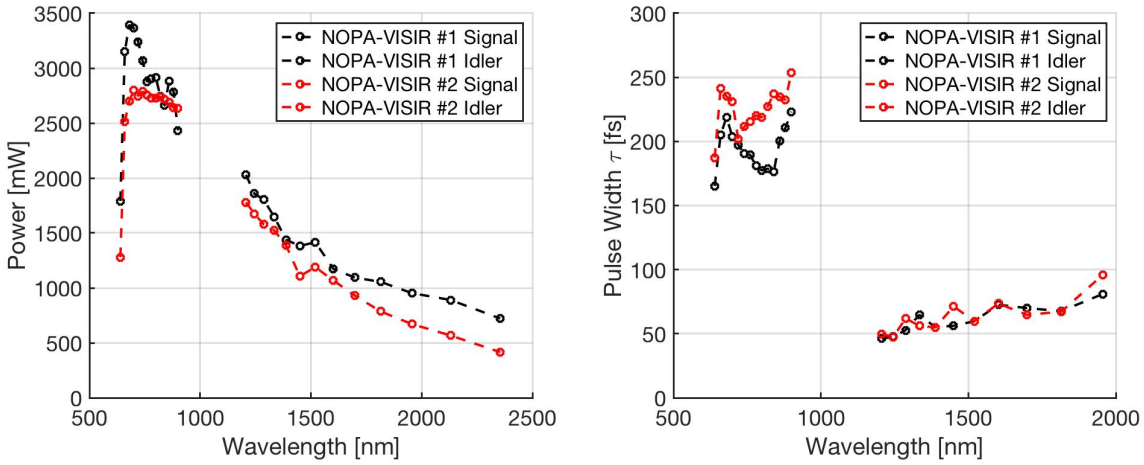

Figure 2.4: **Generation two of the Spirit laser system**. The system consists of two non-collinear optical parametric amplifiers (NOPA), both of which emit in the visible (NOPA-VISIR signal) and near-infrared spectrum (NOPA-VISIR idler). (*Left*) Power as a function of wavelength is plotted for all four outputs. (*Right*) Pulse width as a function of wavelength is plotted for all four outputs.

2.2.3 Conventional Contrast Agents and Deep Imaging

The discovery, development, and characterization of bright, biocompatible contrast agents that excite at longer wavelengths are crucial aspects to the advancement

of deep *in vivo* multiphoton microscopy [86]. Fluorophores that excite near 1300 nm or 1700 nm are of particular interest due to minimal absorption by water and reduced scattering. The choice of contrast agents used for multiphoton microscopy can be categorized into two groups: organic and inorganic contrast agents. The former class encompasses conventional organic dyes such as Texas red, fluorescein, and indocyanine green, which are extremely popular due to minimal aggregation issues and low cytotoxicity [87]. However, it is difficult to control the excitation and emission wavelengths of these dyes since their spectra are dependent on their chemical structure. In addition, fluorescent dyes commonly exhibit low quantum yields in aqueous environments, which reduces brightness in biological settings [54]. Moreover, organic dyes are problematic for immunolabeling assays, where detectability is a strong function of concentration. Nevertheless, our experiments empirically demonstrate that organic dyes are a fantastic and versatile choice for deep imaging, particularly Texas Red (**Figure 2.5**). Using an OPA to excite a 150 μl injection of 5% w/v of Texas Red in a C57 mouse prepped with an optical cranial window, we were able to achieve an imaging depth greater than 1.5 mm with excellent signal-to-background ratio even beyond 1350 μm (**Figure 2.5(b)**). Approximately 292.5 mW of power was available at the objective back aperture and an emission filter of 609/181 was used. The first half of the stack was recorded using an Olympus XLUMPLFLN20X and the bottom half was recorded using an Olympus XLPLN25XSVMP2 objective to circumvent working distance limitations.

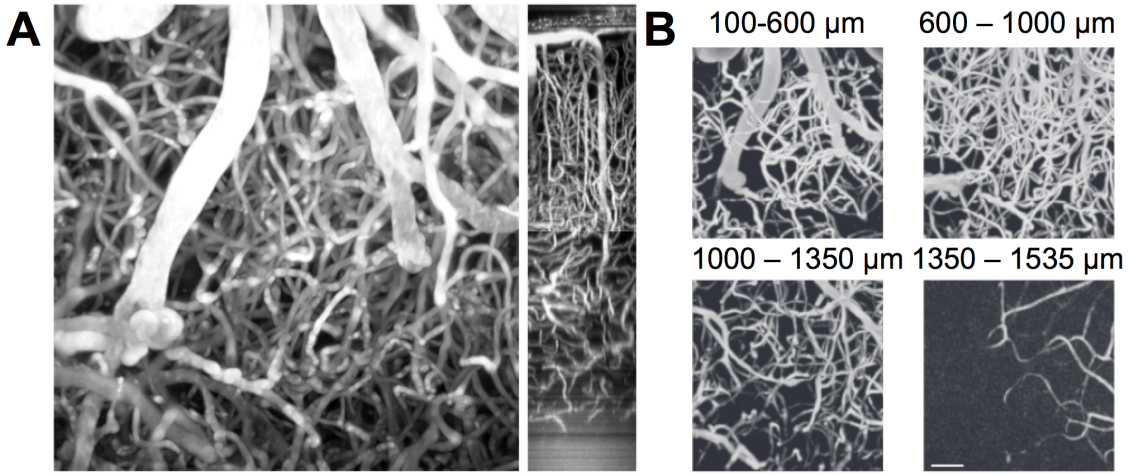

Figure 2.5: **Deep imaging with intravenously injected organic dyes**. (*A*) Tangential (left) and sagittal (right) maximum intensity projections of a 365 x 365 x 1535 µm volume of a C57 mouse injected with 150 µl of 5% Texas Red and imaged at 1225 nm. (*B*) Tangential maximum intensity projections of stack shown in (*A*). Scale bar = 50 µm.

Organic contrast agents also include fluorescent proteins, such as the omnipresent and well-heralded green-fluorescent protein (GFP). Unlike fluorescent dyes, whose targeting is usually predicated on passive bonding interactions, fluorescent proteins can be engineered to express along highly localized structures, usually by functionalization or genetic fusion to another protein of interest. Factors that influence the measured brightness of a fluorescent protein are quite unique relative to any other class of contrast agent. For example, labeling density is a major concern, along with specificity, fluorophore maturation in the context of the specimen's development, and the long-term stable expression of the fluorescent protein [88]. Moreover, fluorescent protein brightness is highly subject to environmental considerations; for example, anoxia can stunt fluorophore development and expression [88]. Beyond this, general brightness factors such as quantum yield, photostability, and the system's commensurate collection efficiency remain salient concerns as well. All in all, these characteristics make it quite

difficult to employ fluorescent proteins in a turnkey fashion, as each living organism is unique and certain environmental factors such as the presence of molecular oxygen cannot be well controlled. In the past, the adoption of far-red variations of fluorescent proteins for multiphoton microscopy has been obfuscated by their low brightness, but mKate, the pseudo-monomeric tdKatuska2, and tdTomato collectively represent a newer generation of bright, far-red emitters with substantial potential for deep *in vivo* imaging [89,90]. In collaboration with the Jones Lab (The University of Texas at Austin; Department of Psychology), we were able to obtain two-photon images of vascular structures transgenically labeled with GFP (**Figure 2.6(a-b)**). We found the appearance of the vasculature to be quite distinct from images generated with intravenous injections of organic dyes, as only the endothelial cell walls of the vasculature were subject to labeling, the end result being a series of hollowed out tube-like structures rather than filled vessels. Moreover, we observed that the connectivity was lacking, as expression wasn't continuous along the entirety of the vessel walls. In contrast, vascular images of injectable dyes are extremely continuous, the only limiting factor being how well perfused a vessel is. In fact, this may be considered an advantage for organic dye vascular imaging, as perfusion grants functional information which vascular imaging of fluorescent proteins fails to capture. Furthermore, one cannot use fluorescent protein labeling done in this fashion to gather axial line scans and infer blood flow velocity. Overall, we found that imaging depth is severely stunted (z = 250 μm) relative to what we can typically accomplish with organic dyes at similar excitation wavelengths (λ_{ex} = 790 nm). However, fluorescent proteins possess a major advantage over organic dyes in that they can be used for both neural and cerebrovascular imaging. Of course, there is nascent work being done on blood brain barrier disruption to investigate the potential of dye delivery to extravascular structures; however, these typically require additional

instrumentation such as high intensity focused ultrasound (HIFU). Here, we demonstrate OPA imaging of YFP-labeled neurons in a perfusion fixed brain slice at 1300 nm excitation without any need for HIFU or other forms of blood brain barrier disruption (**Figure 2.6(c)**). We are able to image the entire axial thickness of the brain slice without limitations from poor signal-to-background ratio.

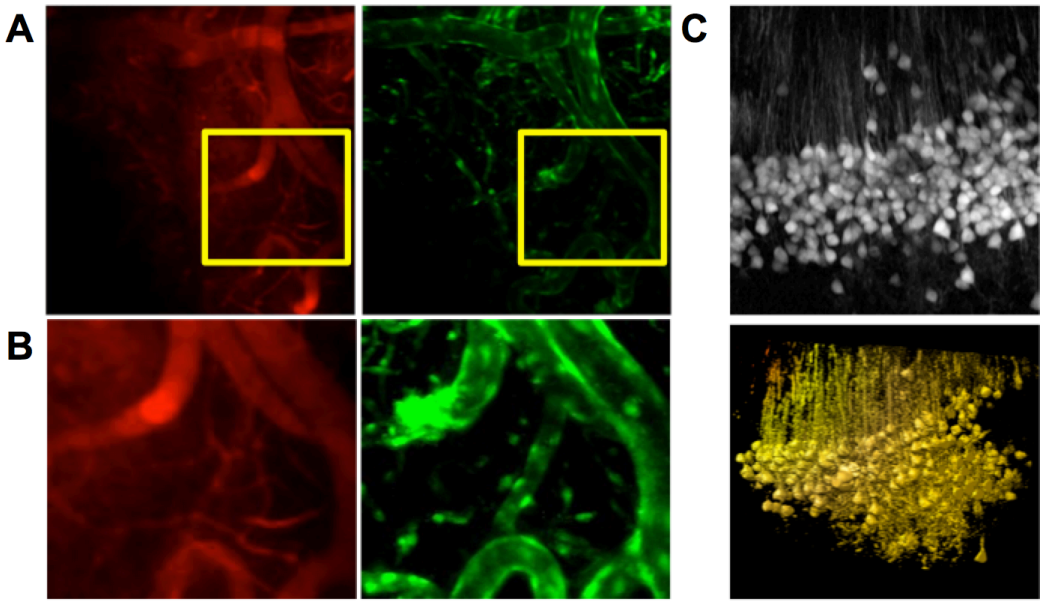

Figure 2.6: ***In vivo* imaging with genetically encoded fluorescent proteins**. (*A*) Average intensity projections of a 365 x 365 x 250 µm volume of a C57 mouse injected with (*left*) Texas Red and imaged at λ_{ex} = 1300 nm or (*right*) transgenically labeled with GFP and imaged at λ_{ex} = 890 nm. (*B*) Cropped insets corresponding to the yellow boxes in *A* show that GFP labeling is discontinuous, resulting in missing vessels. However, Texas Red excitation at 1300 nm results in significant background signal from second harmonic generation imaging of collagen. (*C*) A maximum intensity projection (*top*) and a 3D rendering (*bottom*) of a 512 x 512 x 300 µm volume of yellow-fluorescent protein labeled neurons from a perfusion fixed brain slice made in UCSF Chimera; λ_{ex} = 1300 nm.

Importantly, specially engineered adeno-associated viruses (AAVs) expressing fluorescent proteins can be used for highly-specific labeling and even functional control

of unique classes of neurons [91]. In collaboration with the Zemelman Lab (The University of Texas at Austin; The Center for Learning and Memory), we injected C57 mice with AAVs expressing Arc/Cre tdTomato to broadly target all neuron layers in the cortex and hippocampus (**Figure 2.7**). TdTomato is a bright red dimeric protein emitting at ~581 nm, a highly desirable emission wavelength for deep imaging. The main advantage of Cre recombination is it enables knockout studies of genes that are required for embryonic survival. Since the vast majority of gene knockout assays cannot easily be controlled along the organism's developmental cycle or by anatomical region, many knockout studies can be lethal. However, localized AAV injections allow us to identify and target the anatomical region of interest, meaning that tdTomato expression is limited to an empirically determined ~300 μm radius from the site of injection. Therefore, AAV injection was performed along vertical columns within the somatosensory cortex and underlying tissue at positions spaced 200 μm apart under control of a motorized three-axis stage.

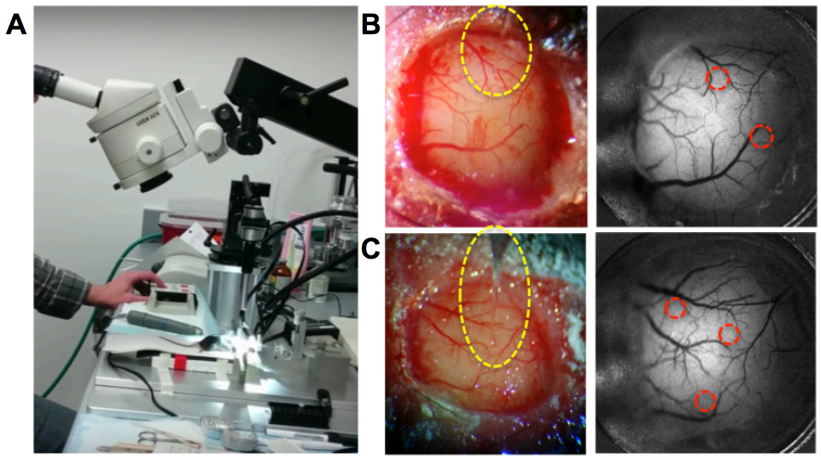

Figure 2.7: **Adeno-associated viral injections for transgenic labeling with fluorescent proteins**. (*A*) A surgical set up includes a microscope, a micromanipulator to actuate the glass capillary containing the viral injection, a drill, and an anesthesia delivery system. (*B*) A dashed yellow region-of-interest highlights a glass capillary being inserted into the cortex (*left)*, and dashed-red circles demonstrate multiple injection sites, which are intentionally selected to be free of large surface vessels to prevent excessive bleeding (*right*). (*C*) A second still image of a live injection (*left*), and an atlas of labeled regions (*right*) reinforces the critical nature of choosing areas with sparse vascular density.

Briefly, Cre recombinase catalyzes DNA recombination between flanking loxP sites to turn gene expression on or off [92]. In our Arc/Cre tdTomato mice, Cre recombinase is associated with estrogen receptors and inactive in normal mice. It is followed by a stop sequence flanked by loxP sequences, and injected Tamoxifen will bind to the estrogen receptors, inducing Cre recombinase activity and removal of the stop sequence, which in turn leads to expression of tdTomato. In this manner, tdTomato levels are under the control of Tamoxifen dosage, and expression remains stable upon induction. More sophisticated inducible Cre recombinase experiments can utilize photo-activation as a stimulus in place of Tamoxifen [93]. Regardless of the stimulus, we found inducible expression to be a significant advantage of the Cre recombinase system since we were able to directly control labeling density, and fluorophore sparsity is a major

factor dictating imaging depth. When expression reaches a critical density, out of plane excitation leads to insurmountably high background levels. Unfortunately, there is compelling evidence that Tamoxifen introduces confounding effects to genetic activity and neurophysiological functions in mouse models, meaning that structural or functional studies performed on mice with Tamoxifen induced Cre-recombinase gene inactivation must be looked at critically and with suspicion [94]. Ultimately, with some experimentation we were able to find a balance of mouse age, which affects natural estrogen levels in the body, and Tamoxifen injection volumes to yield a sufficient level of expression and image down to 1160 μm beneath the pial surface of a C57 Arc/Cre tdTomato mouse brain using 1150 nm excitation from an OPA (**Figure 2.8**).

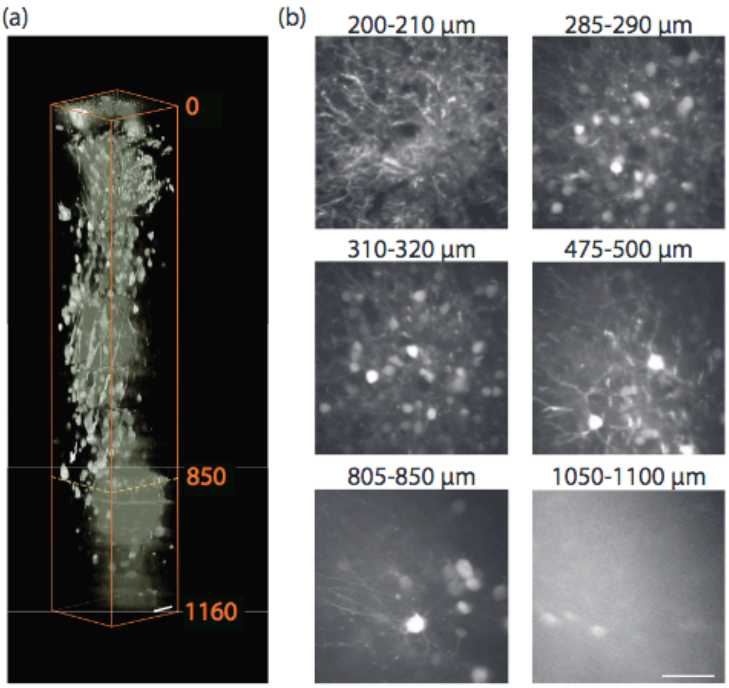

Figure 2.8: ***In vivo* multiphoton microscopy of neurons labeled with tdTomato via adeno-associated viral vectors**. (*A*) A three-dimensional reconstruction of an 1160 µm stack of neurons within a C57 mouse brain. (*B*) Tangential maximum intensity projections from the stack shown in (*A*). All scale bars = 50 µm. λ_{ex} = 1150 nm.

The latter category of fluorescent contrast agents, inorganic probes, includes the well-established quantum dot, bright fluorescent semiconductor nanocrystals with broad absorption and discrete, tunable emission wavelengths that are highly resistant to photobleaching [95,96]. More recently, the polymer dot has emerged as an even brighter, comparable alternative to quantum dots with decreased cytotoxicity [97–99]. Regardless of their function or organic/inorganic classification, characterization of the nonlinear properties of existing contrast agents to determine their compatibility with longer-wavelength excitation sources is a crucial first step towards their adoption as probes for multiphoton microscopy. There are a myriad of properties by which one can evaluate fluorophores, but action cross section measurements, a product of absorption cross section and quantum yield, are a particularly useful metric to evaluate brightness [100]. Unfortunately, accurate determination of cross sections is a complicated endeavor that requires detailed information of the spectral properties of a chromophore, sample concentration, and a well-characterized standard (**Appendix I**) [101,102]. As a result, the nonlinear properties of very few fluorophores have been reported, and in those limited instances, analysis has been limited to non-physiological solvents at wavelengths mostly within the Titanium:Sapphire range [103–107]. This wavelength limitation is in part due to the absence of reliable longer wavelength, ultrafast laser systems; however, given recent technological advances, two- and three-photon cross section measurements further out in the near-infrared is now achievable. In the following section, we will detail our own effort to perform multiphoton characterization of the under-the-radar polymer dot and demonstrate its use for deep imaging.

2.2.4 Polymer Dots for *In Vivo* Vascular Imaging

Multiphoton microscopy of vasculature requires the intravenous injection of bright, biocompatible contrast agents that preferably exhibit large absorption cross sections under near-infrared excitation and prolonged blood circulation times. Traditional exogenous contrast agents for *in vivo* multiphoton microscopy include organic dyes such as dextran-conjugated fluorescein and indocyanine green or inorganic semiconductor quantum dots [54,87]. Organic dyes, however, suffer from poor photostability and low quantum yields in aqueous biological environments [108–110]. Although quantum dots offer improved brightness and photostability, they present substantial toxicity concerns and are prone to bioaccumulation in organs and tissues [111–113]. Thus, the biological imaging community is eager for a safer, brighter, and more stable probe for deep, high-resolution *in vivo* imaging.

The highly fluorescent semiconducting polymer dot (pdot) is a promising candidate for *in vivo* multiphoton microscopy with material properties that can potentially overcome many of the limitations faced by other probes [97]. Although pdots are similar to quantum dots with respect to size (~10 – 100 nm, **Figure 2.9**) and quantum yield, pdots are brighter, more photostable, and present no clear evidence of biotoxicity [97,114]. A useful measure of fluorescence brightness is the action cross section, which is given by the product of the peak absorption cross section and the fluorescence quantum yield [97,115]. Pdots rival both quantum dots and organic dyes in that their two-photon action (2PA) cross sections are one to two orders of magnitude larger than inorganic quantum dots and three to five orders of magnitude greater than commonly used fluorescent dyes [97,98]. Moreover, polymer dots are readily amenable to functionalization and bioconjugation, enabling their use for tagged localization assays and molecular targeting [114,116]. Here we present evidence that we can take advantage

of pdots' many favorable properties to produce high-quality *in vivo* multiphoton images of vasculature with excellent signal-to-background ratio (SBR) at depths exceeding 1 mm.

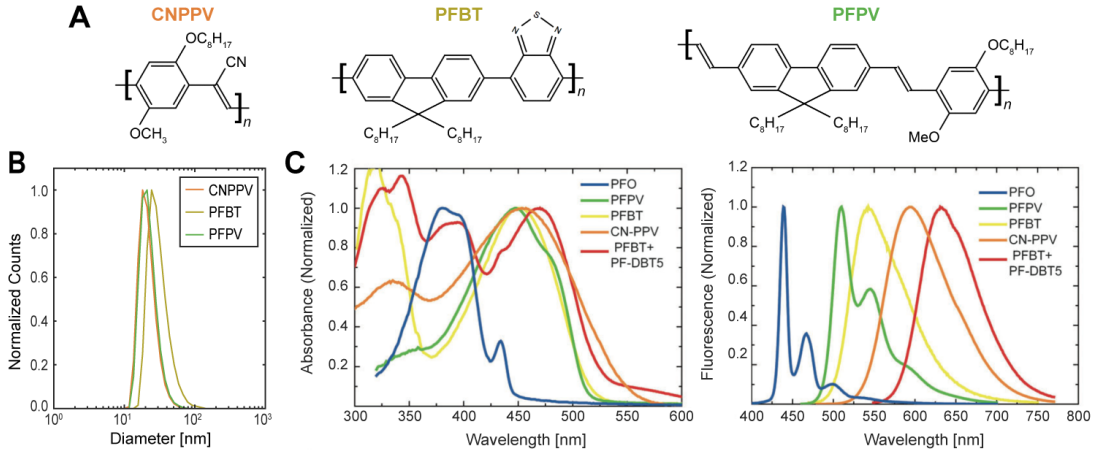

Figure 2.9: **Polymer dot structures and spectra**. (*A*) Molecular structures of three polymer dot variants: CNPPV (*Left*), PFBT (*Center*), and PFPV (*Right*). (*B*) Size distributions of CNPPV (21.89 nm), PFBT (31.47 nm), and PFPV (22.74 nm) as measured by dynamic light scattering. (*B*) Size distributions of CNPPV (21.89 nm), PFBT (31.47 nm), and PFPV (22.74 nm) as measured by dynamic light scattering. (*C*) Absorption (*Left*) and emission (*Right*) spectra of CNPPV, PFBT, and PFPV [97].

Another advantage of pdots is their broad absorption, which enables multiphoton imaging with a variety of ultrafast laser sources, including ytterbium-fiber lasers (yb-fiber, λ_{ex} = 1060 nm) and longer wavelength optical parametric amplifiers (OPA). Such broadband compatibility takes advantage of the favorable photophysical characteristics of these unique laser sources to improve SBR beyond the capabilities of conventional two-photon titanium-sapphire (Ti:S) microscopy. Moreover, the ability to excite pdots at longer wavelengths allows us to approach an ideal biological imaging wavelength situated around 1300 nm where absorption and tissue scattering events are minimized [46,84]. For instance, the photophysical advantages of longer wavelength excitation of

poly[{9,9-dioctyl-2,7-divinylene-fluorenylene-alt-co-{2-me-thoxy-5-(2-ethylhexyloxy)-1,4-phenylene}] (PFPV; λ_{ex} = 1060 nm) coupled with the ytterbium-fiber laser's intrinsic pulse characteristics results in a 3.5-fold improvement in SBR, and an overall 50 μm gain in penetration depth *in vivo*. Multiphoton imaging of poly[2-methoxy-5-(2-ethylhexyloxy)-1,4-(1-cyanovinylene-1,4-phenylene)] (CNPPV) labeled vasculature using an OPA (λ_{ex} = 1225 nm) increases SBR by ~8.2 fold (z = 700 μm), and extends imaging depth 450 μm further into the brain. Notably, PFPV and CNPPV both exhibit a partial three-photon power dependence at these longer wavelengths, which contributes to a larger SBR by the suppression of out-of-focus fluorescence [84,117]. Overall, semiconducting pdots are ideal for MPM due their enhanced brightness over traditional fluorophores, and spectrally wide absorption range. These advantages coupled with their intrinsically low cytotoxicity help overcome the longstanding limitations of quantum dots and establish the immense potential of pdots for *in vivo* biological imaging.

2.2.5 Multiphoton Power Dependence of Polymer Dots

Two-photon excitation of pdots has been successfully demonstrated by other research groups, although it has been more generally referred to under the larger and less specific umbrella of multiphoton imaging [98]. With mounting evidence of the advantages of three-photon microscopy over 2P imaging for deep *in vivo* imaging, such as the suppression of out-of-focus fluorescence, reduced scattering, and improved SBR, the need to identify specific excitation wavelengths that produce two- versus three-photon absorption becomes imperative [84,118]. Thus, we tested the excitation power dependence of various pdots including a CNPPV and two fluorene-based copolymers, PFBT and PFPV, at wavelengths ranging from 790 - 850 nm, 1060 nm, and 1200 – 1350 nm (**Figure 2.10**). We find that all three semiconducting polymers exhibit a strong two-

photon dependence at 800 nm. In the case of CNPPV and PFBT, this effect persists out to 1060 nm whereas PFPV begins to demonstrate a partial three-photon power dependence at this wavelength. Pure three-photon fluorescence is most strongly demonstrated at 1300 nm for CNPPV, 1350 nm for PFBT, and 1325 nm for PFPV (**Figure 2.10**). Within the 1060 – 1300 nm excitation range, there is a clear rising transition from two-photon to three-photon excitation. This data is especially instructive in that it serves as a reference for the selection of appropriate excitation sources and wavelengths for MPM experiments with pdots.

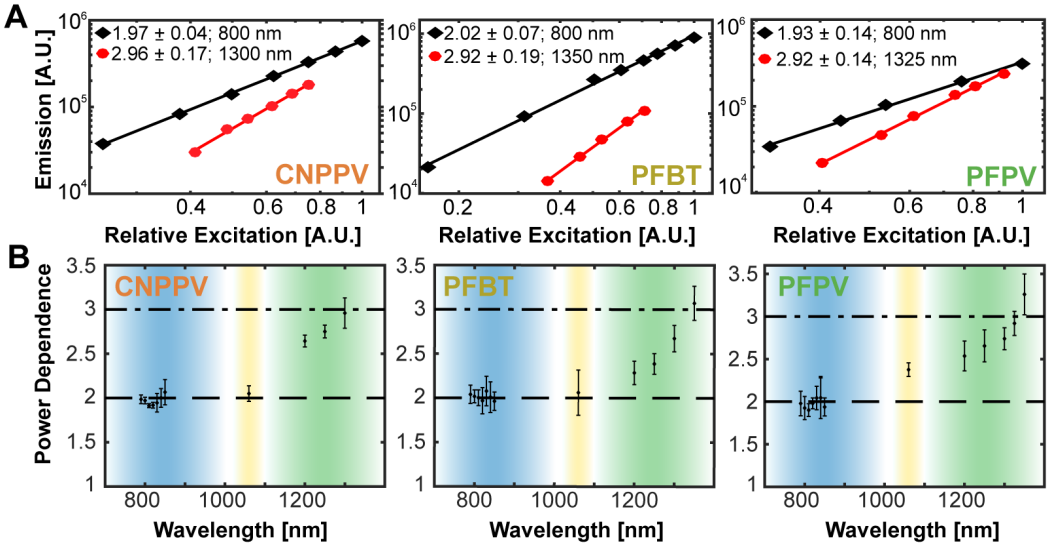

Figure 2.10: **Polymer dot power dependence**. (*A*) Logarithmic plots of the dependence of two- and three-photon induced fluorescence on excitation power. The excitation wavelength and fitted slope is indicated in the legend of each graph. The estimated uncertainty of each slope is reported as a standard deviation. Each plot corresponds to a distinct polymer dot species. (*B*) CNPPV (*left*), PFBT (*middle*), and PFPV (*right*) power dependence versus wavelength. The dashed and dash-dotted lines correspond to pure two- and three-photon power dependence, respectively. The blue shaded region represents the titanium-sapphire tuning range (λ_{ex} = 700 – 1000 nm), the yellow shaded region represents the ytterbium-fiber laser's bandwidth (λ_{ex} = 1060 nm; $\Delta\lambda$ = 40 nm), and the green shaded region represents the optical parametric amplifier tuning range (λ_{ex} = 1100 – 1400 nm).

However, it is interesting to note that CNPPV undergoes a three-photon transition at a higher energy wavelength than either PFBT or PFPV, despite being the most red-shifted of the three. This can potentially be explained by the unique chemical structure of poly(phenylene vinylene) polymers relative to fluorene-based co-polymers. The distinct molecular structures of the conjugated polymers affect the final energy levels of the pdot species in their excited states. Specifically, CNPPV has a donor-π-acceptor arrangement whereas PFBT and PFPV have donor-acceptor and donor-π-donor configurations, respectively, which leads to differences in the energy levels of their three-photon transitions.

2.2.6 Polymer Dot Brightness Enhances Two-Photon Signal-to-Background Ratio

The primary goal of this study is to evaluate the use of pdots for deep *in vivo* vascular imaging. C57 mice with intravenous injections of fluorescent dye, quantum dots, or pdots were imaged through an optical cranial window [119] using 800 nm excitation. All imaging experiments were performed in age-matched mice from the same litter to minimize any sources of variability in tissue properties that could potentially obscure depth comparisons. The C57 mice were prepared with cranial window implants and administered with retro-orbital injections of fluorescent contrast agents using methods previously described in Perillo et al. [120]. Dextran-conjugated fluorescein (λ_{em} = 524 nm; FD2000S, Sigma-Aldrich) served as the organic dye of interest, chosen because of its prevalent usage as a contrast agent in biological experiments [95,115,121,122]. QD605 (λ_{em} = 605 nm; Q10001MP, ThermoFisher Scientific) was the selected semiconductor quantum dot, a probe known for its large quantum yield, atypically high brightness, and photostability [95,123]. Lastly, three pdot variants, PFBT (λ_{em} = 538 nm), PFPV (λ_{em} = 520 nm), and CNPPV (λ_{em} = 590 nm), were selected as they represent

different classes of polymers, including poly(phenylene vinylene) and fluorene-based copolymers [97]. Comparing 100 µm thick maximum intensity projections at the same cortical depths, the pdot data visually appears much brighter than either the fluorescein or quantum dot images, demonstrating an enhanced signal-to-background ratio given by pdots (**Figure 2.11**).

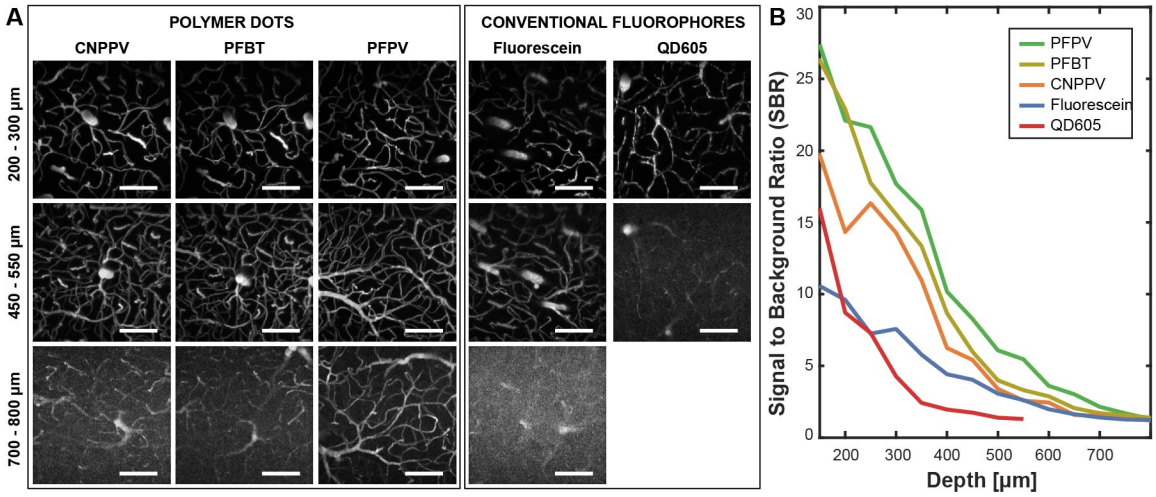

Figure 2.11: **Signal-to-background ratio is enhanced by polymer dots**. (*A*) Logarithmic plots of the dependence of two- and three-photon induced fluorescence on excitation power. The excitation wavelength and fitted slope is indicated in the legend of each graph. The estimated uncertainty of each slope is reported as a standard deviation. Each plot corresponds to a distinct polymer dot species. (*B*) Normalized signal-to-background ratio (SBR) versus depth comparison of polymer dots relative to fluorescein and QD605; λ_{ex} = 800 nm. SBR is diminished at the surface due to high background signal from the dura resulting from second harmonic generation of collagen. At ~150 µm SBR is at a maximum for all contrast agents and gradually decreases with depth. Relative to QD605 and fluorescein, all three polymer dots retain a higher SBR beyond ~150 µm. To ensure fair comparisons, the average laser power at each depth was maintained at consistent levels across the separate imaging experiments.

A quantitative comparison of the contrast agents reveals that PFPV produces the largest signal-to-background ratio, followed by PFBT then CNPPV. Relative to QD605

and fluorescein, pdot signal-to-background ratio is larger throughout the entire depth range. To ensure fair comparisons, the average laser power at each depth was maintained at consistent levels across the separate imaging experiments. Furthermore, appropriate filters were selected for all experiments to maximize the collection efficiency of each fluorophore and ensure fair comparisons of the separate image stacks. Vasculature in mice labeled by QD605 (**Figure 2.11**) appeared noticeably distorted and discontinuous, and imaging was limited to a 550 μm depth relative to the cortical surface. This is explained by the fact that the mouse did not survive the retro-orbital injection of inorganic quantum dots due to toxic effects, resulting in an absence of active circulation to evenly distribute the contrast agent in plasma. Meanwhile, chronic *in vivo* imaging experiments with repeated intravenous injections of pdots in the same mice over the course of several months showed no signs of cytotoxicity or deleterious effects on the animals, supporting several published claims of pdot biocompatibility [114,116,124,125]. An example of two-photon data collected from a mouse injected with 50 nM of PFPV showcases excellent signal-to-background ratio up to 650 μm deep and appreciable signal levels highlighting clearly delineated blood vessels from 750 – 850 μm (**Figure 2.12**). The enhanced signal-to-background ratio diminishes the requirement for increased frame averaging, enabling rapid data acquisition of dynamic processes.

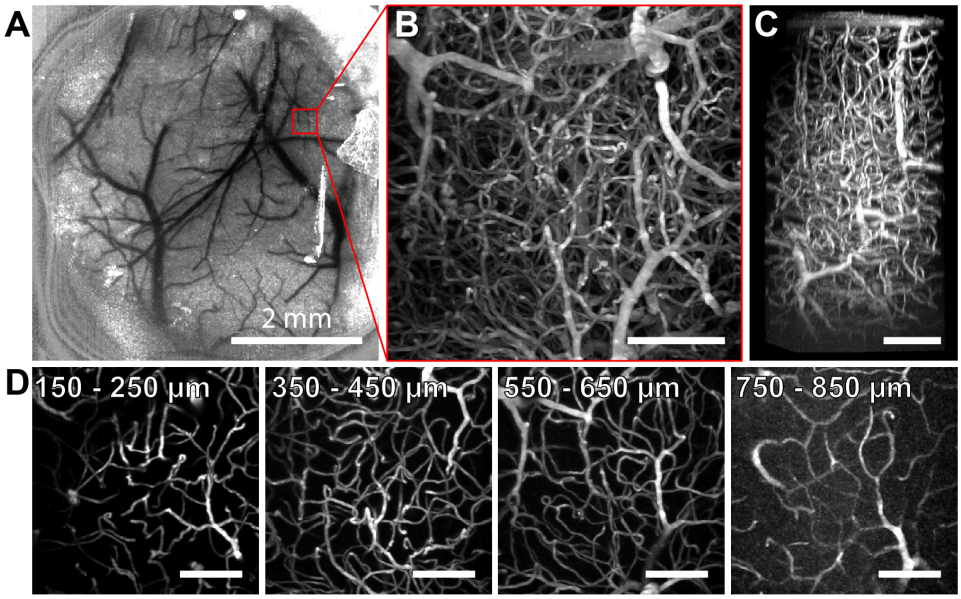

Figure 2.12: **Two-photon imaging of PFPV polymer dots intravenously injected in C57 mice**. (*A*) Laser speckle contrast image of surface blood vessels. (*B*) A tangential (*xy*) maximum intensity projection of a 365 × 365 × 850 μm^3 image stack collected from the region of interest (ROI) delineated in red in panel *A*. (*C*) A max intensity projection of a 3D reconstruction from the same data. (*D*) 2D tangential (*xy*) projections over shorter depth ranges of the stack. Unlabeled scale bars = 100 µm.

2.2.7 Longer Wavelength Excitation of Polymer Dots

A distinct characteristic of pdots is their wide absorption range [97]. The broad excitability of pdots enables their compatibility with a number of excitation sources including long wavelength, tunable laser sources between λ_{ex} = 1100 and 1400 nm. The maximum imaging depth of multiphoton microscopy is ultimately determined by signal-to-background ratio (SBR), which is influenced by the scattering and absorption events that occur in biological tissue as well as the power dependence of an emitter. Excitation light that is attenuated by scattering or absorption before reaching a contrast agent fails to produce any emitted fluorescence, and the fraction of attenuated photons is heavily dependent on wavelength. The fraction of excitation light reaching the focal volume at a

depth, z, can be approximated as $\exp[-(\mu_a(\lambda)+\mu_s(\lambda))z]$, where $\mu_a(\lambda)$ and $\mu_s(\lambda)$ are wavelength-dependent absorption and scattering coefficients [46,126]. Experimental data of effective attenuation lengths in biological tissue between 1300 nm and 1700 nm supports the accuracy of this theoretical model [57]. Modeling of this function reveals that there is an ideal biological imaging wavelength situated around 1300 nm [46] where photo-attenuation is minimized in brain tissue (**Figure 2.13**). In addition, 1300 nm light can be used to achieve three-photon excitation of many fluorophores, which reduces out-of-focus excitation and thereby decreases background [82,83,127] compared with two-photon excitation.

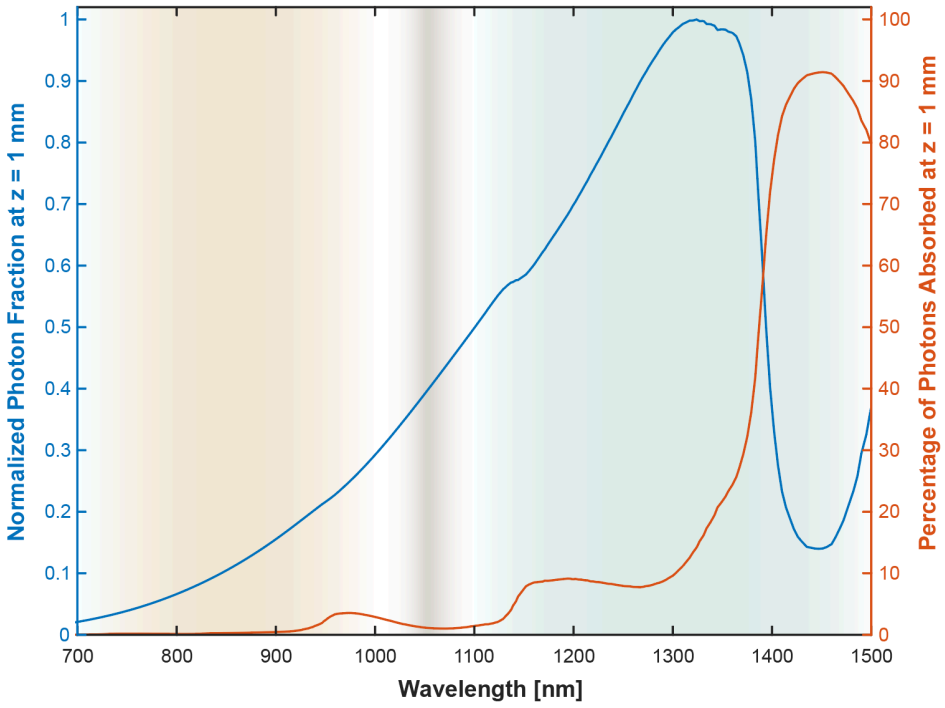

Figure 2.13: **An ideal biological imaging wavelength is situated at 1300 nm** [46,126]. The blue line indicates the photon fraction at a 1 mm depth in brain tissue versus wavelength. The red line indicates the percent of photon absorbed versus wavelength. The wavelength excitation regions of the titanium-sapphire (beige), ytterbium-fiber laser (gray), and optical parametric amplifier (blue) laser systems are delineated by color.

Therefore, it is readily understood that brighter fluorophores such as pdots that exhibit a strong 3P power dependence in response to 1300 nm excitation should yield a markedly improved SBR and maximize imaging depth. Unfortunately, the three photon action cross section of a pdot such as CNPPV is quite low at 1300 nm. However, a suitable compromise for an optimal imaging wavelength is at 1225 nm where attenuation length remains relatively close to its maximum (**Figure 2.13**) and the slope of CNPPV's power dependence is ~2.5 (**Figure 2.10**), representing a combination of two- and three-photon excitation processes. Indeed, longer wavelength excitation of CNPPV-labeled vasculature (λ_{ex} = 1225 nm) allows us to exploit these principles for optimized deep imaging and achieve a tissue penetration depth up to 1.3 mm beneath the pial surface (**Figure 2.14**). In contrast, two-photon imaging (λ_{ex} = 800 nm) of the same region of the same mouse only reached a maximum imaging depth of 850 μm (**Figure 2.14(b)**). A comparison of the CNPPV-labeled vascular networks imaged at the different wavelengths shows that SBR is vastly improved by 1225 nm excitation and a higher-order power dependence (**Figure 2.14(c-d)**). The effect is pronounced enough that the SBR of the 1225 nm image stack at z = 900 μm (SBR ~ 7.8) exceeds the SBR of the 800 nm image stack near the cortical surface (SBR ~ 7.2; z = 350 μm). A plot of background signal versus depth shows that the difference in SBR is directly owed to the rapid increase of background introduced by 800 nm excitation relative to the modest rise of background seen from 1225 nm excitation (**Figure 2.14(d)**). Quantification of SBR and background throughout the superficial dura (z ~ 0 – 150 μm) is omitted from these plots due to high background caused by second harmonic generation of collagen.

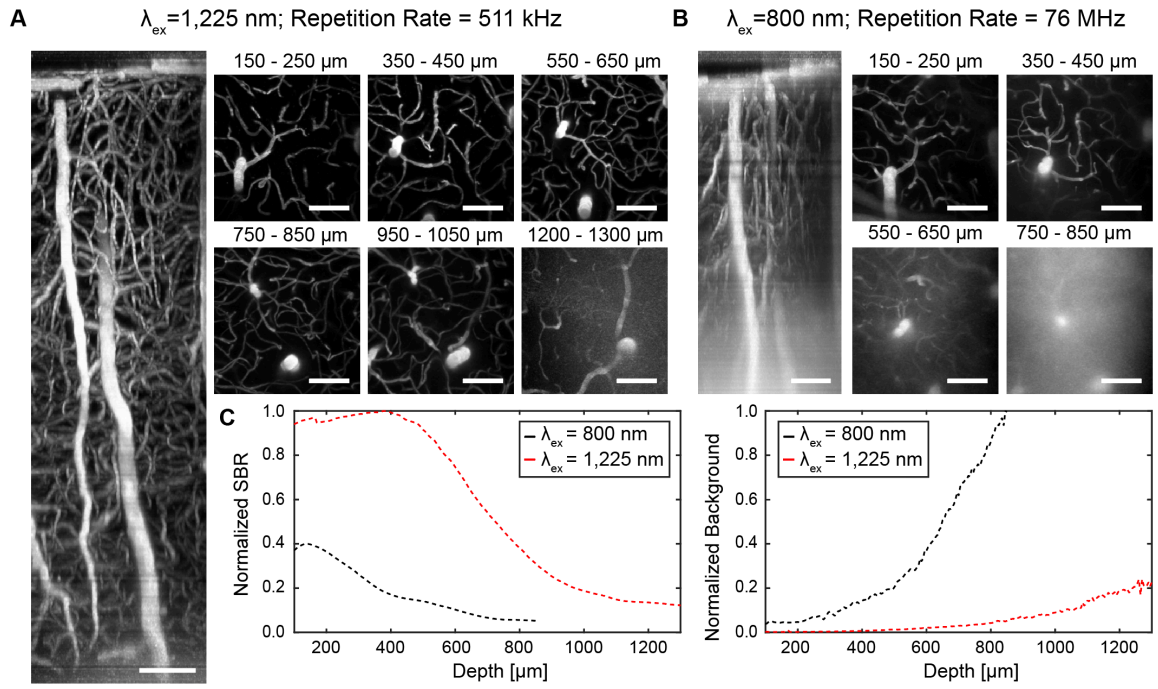

Figure 2.14: **Longer wavelength excitation (λ_{ex} = 1225 nm) versus shorter wavelength excitation (λ_{ex} = 800 nm) of CNPPV-labeled C57 vasculature**. *(A)* Sagittal (*xz*) projection of a 365 × 365 × 1300 µm^3 image stack at λ_{ex} = 1225 nm using an optical parametric amplifier source. *(B)* Sagittal (*xz*) projection of a 356 × 365 × 850 µm^3 image stack of the same region show in *A* at λ_{ex} = 800 nm using a titanium-sapphire source. *(C)* 2D tangential (*xy*) projections over shorter depth ranges of the stacks shown in *A* and *B*. *(D)* Comparison plots of signal-to-background ratio (SBR) versus depth (*Left*) and background intensity versus depth (*Right*). Scale bars = 100 µm.

In the two-photon laser system, a titanium:sapphire (Ti:S) oscillator (Mira 900, Coherent) beam is steered to a pair of galvanometer scanners (6125HB, Cambridge Technology) driven by servo driver amplifier boards (671215H-1HP, Cambridge Technology). A Keplerian telescope beam expander which consists of a B-coated scan lens (f = 80.0 mm, AC254-080-B, Thorlabs) and tube lens (f = 200.0 mm, LA1979-B-N-BK7, Thorlabs) is used to fill the back aperture of the microscope objective (XLUMPLFLN20XW 0.95 NA or XLPLN25XSVMP2 25X 1.0 NA, Olympus).

Excitation and emission paths are separated with a 775 nm cutoff dichroic mirror (FF775-Di01-52x58, Semrock). Fluorescence is epi-collected, transmitted through either a 510/84 bandpass filter (FF01-510/84-25, Semrock) or a 609/181 bandpass filter (FF01-609/181-25, Semrock), and detected by a photomultiplier tube (H10770PB-40, Hamamatsu Photonics). Image acquisition was controlled using custom software (LabVIEW, National Instruments) and image frames were collected at a 512 x 512 pixel size. Image stacks were collected at a z-resolution of 5 μm and three frames were averaged from 0 – 200 μm cortical depths, five frames from 200 – 500 μm, eight frames from 500 – 700 μm, and twelve frames beyond 700 μm. All mice specimens imaged by Ti:S were excited at λ_{ex} = 800 nm.

The three-photon laser schematic for this study is provided below (Figure 2.15). A 5W laser is used to pump a λ_{ex} = 800 nm mode-locked Ti:S oscillator (Mira 900, Coherent) which is stretched by an external stretcher/compressor to seed a regenerative amplifier (RegA 9000, Coherent). The amplified pulse is compressed and the spectrum of this 800 nm pulse can then be shifted and tuned by a customized optical parametric amplifier at 511 kHz (OPA 9800, Coherent) [81]. Three-photon *in vivo* imaging was performed at λ_{ex} = 1225 nm using a 25x multiphoton objective (XLPLN25XSVMP2 25x 1.0 NA, Olympus). Again, image stacks were collected at a z-increment of 5 μm and all frames were 512 x 512 pixels. Three frame running averages were recorded for the first 500 μm and an additional two frames were averaged each 200 μm interval beyond that.

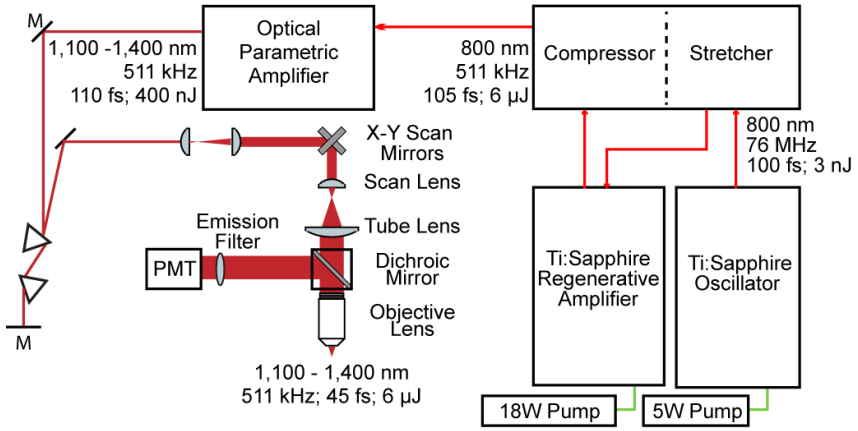

Figure 2.15: **Three-photon imaging schematic.** A 5W pump (Verdi, Coherent) is used to seed a Ti:Sapphire (Ti:S) oscillator (Mira 900, Coherent), which is then stretched by a modified external stretcher/compressor and amplified by a Ti:S regenerative amplifier (RegA, Coherent) seeded by a 18W pump (Verdi G18, Coherent). The amplified pulse is then converted to a longer wavelength by an optical parametric amplifier tunable over a 1100 – 1400 nm range. The OPA output is compressed by a set of prisms before entering the scanning optics resulting in an objective-focused beam with a pulse width of ~45 fs.

2.2.8 High Power Fiber Laser Imaging of Polymer Dots

Pdots' broad light absorption further permits excitation by a high average power ytterbium-fiber laser (yb-fiber; λ_{ex} = 1060 nm). Fiber lasers are a lower-cost alternative to OPA imaging, and offer excellent pulse characteristics as well as ease-of-operability to the user [128]. Although the fiber laser's fixed output wavelength (λ_{ex} = 1060 nm) does not coincide with the ideal biological imaging wavelength (λ_{ex} = 1300 nm), a comparison of *in vivo* image stacks of PFPV-labeled C57 vasculature collected at λ_{ex} = 1060 vs 800 nm clearly illustrates the advantages of the pdots' excitability by a fiber laser (**Figure 2.16**). Although the Ti:S penetration limit (z = 850 µm) is not significantly extended, the image quality (contrast and signal-to-background ratio) of the yb-fiber images is substantially improved under 1060 nm excitation, an effect which is most prominent beyond ~600 µm (**Figure 2.16(a)).** This corresponds to the z-position at which maximum

Ti:S output power was reached whereas the upper limit of fiber laser output power was not met before all signal was lost. In addition to the higher average power of the yb-fiber relative to the Ti:S source, two primary advantages can be attributed for the improvement in signal-to-background ratio. First, the number of photons lost to scattering and absorption events is reduced by longer wavelength excitation (λ_{ex} = 1060 nm vs. 800 nm) (**Figure 2.13**). At an 850 μm depth, the remaining photon fraction at λ_{ex} = 1060 nm is approximately five times greater than at λ_{ex} = 800 nm. Second, PFPV exhibits partial three-photon power dependence at 1060 nm (n ~ 2.38 ± 0.08) versus a two-photon excitation signature at 800 nm (n ~ 1.93 ± 0.14) (**Figure 2.10**). This partial three-photon dependence at λ_{ex} = 1060 nm further improves signal-to-background ratio through suppression of background fluorescence due to a higher-order nonlinear dependence on excitation intensity. Thus, longer wavelength excitation of PFPV is expected to improve both the signal and background of images at all depths. This expectation is empirically demonstrated by line profiles drawn across identical in-plane blood vessels located 700 μm beneath the surface imaged separately at λ_{ex} = 1060 and 800 nm (**Figure 5(B-C)).** The data reveals that the signal-to-background ratio of the λ_{ex} = 1060 nm image is ~3.5 times greater than the λ_{ex} = 800 nm signal-to-background ratio. Signal-to-background ratio improvement at z-positions beyond the depth at which Ti:S excitation becomes power-limited demonstrates that the higher output power of the yb-fiber laser coupled with longer wavelength excitation is a critical advantage for deep *in vivo* imaging. We emphasize that similar improvements made by longer wavelength excitation cannot be achieved with conventional fluorophores such as fluorescein (σ_2 = 0.31 at λ_{ex}=1050 nm), which exhibits low action cross sections beyond the Ti:S range (>1000 nm) and are unlikely to undergo a three-photon transition at 1060 nm [81,129]. A major practical benefit of improved SBR is the ability to collect high-quality vessel line scans at greater

depths to quantify blood velocity. Vessel line scanning quantifies flow velocity along the central axis of blood vessels at high frequency, relying on the contrast between injected plasma fluorophores and red blood cells (RBCs) which remain dark [41]. Therefore, high signal-to-background ratio is essential to accurately differentiate RBCs and fluorescent plasma and obtain precise flow velocity measurements. Here, we show that vessel line scans of PFPV-labeled mice form an image containing distinct streaks that represent RBCs traveling at a mean velocity of 1.28 ± 0.20 mm/sec at a depth of 750 μm beneath the pial surface (**Figure 2.16(d)**).

Fiber laser imaging was accomplished with a commercial fiber oscillator (Origami-10, OneFive GmbH) that was used to seed a custom-built ytterbium fiber amplifier [130]. The amplifier consisted of a 6-meter long segment of double-clad ytterbium-doped polarization-maintaining large-mode-area optical fiber with a core diameter of 25 μm and cladding diameter of 250 μm (YB1200-25/250DC-PM, Thorlabs), coiled to a radius of less than 7 cm to suppress higher-order modes and achieve single-mode output. The fiber was pumped by a fiber-coupled laser diode emitting up to 30 W of 915-nm light (K915FA3RN-30.00W, BWT Beijing). With a pump power of 23W, the amplifier produced 6 W of output at 1060 nm with a repetition rate of 80 MHz, and a grating pair was used to compress the pulse width to ~120 fs in the sample plane. The laser power was adjusted using a Glan-type calcite polarizer/half wave-plate combination. Line scans were acquired along vessel axes by collecting the fluorescence intensity while the galvo mirrors rapidly scanned a linear, user-defined path along a capillary. Each line consisted of 200 pixels imaged at a rate of 450 kHz, enabling a line rate of 940 Hz. To build a trajectory, the fluorescence intensity is plotted as a function of time (line number) and space (xy-coordinate, or pixel in one line). A sufficient number of lines were scanned along a trajectory to quantify the blood flow from analyzing the dark

streaks. A Radon transform was used to determine the inclination angle of the dark streaks which, when combined with the known temporal and length scales, allowed for calculation of the RBC velocity [41,131,132].

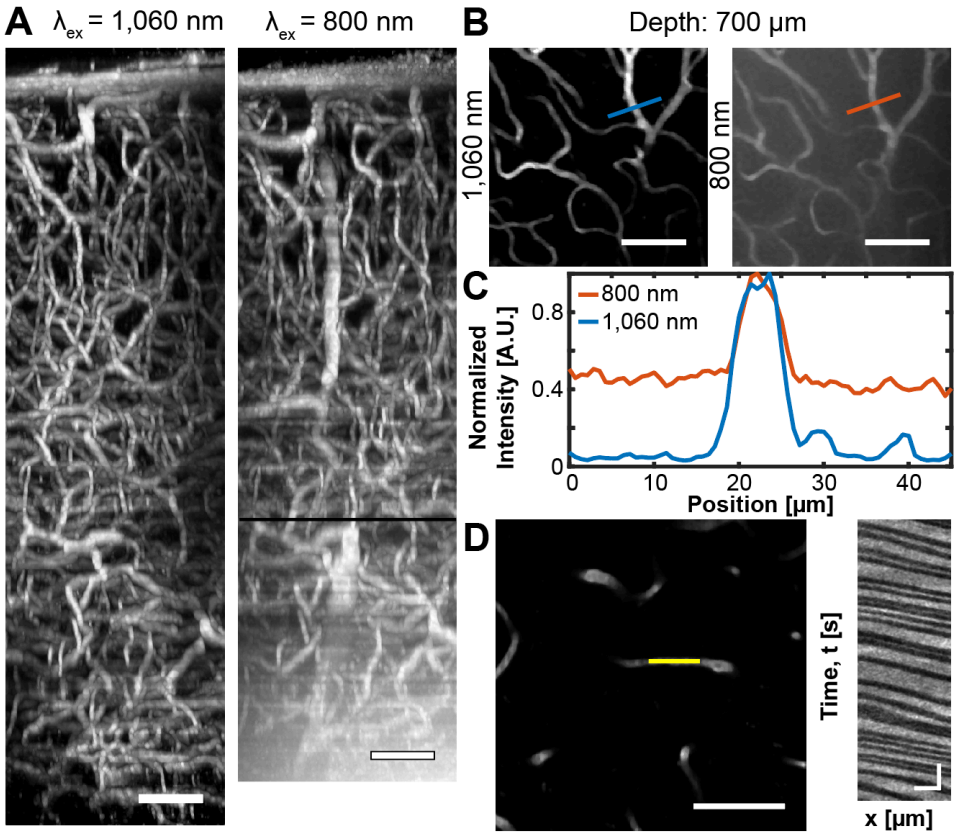

Figure 2.16: **High power fiber laser imaging of PFPV-labeled vasculature improves the SBR of images.** *(A)* Image stacks of the same cortical region collected using a 1060 nm ytterbium-fiber laser (*left,* 256 x 256 x 900 μm^3) or a 800 nm Ti:S excitation source (*right,* 256 x 256 x 850 μm^3). The depth at which maximum power output from the Ti:S laser was reached is marked by a black line (z = 600 µm). Scale bars = 75 µm. (*B*) 50 µm thick maximum intensity projections of the images stacks shown in *A* centered at 700 µm. The blue and red lines denote the positions of analyzed 45 µm long line profiles. Scale bars = 75 µm. *(C)* A plot of normalized signal intensity relative to position. (*D*) *Left*, a vessel line scan collected at a depth of 750 µm; scale bar = 75 µm. *Right*, the analyzed blood flow velocity is 1.29 ± 0.20 mm/sec; scale bar = 25 ms and 20 µm.

2.2.9 Polymer Dot Discussion and Future Directions

To evaluate pdots' multiphoton properties, we prepared multiple polymer variants via nanoprecipitation, a simple and rapid procedure. The batch size could be easily varied to prepare ample amounts of the nanopolymers for vascular imaging of tens of mice per preparation. The polymer dots had the additional advantage of a long shelf life (upwards of 5 months) and easy storage, characteristics that allow them to be easily disseminated for broad use [133]. Through our imaging experiments, we demonstrate that pdots offer a wealth of optical properties that make them very well suited for deep, *in vivo* multiphoton fluorescence microscopy. However, the lack of knowledge surrounding their nonlinear excitation properties has prevented their widespread adoption as popular contrast agents in multiphoton fluorescence imaging. To remedy this, we have characterized the two- versus three-photon power dependence of three pdot variants (CNPPV, PFBT, and PFPV) representing different polymer classes including poly(phenylene vinylene) and fluorene-based copolymers. We found that all three pdot species demonstrate a two-photon power dependence across the conventional Ti:S tuning range (λ_{ex} = 780 – 850 nm). Meanwhile, researchers who rely on the photophysical advantages that accompany three-photon microscopy, such as reduced out-of-focus fluorescence and diminished scattering, in order to improve the signal-to-background ratio in their imaging experiments can do so via excitation of CNPPV at 1300 nm, PFBT at 1350 nm, and PFPV at 1325 nm. In contrast, two of the conventional organic dyes evaluated, Texas Red and indocyanine green, remain rooted in the two-photon regime at comparable wavelengths (λ_{ex} = 1350 nm and 1280 nm, respectively) whereas only fluorescein possessed a three-photon power dependence near this spectrum [81].

Furthermore, we justify the use of pdots over conventional fluorophores for multiphoton imaging experiments in the 800 – 900 nm excitation range due to their

increased brightness relative to quantum dots, organic dyes, and fluorescent proteins. However, we were unable to measure absolute cross sections at longer wavelengths since excitation becomes a mixture of two- and three-photon absorption processes, which makes defining a cross section ambiguous. Nevertheless, previously reported cross section measurements demonstrate that pdots [98] are brighter than quantum dots, organic dyes, and fluorescent proteins [87,129] within a 770-870 nm excitation range with peak cross sections around ~2.02 to 5.50×10^5 GM, as illustrated in **Figure 2.17**. When compared to fluorescent dyes and proteins, pdot cross sections are three to five orders of magnitude larger. Most notably, this comparison includes organic molecules specifically engineered for enhanced two-photon absorption [95,134]. In particular, many fluorescent dyes can be problematic within *in vivo* biological settings due to a reduced quantum yield and poor photostability in aqueous environments [108–110]. In contrast, pdots composed of hydrophobic conjugated polymers are strongly resistant to this effect [97]. Of course, highly emissive quantum dots such as QD605 [95] and QD535 [129] do come close to matching a dimmer pdot such as MEH-PPV in brightness. Therefore, one might be tempted to employ quantum dots as their preferred class of contrast agents due to their well-regarded photostability and spectrally broad light absorption, an essential feature for multicolor imaging experiments. However, pdots share these same properties [114] as well as the critical advantage of exhibiting no evidence of cytotoxicity. There are conflicting reports regarding quantum dot biocompatibility which can most likely be attributed to physiochemical and environmental factors [113]; yet in our hands, intravenous injection of QD605 was acutely toxic and fatal to mice whereas identical chronic studies with pdots did not produce any observed health concerns. Nevertheless, a biological mechanism of pdot blood clearance has yet to be thoroughly assessed and

future research efforts should be directed to determine whether bioaccumulation in the spleen, liver, kidney or other major organs is a valid concern.

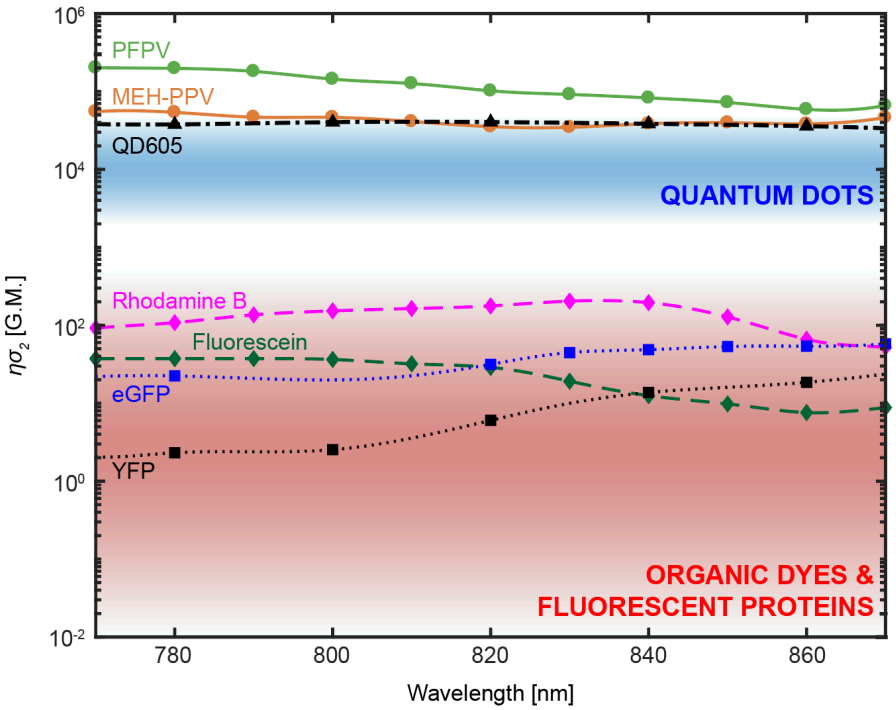

Figure 2.17: **Semilog plot of polymer dot brightness relative to quantum dots (QDs), organic dyes (ODs), and fluorescent proteins (FPs).** The two-photon action cross sections of polymer dots are plotted as circles connected by a solid line (PFPV in green, and MEH-PPV in red-orange) [98]. The blue shaded region corresponds to the expected range of quantum dots' two-photon action (2PA) cross sections [87,95]. The wavelength-dependent 2PA cross section of an atypically bright quantum dot species, QD605, is represented by black triangles with a dashed and dotted line [95]. The red shaded region corresponds to the expected range of 2PA cross sections of fluorescent dyes and proteins [87]. The 2PA cross sections of two typical fluorescent dyes are represented by diamonds connected by dashed lines (rhodamine B in magenta, fluorescein in dark green) and the 2PA cross sections of two typical fluorescent proteins are represented by squares connected by dotted lines (eGFP in blue and YFP in black) [129].

Next, we were able to show that pdots' brightness and excitability in the NIR regime improves SBR at considerable depths in mouse cortex at an 800 nm excitation

wavelength relative to identical experiments performed with an exceptionally bright quantum dot species, QD605, and a commonly used organic dye, dextran-conjugated fluorescein. As noted above, QD605 is cytotoxic when administered intravenously, particularly at the high concentrations necessitated by deep imaging experiments. *Ex vivo* animal studies may not be hindered by such a consequence; however, in the case of vascular imaging, continuous circulation and blood flow is essential to avoid distorted vessel appearance and photobleaching of the now stagnant probes. The overall imaging depth of the fluorescein-labeled vasculature matched that of the pdot-labeled mice; however, the signal-to-background ratio of the fluorescein images were less satisfactory resulting in reduced vascular clarity (~1.8-fold at z = 550 μm). The implications of poor signal-to-background include obfuscated analysis and degradation of automated image segmentation schemes. In this case, signal-to-background improvement from brighter contrast agents implies that depth penetration and corresponding signal-to-background was signal-limited. However, in contexts where background fluorescence becomes the limiting factor, such as in regions with large overlying blood vessels or high vascular density, background increases commensurately with signal, and signal-to-background is predicted only by numerical aperture, depth, wavelength, and attenuation length, rather than by the brightness of the contrast agent [84].

Another substantial limitation of fluorescein and other conventional organic dyes is their narrow absorption range. At λ_{ex} = 800 nm, fluorescein's two-photon action cross section is ~36 GM and at λ_{ex} = 1050 nm its cross section is a barely detectable 0.31 GM [129]. In contrast, pdots exhibit broad multiphoton absorption, meaning that they can be efficiently excited with a variety of laser sources all the way out to 1400 nm. We were able to demonstrate that the use of longer excitation wavelengths and higher-order nonlinear excitation allows us to improve signal-to-background ratio and overcome the

tissue scattering limits of imaging depth observed with conventional 2PM (**Section 2.2.7**). Specifically, excitation at λ_{ex} = 1225 nm attains a 1300 μm imaging depth whereas λ_{ex} = 800 nm results in an 850 μm cortical depth (**Figure 2.14**). Moreover, the signal-to-background ratio of the images collected at the longer wavelength excitation greatly exceed those recorded at an 800 nm excitation at all depths, producing a much higher quality three-dimensional volume. Through modeling and our power dependence characterization we are able to attribute this gain in penetration depth and signal-to-background ratio to the reduced scattering and photo-attenuation of longer excitation wavelengths, and the ancillary reduction of background signal due to CNPPV's partial three-photon power dependence at 1225 nm. In regard to the neuroscience community, the extended imaging depth with longer wavelength excitation enables researchers to investigate neural layers of anatomy beyond the cortex and corpus callosum, most notably the hippocampus [82]. In addition, the biological imaging community can take advantage of pdots' overlapping broad absorption spectra, which permits several pdot species emitting at discrete bands to be excited simultaneously at a single wavelength. This characteristic coupled with the fact that pdots can be readily functionalized and used to tag unique cellular structures [116] allows researchers to design simple and effective multicolor imaging experiments. An important caveat to consider, however, is that pdots were delivered intravenously in our studies, and labeling neural structures located in high-density extravascular brain tissue could pose a challenge due to the relatively large diameters of pdots (~20-30 nm). Recent efforts have produced pdot nanoparticles with sub-5 nm diameters, yet the yield from these preparations is still quite low [135].

We also take advantage of pdots' broad light absorption to image PFPV-labeled mice and resolve vasculature using a custom, home-built ytterbium-fiber laser (**Section 2.2.8**) [130]. Again, we observe that reduced scattering of longer wavelength excitation

light and a partial three-photon power dependence improves imaging depth slightly ($z_{800\,nm}$ = 850 μm; $z_{1060\,nm}$ = 900 μm) (**Figure 2.16**). We note that the signal-to-background ratio of the 1060 nm excitation images is improved most substantially beyond ~600 μm, an imaging depth which corresponds to the *z*-position at which the Ti:S output power was saturated.

Future advances in polymer engineering, structure based-design, and mutagenesis can vastly improve pdot performance and enhance multiphoton absorption at 1300 nm for optimized deep imaging. Redesign and optimization of pdots' molecular structure for improved three-photon imaging will involve an exploration of the effects of donor-π-donor, donor-π-acceptor-π-donor, and acceptor-π-donor-π-acceptor conformations on absorption cross sections and quantum yield. Overall, pdots present an exciting new approach to multiphoton *in vivo* imaging due to their enhanced brightness, broad excitability, and nontoxic features. With brighter, biocompatible probes, researchers will be able to resolve vascular architecture in living organisms with improved clarity and depth, enabling critical insights into fundamental biological problems.

2.2.10 Cranial Window Quality Impacts Imaging Depth

Thus far, factors that influence imaging depth have been discussed scientifically and without much ambiguity. Certainly, using a high power, short pulse duration, low-repetition rate ultrafast laser to target a far-red fluorophore that has been engineered to exhibit a three-photon power dependence at its peak action cross section wavelength is a sound strategy for deep imaging. Bonus points in the form of added penetration depth are awarded if that excitation wavelength resides within an ideal biological imaging band that minimizes tissue scattering and water absorption. However, in this section I would like to acknowledge the surgical art that accompanies the science of deep imaging. Given

that the aforementioned factors are all optimized, the clarity of an optical window can make or break a deep imaging experiment. The density and thickness of rodent skull severely limits excitation and emission light transmission, meaning that "non-invasive" procedures that either thin or remove the skull cap overlying the cortex are needed for *in vivo* imaging. Thinned skull procedures are perhaps the least disruptive surgical procedure, as they circumvent the activation of microglia and astrocytes seen with craniotomies, but limit access to small regions around ~0.2 mm^2 [72]. Moreover, bone regrowth is a salient concern, especially in younger mice, leading to an inconsistency in imaging depth with younger mice in particular. In contrast, polished and reinforced thinned skull (PoRTS) preparations achieve similar minimally invasive outcomes, with the added benefit of creating a larger and chronically stable window by fusing transparent glass-cement to the thinned skull [72]. However, imaging depth through thinned windows remains limited to a few hundred microns. On the other extreme end of the spectrum, endoscopic insertions of embedded prisms or gradient index lenses represent viable methods to maximize imaging depth, but are extremely invasive. These procedures generally rely on the excavation and removal of overlying tissue layers (e.g. cortex) to gain optical access to otherwise inaccessible anatomical regions (e.g. hippocampus). Despite contrary claims received in personal communications, common sense dictates that surgical preparations that remove entire sections of brain matter cannot be considered non-invasive. Moreover, resulting multiphoton images are lower in resolution due to the stunted numerical aperture of an optic like a gradient index lens (e.g. 0.6 NA) [25] relative to that of a much larger diameter, specialized multiphoton objective (e.g. 1.0 NA) [81].

A reasonable middle ground to skull thinning or pseudo-endoscopic procedures is the well-established optical cranial window, in which a circular bone flap is removed and

substituted with a coverslip. The coverslip is then secured through a combination of cyanoacrylate and dental cement [74]. It has been my frustrating experience that the quality of the cranial window is perhaps *the* most important consideration with respect to imaging depth. I will choose a skilled surgeon over an expensive laser system or a well-designed microscope every time if my experimental goal is strictly to maximize imaging depth. What follows then are lessons I've learned in the operating room, which I hope to impart to the future generation of surgeons to follow.

First and foremost, imaging depth has an inverse association with mouse age and one should aim to procure ~18/21 gram (female/male) C57 mice which are approximately ~five weeks old [136]. Younger mice are much more amenable to deep imaging, perhaps due to the reduced myelinization of their still developing brains [137]. However, for chronic imaging experiments, where the same specimen will be imaged for months, it is prudent to wait until the ~20/25 gram mark around ~eight weeks. If a chronic window is implanted too early, the effects of bone regrowth will obscure the window. More drastically, the physical growth of the mouse's head can cause the non-pliable head stage to become insecure. For non-chronic preparations of younger mice, where growth is irrelevant, an entirely different set of concerns take precedent. Coverslips, which are generally circular and 5 mm diameter, become much harder to place within the confines of the coronal or lambdoidal sutures, off to either side of the sagittal suture, simply because the mouse's skull is much smaller. One option is to drill over the sagittal line, but this is quite risky due to the proximity of delicate and critical blood vessels. Another option is to use a smaller diameter coverslip (e.g. 3 mm). Although this avoids complications during surgery, it becomes extremely difficult to suspend water immersion media between the small coverslip and imaging objective at longer working distances. Moreover, a smaller window limits the anatomical imaging access.

Upon selecting an appropriately aged mouse for single or chronic imaging studies, good surgical technique then determines cranial window quality. Please note that the following is not meant to be a substitute or alternative to approved animal protocols or institutional policies, which always take precedent to any information contained here. This documentation is simply meant to outline supplementary tips and tricks to ensure better outcomes for the patient and the experiment. With that in mind, it is good practice to fully remove exposed periosteum and other remaining connective tissue following scalping procedure. In the short-term, omitting this step introduces the risk of loose tissue catching the drill bit. In the long-term, the periosteum acts as a semi-aqueous layer between the skull and the fixed head stage, resulting in an impermanent bond. Once the periosteum is removed, I advise the surgeon to scuff the skull surface with a coarse dental burr at low speeds, apply a thin layer of cyanoacrylate, and allow it dry completely. The additional grit and surface area introduced by the coarse drilling allows the cyanoacrylate to adhere to the parietal bone with greater strength and reduces the likelihood that the rodent is able to pry the head stage free in the following weeks or months. Applying a thin layer of cyanoacrylate before drilling the cranial window has the added benefit of making a non-physiological layer available on which one can lightly trace an outline in order to guide the position and placement of the coverslip. It is far easier to adjust this outline on cyanoacrylate than it is on skull.

Once this layer is fully dry, it is time to drill through the skull. It is extremely important to stabilize your wrists and forearms. If your drill yielding limb is floating unsupported, your hand and arm will tire out more quickly, increasing the likelihood of a mistake. A simple solution is to use a free hand to prop up your wrist, or to rest a forearm on the edge of the surgical table while being careful to maintain a sterile field. In addition, it is wise to fully exhale prior to a delicate operation. The intuitive action is to

take a deep breath; however, holding in a deep breath as carbon dioxide accumulates in your lungs is not advisable while holding a rapidly spinning dental burr just microns away from a live pulsating brain. Also, this may seem obvious, but it is always best to use a fresh and sharp dental burr. All burrs, used or new, must be sterilized, but an older, dull burr is decidedly less effective for craniotomies. Considering the delicacy of the surgical procedure, the cost savings of reusing a dental burr is difficult to justify. When creating the cranial opening, it is best to use low drill speed and more passes. High drill speeds can actually result in charring of the skull surface, and this heat is eventually transferred to the cortex. Even at lower drilling speeds, one should continually bathe the region of interest in sterile saline to keep the area lubricated and cool. If the dental burr repeatedly snags onto rough edges during the passes, two remedies work well. One is to change the direction of the circular passes – clockwise to counter-clockwise or vice versa. Another option is to change the direction of drill rotation if the model of drill being used has this feature. Finally, be very aware of the age of the mouse specimen. Young mice have much thinner skulls and it is all too easy to mistakenly drill through the parietal bone and into the brain if operating under the assumption that the mouse is older and thick-skulled.

Once the skull incision starts to loosen, a flap should form. Intuitively, a novice surgeon will attempt to pry or lever this flap to remove it. This is ill-advised, as the see-saw effect will drive the opposite end of the flap directly into the cortex. Instead, one should pull this flap upwards and out to prevent lacerating the exposed tissue. Nonetheless, some bleeding is expected and it is important to have sterile surgifoam available to clot any active sites. If ignored, these areas will scab up and remain permanent even when healed, since the scab is unable to fall free when trapped beneath a coverslip. In addition, it is imperative to keep the exposed brain bathed in sterile saline,

otherwise the surface tissue will dry out quickly and fail to return to a healthy state. When placing the coverslip, I suggest that it should be embedded *in* the cranial opening, not *on* it. This means the drilled opening will have to be slightly larger than the coverslip's diameter. Otherwise, an air gap will form between the cortical surface and the coverslip bottom. Of course, this gap will eventually become imbued with cerebrospinal fluid; however, the more interfaces between the sample plane and the objective, the more scattering events that will take place to diminish imaging depth. In addition, this gap will unnecessarily detract from your objective working distance and further limit imaging depth. Therefore, it is also critical to firmly apply pressure orthogonally to the coverslip to ensure even contact with the cortex until it is secured in place with cyanoacrylate. Once the coverslip is attached, the rest of the head stage is formed using a layer of dental cement. It is important to apply a layer of dental cement thin enough to avoid eating into the working the distance of the objective, but thick enough to create raised edges along the coverslip perimeter. This rim will act as a well to hold immersion media beneath the objective. Finally, it is prudent to apply a sealing layer of cyanoacrylate over the dental cement; this hardens the cement and lessens the probability that it will be scratched off or damaged by the specimen. Once the cranial window is in place, it is tempting to commence imaging experiments. However, it is best to give the subject at least ~two weeks to heal, and more if possible. Otherwise, macrophages and microglia activated during surgery will roam the cortex and engulf any foreign contrast agents they encounter. This results in fluorescent cells making an unwanted appearance in the vascular images, particular towards the dura (**Figure 2.18**).

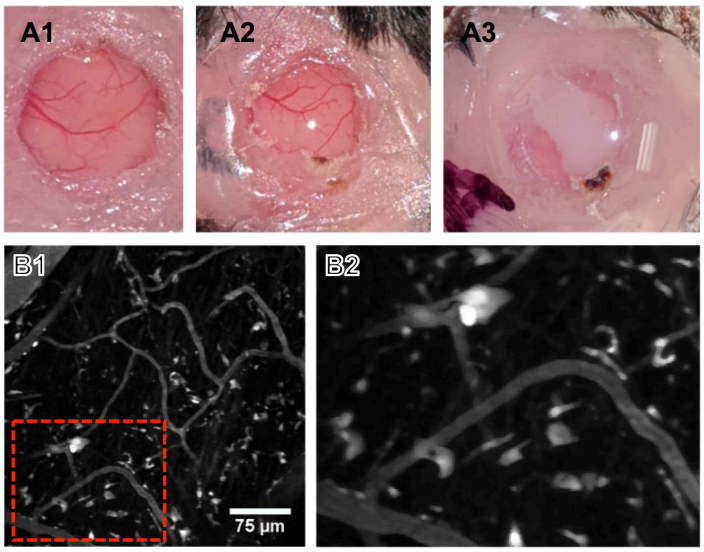

Figure 2.18: **Issues with cranial window preparation.** (*A*) An example of an (*A1*) intact cranial window, (*A2*) partial skull regrowth, and (*A3*) severe skull regrowth. (*B1*) If the animal is not given at least two weeks of recovery time, activated macrophages and microglia will phagocytose fluorescent dye molecules and become visible in the dura. (*B2*) Inset of the 25 – 50 µm deep max intensity projection in *B1*.

Securing the animal during an imaging session is yet another quagmire the researcher will encounter, as multiphoton microscopy is a highly motion-sensitive technique. More specifically, two forms of pulsatile motion will introduce noticeable image artifacts. First, pulsatile brain motion as a result of arterial expansion following heart muscle contraction is inevitable [138]. It is possible to devise data acquisition or image processing schemes to circumvent resulting image artifacts; however, passive correction techniques are sub-optimal due to the nonlinearity of pulsatile brain motion and more sophisticated correction methods seek to actively monitor cardiac activity. This challenge reinforces the importance of firmly securing the coverslip against the brain surface rather than the parietal bone, since the additional compression serves to dampen pulsatile brain activity. A second type of motion artifact arises from rodent respiratory activity. In principle, image artifacts from this motion are easily eliminated by rigidly

securing the rodent head with a stereotaxic fixation. Our lab uses two frames (SG-4N and SGM-4; Narishige), which use a three-point fixation clamping method of the mouth, nose, and ear. In our experiments, we find that ear fixation is inconsistent and that respiratory motion artifacts are visible in smaller, higher resolution scans. To remedy this, I developed a clamping method to directly secure the cranial window to the stereotaxic frame (**Figure 2.19**). The main arm is compatible with the SG-4N and SGM-4 base plates, and the forked cranial window attachment is implanted into the rodent's head stage during surgery. The design has the additional benefit of ensuring that the cranial window is centered with respect to the stereotaxic frame and normal to the imaging system's optical axis. In addition, a custom nose cone was designed featuring two valves, one inlet for isoflurane delivery and one outlet for exhaust sequestration using a charcoal canister.

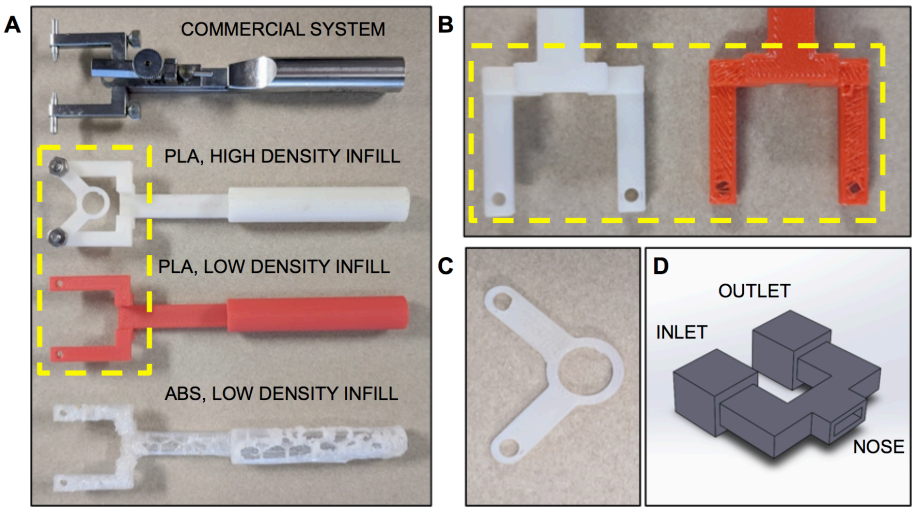

Figure 2.19: **Secure stereotaxic frame.** (*A*) A comparison of the commercial (*top*) and custom (*bottom three*) stereotaxic frames. Initial prototypes with ABS were more prone to warping than PLA. (*B*) PLA frames with a low density infill were also prone to warping. (*C*) A forked head-bar is cemented directly to the head stage during surgery, and then attached to the stereotaxic arm with two 4-40 screws. (*D*) A custom nose cone is inserted into the notched stereotaxic arm.

2.3 Expanding Multiphoton Imaging Field-of-View

In addition to extending imaging depth, expanding the field of view of microscopy (i.e. mesoscale optical imaging) is an equally valid approach to increase optical access and sampling volume. Conventional multiphoton microscopy is limited to fields of view on the order of 500 x 500 μm^2, which fundamentally restricts observation of large-scale vascular and neural dynamics [139]. The ratio of an objective's field number (FN) and magnification (M) determines the scanning field of view radius, $2F_0 = FN/M$ [139]. A smaller magnification increases field of view radius, which can be accomplished by either extending the objective focal length (f_0) or decreasing the focal length of the tube lens (f_t), $M = f_t/f_0$. The former usually comes with the tradeoff of reduced numerical aperture (NA), which is detrimental to efficient multiphoton excitation. The latter, however, requires an increased field number or acceptance angle (θ_0) at the objective rear aperture to maintain the same field of view, $\sin(\theta_0) = FN/2f_t$. Thus, for a given NA, larger fields of view require custom, larger diameter objectives. Unfortunately, even with scaled up microscope objectives, larger scanning angles lead to extensive aberrations at the cost of reduced spatial resolution and lower excitation efficiency [140]. Even more problematic is the fact that the light throughput of an ideal objective that solves these design obstacles still remains restricted by the optical invariant of all associated optics. Currently, effective mesoscale optical imaging remains an unsolved challenge limited by high magnification objective lenses, sub-optimal afocal relays, and small field collection optics [139]. In the following section we detail a comprehensive approach to multiphoton optical design to accomplish large field of view imaging of microvasculature. Ultimately, increasing optical access to the cerebral angiome beyond cubic millimeter volumes and producing vectorized vascular networks

enables a thorough understanding of vessel topology, connectivity, and blood flow patterns in healthy and disease states.

2.3.1 The Case for Optical Invariant Analysis and Evaluating Objectives

A standard multiphoton microscope consists of a high numerical aperture objective, a beam scanning system, an afocal relay that conjugates the objective and scanning planes, and a detection module [139]. A well-designed system can maximize optical access to large volumes by increasing its optical extent or light grasp; a concept understood as etendue in the field of optics. Each component in a complete optical system can be optimized independently, but due to the conservation of radiant power, the overall light gathering properties of a system will be dictated by the component with the lowest optical invariant in isolation. In an ideal optical system free of any aberrations, the optical invariant remains a conserved constant calculated by height and angle of the chief and marginal rays in any given transverse plane [139]. Because the component with the lowest optical invariant ultimately bounds the system's performance, the best approach to designing an optimized scan engine, and the one utilized herein, is to select a high-throughput objective and identify optical components that exceed or support that invariant.

Multiphoton microscopy requires the spatial and temporal overlap of two or more photons to incite a single excitation event. The temporal overlap is achieved by use of ultrafast lasers, which deliver high pulse energies to increase the probability of a multiphoton event. The spatial overlap of photons is accomplished with high numerical aperture objectives. However, large numerical apertures are typically associated with higher magnification, which comes with specific tradeoffs [139]. First, higher magnification generally results in reduced multiphoton image contrast and a limited

ability to probe deeply into heavily scattering environments. Second, the field of view (FOV) radius is limited by increased magnification. Specifically, FOV is calculated by $2F_0 = FN/M$, where F_o is the FOV radius, FN is the objective field number, and M is magnification. This second attribute can help us better understand the former explanation of reduced signal deep in biological tissue - in scattering environments, emitted photons appear to originate over an expanded diffuse area, meaning an objective with a larger field of view can more efficiently capture these widely scattered photons. Therefore, it is generally advisable to select an objective with as low of a magnification and as large of a numerical aperture as possible for optimized multiphoton microscopy. The larger the NA, the more efficient the multiphoton excitation, at the cost of increased magnification. The larger the magnification, the less efficient fluorescence collection becomes. It is up to the researcher and their specific biological inquiry to balance these diametrically opposed trade-offs. In my musings, I suppose an ideal microscope objective would be severely achromatic, and cause longer excitation light to refract strongly and shorter emission wavelengths to refract at more shallow angles. This would result in efficient, high numerical aperture excitation and lower magnification fluorescence collection. Alas, no such objective exists to the best of my knowledge.

A third consideration in selecting the optimal objective is its transmission characteristics. Higher-performance objectives are typically composed of more lenses, each of which compensates for the aberrations of the others in order to deliver a tight focal point spread function in the lateral and axial dimensions. As the complexity of these objectives increases, the greater the number of total surfaces becomes. If one considers loss through these objectives due to Fresnel reflections off of each individual surface, it becomes apparent that transmission is generally diminished with complex objectives. Therefore, one must identify objectives with anti-reflective (AR) coatings

specific to the excitation wavelengths intended for use. In our proposed aim to achieve deep vascular imaging, the Olympus XLPLN25XSVMP2 emerges as the clear candidate to maximize transmission at longer wavelengths due to its optimal coating characteristics. However, its larger magnification relative to the Olympus XLUMPLFLN 20X equates to reduced collection efficiency despite enhanced excitation efficiency. Furthermore, its extremely large front aperture diameter and long working distance can create physical challenges in suspending immersion media between the objective tip and the sample meaning that there is great difficulty in using the XLPLN25XSVMP2's full numerical aperture. In contrast, the XLUMPLFLN 20X has a shorter working distance and smaller front aperture and avoids this set of problems entirely. Therefore, we prioritize the use of the XLPLN25XSVMP2 as the best choice for large-scale multiphoton microscopy in laser power-limited contexts where transmission must be maximized, especially if there is a particular demand for longer wavelength, AR-coating compatible excitation. In contexts where we are not power-limited, and more so directly limited by sample dimness due to low fluorophore quantum yield or strong scattering in the sample environment, or imaging at shorter wavelengths, we prioritize the use of the XLUMPLFLN 20X for best performance. Since we encounter both contexts in performing our *in vivo* studies, we have designed a versatile imaging system able to accommodate both objectives.

2.3.2 Galvanometer Scanning System

The optical invariants of the selected objectives when calculated at either their rear aperture, $I = r_0 sin\theta_0$, or front focal plane, $I_{obj} = nF_0\alpha_0$, are 0.55 (20x, XLUMPLFLN) and 0.36 (25x, XLPLN25XSVMP2). Thus, it is was our goal to select a galvanometer mirror pair with an optical invariant that exceeds 0.55. The invariant of a

scanner (I_g) is calculated using the expression $I_g = r_g sin\theta_g$, which accounts for incident beam radius (r_g) and maximum scan angle (θ_g). To satisfy the condition that $I_g \geq I_{obj}$, we use the previous equation to determine the minimum required scanning angle, θ_g = 12.71º. Our previous microscope's mirror scanner (6215H, Cambridge Technologies) had a maximum scan angle of 40º and seemingly satisfied this requirement. However, as the scan angle increases, a beam's footprint on the scanner also increases. Thus, maximum scan angle is typically limited by vignetting, rather than the physical scanning limit of the mirror. The footprint (*W*) of a beam with a known diameter (*d*) is calculated using elementary trigonometry, $W = d\left(cos\theta_g\right)^{-1}$. At θ_g = 12.71º, the expected footprint of a 5 mm diameter beam is ~8 mm, which exceeds the 7 mm clear aperture of the Cambridge scanning mirrors. Thus, our optimized large field-of-view system was upgraded to include a large beam diameter dual-axis scanning galvanometer system (GVS012, Thorlabs) with a physical scan limit that exceeds the minimum required θ_g, and a 10 mm clear aperture that fully supports a 5 mm beam diameter's footprint at that angle. With this mirror scanner, we are able to fully support the optical invariant of both objectives in the proposed system.

The disadvantage of this larger diameter galvanometer system is that their larger format widens the coupling distance of the independent mirrors. The small diameter galvanometers were coupled as well, which is generally a disadvantage since the conjugate point at the objective rear aperture extends to an imperfect, non-stationary point from the galvanometer pair. However, this imperfection is dramatically heightened by the large diameter galvanometers. The effect is a distortion that arises from the fact that the distance between the fast (i.e. first) scanning mirror and the image plane directly depends on the mechanical scan angles of both mirrors, where larger scan angles result in a longer distance (Thorlabs communication; **Figure 2.20**). Problematically, the distance

from the first scanning mirror to the image plane is nonlinear as a function of scan angle, and instead depends on the tangent of the scan angle. Thus, without the use of custom, compensating lenses, the focus lies on a sphere rather than a plane. If a perfect monolayer is imaged, then the point spread function's size varies across the surface of the sample, with greater excitation efficiency where the monolayer intersects within the spherical 'plane' of focus. Moreover, the actual scan pattern across the monolayer is not square, unlike a decoupled or close-coupled mirror system, but pillow-shaped due to the field distortion introduced by the decoupled arrangement of the large diameter galvanometers (**Figure 2.20**). Our acquisition software assumes a square image pattern for image reconstruction, which results in warped structures most prominently towards the borders of the image frame. Overall, these issues only manifest noticeably at larger scan voltages (>1.5V) and future work can be implemented to minimize the effect of distortions. For instance, a non-uniform sampling technique that is proportional to the tangent of the scan angle can be applied to avoid warping a pillow-shaped image field to a rectangular image frame. Moreover, specialized optics (i.e. non-rectilinear lenses) can be used to correct for a spherical focus and ensure a minimal spot size at all portions of the two-dimensional image plane.

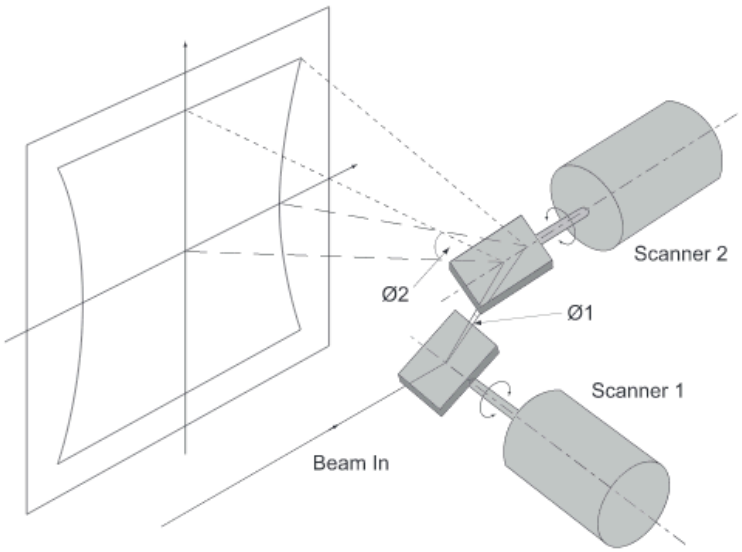

Figure 2.20: **Coupled, large diameter galvanometer mirrors introduce significant field distortion.** The distance between scanner one and two varies as a function of a scan angle, with longer distances resulting at steeper scan angles. This introduces a pillow-shaped field distortion. Without the use of custom, compensating downstream lenses, laser focus lies on a sphere rather than a plane.

2.3.3 Afocal Relay Selection

Similar to our analysis that ensures the multiphoton system's beam scanners fully support maximum light throughput, our design strategy must identify relay lenses with large optical invariants. An afocal relay consists of a scan lens and tube lens, and the invariant of each lens is given by $I_L = r_L sin\theta_L$. The maximum scan angle of a relay lens is typically limited by vignetting at small input beam diameters and optical aberrations at large input beam diameters. In practice, most scan optics are prone to aberration at shallow angles, which drives one to work with smaller beam diameters and identify various combinations of scan and tube lenses that minimize vignetting, where the minimum beam diameter is dictated by the rear aperture diameter of the imaging objective (20 mm) and the beam expansion of the relay lens combination. Thus, our

overall design strategy for this segment employs Zemax to model various commercial scan and tube lenses using appropriately sized beams (r_L) and evaluates the maximum angle (θ_L) attained before either vignetting occurs or optical performance is no longer diffraction limited to calculate the optical invariant I_L of each relay pair, until the light throughput of the proposed imaging objectives are met.

As a starting point, we evaluated the optical invariant of the relay in the former, suboptimal field of view multiphoton microscope, which consists of an f = 40 mm Plössl scan lens (2x AC254-080-B; Thorlabs) and a f = 200 mm plano-convex tube lens (LA1979-B; Thorlabs). We found that it was aberration limited at all scan angles, including on-axis performance at a 1050 nm excitation wavelength. Effectively, this means that the system had an optical invariant of zero, which indicates that the no portion of the visible field of view features sub-diffraction limited resolution. Thus, we were determined to redesign our relay, and free to rethink our use of a 4 mm input beams and a 5-fold beam expansion factor.

As stated above, the initial beam diameter is constrained by the beam expansion of the relay lens combination and the objective rear aperture diameter. Small beam diameters are typically limited by vignetting and larger input beam diameters are typically limited by optical aberrations [139]. Therefore, it is preferable to work with smaller beams with respect to relay optical performance. However, unduly small beam diameters are quite difficult to align and are prone to Gaussian beam divergence. This poses a delicate balance, where the use of high quality relay optics that minimize aberrations is preferred to reducing the beam radius. Thus, we opted for a 5 mm diameter beam (r_L = 2.5 mm) as a reasonable size, which represents a 1 mm increase to our previous multiphoton system and therefore mandates the selection of higher quality relay optics. Further considerations must be paid with respect to the tube lens focal length,

which is determined by the objective manufacturer. For instance, Leica and Nikon objectives are designed to accommodate 200 mm focal length tube lenses, whereas Olympus objectives are meant to be used with 180 mm focal length tube lenses. Given a 5 mm beam and a 20 mm diameter rear aperture, this required a 45 mm focal length scan lens and a 180 mm focal length tube lens for compatibility with our Olympus objectives. Unfortunately, we were unable to identify a high performance scan lens with this specification, but previous research from lab alumni Dr. David Miller uncovered that the f = 50 mm SL50-2P2 scan lens offered ideal optical performance. This left us with the decision of (1) continuing to use a 180 mm focal length tube lens, which would result in underfilling the 25x objective's rear aperture without capitalizing on its full numerical aperture or (2) opting for a 200 mm focal length tube lens and thereby increasing objective magnification and reducing field of view radius slightly. We opted for the latter, although this decision clearly detracts from ultra wide field of view imaging capabilities and has ambiguous effects on deep imaging. In one sense, by utilizing the full objective NA, we may be able to image deeper due to optimal excitation efficiency. On the other hand, increased objective magnification limits our ability to collect scattered emission light, which may hinder imaging depth. An alternative option is to use the 50 mm focal length SL50-2P2 and a 180 mm focal length tube lens, and increase the input beam diameter from 5 to ~5.5 mm. However, Zemax modeling showed that this resulted in non-diffraction limited optical performance at smaller scan angles than would a 5 mm beam, which had a more severe consequence with respect to limiting the relay's overall optical invariant.

Thus, we chose to proceed with a 5 mm input beam diameter and with knowledge of our scan lens choice (Thorlabs, SL50-2P2) and a requirement for a 200 mm focal length tube lens, we then endeavored to evaluate three tiers of tube lens options used in

conjunction with the SL50-2P2: low-cost (Thorlabs, LA1979-C), mid-range (Thorlabs; 2x AC508-400-C Plössl Design), and expensive (Thorlabs, TL200-2P2). Since the optical invariant is dictated by either vignetting or aberrations, we first sought to evaluate at which scan angle each relay exhibited vignetting as determined by our inability to no longer trace the chief ray in a Zemax model. All three relays exhibited vignetting at $\geq$7.5º mechanical scan angle (**Table 2.1**), which reflects that the limiting factor is the SL50-2P2's moderate clear aperture (24.4 mm) and not the tube lens options (47.0 mm clear aperture). Surprisingly the low- (LA1979) and mid-cost (AC508-400-C Plössl) *relays* were aberration limited at all scan angles including 0º at 1050 nm (**Figure 2.21**). In contrast, the high-tier relay with the TL200-2P2 tube lens is only aberration limited beyond a ~6.87º mechanical scan angle at 1050 nm (**Figure 2.21**). Ultimately, this means that the optical invariant of the final relay is ~0.647, and its diffraction limited invariant is ~0.594. Notably, the mid-cost relay outperformed the less expensive alternative, as the former was not aberration limited below 5º scanning angles at 800 nm and 1300 nm excitation wavelengths. For this study, aberration was defined as a wavelength dependent RMS wavefront error greater than 0.072 waves [141]. To ensure fair comparisons across the three tiers, each relay was modeled, optimized, and evaluated in Zemax using a custom merit function corresponding to excitation wavelengths we expected to use frequently with the system (800, 1050, and 1300 nm).

Input Beam Angle		0º	3º	5º	6º	7º	8º
λ [nm]	Relay	RMS Wavefront Error	RMS Wavefront Error	RMS Wavefront Error	RMS Wavefront Error	RMS Wavefront Error	RMS Wavefront Error
800	Low-Cost	0.1080	0.2231	0.3945	0.5222	0.9201	N/A
	Mid-Range	0.0078	0.0248	0.0534	0.0852	0.1013	N/A
	High-Cost	0.0159	0.0267	0.0395	0.0337	0.1286	N/A
1050	Low-Cost	0.2506	0.2664	0.3314	0.3965	0.6107	N/A
	Mid-Range	0.0897	0.0895	0.0927	0.0981	0.1470	N/A
	High-Cost	0.0114	0.0180	0.0268	0.0235	0.0984	N/A
1300	Low-Cost	0.3078	0.3051	0.3285	0.3608	0.4597	N/A
	Mid-Range	0.0663	0.0669	0.0709	0.0764	0.1208	N/A
	High-Cost	0.0035	0.0118	0.0205	0.0239	0.0868	N/A

Table 2.1: **The root mean square wavefront error of three different afocal relays modeled at different excitation wavelengths as a function of mechanical scan angle**. All three relays featured the same f = 50 mm specialized multiphoton scan lens (SL50-2P2; Thorlabs; 680 – 1300 nm). Low-Cost Relay: f = 200 mm plano-convex tube lens (LA-1979-C; Thorlabs). Mid-Range Relay: 2 x f = 400 mm achromatic doublet; Plössl design *(AC508-400-C;* Thorlabs). High-Cost Relay: specialized two-photon laser scanning tube lens (TL200-2P2; Thorlabs). Shaded orange regions indicate that the relay reached its scan limit due to vignetting and the chief ray could no longer be traced. Shaded red regions indicate the relay is aberration limited at that wavelength and scan angle as determined by root mean square (RMS) wavefront error.

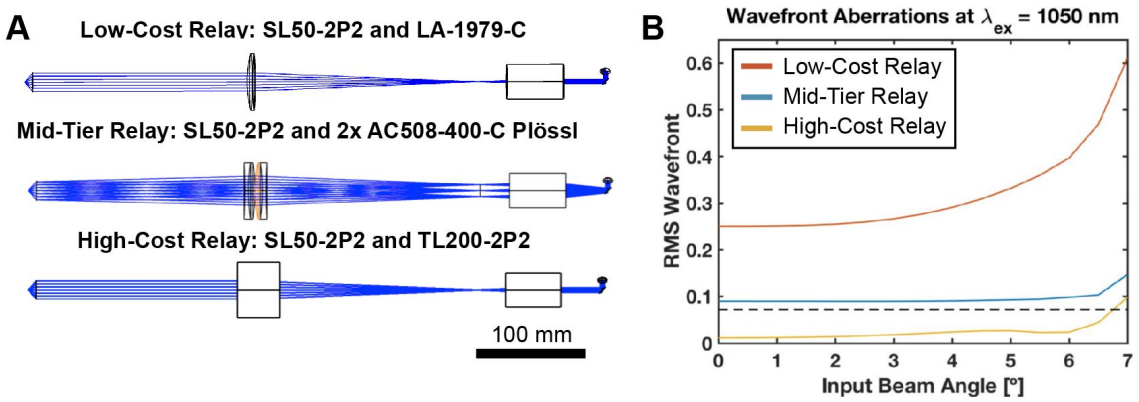

Figure 2.21: **Multiphoton scan engine relay.** (*A*) Zemax models of three afocal relays at different price points. (*B*) Root mean square (RMS) wavefront error as a function of mechanical scan angle for all three relays at a 1050 nm excitation wavelength.

In my own musings, I have given some thought as to what the ideal afocal relay would look like in a system unconstrained by some of the aforementioned practical requirements. In a perfect world, we would be unhindered by the diameter of the optical elements nor by the optical path length between the scanning mirrors and objective. Thus, the ideal relay would feature very large diameter, long-focal length lenses. Large diameter lenses are not only less prone to introducing vignetting, but offer an additional benefit in that the relatively small beam diameter would occupy a smaller footprint on its surface, and would therefore be less prone to aberration. Moreover, longer focal length, moderately curved optics would minimize aberrations as well. Of course, a commensurately large diameter objective with an appropriate field number and focal length would need to be designed to accommodate this relay. To better explain this, a longer focal length tube lens would result in a higher magnification objective in the absence of an adjustment to the objective focal length ($M = f_t/f_0$), and a larger magnification would reduce field of view radius in the absence of a larger field number. Assuming that field number and f_0 were increased, a longer focal length objective would

need a very wide aperture to accomplish high numerical aperture focusing; hence the requirement for a large diameter objective. Given an ideal large-diameter, longer focal length system a limiting factor would be Gaussian beam divergence over long scan paths and no longer the relay optical performance. Moreover, the scan lens focal length could remain constrained by the galvanometer scanning motion since a very long focal length scan lens would quickly clip the incoming beam at even shallow scan angles. Therefore an alternative solution would be to design large diameter doublet or triplet lenses with shorter focal lengths, with minimal aberrations.

2.4 Improving Sampling Speed Throughput

2.4.1 Resonant Scanner and High Repetition Rate Laser Integration

There have been a number of advances that have taken aim at high-speed volumetric imaging, including random access scanning [142–144] and remote focusing [145,146]. Arbitrary scanning neglects entire swaths of imaging real estate, which leaves structural and functional connectivity uncaptured, whereas the latter only increases sampling speed in a single dimension over a limited range. Other approaches have used swept planar excitation to increase volumetric throughput, but the majority of these implementations are either incompatible with intact whole-brain imaging due to stringent sample thickness and mounting criteria, [147,148] or limited by depth and spatial resolution [149–151]. At its core, multiphoton microscopy is a point-scanning technique, meaning that information is collected voxel by voxel as *xy* scanners and *z* stages manipulate the relative position of a focused beam. Thus, the most straightforward approach to increase temporal throughput is to use higher repetition rate lasers and faster beam scanners to improve acquisition line- and frame-rates. To address this first requirement, our lab is actively engaged in the development of low-cost, high-repetition

rate lasers [120,130]. Meanwhile, scan speed is restricted by the inertia of the oscillating mirrors [67]. Exotic methods to circumvent this include acousto-optic deflectors [4,152] or polygon-scanners [153]. Unfortunately, these come with their own tradeoffs, including dispersion in acousto-optic deflectors [154] and the inferior accuracy of polygon scanners for high-resolution, flat field applications [155]. Fortunately, resonant scanners, which oscillate at a fixed frequency, have been shown to provide a ~10-fold increase in sampling speed relative to conventional galvanometer mirrors and provide ample frame rates to capture transient neural activity for functional calcium imaging [140,156]. Thus, we have designed our system to integrate novel, high-repetition rate lasers with a resonant-scanning system for increased sampling speed and identified compatible data acquisition hardware.

In brief, the microscope system is designed to accommodate three unique ultrafast laser sources: a ytterbium fiber amplifier (developed), a Raman diamond laser (version two in development), and a tunable optical parametric generator (to be developed). Collectively, these lasers provided 80 MHz repetition rates at wavelengths ranging from 1050 – 1800 nm. However, given these sufficiently fast lasers, the rate-limiting step on temporal acquisition throughput becomes scanning speed. Therefore, we have substituted the slow scanning galvanometer mirror with a resonant mirror able to offer ultrafast speeds due to its fixed frequency oscillation and low inertia. Specifically we opted for an 8 kHz scanner (CRS-8kHz, Cambridge Technology), which provides some tradeoffs relative to the 4 and 12 kHz options. The 4 kHz option offers a larger clear aperture (12 x 9.25 mm vs 7.2 x 5.0 mm) meaning that its optical invariant is maximized, but does not offer a substantial upgrade in sampling speed. Meanwhile, the 12 kHz model provides a modest throughput enhancement relative to the selected 8 kHz scanner with a matching clear aperture, but a severely stunted scan angle (10º vs 26º, peak to peak). Ultimately,

the employed resonant scanner provides variable amplitudes at a fixed frequency, allowing us to vary our imaged field of view and maintain a high throughput sampling speed.

This augmentation vastly improves our vessel image acquisition speed which previously featured a frame rate of ~1.4 Hz (small diameter galvo-galvo scanning; 6215H, Cambridge Technologies) and ~0.7 Hz (large diameter galvo-galvo scanning; GVS012, Thorlabs) for 512 x 512 images to a frame rate of ~30 Hz for 512 x 512 images and ~8 Hz for 1024 x 1024 images (resonant-galvo scanning). To ensure full imaging flexibility, resonant-galvo and resonant-galvo-galvo configurations were both considered and compared relative to the benefits and capabilities of a basic galvo-galvo configuration. Since signal is expected to be much lower at deeper layers of anatomy, the ability to park the resonant galvanometer and reduce scan speed with a galvo-galvo pair helps ensure high signal-to-background ratio. Moreover, a resonant galvo-galvo configuration allows for arbitrary scan patterns in two dimensions, whereas a simpler resonant-galvo does not. Thus, we have opted for a more robust resonant-galvo-galvo set-up in our system. Critically, the resonant scanner enables functional imaging as well, meaning that neural activity using calcium indicators can be recorded in real time. Unfortunately, it bears mention that a resonant galvanometer's position does not vary uniformly in time unlike conventional galvanometers. This can lead to image compression artifacts if digital sampling corrections are not applied during image acquisition. Some groups handle this by manufacturing variable spatial line grid masks that impose a temporally uniform acquisition trigger. Instead, our method uses an open source MATLAB-based software (Scan Image, Vidrio Technologies) to sample at an extremely high rate and apply a greater binning factor at the edges of the image frame corresponding to slower scan speeds to eliminate compression artifacts. Imaging

identical regions of C57 mouse Texas red injected vasculature with both resonant-galvanometer and galvanometer-galvanometer scanning showed very good structural agreement across both volumes; an R^2 correlation value of 0.9305 was achieved after co-registration using image shifts and rotations (**Figure 2.22**).

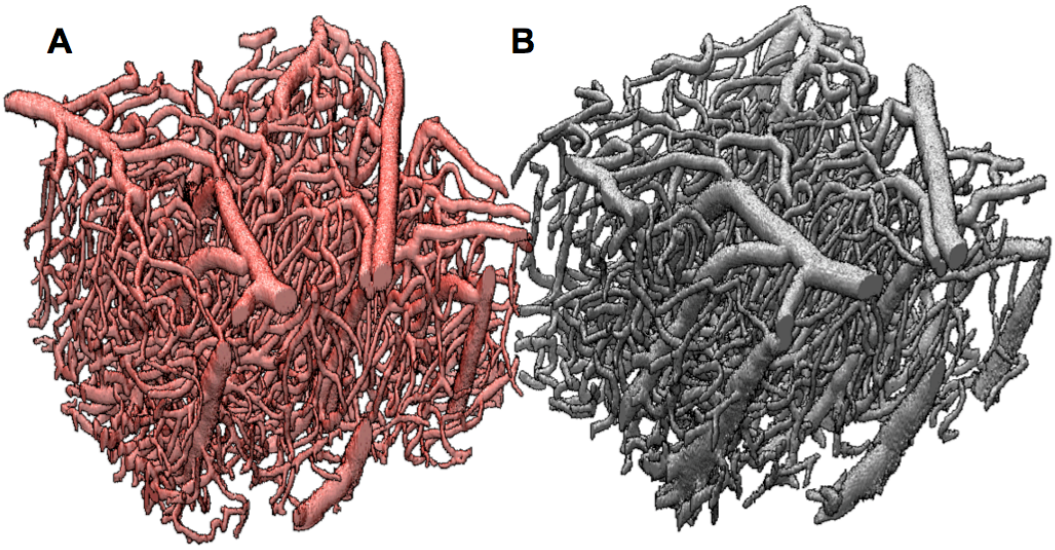

Figure 2.22: **High-speed scanning of murine vasculature.** 500 x 500 x 500 µm cubic volumes of C57 mouse vasculature imaging using a (*A*) resonant-galvo scanning configuration and a (*B*) galvo-galvo scanning configuration produce similarly high-quality renderings and present high levels of structural agreement (R = 0.9305).

2.4.2 High Speed Data Acquisition Electronics

Due to the high data collection speeds of resonant-galvanometer imaging, writing out this quantity of information is a not a trivial task. To meet this demand, the data acquisition hardware (**Figure 2.23**) must be redesigned to achieve rapid signal collection. Specifically, a field-programmable gate array, or FPGA, (PXIe-7961R, National Instruments) is needed to process the photomultiplier tube (PMT) data stream following analog to digital (A/D) conversion (Digitizer NI-5731, National Instruments) of the amplified PMT voltage signal. A chassis (PXIe-1073, National Instruments) provides

power to the data acquisition boards (DAQs) and FPGA-digitizer module, and enables communication with the acquisition computer via a PCI express communication card (PCIe-8361). To handle analog outputs, two DAQs (PXIe-6341, National Instruments) are housed on the same PXI chassis. The first is dedicated to driving an electro-optic modulator (EOM 350-80, Conoptics) and the resonant scanner (CRS-8kHz, Cambridge Technologies), split via a breakout box (BNC-2110, National Instruments). The second DAQ is split using an identical breakout box, with one analog output dedicated to the fast galvanometer mirror and the other dedicated to the slow galvanometer mirror (GVS012, Thorlabs). An automated laser shutter that is used to gate high-intensity beams during interruptions in image acquisition is also routed by this DAQ. Altogether, these scanning and data acquisition hardware upgrades allow our system to effectively take advantage of higher repetition rate lasers for rapid multiphoton sampling speeds.

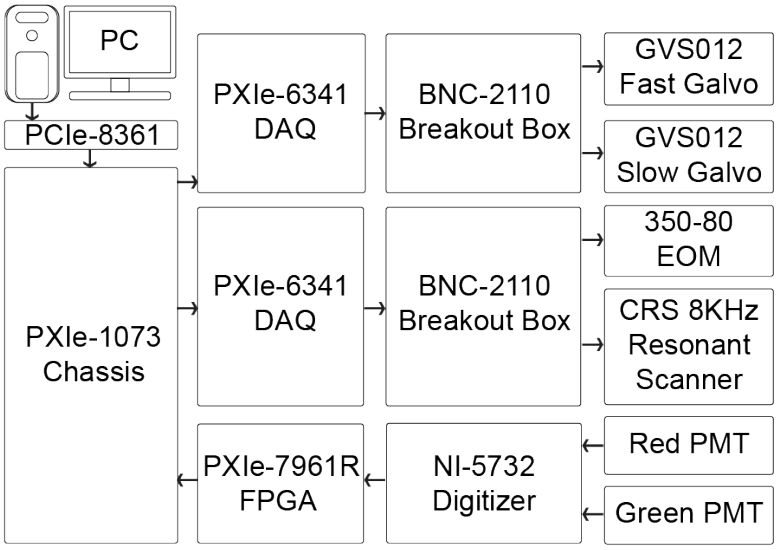

Figure 2.23: **High-speed data acquisition schematic.** A central chassis powers two DAQ outputs and an FPGA-digitizer module, and serves as a PCI communication hub between hardware instruments and PC. Scanning mirrors and an EOM attenuator receive analog outputs, and the PMT current stream is amplified into a voltage signal before A/D conversion and FPGA processing.

2.5 Microscope Enhancements and Modifications

2.5.1 Photomultiplier Tube and Pre-Amplifier Selection

A well-designed collection optics system delivers as many fluorescent photons as possible to the photocathode window of the photomultiplier tube (PMT) sensor. The PMT sensitivity should be as large as possible across the spectrum corresponding to the intended fluorophores' emission wavelengths. Our former upright microscope contained a pair of Hamamatsu H7422P-40 PMTs for typical fluorophores such as Texas Red and fluorescein, which emit at ~610 nm and ~515 nm, respectively. However, dyes that emit at much longer wavelengths, such as indocyanine green, elicit a low response from the H7422P-40 PMTs due to their reduced sensitivity beyond ~680 nm. In these extreme cases, one of the H7422P-40 PMTs was substituted with the H7422P-50 PMT. However, that implementation of the H7422P-40 and -50 PMTs was quite susceptible to noise amplification. Amplification is achieved with stand-alone pre-amplifiers (SRS570, Stanford Research Systems), and the current outputs of the PMTs were delivered to the pre-amplifiers via ~3 foot Bayonet Neill–Concelman (BNC) cables. Ideally, amplification should be in close physical proximity to the transducer whenever possible in order to maximize signal-to-noise ratio. Thus, we initially considered a pair of GaAsP amplified PMT modules (PMT2101, Thorlabs) for our improved upright scanning system, which offered excellent sensitivity over conventional fluorophore emission ranges (300 – 720 nm) and, most importantly, included built-in amplifiers, allowing us to maximize signal-to-noise ratio. More specifically, the package combined the Hamamatsu H10770PA-40 PMTs with a proximal high-frequency response, low-noise transimpedance amplifier. Initially, we suspected this PMT option would perform well, especially in consideration to its clear aperture, since another crucial consideration in the

selection of an optimal PMT to detect low-intensity fluorescent signals is the size of its active area and aperture acceptance angle. Our former multiphoton microscope's PMTs (active area diameter = Φ5.0 mm) had been customized to maximize their entrance angle by removing their stock thermoelectric cooling units. This effectively increased their clear aperture, granting a 10 mm diameter opening recessed by a 1.5 mm depth. This corresponds to an entrance angle of ~59º, at the cost of increased thermal noise, which is a decidedly unfortunate tradeoff. Notably, our proposed Thorlabs PMT upgrades maintained an identical active area diameter, Φ5.0mm, and clear aperture, 10 mm. However, the entrance angle is improved to 79.6º. Overall then, it seemed clear that the Thorlabs PMTs would outperform the existing instrumentation in two key aspects: (1) the proximity of the transimpedance amplifier to the transducer minimizes noise amplification and thereby increases signal-to-noise ratio, and (2) they provide a larger acceptance angle without compromising on the size of the active area, and thereby increase signal collection.

However, we quickly learned that the PMTs' built-in transimpedance amplifiers lacked the sensitivity to sufficiently amplify dim fluorescent signals relative to the Hamamatsu PMTs and Stanford Research Systems amplifiers (**Table 2.2**). We determined that we typically generated PMT current signals of around 2 μA and unfortunately required an amplified voltage signal of at least $\pm$ 0.2 V and ideally $\pm$ 1.0 V given the analog-to-digital (A/D) input of the data acquisition (DAQ) module being used. At this current level, using a 300 KHz bandwidth and a 2 μA/V gain setting (i.e. 5.0 x 10^5 V/A sensitivity) on the SRS570 results in an ample 1.0 V output. In contrast, the PMT2101 gain setting (1.1 x 10^4 V/A sensitivity) results in a near 50-fold smaller voltage signal of 22 mV at the same current level. We attempted using voltage amplifiers in conjunction with the PMT2101, but found that the amplification introduced substantial

noise into the final image. In the Thorlabs PMT and amplifier package's defense, this gain sensitivity is fixed at all bandwidth settings (80, 2.5, 0.250 MHz), whereas the SRS570 sensitivity drops off dramatically as bandwidth is increased. Moreover, the SRS570 bandwidth is capped at 1.0 MHz. This suggests that neither system is suitable for a flexible upright scanning system intended for both galvo-galvo scanning (low bandwidth) and resonant-galvo scanning (high bandwidth). Thus, we continued our search for a PMT and pre-amplifier combination that would maximize sensitivity at all bandwidths and identified the Femto DHPCA-100 as an ideal option. At a 220 kHz bandwidth using the less noisy low gain setting (1.0×10^7 V/A sensitivity) we could easily generate 20 V signals for galvo-galvo scanning. In practice, we are far more likely to use the 3.5 or 1.8 MHz bandwidths low gain settings (1.0×10^5 or 1.0×10^6 V/A sensitivity, respectively) in conjunction with an external 240 kHz low-pass filter (EF504, Thorlabs). During resonant-galvo scanning, we are able to use the Femto DHPCA-100's 14 MHz bandwidth setting (1.0×10^5 V/A sensitivity) to generate $\pm$ 0.2 V output signals, which does a sufficient job of filling out the high speed digitizer's dynamic range (NI 5732, National Instruments) voltage input range (0.5138 $V_{pk\text{-}pk}$ when gain = 12 db).

Pre-Amplifier	Band-width	Gain Setting	Sensitivity [V/A]	Current Input [A]	Output [V]	1 V DAQ A/D Input Range Utilization	0.2 V DAQ A/D Input Range Utilization
SRS570	0.3	2 μA/V	5.0E+5	2.0E-6	1.0E+00	100%	>100%
TIA60	60	Fixed	3.0E+4	2.0E-6	6.0E-02	6%	30%
PMT2101	Variable [80, 2.5, 0.250]	Fixed	1.1E+4	2.0E-6	2.2E-2	2.2%	11%
Femto DHPCA-100	200	Low Gain	1.0E+2	2.0E-6	2.0E-4	0.02%	0.1%
		High Gain	1.0E+3	2.0E-6	2.0E-3	0.2%	1%
	80	Low Gain	1.0E+3	2.0E-6	2.0E-3	0.2%	1%
		High Gain	1.0E+4	2.0E-6	2.0E-2	2%	10%
	14	Low Gain	1.0E+4	2.0E-6	2.0E-2	2%	10%
		High Gain	1.0E+5	2.0E-6	2.0E-1	20%	100%
	3.5	Low Gain	1.0E+5	2.0E-6	2.0E-1	20%	100%
		High Gain	1.0E+6	2.0E-6	2.0E+0	>100%	>100%
	1.8	Low Gain	1.0E+6	2.0E-6	2.0E+0	>100%	>100%
		High Gain	1.0E+7	2.0E-6	2.0E+1	>100%	>100%
	0.22	Low Gain	1.0E+7	2.0E-6	2.0E+1	>100%	>100%
		High Gain	1.0E+8	2.0E-6	2.0E+2	>100%	>100%

Table 2.2: **Pre-amplifier sensitivities for photomultiplier tube current signal amplification.** For low-bandwidth applications (i.e. galvo-galvo scanning), the Stanford Research Systems (SRS570) and Femto (DHPCA-100) pre-amplifiers offer sensitivity settings that provide sufficiently large voltage signals to utilize a significant portion of the data acquisition (DAQ) module's dynamic range. For high-bandwidth applications (i.e. resonant-galvo scanning), the SRS570 lacks the frequency range and only the Femto pre-amplifier offers sensitivity settings that yield a high dynamic range utilization. The Thorlabs PMT's built-in amplifier (PMT2101) lacks sufficient sensitivity for either application, as does the standalone pre-amplifier (TIA60). Red shaded regions indicate low (<50%) dynamic range utilization.

2.5.2 Photomultiplier Tube Collection Optics

A series of lenses must be positioned between the objective rear aperture and the PMT photocathodes to collect as much signal as possible. Two specific challenges

present themselves in this task. First, fluorescent light captured by the objective exits the objective aperture in a divergent state; more specifically, it emerges in a roughly isotropic fashion over a maximum angular distribution of ±12 to 15 degrees. Second, the collection optics must minify the emerging light-field by a factor of 3.6 (Olympus XLUMPLFLN-20X) to 4-fold (Olympus XLPLN25XSVMP2) to successfully image the objective rear aperture onto the smaller photocathode sensor. In this scenario, the four fold minification factor becomes the more limiting configuration, and it was therefore determined the collection optics lenses should generate a 0.25x magnification.

To begin the design process, the original 60 mm upright collection optics were modeled in Zemax (designed by Dr. Arnold Estrada), with a simple revision to include our 25x objective (back aperture diameter = 20 mm) with an assumed 15º isotropic angular distribution, since this would represent the most extreme and stringent configuration in the optical system (**Figure 2.24**). Following the objective is a 76.2 mm dichroic cube, 23.8 mm of free space, and the first collection lens (achromatic doublet, f = 100 mm, AC508-100-A; Thorlabs). Sufficient distance was added between the second dichroic cube, which is used to split red and green channel images, and the first collection lens to accommodate for the spatial requirements of the tube mounts. The second collection lens system consisted of an f = 50 mm plano-convex lens (32971; Edmund Optics) and an f = 40 mm aspheric lens (023-2250; Optosigma), with a roughly ~22.22 mm combined focal length. Unfortunately, this lens system exhibits a few key shortcomings. In practice the objective's rear aperture must be the stop in the optical system to preserve maximum etendue through to the photocathode. Unfortunately, in this former system, the distance of the first collection lens from the objective's rear aperture means that the clear aperture of the initial achromatic doublet lens becomes the stop. The second issue is that fluorescent light exiting the second collection lens system focuses at a

distance that is less than the thickness of the emission filter mount (12.7 mm) and the photocathode recess meaning that the sensor plane is past the focal plane. This second point was far less problematic with the original collection optics as designed by Dr. Estrada since the photocathode was only recessed by 1.5 mm (H10770PB-40; Hamamatsu) and not 8.6 mm (PMT2101; Thorlabs). At the sensor plane, the out-of-focus image of the 20 mm rear aperture constitutes a ~14.90 mm spot radius at 450, 550, and 650 nm emission wavelengths, which is well beyond the 5 mm photocathode size. In total, vignetting on the achromatic doublet tube mount and photocathode aperture leads to a combined loss of ~55% of rays. Ultimately, this means that the collection optics on the former upright microscope were severely sub-optimal.

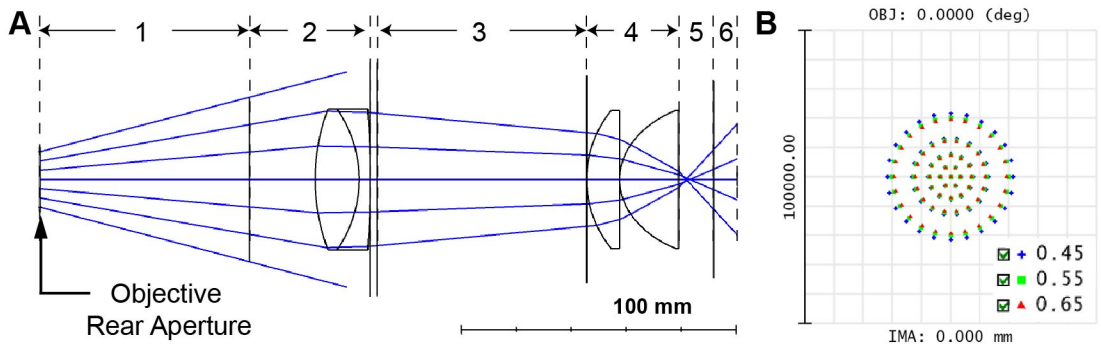

Figure 2.24: **Former collection optics design.** (*A*) The former collection optics had two major shortcomings. First, the distance of the initial collection lens was positioned far from the objective rear aperture, resulting in severe vignetting. Second, the objective rear aperture is imaged at a plane several millimeters before the photomultiplier tube photocathode. Position 1: dichroic cube; 2: first collection lens system mount; 3: dichroic cube; 4: second collection lens system mount; 5: emission filter; 6: photocathode recess. (*B*) Root mean square (RMS) spot radius of the former collection optics is ~14.90 mm weighted across 450 (blue), 550 (green), and 650 (red) nm wavelengths.

To remedy the first issue of excessive vignetting on the initial achromatic doublet, the intuitive solution is to increase the clear aperture of this lens by adopting a three-inch

collection optics system. However, this option proved unrealistic due to the availability of the off-the-shelf components, and we were restricted to a 60 mm cage cube system. An alternate solution is to move the first collection lens closer to the dichroic cube. In fact, this has the ancillary benefit in that light will exit the first collection lens in a better collimated state. Therefore, the Zemax model was revised, positioning the achromatic doublet as close to the first dichroic cube as possible and mounting it within a shortened lens tube (**Figure 2.25(a)**), which dramatically decreases the proportion of vignetted rays from ~55% to ~35%. However, the shorter focal length of the second collection lens system still poses a significant issue considering the emission filter and recessed photocathode need to be accommodated within that focal distance. As is, the photocathode rests 15.763 mm beyond approximate focus (solved by a marginal ray height of zero), and the root mean square (RMS) spot radius remains an excessively large ~12.539 mm.

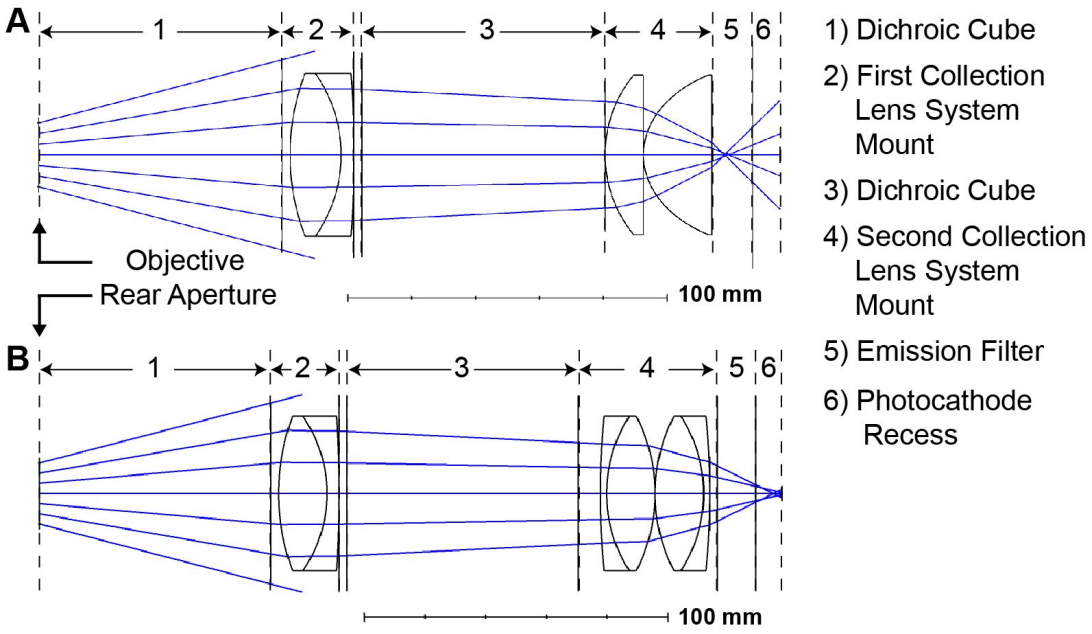

Figure 2.25: **Redesigned collection optics system.** (*A*) Moving the first collection lens closer to the first dichroic cube has a major benefit over the former design in that fewer rays vignette on its clear aperture. (*B*) Replacing the former second collection lens system with an f = 40 mm achromatic Plössl doublet successfully images the objective rear aperture onto the photomultiplier photocathode. Both models correspond to the 25x objective (XLPLN25XSVMP2; Olympus)

Our next goal is now to replace the second collection lens system consisting of the planoconvex and aspheric lenses with a longer focal length system (**Figure 2.25(b)**). The thickness of the emission filter (12.7 mm) and the recessed photocathode (8.6 mm) constitute a 21.3 mm width, meaning that a ~25 mm focal length appears to be appropriate. Empirically, however, a Plössl design with a 40 mm focal length was found to perform much better. This discrepancy can be accounted for by the fact that the light does not exit the initial collection lens in a perfectly-collimated state, and is already converging. The Plössl design, which consists of two f = 80 mm achromatic doublets (AC508-080-A) performs satisfactorily at 450, 550, and 650 nm emission wavelengths,

successfully imaging the objective rear aperture onto the photocathode. Notably, the dimensions of the second collection lens system are quite important. It is assumed that the first surface of the f = 80 mm achromatic doublet is 7.3 mm from the last surface of the second dichroic cube, and that the two achromatic doublets are flush with one another. The last surface of the second doublet is separated from the emission filter by 2.5 mm, which corresponds to the width of a retaining ring. These widths are accomplished by mounting each doublet in a thick 60 mm cage plate (LCP01T; Thorlabs). It is therefore clear that the collection optics are high performance in the case of the of the 25x objective. However, it remains imperative that optical performance remains robust when the 20x objective is used, the major change being that aperture diameter decreases from 20 mm to 18 mm. With no changes made to the collection lens system, the RMS spot radius remains smaller than the photocathode diameter with the 20x model when weighted at equivalent wavelengths, which remains consistent with our prior assertion that the 25x objective represented the more stringent design condition.

This new design intentionally uses achromatic doublets for all collection lenses, whereas the original design relied on the use of a hybrid lens system consisting of achromatic, a plano-convex, and aspheric lenses. While a fully achromatic set-up may not be the best for imaging applications where aberrations lead to substantial performance degradation, for a point detection system employed with a PMT it is quite satisfactory. In fact, the major advantage is that the RMS spot radius at the photocathode remains equal to or less than the photocathode diameter across all wavelengths, which is especially important in consideration of the diverse array of fluorophores to be used with the system. To evaluate this, the collection optics were modeled with 450, 550, and 650 nm input wavelengths, representing fluorophores in the blue to red spectrum, and all wavelengths are within an acceptable range.

2.5.3 Folded Microscope Design

Due to overhead lab shelves, a fully upright microscope design was physically unable to be mounted on a breadboard perpendicular to our optical table. Thus, we were forced to consider a folded microscope. There are several considerations to be weighed when introducing a folded design. First, it is unwise to create a fold at any position where the beam is focused. Doing so will result in any micro-defects in the fold mirror's surface being propagated forward into the optical system. Another option is to replace the scan lenses with scan mirrors, and to have those mirrors introduce the folds directly. This minimizes the number of optical elements, conserves optical real estate, and minimizes effects of chromatic aberration, which can be considerable in thicker scan and tube lenses. However, these mirrors can be highly astigmatic, although commonly the astigmatism introduced by one reflector is compensated for by the other.

In our particular system, we prioritized a scan lens (SL50-2P2) and tube lens (TL200-2P2), which were low aberration and coated to maximize transmission in the near-infrared spectrum. As mentioned above, we found it unwise to position a fold mirror between the scan lens and tube lens, where the beam was coming to a convergence. Since our tube lens has a considerably long focal length (200 mm) and the beam emerges collimated beyond it, this becomes a natural position for a fold mirror. However, it is necessary to ensure that the introduction of this fold allows the beam to remain conjugated at a center position on the objective's rear aperture. Thus, a scan engine with (**Figure 2.26(a)**) and without a fold (**Figure 2.26(b)**) was modeled in Zemax's OpticStudio to evaluate this. It was found that at severe tilt angles (5 degrees) that the beam does deviate slightly off position (~2.347 mm). However, this value was the same for the unfolded design, and it was concluded that the fold did not individually contribute to any issues with optical alignment. Rather, the deviation at severe tilt angles

could more likely be attributed to the imperfect coupling of the mirror pair in the galvanometer scanning system.

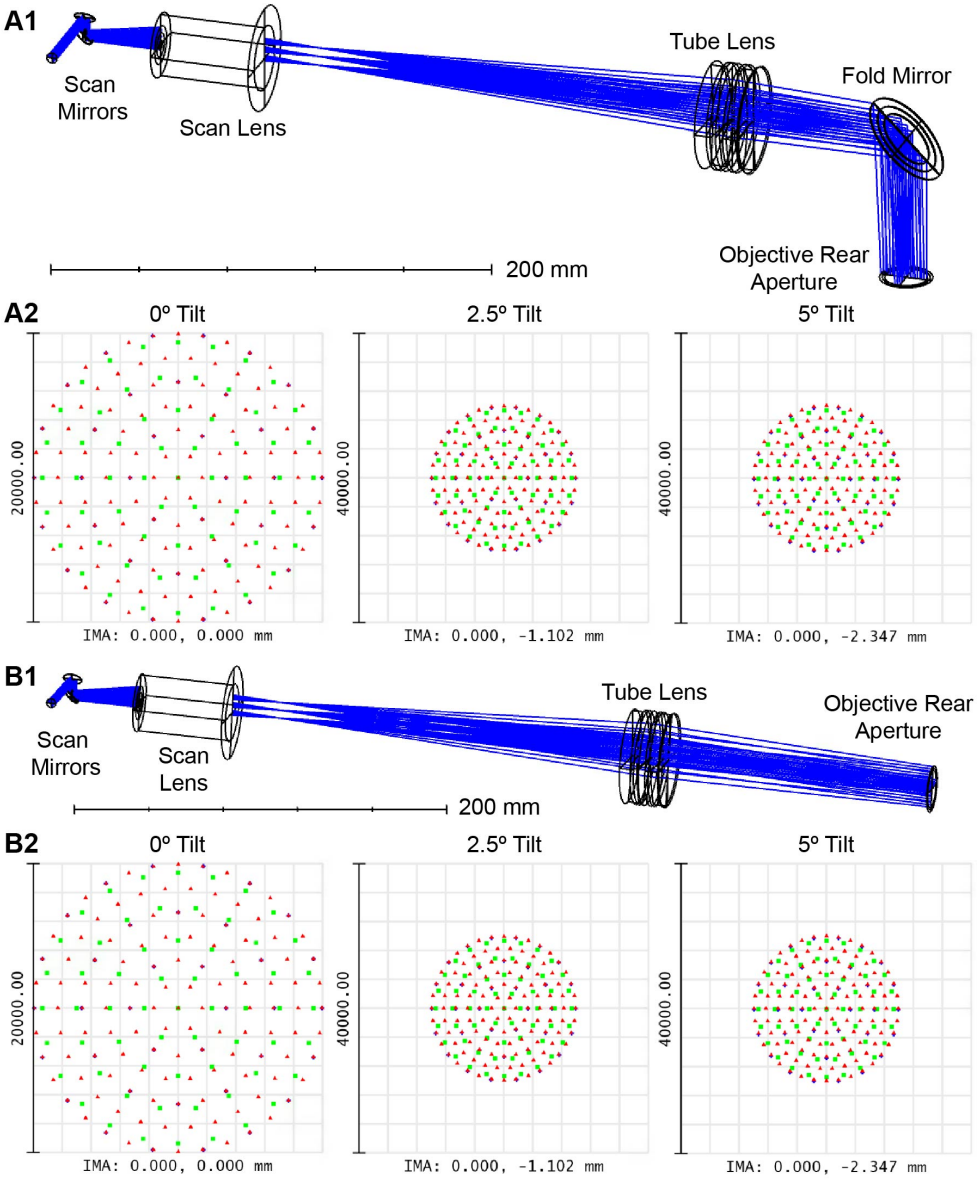

Figure 2.26: **A folded relay does not affect beam position on the microscope objective back aperture.** (*A1*) Three-dimensional viewer and (*A2*) spot diagram of the folded relay design displayed with three configurations at 0º, 2.5º, and 5º scan angles. (*B1*) Three-dimensional viewer and (*B2*) spot diagram of the unfolded relay design displayed with three configurations at 0º, 2.5º, and 5º scan angles.

2.5.4 Microscope Mechanical Design

The entire microscope design was prototyped in SolidWorks computer aided design (CAD) software to ensure that the final assembly would include fully compatible components and fit in the allotted space on our optical table. For the vast majority of components, such as the periscope onto the optical breadboard platform, optical distance and precise dimensions were unnecessary. However, for other modules, including the resonant-galvanometer relay and the galvanometer-objective relay, precision was paramount to optical performance (**Figure 2.27(a-b)**). Thus, we capitalized on using CAD modeling to select mounts and fabricate shims that would ensure that prescribed optical path lengths determined in Zemax could be met in the final hardware assembly. Moreover, we took this opportunity to prototype experimental concepts for auxiliary modules and enhancements (**Figure 2.27(c-d)**), such as an autocorrelator that could enable pulse width measurements in the sample plane and a rotating objective turret that would maintain laser alignment and enable multiphoton scanning along an optical axis perpendicular to tilted specimens, such as live mice.

The final microscope assembly (**Figure 2.28**) was primarily constructed from off-the-shelf components purchased from Thorlabs, and relied on 60 mm and 30 mm cage assembly systems to ensure concentric alignment of optical and optomechanical components. The microscope rests on a large optical table, but a smaller 18” x 36” breadboard is suspended to elevate the bulk of the microscope itself above the specimen (e.g. live rodent). Importantly, the breadboard height is adjustable using a set of four adjustable rigid stand post holders (LPH150; Thorlabs). The specimen itself is spatially manipulated using a three-axis stage in the XY (50.8 mm range; MTS50Z8; Thorlabs) and Z dimensions (50 mm range; MLJ050; Thorlabs). A periscope is used to send the beam from the optical table onto the breadboard and into the resonant scanner.

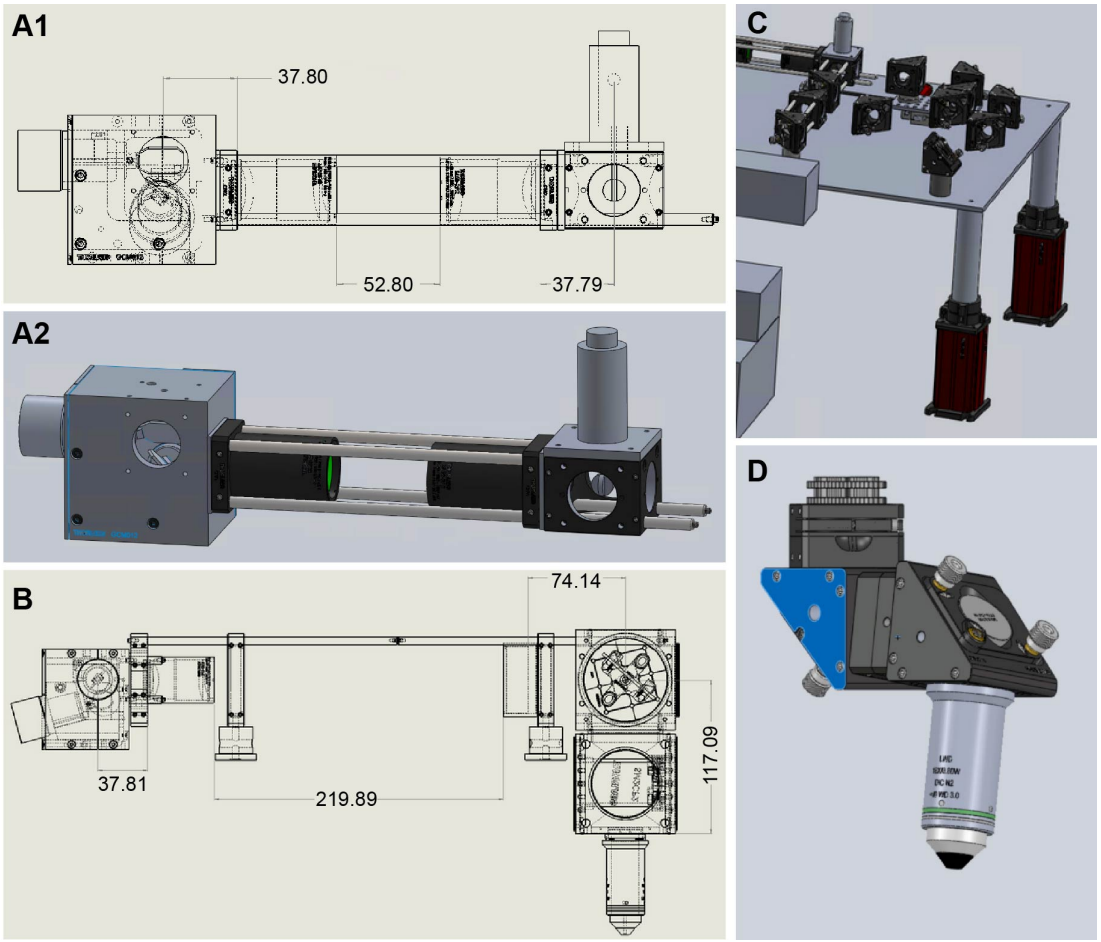

Figure 2.27: **Computer-aided design (CAD) modeling of the upright microscope.** (*A1*) Dimensions for the resonant-galvanometer relay and a look at the corresponding (*A2*) 3D rendering. (*B*) Dimensions of the galvanometer-objective relay. (*C*) Using CAD to prototype an in-line autocorrelator for pulse-width measurements. (*D*) An experimental CAD prototype for a two-axis rotating objective turret. All distances in millimeters.

For routine operation, an alignment jig before the resonant scanner ensures beam centering on the objective back aperture. However, the resonant scanner is mounted to a three-axis XYZ stage as well as a three-axis pitch, roll, and yaw stage to enable precision alignment. The scan lens and tube lens are easily swapped out with alignment modules to aid in guiding this precision alignment. Moreover, a mirror can be flipped into place between the scan and tube lenses to record laser speckle contrast images; the illumination

module can be found mounted to the underside of the breadboard. Meanwhile, a two-channel photomultiplier tube (PMT) assembly is mounted to the side of the excitation/emission dichroic for multiphoton fluorescence collection. An interesting feature of this microscope is its flexibility – the microscope head (i.e. fold mirror, dichroic cube, PMT module, and objective) can be rotated 180º for operation as an inverted microscope, which is necessary to image certain samples such as suspended liquid aliquots on glass slides un-sandwiched by coverslips.

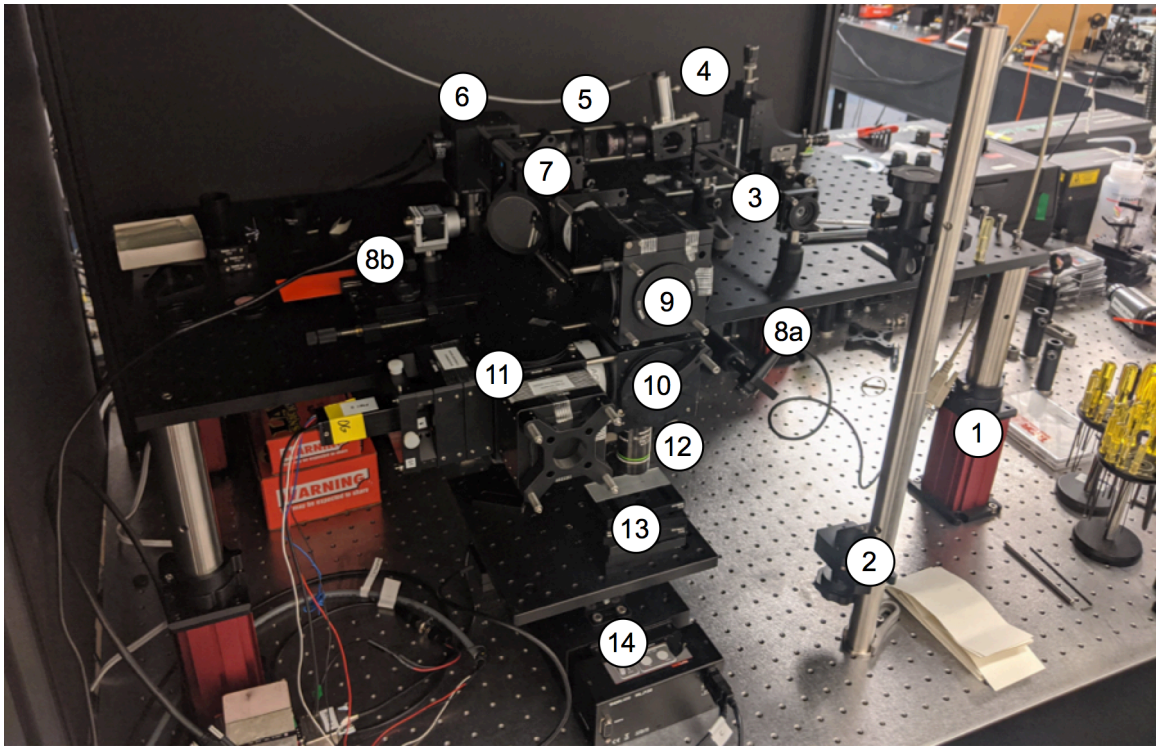

Figure 2.28: **Final microscope assembly.** The wide field-of-view, high throughput microscope contains many modules of interest. 1) Adjustable post holders allow users to adjust the microscope's height. 2) Periscope. 3) Alignment jig. 4) Resonant scanner with six adjustable axes. 5) Resonant-galvanometer relay. 6) Galvanometer-galvanometer scanner. 7) Galvanometer-objective relay. 8a) Laser speckle diode. 8b) Laser speckle camera. 9) Fold mirror. 10) Dichroic mirror. 11) Two-channel photomultiplier tube detection module. 12) Objective. 13) Specimen. 14) Three axis stage to translate specimen.

Chapter 3: Automated Curation of Vectorized Cerebrovascular Networks

3.1 INTRODUCTION

Stroke is a shockingly common event that can lead to critical, chronic disability. In order to characterize the extent and severity of ischemic events, as well as recovery post-ischemia, cerebrovascular imaging is essential. Repeated large field of view imaging and vectorization of the cortical angiome encompassing > 1 mm^3 volumes will contribute to a refined understanding of the chronic topology, connectivity, and hemodynamics of vascular networks in healthy and disease states. Resulting image data imposes a large computational burden and is difficult to analyze quantitatively, meaning that vectorization is required to transform the structural images into data sets that can be analyzed and manipulated more easily. More specifically, vascular vectorization is the process by which blood vessels are located, sized, and split into individual strands, allowing the investigator to efficiently filter and isolate regions and features of interest and quickly calculate corresponding descriptive summary statistics without the need for additional image analysis. Analytical metrics of interest used to understand the chronic evolution of healthy and diseased vascular morphology include geometric and spatial features such as strand length, tortuosity, and vessel radius as well as basic image characteristics, such as vessel brightness, which may be used to indicate perfusion.

In particular, our lab has used Volumetric Image Data Analysis (VIDA) Suite to enable macroscale data analysis of morphological details and longitudinal changes [157]. VIDA accomplishes vectorization in a multi-step process that begins with matched filtering to 82 rods in various orientations to produce “rod-enhanced” sub-blocks [158]. Maximal responses across these volumes is used to identify a vessel enhanced grayscale volume, followed by local filtering and variable local thresholding to produce an

enhanced vascular mask. Next, connectivity-conserved thinning is applied to the mask to create a monofilament centerline. Additional transformations and auxiliary processes lead to the final set of strands, where each strand is a junction-to-junction, junction-to-endpoint, or endpoint-to-endpoint set of vertices with a defined radius at each point. Given ideal low noise and high signal-to-background ratio images, VIDA segmentation performs admirably. However, border cut-off effects, image distortions, and sample dimness can lead to significant vectorization errors. Thus, a robust curation approach is required to accompany vectorization to ensure that bulk statistics are reliable and meaningful. Manual curation is infeasible due to the enormous number of strands that occupy a mere cubic millimeter volume of cortex. Therefore, an automated classifier was developed where more than 2,000 strands were manually classified for ground truth, and strand features describing the geometric, microscopic, and vascular characteristics of each strand were extracted. Exploratory data visualization was performed to gain insight on which features may function as viable predictors in a classifier, and to guide troubleshooting efforts. Subsequently, interrelated and non-significant features were removed using multicollinearity analysis and backwards feature elimination respectively. Two learning algorithms were trained using the remaining feature set: binary logistic regression and Adaboost. Model evaluation via receiver operating characteristics area-under-the-curve showed acceptable performance (AUC > 0.85) without overfitting, as evidenced by similar performance on test and train fractions. Finally, data curation using a single decision threshold (fully automated curation) or multiple decision thresholds (semi-automated curation requiring manual intervention) was evaluated. For both approaches, Adaboost was shown to outperform binary logistic regression. For fully automated curation, logistic regression results in a ~0.78 classification accuracy relative to Adaboost's modestly larger ~0.805. Using multiple decision thresholds to achieve a

0.90 classification accuracy, the logistic regression classifier required ~30% of strands to be manually curated compared to Adaboost, which required ~20% be subject to manual intervention. While these results are promising, the inclusion of a more robust initial feature set should improve model performance, and future efforts should examine how well trained classifiers perform across healthy and post-ischemic specimens.

3.2 Manual Classification Of Positive and Negative Strands

A curation approach requires ground truth, or hand labeled strands that are denoted as either "true" or "false." Thus, a MATLAB program was developed to allow each vectorized strand to be overlaid onto max intensity projections of the vascular volume in the *XY*, *XZ*, and *YZ* planes. A 3D version of this graphical user interface was developed as well using UCSF Chimera scripting functions (**Figure 3.1**); however, this proved to be more computationally intensive without any clear advantages in terms of ease of identification or hand labeling accuracy, with the exception of being able to visualize vectorized vertex radius. By overlaying each strand with the raw data, the user is able to assess whether the VIDA Suite vectorization program appropriately (class = 1) or falsely (class = 0) identified the strand with a single keypress. In ambiguous cases, the user is instructed to enter (2), which denotes an uncategorized strand. Uncategorized strands were omitted from training data sets used for fitting the learning classifiers, and from test data sets used for model evaluation. With each keypress event, the manual classification is logged along with strand ID and general strand features, as elaborated upon in the following section.

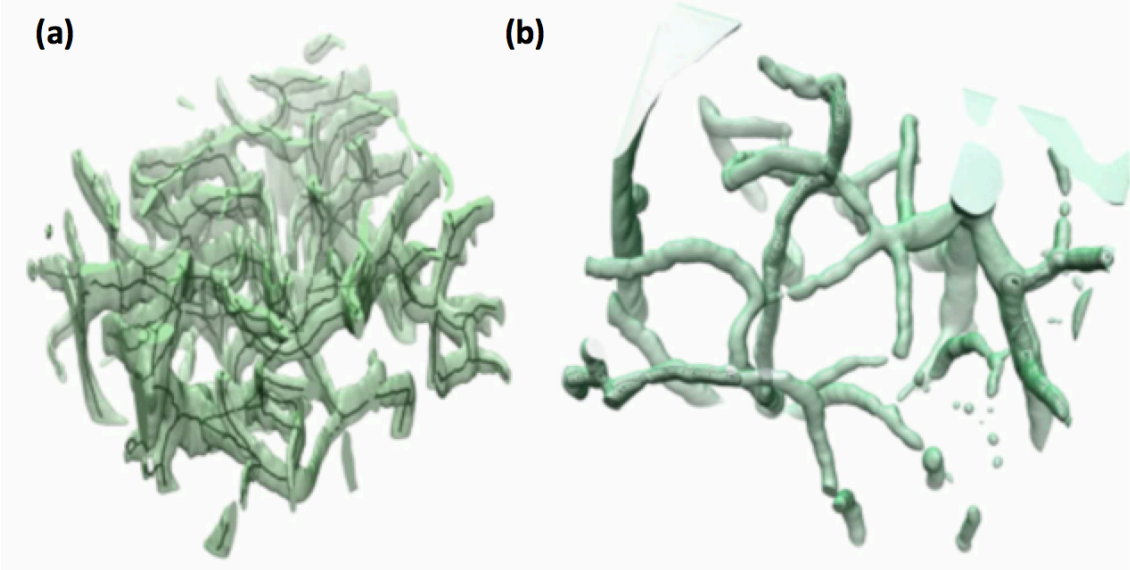

Figure 3.1: **A three-dimensional graphical user interface (GUI) for hand labeling strand vectorizations.** A 3D curator GUI allows (*A*) vectorized strand centerlines or (*b*) vectorized strand vertices with true radii to be overlaid with renderings of original multiphoton microscopic vascular density (light green) for manual classification.

3.3 Feature Extraction

As each strand was manually classified, a variety of features were extracted and associated with each strand. These features could stem from the vectorized data (geometric and spatial characteristics) or the raw data (microscopy characteristics) (**Table 3.1**). Geometric and spatial characteristics would describe the length, size, position, and travel of a specific vessel segment. In this case, travel refers to the tortuosity of a vessel, which is a descriptor of how entangled it is. In addition, the vectorized data could report on relational features of strands, including how many junctions or free endpoints they possessed. Finally, microscopy characteristics included brightness and signal-to-background ratio. The rationale behind the inclusion of each of these features is that they may hold some predictive power with respect to differentiating the two classes of strands.

For instance, it was posited that a lower signal-to-background ratio might increase the likelihood of strand misidentification. Unfortunately, signal-to-background ratio was ultimately omitted as a feature from the final curation method. To calculate signal-to-background ratio for a given strand, each *z*-plane encompassed by that specific strand was individually thresholded using Otsu's method, and an intensity ratio was calculated from that binary thresholding. Finally, the collective *z*-plane intensity ratios were averaged to compute a single aggregate signal-to-background ratio for the entire strand. Unfortunately, manual inspection of the Otsu binarization revealed some inconsistencies stemming mainly from poor threshold placement. Thus, this method of signal-to-background calculation was deemed to be unreliable and therefore omitted from inclusion as a strand feature.

General Features	
strandID	Strand index number; corresponds to numbered output from VIDA Suite vectorization
class	Classification of each strand. 0: Faulty Vectorization; 1: Accurate Vectorization; 2: Unclassified, Ambiguous Vectorization
Geometric and Spatial Features	
size	Number of vertices in strand multiplied by voxel size in units of microns.
minZ	Minimum *z* position
maxZ	Maximum *z* position
meanZ	Mean *z* position
minX	Minimum *x* position
maxX	Maximum *x* position
meanX	Mean *x* position
minY	Minimum *y* position
maxY	Maximum *y* position
meanY	Mean *y* position
meanRadius	Mean radius of strand
stdRadius	A measure of radius uniformity for each strand
length	Distance from endpoint to endpoint of strand
tangleFactor	Size divided by length. The larger the tangle factor, the more tortuous the vessel.
junctionPoints	Number of junction points per strand
freeEndPoints	Number of free endpoints per strand
edgeX	Mean distance from edge in *x* dimension
edgeY	Mean distance from edge in *y* dimension
Microscopy Features	
strandBrightness	Average intensity of pixels encompassed by each strand
signalToBackgroundRatio	Mean signal-to-background-ratio (SBR) of all z-planes encompassed by each strand. **Note**: this feature was omitted from remaining analysis due to inconsistencies in calculation, as discussed above in this section.

Table 3.1: **Summary of strand features**. Three categories of features were extracted from each vectorized strand to aid prediction of false positives. General features consisted of a strand identification number and a true class label from manual curation. Geometric and spatial features were extracted from the vectorized set. Microscopy features were calculated from the original multiphoton images at the locations of each strand.

3.4 Exploratory Data Visualization

It is often useful to build an intuition for which features may help provide a descriptive analysis of good and bad strands and provide a basis for strand classification and differentiation. Such an intuition will not only make it easier to interpret, optimize, and troubleshoot any developed classification algorithms, it also provides the additional benefit of highlighting what goes awry during vectorization and data collection. This awareness leads to better practices that will ultimately reduce the number of misidentifications and reduce the burden for data curation post-vectorization. One of the more effective methods for building such an intuition is exploratory data visualization. Below, each of the included features has been plotted in a format (e.g. boxplot or scatter plot) that most naturally draws comparisons of the faulty and accurate strand vectorizations.

3.4.1. Exploratory Data Visualization: Strand Size

Here, the size in microns of `class 1` and `class 0` strands (i.e. number of vertices, multiplied by the voxel size) was compared using a boxplot (**Figure 3.2**). The box represents the interquartile range (*IQR*), which spans the *Q1* (25th percentile) and *Q3* (75th) percentiles. The boxes' midlines correspond to the median values for each class. Extended lines emanating from the boxes indicate the minima and maxima. In the event that there are outliers, depicted here as scatterpoints, the lines do not represent the true maxima or minima, but rather $Q1 - 1.5 \times IQR$ or $Q3 + 1.5 \times IQR$, respectively. Our first discovery is that misidentified strands tend to be very short, and correctly classified strands tend to be much longer. This makes logical sense, as many faulty strands seem to arise from Volumetric Image Data Analysis (VIDA) Suite detecting clusters of noise and creating one or two voxel "strands." In some cases, VIDA Suite manages to misidentify

very long strands, even approaching 500 μm in length. However, these are clear outliers, as depicted in the boxplot on the left. Generally, these sort of errors correspond to VIDA Suite jumping across two or more adjacent vessels. For example, in a single plane or in a projection image, two distinct vessels may appear as continuous rather than contiguous, and VIDA will make a false interpretation. However, comprehensive curation by scanning several *z*-planes or maximum intensity projections along different axes quickly reveals these examples of vectorization to be erroneous.

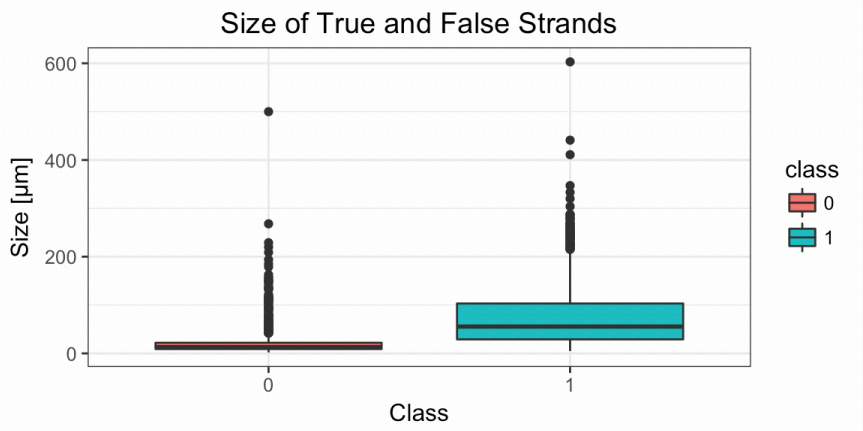

Figure 3.2: **Size of true and false strand vectorizations.** Class 1 (true) strands tend to be a larger size then class 0 (i.e. false) strands. Size is given by the number of vertices multiplied by the voxel size.

3.4.2 Exploratory Data Visualization: Transverse Position

Subsequently, I strived to determine whether or not transverse (i.e. *xy*) position had any bearing on whether a strand was classified correctly or not. A violin plot would prove to be more useful than a standard boxplot. Whereas a boxplot might show you where the bulk of the data lies and provide a very coarse sense of distribution, a violin plot behaves more similarly to a histogram in its ability to depict where several clusters of data points might group together. What we see by looking at the minimum, maximum,

and mean *x* position is that bad strands (`class 0`) overwhelmingly reside at the edges of the image planes, and that true strands are more evenly distributed, with a slight tendency to emanate from the centers of the images (**Figure 3.3(a)**). The same trends ring true for the *y*-dimension (**Figure 3.3(b)**). Interestingly, the `class 1` strands do not appear to be symmetrically distributed in *x* and *y*. More specifically, properly vectorized strands are more often located at smaller *x* coordinates (i.e. left of image) and larger *y* coordinates (i.e. top of image) than they are at larger *x* coordinates and smaller *y* coordinates. This may be an indicator of non-uniform illumination during multiphoton imaging. This hypothesis is supported by the fact that `brightness` emerges as a predictive feature of strand classification.

Perhaps a more intuitive way of visualizing transverse spatial position trends is to plot each strand as an individual point, colored by class, where a good strand is shown as mint green and a misvectorized strand is colored red. With this plot, we immediately capture the general information conveyed by the violin plots - bad strands tend to reside near the borders of the microscopy volume (**Figure 3.3(c)**). This is a reasonable discovery, as we might expect Volumetric Image Data Analysis (VIDA) Suite to struggle with cut-off, border effects and to experience difficulty with tracing vessels that end abruptly. This suggests that an important actionable step to be taken during data acquisition is to first determine the volume of interest needed for analysis (e.g. 500 μm x 500 μm x 1 mm), and to apply an overscan to ensure that a sufficient number of accurately vectorized vessels reside within that final analysis volume after curation. It may be worth noting that ease of interpretability of the *xy* scatter plot may imply that the less intuitive violin plots above were redundant and unnecessary. However, the violin plots contained valuable information in that they were able to capture the subtle asymmetry of the class 1 strands in a way that a cluttered scatter plot cannot.

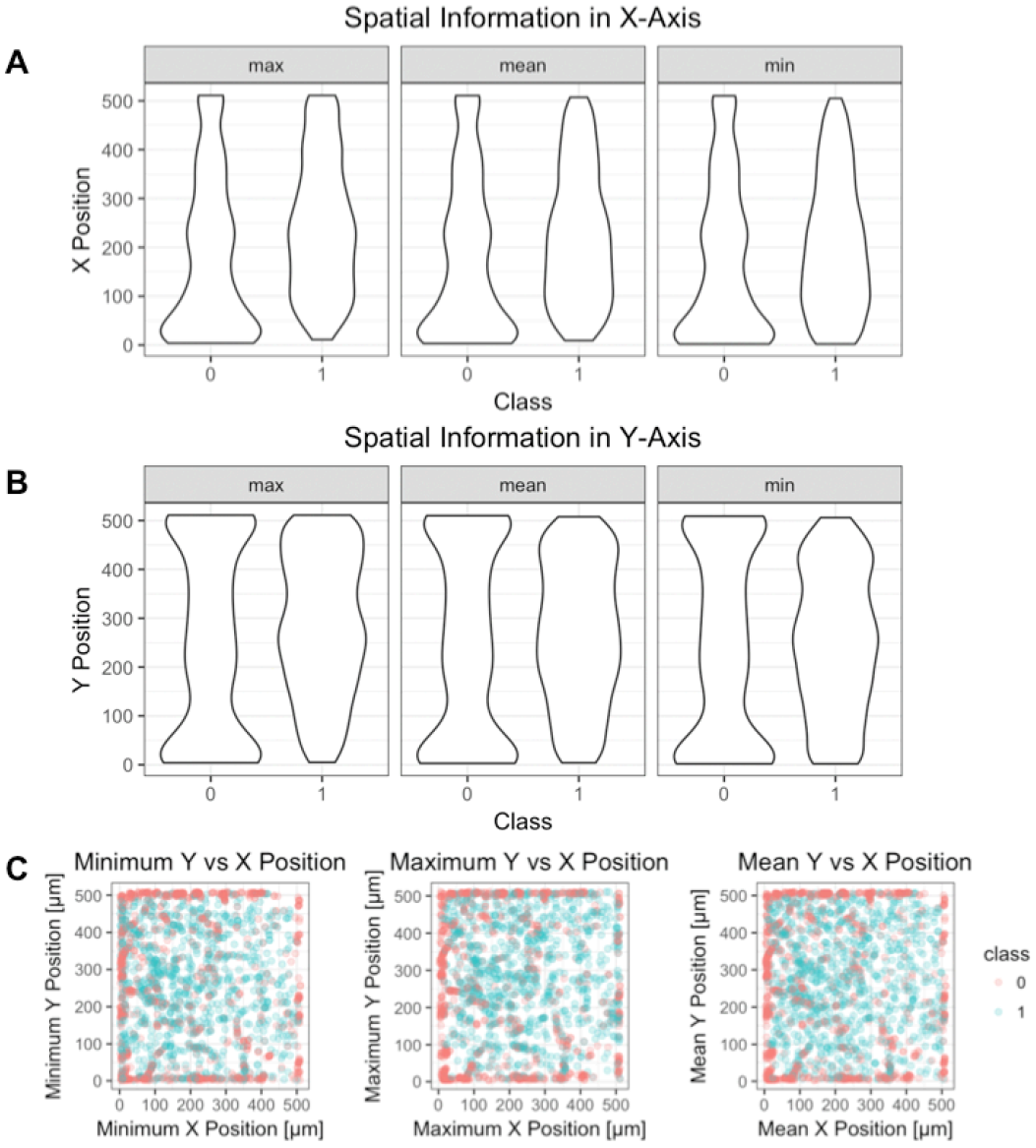

Figure 3.3: **Transverse position of true and false strand vectorizations.** Class 0 (false) strands tend to reside at the image borders in the (*A*) *x* and (*B*) *y* dimensions. (*C*) A scatter plot of class 0 (false) and 1 (true) strands' minimum, maximum, and mean position.

3.4.3. Exploratory Data Visualization: Stand Radius

The next pieces of information that were explored visually were mean radius and radius standard deviation. To elucidate what each feature means, it must be understood

that each strand is composed of one or more vertices. While each vertex occupies a single voxel, the "radius" of each vertex denotes the vectorization software's assessment of the blood vessel radius at that position. Vascular radius is quite heterogeneous, with surface vessels typically having larger radii, and deeper microvasculature typically exhibiting smaller radii. It was worth exploring whether Volumetric Image Data Analysis (VIDA) Suite had a tendency to make errors in identifying larger or smaller vessels. Ultimately, the distribution of faulty and accurate strands was very similar with respect to radius, indicating that VIDA Suite vectorization is not very sensitive to vessel size (**Figure 3.4(a)**). However, if we instead look at the standard deviation in radius, `stdRadius` = $\sqrt{\frac{\sum_i^N x_i - \bar{x}}{N-1}}$ where x_i is the ith vertex radius of N vertices, we do note some differences between properly and improperly vectorized strands (**Figure 3.4(b)**). The miscategorized strands tend to have a more constant radius (i.e. smaller `stdRadius`), whereas the properly categorized strands display a distribution that shows a more fluid radius along the vessel. In other words, accurately vectorized vessels can taper off, thicken, or otherwise have variability in their thicknesses. However, one thing this exploratory data visualization fails to determine conclusively is whether or not bad strands' predilection for lower radii standard deviation is simply a consequence of bad strands' greater likelihood of being shorter, as seen above in the section on `size`. Although this specific point is not directly address by these plots, later sections (multicollinearity analysis) will identify redundant or overlapping features and identify whether or not faulty strands' tendencies to be shorter and more uniform are correlated.

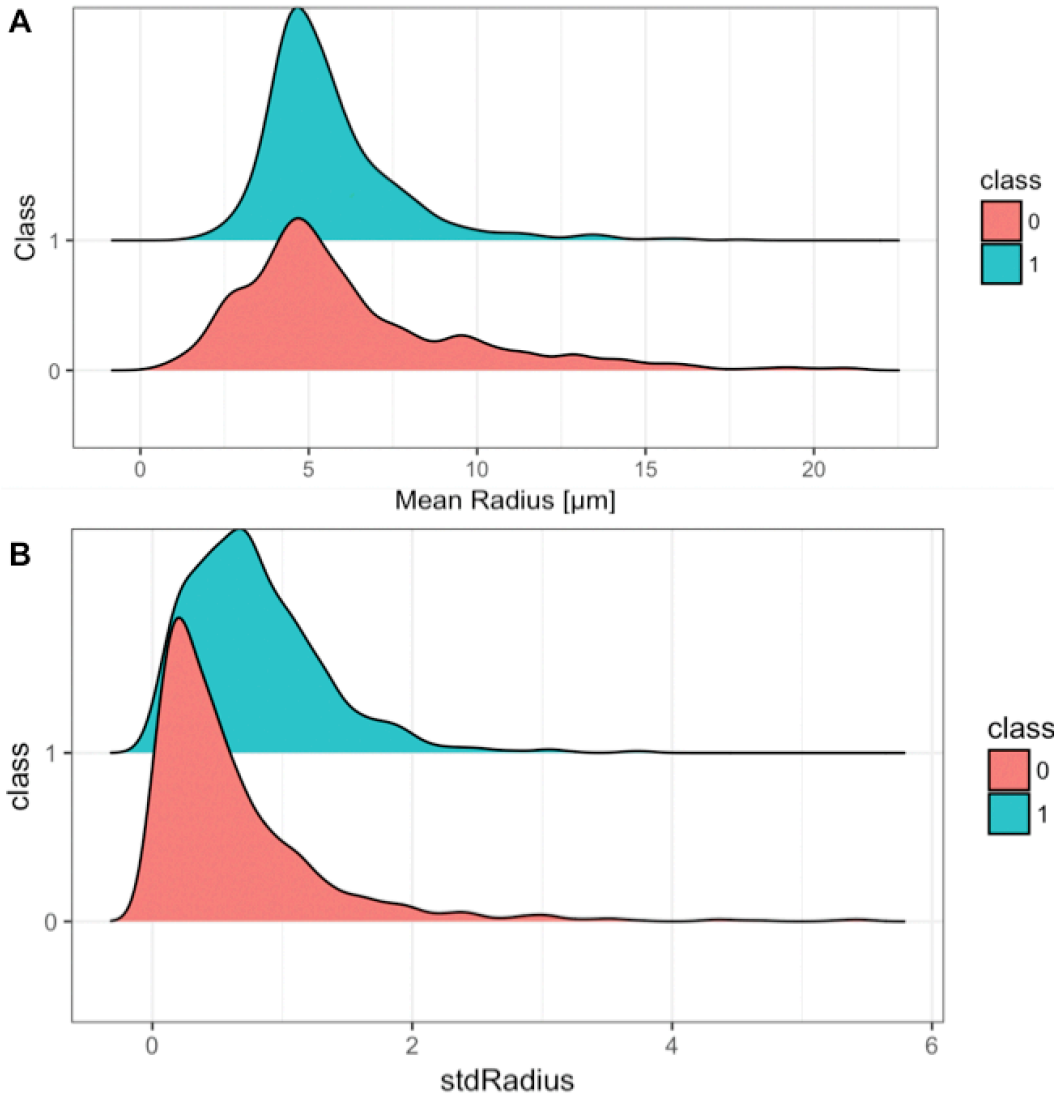

Figure 3.4: **Radii of true and false strand vectorizations.** (*A*) Class 0 (false) and class 1 (true) strands exhibit similar radii distributions. (*B*) False strands have a more constant radius (i.e. uniform tubes) than true strands.

3.4.4. Exploratory Data Visualization: Strand Length

Examining vessel `length`, i.e. endpoint-to-endpoint distance, the class trend echoes the observation made with `size` - erroneous vectorizations tend to be much shorter than accurate strands. By looking at bar histograms for various length bin sizes, we see that greater lengths predominantly correspond to true `class 1` vectorizations,

and shorter ones are overwhelmingly false `class 0` strands (**Figure 3.5(a)**). We can also look at `length` strictly in the *x*, *y*, and *z* dimensions. This is a valuable exercise, since we may discover that VIDA Suite has difficulties tracing descending arterioles with high fidelity for example. However, this suspicion is unfounded based on the plots shown below. Vessels that span the *z* dimension along considerable lengths are no more likely to be misclassified than longer vessels that span the transverse plane (**Figure 3.5(b)**).

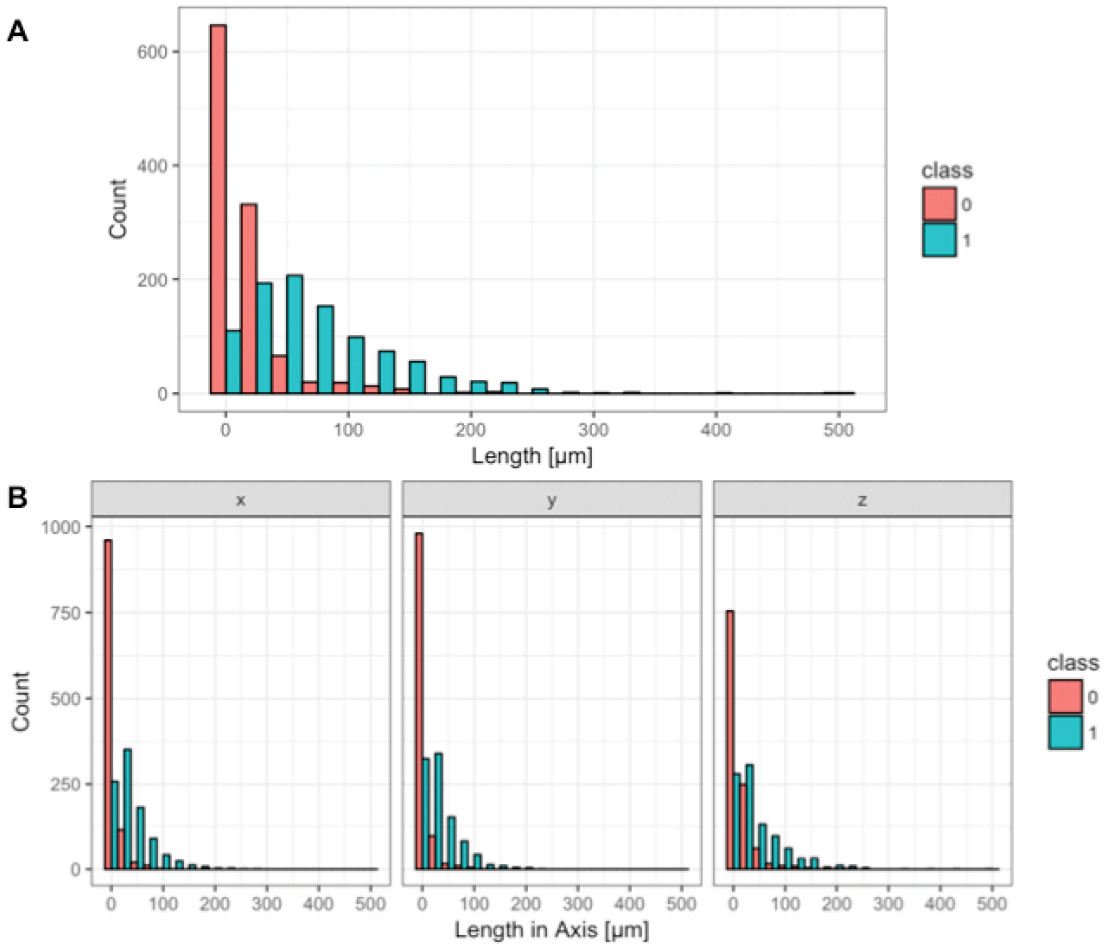

Figure 3.5: **Length of true and false strand vectorizations.** (*A*) Length (i.e. endpoint-to-endpoint) distribution of class 0 (false) and class 1 (true) strands. (*B*) Length distribution of strands in the *x, y*, and *z* dimensions.

3.4.5. Exploratory Data Visualization: Strand Tangle Factor

The next feature subject for visual analysis is tangle factor. Tangle factor is meant to be an assessment of tortuosity, which describes how curved, twisted, and convoluted a strand is. There are many ways to quantify tortuosity, but perhaps the simplest way is to calculate the ratio of the strands' size (μm) to the endpoint-to-endpoint distance (μm), which yields the unitless arch-chord ratio, [13] here-on referred to as a tangle factor. Tangle factor yields some very promising results with respect to strand classification. Proper vectorizations seem to be slightly (tangle factor ~1.5) or moderately curved (tangle factor ~3.2) strands (**Figure 3.6**). Improper vectorizations can be slightly to moderately curved as well, but are unique in exhibiting severely twisted strands (tangle factor > 3.5). We immediately note that *any* strand with a tangle factor above 3.5 is unambiguously improperly vectorized in this data set. This suggests that naturally occurring cerebrovasculature is not excessively tortuous and that tangle factor will emerge as a critical feature for differentiation in automated curation efforts. If any successive steps eliminate tangle factor as a metric for differentiation, that model should be scrutinized more critically, as this visualization confirms it as an integral feature. To expand on the presence of highly tortuous misfires by Volumetric Image Data Analysis (VIDA) Suite - occasionally the vectorization software produces what I refer to as pigtails or corkscrews, where the vectorized centerline twists back and forth aimlessly within a pocket of noise or from overlapping vessel-to-vessel, leading to the inclusion of faulty strands with large `tangleFactor` values.

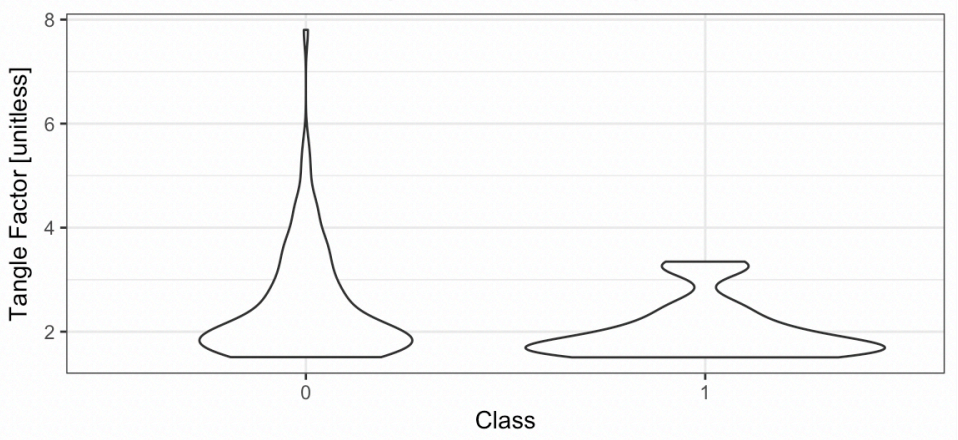

Figure 3.6: **Tangle factor of true and false strand vectorizations.** The tangle factor, or arch-chord ratio (strand size to endpoint-to-endpoint distance), of class 0 (false) and 1 (true) strands.

3.4.6. Exploratory Data Visualization: Strand Brightness

Finally, I was ready to look at microscopy image features, rather than raw geometric information derived from vectorization, as a predictor of vessel accuracy. Initial expectations were that strand brightness, which is closely related to signal-to-background ratio, would inform curation, with a brighter strand more likely to be classified correctly. However, this data visualization informs us that the opposite is true - very bright image regions are more likely to produce an improper vectorized strand (**Figure 3.7**). When this piece of information is coupled with our earlier discovery that `class 0` strands tend to be much smaller, we can surmise that misvectorized strands are often just bright specks of noise. However, it will be important to use this feature in conjunction with geometric ones for an automated classifier. Otherwise, we will simply threshold strands from high signal regions out of the final vectorized data set.

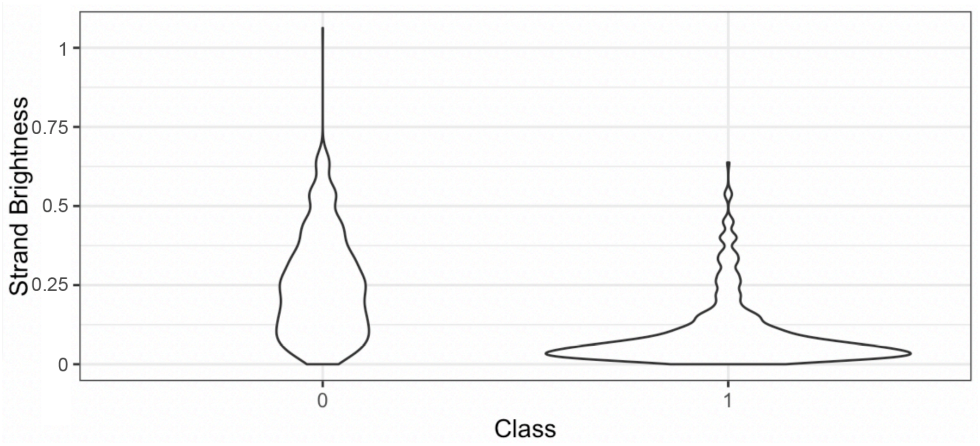

Figure 3.7: **Multiphoton image brightness at the location of true and false strand vectorizations.** Mean brightness (arbitrary units) along the length of a strand is calculated, and used to construct a violin plot for class 0 (false) and 1 (true) strands.

3.4.7. Exploratory Data Visualization: Junction Points

Junction points are an indicator of vascular connectivity. Every strand extends from endpoint-to-endpoint, junction-to-junction, or endpoint-to-junction. An endpoint denotes there is no contiguous vessel connected on that side of the strand. On the other hand, a junction point denotes that there is a neighboring strand perfused with a given strand. Inspecting the bar plot below, there are more faulty strands represented in each of the three categories (**Figure 3.8**). However, this difference can simply be attributed to the greater number of false strands in the data set (n = 1110) relative to true strands (n = 976) leading to their over-representation in each cell. Nevertheless, the proportion of bad-to-good strands in the zero junction point category (i.e. misvectorized endpoint-to-endpoint vessels to properly vectorized endpoint-to-endpoint vessels ratio = 2.667) is much greater than the overall proportion of bad-to-good strands in the data set (1110/976 = 1.137). This suggests that an isolated, or low-connectivity, strand is much more likely to be a class 0 strand. This aligns with our earlier conclusions, that faulty strands tend to be

vectorizations of pocket of noise, which are randomly distributed and would not lead to continuously connected strand networks. Therefore, junction point number should serve as a valuable identifier of improperly vectorized vessel segments.

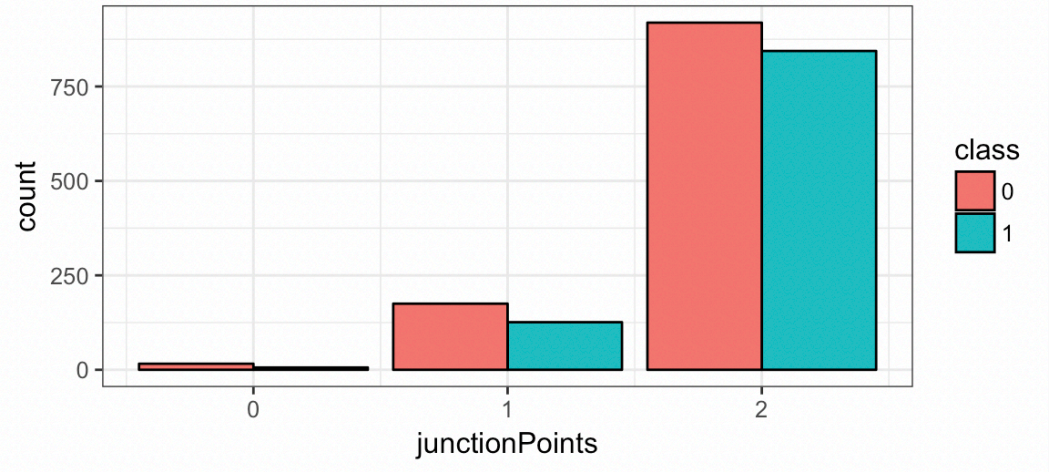

Figure 3.8: **True and false strand vectorization junction points.** Vectorized strands are either isolated (0 junction points), connected on one side (1 junction point), or both sides (2 junction points). Class 0 = false vectorizations; Class 1 = true vectorizations.

3.5 Partition Data into Test and Training Fractions

When fitting a model to your data, it is important to reserve some observations as a test fraction. That is, the weights and parameters of your fitted model should be trained on only a subset of the data, and the generalizability and transferability of that fitted model should be assessed using the test fraction. If sensitivity and specificity on the test fraction falls far behind corresponding metrics on the training fraction, then the model either suffers from high bias or high variance. In colloquial terms, this means the model is under- or over-fitted, respectively. In the case of high variance, or overfitting, the error of the parameters as measured on the training data is likely to be lower than the actual generalization error. In the case of high bias, or underfitting, the training and cross

validation errors are both likely to be above acceptable levels. In high variance contexts, getting more training data is helpful in reducing the gap between training and test metrics. Unfortunately, learning algorithms afflicted by high bias will not likely improve solely by the inclusion of more training data. However, bias is not aggravated by larger sample sets, thus, to reduce the likelihood of overfitting, one can include more observations in the training fraction. In a perfect world, where data is inexpensive to collect and abundantly available, as many observations as possible should be included in the both the test and training fractions, with the only tradeoff being increased computation time. However, due to the slower speed of vectorization and the manually intensive need for hand labeling, only 2,086 observations were available. Since there was no way of knowing *a priori* how many of those observations needed to be reserved for training to avoid high bias, the fractional split was heuristically determined to be 0.7:0.3, with roughly ~1,500 training examples. To elaborate, this cutoff was determined at a threshold where test receiver operating characteristics area the curve approached training area the curve values.

3.6 Feature Selection: Multicollinearity Analysis

As noted above, the inclusion of more observations mainly benefits learning algorithms suffering from high variance, but is less likely to aid algorithms plagued by high bias. A prominent method to prevent high bias is to obtain additional features, or add polynomial transformations of existing features. Thus, we begin by fitting each model with our full set of predictors captured during feature extraction. Unfortunately, unlike the number of training examples where there is no concept of "too many", the inclusion of too many features can actually lead to high variance or overfitting. For more advanced learning algorithms, this can be offset with regularization, which retains all

features, but reduces the magnitude of their weight parameters. This class of models is often successful in contexts where we have many weaker features, each of which would fail to independently predict outcomes of *y*. However, in most other contexts, each included feature must be carefully inspected to ensure it will not lead to overfitting. Thus, it is our goal in this section and the next to begin with as many features as possible to avoid high bias, then kick out non-predictive parameters individually.

The first step of this approach is multicollinearity analysis, which specifically seeks to remove redundant, overlapping variables. Often times a researcher will find high intercorrelations amongst their features due to improper data collection or encoding. For example, one feature might be hours of sleep per day and a second might be hours of sleep per week. In other cases, seemingly benign and independent features will subtly reveal themselves be intercorrelated through multicollinearity analysis, and while the discovery may provide valuable insight, one of the two related features must be removed in order to properly fit the model. For example, if we are looking at predicted health outcomes for patients, and age is included as a feature along with blood pressure, we might find a severe degree of multicollinearity. Specific issues that arise from multicollinearity include an inability to fit regression coefficients precisely, numerically unstable least squares estimates, high standard errors, a change in coefficient signs fit-to-fit, as well as difficulties in identifying the predictive power of individual features **[16]**. Finally, the failure to remove multicollinear features tends to produce wide confidence intervals for a given coefficient making it difficult to reject a stated null hypothesis. If we conduct an analysis of variance (ANOVA) using more than two multicollinear predictors, it is often difficult to identify which are specifically intercorrelated. The overall F test may yield a significant *p*-value, but none of the individual coefficient *p*-values are significant **[17]**. However, many methods are available to aid in making this

determination. For example, the sum of squares regression (*SSR*) is particularly useful for identifying multicollinear variables. If X_1 and X_2 are highly correlated, then the *SSR* for the model that includes both features, $SSR(X_1|\ X_2)$, is approximately equal to $SSR(X_1)$. In this example $SSR(X_2|X_1) \approx SSR(X_2)$. In addition, creating a correlation matrix of the predictors is a simple way to identify relationships between features.

In this study, variance inflation factor (VIF) analysis was used to assess multicollinearity. Variance inflation factors are predicated on the fact that multicollinear variables hold a linear relationship. When conducting a general regression, R^2 is the coefficient of *correlation*, and it explains the proportion of total variability in *y* explained by the predictors. When conducting VIF analysis, we instead regress individual predictors against all other predictors to calculate R^2, which is then referred to as the coefficient of multiple *determination*. To elaborate, we can begin with the simple expression below.

$$\sum\sum\left(Y_{ij} - \bar{Y}..\right)^2 = \sum n_i(\bar{Y}_i. - \bar{Y}..)^2 + \sum\sum\left(Y_{ij} - \bar{Y}_i.\right)^2 \tag{3.1}$$

or

$$SSTO = SSR + SSE \tag{3.2}$$

This tells us that the total variability in the data (*SSTO*) is comprised of the total variability explained by the predictors (*SSR*) and the total unexplained variability unaccounted for by the factor levels (*SSE*). If we define the coefficient of *correlation* for a standard regression as below, then we can intuitively understand the R^2 value as a description of how much of the total variability is accounted for by the predictors.

$$R^2 = \frac{SSR}{SSTO} = 1 - \frac{SSE}{SSTO} \tag{3.3}$$

Thus, if we substitute *y* with an individual feature X_k, and regress against the other

remaining features, the coefficient of *determination* will indicate how interrelated that X_k is to any or all of the others *X's,* although it will not reveal to which specifically. A large value for R^2, [0,1], indicates a greater degree of multicollinearity. If we then define the variance inflation factor, [1,∞], as...

$$VIF = \frac{1}{1 - R_k^2} \tag{3.4}$$

...then we can also interpret a larger value of VIF as heightened evidence for multicollinearity. As a general rule of thumb, any VIF greater than 10 for any given *X* is deemed to be multicollinear. In our own statistical analysis of multicollinearity we removed the redundant features in **Table 3.2** and used the remaining features for positive and negative strand classification.

Rejected Multicollinear Features	Remaining Non-Collinear Features	
minZ	size	brightness
maxZ	meanZ	junctionPoints
minX	meanX	edgeX
maxX	meanY	edgeY
minY	meanRadius	
maxY	stdRadius	
length	tangleFactor	

Table 3.2: **Retained and rejected strand features following multicollinearity analysis**. Each feature was regressed against all other features in the data set. A variance inflation factor of 10 or greater was used to identify multicollinear features, which were rejected from subsequent analysis.

3.7 Feature Selection: Backwards Feature Elimination

As mentioned earlier, we would like to include as many features as possible to avoid high bias. However, we underlined the importance that all included features must

be meaningful in terms of their ability to help predict the outcome of the response variable, which we've defined as strand classification. Otherwise, we run the risk of overfitting to empty predictors and our trained model will fail to generalize to unseen observations in our test fraction or to new data. This brings us to the concept behind the second phase of feature selection. By paring our features down to the best subset, we also enjoy the added benefit of reduced computation time, a diminished requirement for a large training set sample size, improved model stability, and increased interpretability **[18]**. Broadly, there are three distinct approaches to feature selection: filter, wrapper, and embedded methods.

Filter Methods: A selection criteria is defined (e.g. *t* statistic, *p*-value, chi-square, etc.) to rank individual features.

Wrapper Methods: Various combinations of some or all features are used to train the model, the final model performance is evaluated using the preferred selection criteria for each combination (e.g. ROC-AUC), and the highest-performing combination is accepted as the final feature subset **[19]**.

Embedded Methods: A diverse class of feature selection techniques, united in that variable selection is directly incorporated into the training method. Common examples include decision trees, which generally have a built-in mechanism for feature selection. A more recent example is LASSO (least absolute shrinkage and selection operator) regression, which uses L1 regularization as a built-in function to penalize certain features [159].

Of the above methods, wrappers are the most likely to require intensive computation, particularly with larger initial feature sets, due to the many permutations of feature combinations that can be trialed. However, efficient search strategies may be designed and applied without hurting prediction performance [160]. Filter methods, are

perhaps the most simple, least computationally burdensome, and the most robust for overfitting, although they may not lead to the most predictive set of features [160]. Two very common wrapper methods are forward selection and backwards elimination. With the former approach, predictors are successively added one at a time, and rejected if the model performance is not improved. With backwards elimination, all predictors are included initially, model performance is evaluated, and the worst performer is removed. This process is repeated until only the most promising features remain **[22,23]**.

In this study, I have used backwards feature elimination. I fit a generalized linear model (*glm*) using a logit link (family = binomial) to all noncollinear features using the training set, i.e. a logistic regression model. The scoring criteria for the predictors was the *p*-value for the *z*-statistic (*Pr(<|z|)*). Upon fitting each model, I evaluated which predictor was least significant, removed it, and fit the model to the reduced feature set. This process was then repeated until only significant features remained. The features that were removed were: `meanY`, `meanRadius`, `meanX`, and `stdRadius`. The features that remained were: `size`, `meanZ`, `tangleFactor`, `brightness`, `junctionPoints`, `edgeX`, and `edgeY`.

3.8 LOGISTIC REGRESSION MODEL FITTING

A simple linear model fits the following equation to the data, where the population parameters β_0 and β_i are the intercept and parameter slopes, respectively:

$$g(y_j) = \beta_0 + \beta_1 size_j + \beta_2 mean_j + \beta_3 tangleFactor_j + \beta_4 brightness_j + \beta_5 junctionPoints_j + \beta_6 edgeX_j + \beta_7 edgeY_j + \epsilon_j \quad (3.5)$$

The generalized linear model contains a fixed component, which specifies the coefficient or degree of association for each predictor and the response variable, along with a random component, which assumes some normally distributed random error term for

each observation. In the above equation, the link between the response and predictor is fully linear, or:

$$g(y_j) = y_j \tag{3.6}$$

This is quite useful for continuous variables; however, in the case of strand classification, where each outcome is a binary Bernoulli random variable - either the strand was vectorized correctly or it wasn't - a nonlinear link function is more sensible.

$$g(\pi) = log(\tfrac{\pi}{1-\pi}) \tag{3.7}$$

where:

$$\pi = \frac{exp(\beta_0 + \beta_1 size_j + \cdots + \beta_7 edgeY_j + \epsilon_j)}{1 + exp(\beta_0 + \beta_1 size_j + \cdots + \beta_7 edgeY_j + \epsilon_j)} \tag{3.8}$$

In this manner we are directly determining the probability, π, that a strand was vectorized correctly or incorrectly based on the available predictors. Odds are then used to compare the relative magnitude of two complementary probabilities, and are typically expressed as the probability that an event will occur (i.e. success) over the probability that an event will not occur (i.e. failure). Unlike probability, odds ω are not bounded on the range [0,1]. For instance, if the probability of an event occurring is 0.99, the odds are equal to 99 (i.e. 0.99 / [1 - .99]). If for example, the probability of an event for a certain group is 0.80, then the odds are equal to 4, since the probability of that event happening is four times greater than the probability that it does not occur. Mathematically, this is denoted by:

$$\omega = odds(event) = \frac{P(event)}{P(\widehat{event})} = \frac{\pi}{1-\pi} \tag{3.9}$$

A logit is then a natural log transformation of odds. It seeks to solve two specific problems of the odds metric. One, a linear model for odds as a function of predictors can lead to nonsensical negative predicted values, since odds are bounded by 0 up to any non-

negative value. Thus, the bounds are problematic where $0 < \omega < \infty$. Secondly, a simple odds scale is asymmetric, meaning that a constant Δ translates to non-constant effects. For instance, $\pi = 0.5$ corresponds to $\omega = 1$, whereas $\pi = 1.0$ corresponds to $\omega = \infty$. The natural logit transformation improves these challenges to make a more useful model, where $\log(\omega) = \log\left(\frac{\pi}{1-\pi}\right)$ is bounded to $-\infty \leq log(\omega) \leq +\infty$.

3.8.1 Logistic Regression: Model Evaluation

Now, armed with a clear understanding of logistic regression, we can observe the fitted model. Ideally all observations on both curves would be assigned a probability of 1 (i.e. $log(\omega) \sim \infty$) or 0 (i.e. $log(\omega) \sim -\infty$), and the characteristic sigmoid curve would not be visually evident. Such a result would indicate that our model was able to identify true and false strands with 100% certainty in all cases. Clearly, this is not the case, as there a few strands with $\pi \approx 1$ values, and there are few strands with $\pi \approx 0$ values, but the vast majority land somewhere between these values (**Figure 3.9**). Observing the "rugs" along the top and bottom, it seems that the log(odds) are between [0, 2.5] for a typical `class 1` strand and between [-2.5, 0] for a typical `class 0` strand. However, when coloring the strands by their true class from the manual labeling, we can certainly see some overlap in the two categories along the fitted logistic regression. This overlap, presented as individual blue data points infiltrating the red half of the sigmoid curve, and vice versa, is an indicator of imperfect model performance, as there is no clearly delineated divide between faulty and accurate strands.

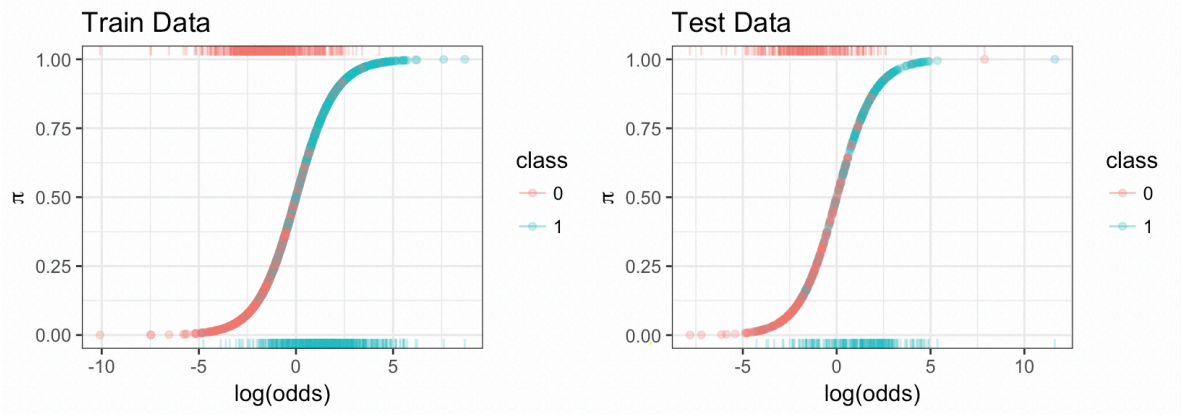

Figure 3.9: **Logistic regression curves on train and test data.** Sigmoid logistic regression probabilities versus predictions (i.e. log odds) on the train and test data, where class 0 (false) and 1 (true) strands are colored as red and green respectively.

To evaluate the model performance quantitatively, we can use chi-square values, or information measures like Akaike or Bayesian information criteria, which provide insight on how parsimonious a model may be. However, a more robust application-motivated evaluation of actual performance and generalization is receiver operating characteristics area under the curve (ROC-AUC). Briefly, a receiver operator characteristic curve is built up from pairs of sensitivity and sensitivity values calculated as a function of decision thresholds. If I was to place a threshold at $log(\omega) = 0 := \pi = 0.5$, and assign all observations above or equal to that threshold as class = 1, and all observations below that threshold as class = 0, I could calculate sensitivity and specificity values for that threshold using a contingency table that tabulates the number of:

- True Positives (TP): correctly identified accurate strands
- False Positives (FP): faulty strands predicted as accurate
- True Negatives (TN): correctly identified faulty strands
- False Negatives (FN): accurate strands identified as faulty

Sensitivity, or true positive rate, for a specific threshold is then calculated as the number

of true positives relative to all positives, $\frac{TP}{TP+FN}$. False positive rate is calculated as the number of false positives to all negatives, $\frac{FP}{FP+TN}$, which is the same as $1 - Specificity$, where specificity or true negative rate is calculated as $\frac{TN}{TN+FP}$. For each decision threshold, unique true and false positive rate values arise, and these can be plotted to form the receiver operating characteristics curve. The curve will always include the points (0,0) and (1,1). The (0,0) point arises from an absolute decision threshold that deems all observations as negative, which will result in zero true and false positives and therefore, null true and false positive rates as well. Conversely, an absolute decision threshold that assigns all observations as positive classifications will yield the maximum number of true and false positives possible, ensuring that both true and false positive rates are maximized as well. The area under this curve is a strong indicator of model performance. An AUC = 1 signifies perfect model performance, where each prediction matches with the true class label. An AUC = 0.5 means that the model is performing no better than random chance. Anything below this indicates a seriously flawed model, which would be better off being substituted with a coin flip.

To summarize the process that has lead to these results thus far: first, the strand features data-set was loaded into RStudio and uncurated strands (class = 2) were omitted from classifier training and model evaluation. Strands with a `tangleFactor` equal to infinity (i.e. strands that loop back to their original position) were filtered out as well because the infinity values would prevent the general logistic model from being able to converge. Next, 70% of observations were partitioned into training data and the remaining 30% were designated as test data. I then fit a logistic regression model on the training data set using features chosen based on the absence of multicollinearity and backwards feature elimination until only predictors with a significance level less than 0.05 and a variance inflation factor less than 10 remained. I then used the model to

predict the outcomes on the test data set and plotted the resulting ROC curves for both the training and test data sets. An ROC analysis is justifiable for the question at hand, because it directly informs us if we are able to successfully predict strand classifications within these two groups solely based on their geometric properties (e.g. position in 3D space) and the gray values of their corresponding multiphoton image data.

Visual interpretation of the ROC curves (**Figure 3.10**) show an initial, sharp increase in sensitivity (i.e. true positive rate) at low false positive rates, with additional modest gains in sensitivity at the cost of an increasing false positive rate. The individual ROC curves corresponding to the training and test sets generally appear to be very similar as expected due to the fact that they are random fractions of the same larger data set and we have minimized overtraining artifacts. The area under the curve provides a quantitative diagnostic summary of ROC analysis and informs us that the final predictors unsurprisingly provide a marginally better fit on the training dataset (~0.89) than on the test dataset (~0.86), but it is unlikely that this discrepancy is statistically significant. From the plot of fitted probability as a function of the linear predictor, colored by true classification, we see that most points are positioned towards the center of the logistic curve which suggests that the model cannot uniquely identify good versus bad strands with high confidence based on the predictors. Ideally, the two positions would be well separated by the linear predictor; however, we see a significant degree of overlap indicating that classification is imperfect.

Ultimately, the ROC curves of the training and test datasets and their associated AUC values (~0.86 - 0.89) indicate that for the most part good and bad strands do possess unique characteristics that can be used as a basis for automatic differentiation (**Figure 3.10**). However, examining the plot of fitted probability versus predictors colored by classification reveals that there are plenty of instances where good strands were classified

as bad strands and vice versa, suggesting that there are atypical instances for both categories that defy accurate categorization (**Figure 3.9**).

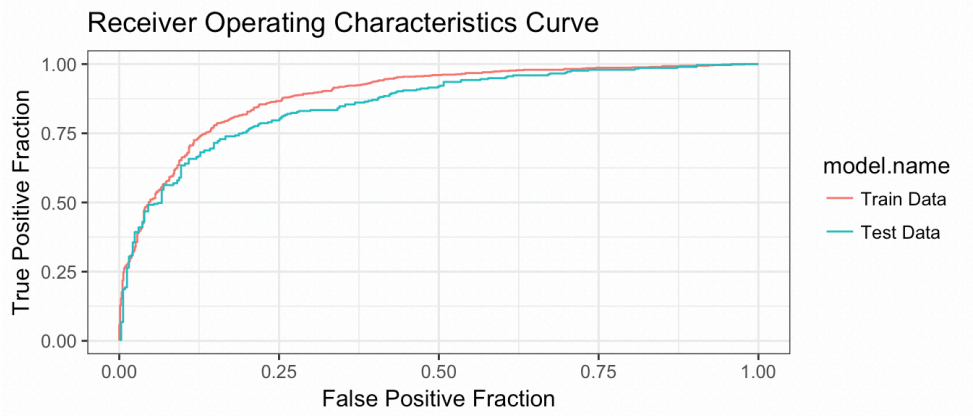

Figure 3.10: **Receiver operating characteristics curves of vectorized strand classifier.** True positive fraction (i.e. sensitivity) versus false positive fraction (i.e. 1 – specificity) receiver operating characteristic curves reveal excellent classifier performance on the training data (area under the curve ~ 0.89) with very modest levels of overtraining on the test data (area under the curve ~0.86).

3.8.2 Logistic Regression: Data Curation – Single Decision Threshold

Armed with a fitted model we hold ample confidence in (test data area under the curve ~ 0.86), we can now apply it to our data and automatically curate strand vectorization. Unfortunately, two factors still remain unclear. First, what decision threshold should we use to most reliably differentiate between the two strand categories? Second, what curation accuracy does this yield? At this point, sensitivity and specificity hold less meaning as individual metrics because our goal is to maximize both in order to include as many good strands in the data set as possible. Therefore, overall accuracy, $\frac{TP+TN}{TP+FP+TN+FN}$, is the metric we would like to optimize. By using our test data to calculate curation accuracy as a function of decision threshold, we can identify the threshold that yields the greatest curation accuracy. We find that curation accuracy peaks at around

~0.78, and that curation accuracy is relatively stable at any decision threshold between 0.4 and 0.6 (**Figure 3.11**). However, ~80% is an unacceptable level of accuracy and we may be able to achieve a better statistic by using more than one decision threshold and curating the observations between these thresholds manually, as further discussed in the following section.

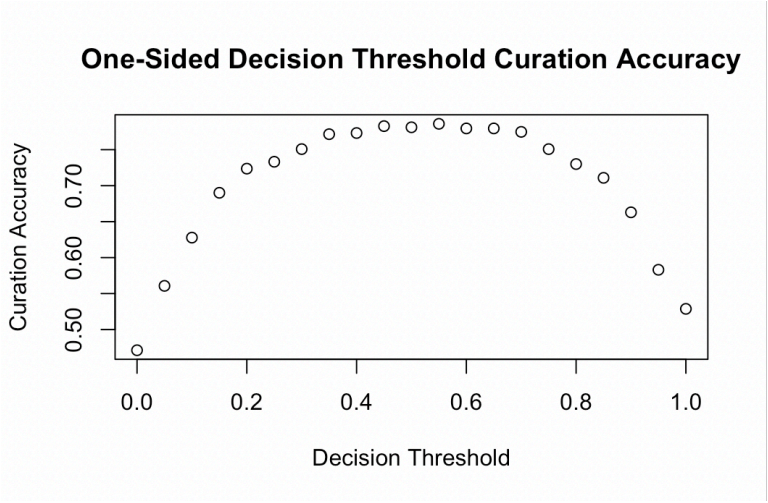

Figure 3.11: **Logistic regression classifier curation accuracy.** A plot of curation accuracy as a function of a single decision threshold shows that overall accuracy peaks at around 78% and is stable at a threshold value range from 0.4 – 0.6.

3.8.3 Logistic Regression: Data Curation – Multiple Decision Thresholds

To illustrate the concept of blending multiple decision thresholds with manual curation, we construct a simple example where we have applied two thresholds such that any strand with a fitted probability of 0.55 or greater is given a class prediction of 1 (green) and any strand with a fitted probability of below 0.30 is given a class prediction of 0 (red) (**Figure 3.12**). All other strands, π = [0.3, 0.55), are not given class predictions (N/A) and will require manual curation. Here, we have also shaped the data points by true class label, where a circle corresponds to false strands and a triangle maps to true strands.

Therefore, of our curated set, only red circles and green triangles were curated correctly based on these applied decision thresholds. By using two thresholds at 0.30 and 0.55, we automatically curate all 87% of strands in the data set, with a sensitivity and specificity of 0.732 and 0.677 respectively. Since the remaining 13% of strands require manual labeling, we can assume that sensitivity and specificity is 100% for this remaining set, meaning that our overall accuracy is 0.834. This represents a modest improvement over our single decision threshold curator (0.78) at the cost of manual intervention.

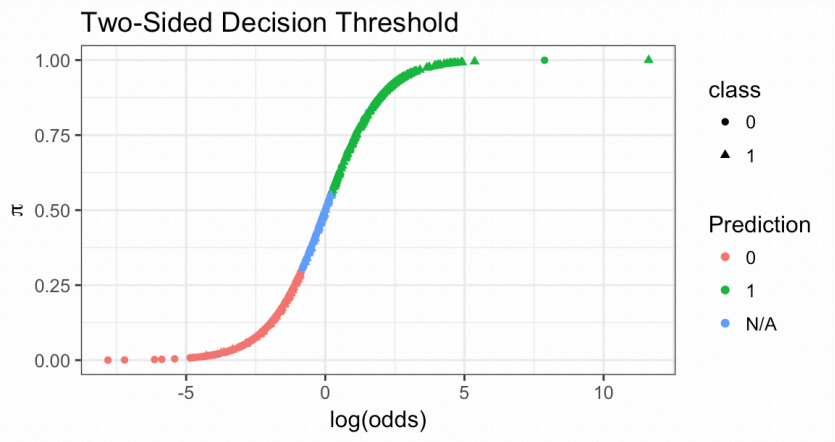

Figure 3.12: **Two-sided decision threshold of a logistic regression-based strand classifier.** A plot of probability (π) versus prediction (i.e. log odds) of class 0 (false; circle) and 1 (true; triangle) strands after logistic regression classification. Above a probability of 0.55, all strands are assigned a class prediction of 1 (green) and below a probability of 0.30, all strands are given a class prediction of 0 (red). This leaves 13% of strands without a class prediction (blue), and thus in need of manual curation. At these thresholds the overall curation accuracy is 0.834, compared to a max curation accuracy of 0.78 using a single decision threshold.

Whereas our earlier question was where to place our single decision threshold to maximize curation accuracy, our question has now changed to where should we place our two decision thresholds to maximize curation accuracy *and* autocuration fraction. Below we can clearly see a trade off between these two desires; if more strands are curated

automatically, the overall classification accuracy decreases (**Figure 3.13**). More specifically, if we accept an increased burden of manual intervention, then we can increase the overall classification accuracy. On the left, we see autocuration fraction as a function of overall classification accuracy for all combinations of low and high decision thresholds. If we are content with an ~80% overall classification accuracy, we can proceed with the autocuration with little to no manual intervention (**Figure 3.13(a)**). However, on the right, the same plot is cropped to show only results using decision thresholds that produced an overall classification accuracy of 90% or greater (**Figure 3.13(b)**). The core idea is to select the logistic regression probability decision thresholds that maximize the autocuration fraction for a given classification accuracy. For example, if we are targeting a ~90% classification accuracy we can use values of 0.20 and 0.70 for our two-sided decision threshold and curate 69% of strands automatically, *or* we could use decision thresholds of 0.40 and 1.00 for a very slight improvement in classification accuracy, but wind up needing to curate ~51% of the data manually. Clearly, given these two options, the first threshold value pair makes the most sense. For the sake of this research study, a ~95% classification accuracy is targeted. We can identify that our best choice for decision thresholds given this target are 0.15 and 0.85, where any strand with a logistic regression probability π = [0.2, 0.85) will need to be manually curated (~50% of data set) to maintain a 95% overall accuracy level.

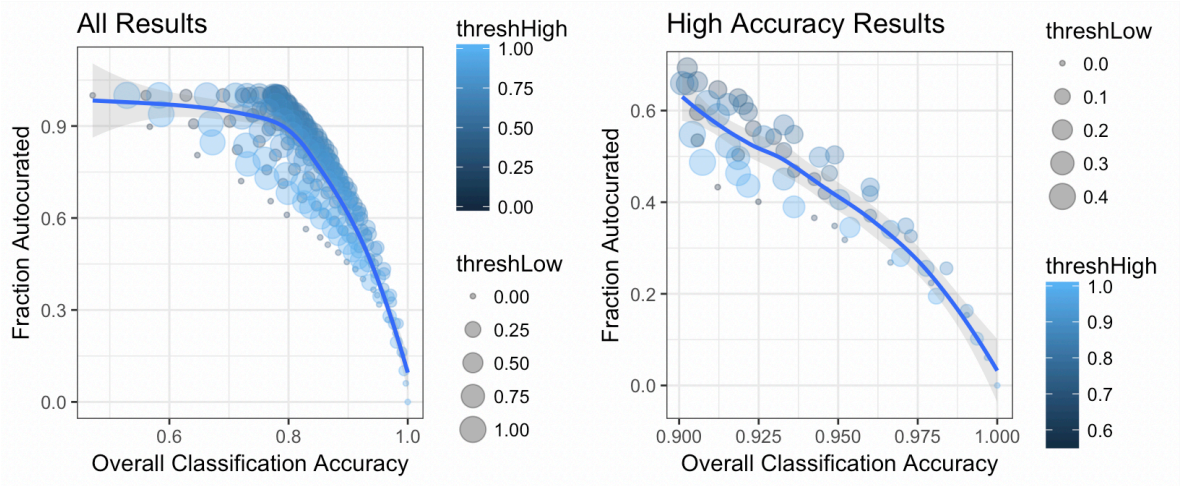

Figure 3.13: **Logistic regression classification accuracy and autocuration fraction tradeoff of a two-sided decision threshold.** (*Left*) It is apparent that there is a negative association between autocuration fraction and overall logistic regression classification accuracy. As the upper decision threshold (threshHigh) and lower decision threshold (threshLow) approach each other, autocuration fraction increases at the cost of a lower classification accuracy. (*Right*) By limiting our plot to only high accuracy results, we can clearly see that specific threshold value pairs will maximize autocuration fraction at a given logistic regression classification accuracy.

3.9 Adaboost Model Fitting

3.9.1 Adaboost: Model Evaluation

Unfortunately, the logistic regression model trained on our data did not produce the level of results we desired since we discovered that we would still need to manually curate every other strand to maintain a 95% classification accuracy level. While the ability to curate half of the data automatically reflects a substantial amount of time saved, it would be nice to reduce the amount of manpower needed further. As we found from our initial data exploration, no one single data feature seemed to be a strong predictor. This makes a strong case for using Adaboost, a learning algorithm that uses several weak linear classifiers and combines them together to build a single strong classifier. By

staging these classifiers (i.e. cascading) in such a way that if initial features reject a new input, remaining features are not calculated and predictions on new data are thereby sped up, saving a considerable amount of computational resources.

We feed all non-collinear features into the Adaboost model for training and produce the following contingency table at a decision threshold of 0.5 (**Table 3.3**). The top class labels are true class labels, and the class labels along the left side are the Adaboost predictions. Thus our sensitivity is calculated as $\frac{242}{242+53} = 0.82$ and specificity is calculated as $\frac{259}{259+72} = 0.782$, respectively.

		True Class Label	
		Positive (1)	**Negative (0)**
Adaboost Prediction	**Positive (1)**	242	72
	Negative (0)	53	259

Table 3.3: **Adaboost strand classifier contingency table**. A table of true and predicted class labels of vectorized strands after Adaboost classification at a threshold of 0.5. Sensitivity = 0.82, specificity = 0.782.

3.9.2 Adaboost: Data Curation – Single and Dual-Sided Decision Thresholds

Now, with a trained Adaboost model with high-level performance as tested by sensitivity and specificity, we are able to automatically curate our test data. As we did with the logistic regression model, we initially test it using a one-sided decision threshold to determine an ideal probability threshold and what classification accuracy this threshold would yield (**Figure 3.14**). We find that curation accuracy peaks at ~0.805, and that curation accuracy is relatively stable at any decision threshold between 0.4 and 0.6. This region of stability closely matches the logistic regression results, although the peak

curation accuracy of Adaboost is slightly better (~0.805 vs 0.78). However, ~80% is still shy of our ~95% classification accuracy target, meaning that we must pursue a two sided decision threshold curation accompanied by manual interventions.

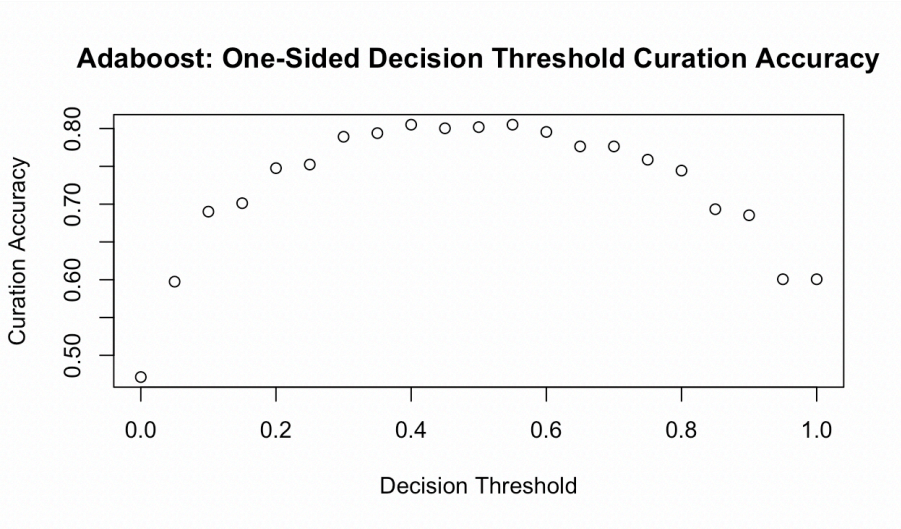

Figure 3.14: **Adaboost classifier curation accuracy.** A plot of curation accuracy as a function of a single decision threshold shows that overall accuracy peaks at around 80.5% and is stable at a threshold value range from 0.4 – 0.6.

Adaboost multiple threshold results are very similar to the logistic regression classifier, with a slight performance edge given to the Adaboost classifier (**Figure 3.15**). On the left, autocuration fraction is plotted against classification accuracy for all decision threshold pairs, where data points are colored by the upper threshold value and sized by the lower threshold value. Whereas logistic regression was able to fully rely on autocuration with a classification performance just shy of 80%, Adaboost exceeds 80%, but not by a significant margin. On the right is the same plot cropped to show decision threshold pairs that results in a classification accuracy above 90% (**Figure 3.15(b)**). We can identify the threshold pairs that maximize autocuration for a given classification

accuracy. If we are targeting a 90% classification accuracy, threshold values of 0.30 and 0.70 result in a 76% autocuration fraction, which is significantly better than the 69% autocuration fraction we were able to achieve with logistic regression at the same accuracy level. If we target a more stringent 95% classification accuracy, then Adaboost thresholds of 0.15 and 0.75 produce a ~56% autocuration fraction, which again reflects that Adaboost is able to outperform logistic regression, which was at 51% autocuration.

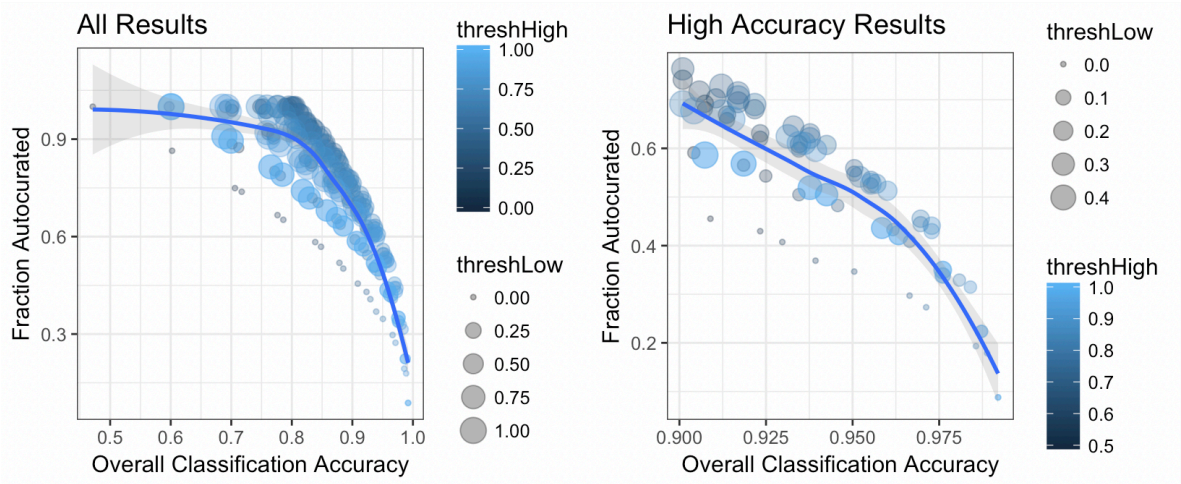

Figure 3.15: **Adaboost classification accuracy and autocuration fraction tradeoff of a two-sided decision threshold.** (*Left*) Autofraction versus overall Adaboost classification accuracy. As the upper decision threshold (threshHigh) and lower decision threshold approach (threshHigh) each other, autocuration fraction increases at the cost of lower classification accuracy. (*Right*) Specific threshold value pairs maximize autocuration fraction at a given Adaboost classification accuracy. Here, lower and upper probability thresholds of 0.3 and 0.7 result in a 76% autocuration fraction and a 90% classification accuracy.

3.10 Conclusion and Future Directions

A fully vectorized cerebrovascular network results in the creation of tens of thousands of strands. Unfortunately, each of these strands requires curation, as the

vectorization algorithm is imperfect. In an effort to save undergraduate and graduate students from endless, painful hours of mind-numbing menial labor, I developed an automated strand classifier using statistics and data science. This was an eight-step process that began with manual classification, feature extraction and exploratory data visualization. Exploratory data visualization suggested that size, length, depth, position, radius, tortuosity, brightness, and junction points were all predictive features of vectorization accuracy. The following two steps of the statistical modeling pipeline - feature selection through multicollinearity analysis and backwards feature elimination - retained size, depth, transverse position, brightness, and junction points as significant features. With a sufficient number of features and training examples to ensure the model would not be susceptible to high bias or high variance, a logistic regression model was fit to the training data. A log link function for the generalized linear model was selected due to its applicability to binary outcome predictions. Upon model evaluation, the training data exhibited a large receiver operating characteristics area under the curve (ROC-AUC; 0.89) and the test data AUC did not lag far behind (0.86), indicating the model was not severely overfit. Fully automated data curation with single decision thresholds and semi-automated data curation with multiple decision thresholds were compared using the fitted logistic regression model, and the following classification accuracy to autocuration fraction splits were identified: 0.78/1.00, 0.90/0.70, 0.95/0.50. To improve upon these results further, an Adaboost learning algorithm was fit to the training data. Fully automated single decision threshold curation with Adaboost edged out logistic regression slightly (~0.805 vs 0.78 classification accuracy), whereas dual decision threshold curation with Adaboost was significantly better than logistic regression (0.76 vs 0.69 autocuration fraction for a 90% classification accuracy).

In our exploratory data visualization, we found that the vast majority of false

strands reside at the image border and greater depths. This begs the question: why not just crop out those strands and avoid the seemingly unnecessary hassle of developing a strand classifier? As it stands, this model is a great deal more sophisticated than just filtering out strands near the volume borders or deep beneath the cortical surface. While those features (`edgeX` , `edgeY`, and `meanZ`) are included as features in the final fitted model, they're accompanied by features such as size, connectivity (`junctionPoints`), and tortuosity (`tangleFactor`). If a strand that seems likely to be misvectorized based on location features (e.g. near an image border and very deep) appears to be very continuous with surrounding vessels, the image brightness indicates decent signal-to-background ratio, and the vessel is not overly tortuous, then this algorithm will retain it in curation. First and foremost, this helps us include as much data in the final vectorization as possible. More importantly, this ensures that we don't systematically filter out vessels stemming from specific regions of the rodent cortex in depth (e.g. layer-V) or in the transverse directions (e.g. periphery of the somatosensory-cortex).

While these results are promising, they're certainly not perfect and there is much room for improvement. I believe a major reason for the logistic regression and Adaboost models' shortcomings relate to the available feature set. The entire curation pipeline is a multi-step process, and it's unclear which feature selection procedure or learning algorithm should be applied. But what is clear is that if we fail to extract features that adequately differentiate true and false strands in the first place, then the curation process has a very little chance of being successful, regardless of how sophisticated any downstream procedures may be. Thus, the need to extract variables that provide real insight on why vectorization may have failed is essential to building a proper curation classifier. For instance, signal-to-background ratio (SBR) should most certainly be an included feature. Early attempts at automatically quantifying SBR were unsuccessful.

Perhaps mean subtracted contrast normalized value distributions for each *z*-plane, which have been used to gauge image distortion in literature [161] may be useful in the absence of a robust SBR measure. In addition, strands with a `tangleFactor` of ∞ (i.e. strands that looped back on themselves) were omitted from data analysis. This was simply because the ∞ values prevented the fitted models from converging. However, instead of omitting these strands, it may be useful to coerce their ∞ values to the largest real-valued `tangleFactor` measured in the data set during preprocessing, as these close-looped strands were distinctly misvectorized and their inclusion would help strengthen the classifier. Finally, future work should focus on characterizing how robust the fitted model is. For instance, a classifier trained on a healthy rodent specimen may find that a highly tortuous vectorized strand is most likely suspect. Perhaps in an unhealthy specimen, highly tortuous vessels are expected to be found in abundance post-ischemia. If it is found that classifiers for a certain disease state, rodent gender, or specimen age are non-transferrable, then it will be necessary to fit several models to data representing each condition, and apply the appropriate trained model to respective future data for curation.

Chapter 4: Super-Resolution and Non-Degenerate Multiphoton Microscopy[2]

4.1 Super-Resolution Optical Imaging

Synaptic communication is dictated by neural architecture, and structural alterations and changes in density are believed to be substrates of underlying cognitive function [162,163]. Two-photon fluorescence microscopy has become the standard modality in neuroscience due to its ability to image neural tissue at greater depths with high resolution [6,8,164]. However, the technique remains diffraction limited, meaning that its spatial resolution cannot exceed ~400 nm at standard imaging wavelengths. Meanwhile, dendritic spines, the tiny protrusions decorating the surfaces of neurons, have neck diameters as small as 70 – 300 nm in size [165]. Thus, optical visualization of spines necessitates a super-resolution system. The neuroscientific significance of such an endeavor cannot be overstated due to the instrumental role spines play in learning and memory, in addition to their being host to over 90% of the excitatory synapses found in the central nervous system [165]. Of course, it is already possible to obtain three-dimensional reconstructions of these small protrusions via serial-section electron microscopy [166]. Unfortunately, electron microscopy limits observation to relatively small volumes and introduces significant distortions through fixation, dehydration, and resin embedding [167]. In addition, only light microscopy enables live cell imaging to gain qualitative and quantitative descriptions of dynamic conditions and changes as they occur. Thus, a non-invasive super-resolution optical technique would be highly beneficial to advancing our *in vivo* understanding of dendritic spines.

---

[2] Portions of Chapter Four are based on a previous publication. Ahmed Hassan conducted all experiments, analysis, and independently wrote, "Hassan, A.M., Engelmann, S. and Dunn, A.K., 2019. Improved nondegenerate multiphoton microscopy and axial registration with a reflective objective. *Optics letters*, *44*(20), pp.5017-5020."

Over the past two decades, many super-resolution imaging methods have emerged to overcome the diffraction limit [168–170]. Some of these techniques rely on the sequential activation and time-resolved localization of photo-activated fluorophores to build an image (e.g. STORM and PALM) [171,172]. Other methods rely on the concept of point spread function engineering where a donut shaped depletion beam is spatiotemporally overlapped with an excitation beam to confine fluorescence to a smaller focal spot [173,174]. The most widely recognized example of this is stimulation emission depletion (STED) microscopy in which the depletion beam decreases the size of the excited region through stimulated emission [169]. Several variations of STED exist, but they are limited by the requirement of a high intensity depletion beam which risks sample damage and photobleaching [168,175,176]. To circumvent this destructive requirement, fluorescence emission difference (FED) microscopy uses excitation and donut beams at lower intensities to alternately excite fluorophores and collect two sequential images [174]. Digital subtraction of the donut point spread function from the excitation point spread function results in a super-resolution difference image.

The size of the hollow spot in FED dictates the resolution-enhancement, with a smaller hole conferring improved resolution. Switching laser mode (SLAM) microscopy attempts to reduce the central dark region by using the smaller dimensions of azimuthally polarized TEM_{01} modes and improves the resolution of conventional fluorescence imaging by a factor of two [177]. Moreover, this technique has been demonstrated as being compatible with two-photon excitation. It is the goal of this project to extend SLAM beyond this two-fold resolution enhancement by creating improved, smaller-diameter null spots from mixing different spatial modes of two synchronized lasers at distinct wavelengths in a photophysical process termed non-degenerate multiphoton excitation [64]. This improvement would harness STED's spatial resolution capability to

visualize dendritic spines, yet minimize the risk of introducing photobleaching and photodamage effects to the sample. In the section that follows, an exhaustive review of existing super-resolution modalities will be presented in order to better explain their limitations and provide context for the significance of a non-degenerate FED-based modality.

4.2 A Review of Super-resolution Optical Imaging Modalities

4.2.1 Localization Based Nanoscopy

A major branch of super-resolution fluorescence microscopy includes localization based approaches. Within this umbrella, stochastic optical reconstruction microscopy (STORM) and photoactivated localization microscopy (PALM) are widely recognized examples, both of which are implementations predicated on the principle of single molecule detection. The localization precision and effective resolution of single molecule detection is theoretically unlimited and determined by the number of collected photons (N) and the numerical aperture (NA) of the imaging system:

$$Resolution = \frac{1.22\lambda}{2NA\sqrt{N}} \tag{4.1}$$

Therefore, these modalities rely on bright, high efficiency fluorophores and the use of sensitive detectors that minimize dark noise. A major caveat to STORM and PALM is they do not provided true structural images. Rather, the relative locations (i.e. centroids) of emitters are recorded and reconstructed into a time-resolved image that can come to resemble a true structural image.

For a single emitter, it is relatively simple and straightforward to identify the centroid position with high localization accuracy provided ample signal-to-noise ratio. In typical fluorescent images, however, we deal with multiple emitters and often have

thousands of overlapping point spread functions. Since the turn of the millennium, several techniques have taken advantage of the principles behind single molecule detection to obtain super-resolution maps of multiple emitters. One such technique known as **S**ingle-Molecule **H**igh **R**esolution **Im**aging with **P**hotobleaching (SHRimP) takes advantage of the quantum photobleaching of fluorescent molecules to resolve two or more fluorophores in the *x*-*y* plane, separated by distances as small as 10 nm [178]. Images are recorded continuously, and a plot of integrated image intensity with respect to time is used to identify signal reductions corresponding to the photobleaching of an individual molecule. Digital subtraction of post-bleaching frames from pre-bleaching frames can be used to isolate individual emitters whose point spread functions can be fit to a Gaussian distribution in order to localize its position. This relatively simple technique was made possible by the advent of low-noise, high quantum yield CCD cameras. A similar technique was developed in 2005 that relied on the photoblinking, rather than the photobleaching, of quantum dots and subsequent component analysis of independent frames to precisely localize and thereby resolve groups of closely spaced quantum dots [179]. Notably, both SHRImP and independent component analysis of photoblinking quantum dots are limited to the localization of only a few emitters within a single frame. This paved the way for more mature techniques like STORM and PALM, which can work successfully with thousands of fluorescent molecules within a single field of view.

STORM and PALM are both super-resolution imaging techniques that use sequential activation and time-resolved localization of fluorophores to create super resolution images. They can, in principle, reach molecular-scale resolution. Both are conceptually identical and were developed and published on independently around the same time. Their major differentiating factor is the applied fluorophore; STORM was

originally described using Cy5 and Cy3 dyes attached to nucleic acids or proteins [170] and PALM was described using photoactivated fluorescent proteins [172]. In each imaging cycle, only a fraction of fluorophores are turned on, allowing their positions to be determined with nanometer accuracy. The fluorophore positions obtained from a series of imaging cycles are used to reconstruct the overall image and the super-resolution image can be thought of as a map of the coordinates found in particle detection. With wide-field approaches such as STORM and PALM, the trade-off between spatial and temporal resolution arises from the fact that a sufficiently large number of localizations need to be detected in order to build the super-resolution image. More localizations require more imaging cycles, which takes more time. Currently, a 40 – 70 nm spatial resolution can be achieved with STORM/PALM with a 30 – 60 second long acquisition window, although it's possible to achieve a ~20 nm resolution with several minutes of data collection. The major limitations of temporal resolution are the switching rate of dyes and camera frame rates. However, faster blinking/switching reduces the number of collected photons and would therefore sacrifice spatial resolution. Thus, the major limitation on spatial resolution is fluorophore brightness and collection efficiency.

4.2.2 Stimulated Emission Depletion Microscopy

Stimulated emission depletion (STED) microscopy is a powerful point-scanning approach to super-resolution imaging that presents notable distinctions to wide-field localization based approaches. With both paradigms, there is a fundamental tradeoff in spatial versus temporal resolution. In point-scanning techniques, higher spatial resolution is achieved using smaller pixel sizes, which results in a slower imaging speed given a matching field-of-view. Unlike localization based approaches where resolution is

determined by the number of collected photons, STED resolution depends on the intensity of the depletion beam (I) relative to saturation intensity (I_{sat}), and numerical aperture (NA).

$$Resolution = \frac{1}{\sqrt{1 + \frac{I}{I_s}}} \frac{1.22\lambda}{2NA} \tag{4.2}$$

STED uses a solid spot for excitation, typically of a Gaussian beam profile, and a red-shifted hollow spot for stimulated emission, where a single image is produced. The hollow spot depletion beam effectively decreases the size of the excited region through stimulated emission. Because STED is a direct, photophysical effect the super-resolution image is created in real time unlike fluorescence emission difference microscopy. Several variations of STED exist including continuous wave and pulsed implementations, but they are mostly limited by the requirement of a high intensity depletion beam which risks sample damage and photobleaching [168,176]. In the following section we will provide a critical examination of *in vivo* STED neuroimaging applications.

4.2.3 *In Vivo* STED Neuroimaging

Perhaps the most striking examples of two-photon stimulated emission depletion (2P-STED) microscopy for neuroimaging applications emerge from the lab Dr. Valentin Nägerl at the University of Bordeaux. In one study, his lab synchronized a Titanium:Sapphire (Ti:S) excitation laser (λ_{ex} = 900 nm; 80 MHz) with a pulse-stretched optical parametric oscillator (OPO) depletion laser (λ_{ex} = 598 nm; 80 MHz) to collect 2P-STED images of the CA1 hippocampus in transgenic mice [180]. Mice were implanted with a specialized hippocampal window, where the outer somatosensory cortex is excised and substituted with a metal cylinder then sealed with a coverslip. A long

working distance is then used to image through this window and into the hippocampus. His results demonstrated that spine density in this region was two-fold greater than previously published reports, a discrepancy which may be explained by the super-resolution detection sensitivity of 2P-STED. Moreover, he found that 40% of spines imaged at t = 0 had turned over after four days, suggesting a high level of neuroplasticity in the CA1 region. By measuring the diameters of these spines, Nägerl was able to show that smaller spines were disproportionately more likely to be affected by spine turnover. It is this last discovery that really highlights the advantage of STED and, more broadly, super-resolution optical imaging. With conventional, diffraction-limited 2P microscopy, spines would appear as amorphous blobs and size measurements would only serve to characterize the imaging system's point spread function rather than the dimensions of the spines themselves. By using 2P-STED, Nägerl is not only able to delineate the structural dynamics of spines more clearly from a qualitative standpoint, he is able to provide more reliable quantitative descriptions as well. Concretely, spine neck widths were measured at 147 $\pm$ 8 nm using 2P-STED and 369 $\pm$ 6 nm with conventional 2P microscopy.

Nägerl does take care to note a critical disadvantage of 2P-STED is susceptibility to image distortions caused by breathing and pulsatile motion, which become more apparent on account of STED's high spatial resolution. Furthermore, this STED implementation was limited to super-resolution in the plane orthogonal to the optical axis, meaning that spines along the axial direction remained obscured. Notably, all spines imaged in this study stemmed no further than 20 μm away from the coverslip. At greater depths, 2P-STED image quality degraded rapidly, and the authors posit that was owed to index mismatches in the coverslip, immersion media, and brain tissue (n ~ 1.37). They note that adaptive optics may play a role in overcoming this limitation, although no follow-up studies using adaptive optics for STED spine imaging has emerged from this

lab or others at the time of this writing. Finally, it is worth noting that a discussion of average depletion laser power was noticeably absent in the description of this imaging study. It is mentioned, however, that excitation laser power ranged around 5-20 mW for 2P and 5 – 15 mW for 2P-STED. I hypothesize that the reduced excitation laser power for 2P-STED was intended to compensate for the high power of the depletion laser. Moreover, we can refer to similar imaging studies to estimate power levels used by Nägerl. For instance, Wang et al.'s 2015 continuous wave STED imaging of actin cytoskeleton used 25 μW and 200 mW of excitation and depletion beam power, respectively. Admittedly, an advantage of pulsed STED is its lower threshold for average depletion power; nevertheless, depletion power is typically two orders of magnitude larger than excitation power using this STED variation [181]. Direct comparisons of STED and FED in integrated microscopy systems show that dark FED imaging reduces STED depletion power intensities anywhere from 200 – 427 fold at commensurate resolution scales [182]. Regardless of the exact ratio, it is well established that STED resolution is a function of depletion laser power, meaning that achieving the ~two-fold resolution enhancement seen here likely risked substantial photobleaching. This calls physiological conclusions drawn from the imaging results into question as spine turnover, particularly spine disappearance, may have been externally triggered by phototoxic laser levels.

4.2.4 Fluorescence Emission Difference Microscopy

Localization based super-resolution imaging techniques like stochastic optical reconstruction microscopy (STORM) and photoactivated localization microscopy (PALM) require time-resolved image reconstruction, which hinders its application to live cell or large volume imaging. On the other hand, stimulated emission depletion (STED)

microscopy's super-resolution point scanning implementation requires the use of a high intensity depletion laser, which can produce symptoms of phototoxicity in live samples. To remedy this, fluorescence emission difference (FED) microscopy serves as a point-scanning approach that mimics the underlying principle of STED where a hollow spot is used to confine fluorescence to a sub-diffraction limited focal spot, without the need for a high intensity depletion beam [174]. Specifically, FED eliminates its reliance on a high power depletion beam by substituting photophysical stimulated emission with digital subtraction. Similar to STED, a TEM_{00} beam is used to initially excite a fluorescent molecule, where TEM denotes **t**ransverse **e**lectromagnetic **m**ode. Following this step, STED uses a hollow TEM_{01} laser to suppress fluorescence at the periphery of this excited region through stimulated emission. Since depletion efficiency is a function of laser intensity, the TEM_{01} STED laser line is typically multiple orders of magnitude higher in power than its TEM_{00} line. The advantage of FED is that the depletion laser is not intended to confine fluorescence through stimulated emission. Rather, it is used to produce a second "dark" excitation image at low powers matching the initial excitation image, and digital subtraction of the dark image from the former is used to accomplish a similar effect to STED, only digitally. This is expressed in Equation 4.3 below, where PSF denotes point spread function.

$$PSF_{FED} = PSF_{excitation} - \gamma PSF_{dark} \tag{4.3}$$

Similar to how one can vary STED depletion laser power to alter final image resolution, one can digitally adjust the FED dark image subtraction factor (γ) to achieve the same result.

The instrumentation of FED is considerably more straightforward than a typical STED set-up. Conventional STED systems rely on two unique laser sources, such as the

one used by Valentin Nägerl in the study discussed in Section 4.2.3. The initial excitation laser is tuned to match the fluorophore of interest's peak action cross section, and an independent depletion laser is tuned to be coherent with the fluorophore's approximate emission and allow for stimulated emission. Of course, sophisticated two-photon (2P) STED variations do allow for a single laser source that is then split into two excitation pathways. The first excitation pathway stimulates a fluorophore with a considerably large Stokes shift, such that one-photon (1P) stimulated emission depletion is possible at the same wavelength as 2P excitation. However, the pool of fluorophores that are compatible with this technique is extremely meager and even when a promising candidate is identified, the possibility of unintended excitation with the depletion pathway remains salient if the selected fluorophore's cross section profile exhibits a longer tail. Moreover, pulsed STED imposes a strict requirement for temporal alignment of the two beams. Incident photons from the depletion beam must strike the fluorescent molecule after initial excitation, and before excited electrons relax back down to ground state. Achieving this temporal alignment is technically complex and can require expensive equipment such as a time-correlated single photon counting board. Alternatively, the depletion beam can stem from a continuous wave source although this is less efficient and requires greater average power. In contrast, FED instrumentation is quite simple. A single excitation source is tuned to the fluorophore's peak action cross section and split into two pathways. The first pathway is used for fluorescent excitation as is. A beam shaping element is introduced to the second pathway, termed the "dark" beam, to introduce a hollow spot at focus. Typical beam shapers include vortex phase plates, azimuthal polarizers, and spatial light modulators. To alternate between excitation and dark imaging, a pair of digital shutters are used. Of course FED does have its own limitations. Since FED requires sequential excitation and dark imaging, it lacks the

temporal throughput of STED. Whereas STED images are created in real-time, FED images are reconstructed digitally, which imposes additional computational burden. In spite of this, FED is capable of matching the resolution enhancement of STED, significantly reduces the risk of phototoxicity, employs a simpler optical system, and provides far greater flexibility and compatibility with respect to fluorophore selection.

4.3 Development of a Two-Color Imaging System

The advantages of non-degenerate multiphoton microscopy (ND-MPM) relative to conventional MPM are well chronicled, including multicolor imaging [63], reduced background fluorescence [64], and improved excitation efficiency [183]. However, it is our belief that the benefits of ND-MPM have yet to be fully explored, and we endeavored to build a two-color imaging system to develop novel non-degenerate use cases and applications. The system relies on the integration of three beam paths to achieve non-degenerate multiphoton excitation of various contrast agents at the sample plane. To achieve ND excitation, the synchronized two-color pulses must overlap in both space and time. To achieve spatial integration, the independent beam paths are made collinear using dichroic mirrors or 50:50 beam splitters depending on the beams' spectral properties. Temporal overlap is straightforward, although technically challenging, and mandates the use of optical delay lines, which can advance or delay a pulse train in time without compromising optical alignment. To assess crude temporal overlap, a variety of equipment was evaluated, including digital- (DPC230; Becker & Hickl GmbH) and time-correlated single photon counting boards (TCSPC-150; Becker & Hickl GmbH) and short- (LNR25ZFS, Thorlabs), as well as long-range travel stages. Empirically, it was determined that the improved temporal resolution of the TCSPC board and the extended optical delay of the long-range travel stage served as a better combination for actuating

coarse temporal overlap. To more precisely evaluate temporal alignment, autocorrelative interference (matching wavelengths) or cross correlation (non-matching wavelengths) is observed using a GaAsP photodiode sensor (G117; Hamamatsu) and oscilloscope.

Due to chromatic aberration, we found that the precise spatial overlap of different beam lines was compromised in the focal plane. In our early efforts, we attempted to use a corrective telescope to impart convergence or divergence to one beam path and thereby reduce focal offset. An initial telescope pair was used to expand and collimate the beam (LA1131C f = 50.0 mm, LA1509C f = 100.0 mm; Thorlabs), and a second pair was used to actuate collimation (2x LA1509C f = 100.0; Thorlabs) using a z-axis translation stage (SM1Z; Thorlabs). To measure axial color shift severity as a function of telescope offset, a photodiode (G117l; Hamamatsu) was mounted to either a horizontal (Z825B; Thorlabs) or a vertical (MLJ050; Thorlabs) translation stage and swept through the wavelength-dependent position of the focal plane using a home-built LabVIEW program. Voltage was then recorded as a function of stage position. The results informed us that, in principle, adjustments to a single excitation beam with a Keplerian telescope can be used to impart divergence or convergence that compensates for the chromatic focal offset and improve two-color overlap. In practice, however, the combined magnification of a complete objective scan engine (~40 – 160x) requires severe acollimation to achieve precise overlap in the objective focal plane. This becomes infeasible because such a divergent beam cannot be successfully transmitted through a microscope's scan path due to vignetting. Moreover, as telescope offset is increased, the objective optical power is effectively reduced, resulting in a focal point spread function broadening and reduced multiphoton excitation efficiency. We found that reflective objectives could successfully circumvent chromatic aberration and after rigorous characterization and evaluation, chose

to employ the LMM-40X-P01 reflective objective from Thorlabs (0.5 NA). Section 4.4 details characterization of this optic relative to traditional refractive objectives.

Results using the two-color imaging system have shown it to be capable of increasing excitation efficiency and extending multiphoton imaging depth. Our lab has demonstrated that ND-MPM imaging of Texas Red-labeled rodent vasculature with a diamond (1240 nm) and fiber laser (1050 nm) enables a cortical imaging depth of ~1 mm, relative to a shallower ~800 μm accomplished by D-MPM imaging solely with a fiber laser, even when total excitation powers are matched [120]. This system is also able to use ND-MPM's unique virtual excitation wavelength properties to efficiently target substrate incompatible fluorophores. Total light attenuation in neural tissue is a complement of scattering and absorption processes, which can be reasonably approximated at a depth (z) using the expression $\exp[-(\mu_a(\lambda)+\mu_s(\lambda))z]$, where $\mu_a(\lambda)$ and $\mu_s(\lambda)$ are wavelength-dependent, tissue-specific absorption and scattering coefficients [46]. Water absorption constitutes a prominent portion of total light attenuation and is highest from 1400 - 1600 nm and above 1800 nm [71]. In fact, greater than 50% of excitation light is lost solely to water absorption in brain tissue in these spectral regions, which results in a potentially harmful thermal heating and a significant loss in fluorescence due to the quadratic nature of two-photon absorption. Thus, there is no way to effectively target fluorophores with peak absorption cross sections in these high absorption zones without risking considerable damage to vasculature and cortical tissue. However, our two-color system can use direct excitation wavelengths λ_1 and λ_2 that straddle high-absorption bands to minimize attenuation and maintain a large photon fraction in the focal plane, while still exciting previously inaccessible substrate-incompatible fluorophores at a virtual excitation wavelength λ_3. Ultimately, this methodology can unlock the utility of a whole class of fluorophores previously

unavailable to the *in vivo* multiphoton imaging community.

4.4 Characterization and Correction of Two-Color Axial Focal Shift

Traditional multiphoton objectives are composed of a series of refractive lenses that compensate for one another's aberrations. High quality objectives are commonly corrected to improve image quality by minimization of spherical aberration, coma, astigmatism, and distortion. Unfortunately, chromatic aberration is unavoidable with refractive objectives, meaning that distinct wavelengths are focused at mismatched optical *z*-planes. Achromat objectives tailored to minimize this undesired effect can only provide chromatic correction over a limited range of wavelengths (e.g. the visible regime) and are ill-suited for non-degenerate multiphoton microscopy (ND-MPM), which can demand the spatial overlap of wavelength combinations spanning both the visible and near-infrared (NIR) spectrum. While electrically tunable lenses and remote focusing enables variable axial focus [184], modulation by these elements is common to both ND scan paths and cannot be used to achieve mutual overlap. In principle, a simple lens pair telescope can be used to apply defocus to a single excitation beam and compensate for chromatic focal offset. In practice, however, it is challenging to avoid vignetting an acollimated beam through an optical system, and this defocus directly broadens the beam's point spread function, which thereby reduces multiphoton excitation efficiency.

An effective and simple solution to entirely circumvent chromatic aberration and successfully overlap the focused profiles of the independent laser sources for ND-MPM is to employ a reflective objective. Typical reflective objectives use a pair of curved mirrors to achieve near- or diffraction-limited focusing and image magnification [185]. Reflective objectives eliminate the adverse effects of chromatic aberration and dispersion entirely [186], yet despite this advantage have yet to be adopted for ND-MPM, perhaps

due to obscuration and their relatively low numerical apertures (NA). Obscuration refers to mechanical light attenuation from mirror design, where a significant portion of light entering a reflective objective fails to reflect to a secondary mirror, and an additional fraction of light is obstructed by thin suspensions used to mount the primary mirror. However, the superior transmission properties of reflective objectives (>99% from 450 nm to 20 μm) vastly outperform traditional refractive objectives with NIR coatings, including optimized multiphoton objectives (~70% from 1100 – 1400 nm) [187]. Recalling that ND-MPM enhances excitation efficiency relative to D-MPM, allowing one to trade excitation efficiency for laser power [183], taken with reflective objectives' improved transmission properties, obscuration becomes a minor drawback. However, the low NA of reflective objectives still poses a major concern. Here we demonstrate that the improved ND axial overlap of reflective objectives increases ND excitation efficiency relative to even higher NA refractive objectives.

4.4.1 Axial Focal Shift Measurements of Refractive and Reflective Objectives

To evaluate the severity of the axial focal shift of refractive versus reflective objectives, a tunable non-linear optical parametric amplifier (Spirit-NOPA-VISIR, Spectra-Physics) was focused onto a photodiode (G1117, Hamamatsu) using a 10x refractive objective (MRL00102, 0.25 NA, Nikon), a 20x refractive objective (XLUMPLFLN, 1.0 NA, Olympus), and a 40x reflective objective (LMM-40X-P01, 0.5 NA, Thorlabs). The 10x is a plan achromat objective whose low NA increases the axial point spread functions (PSFs) of the focused beams, which can be advantageous for two-color overlap. On the other hand, the 20x objective is specialized for multiphoton microscopy (MPM) [188], and offers semiapochromat performance from the visible to infrared range at a high numerical aperture (NA). Thus, it was determined that each

refractive objective could serve as a distinct use case comparison to the reflective objective. The photosensor material, GaAsP, was selected due to its broad multiphoton excitation spectrum, allowing color shift to be evaluated over a wide wavelength tuning range. Fluorescence intensity of the GaAsP film was recorded as a function of axial position, which was dynamically adjusted using a motorized labjack platform (MLJ150, Thorlabs) at excitation wavelengths ranging from 1150 to 1550 nm. Interpolated fits to the resulting fluorescence intensity curves were computed, the peaks of which were used to indicate axial focus at each wavelength (**Figure 4.1(a)**). Axial color shift is most severe with the 10x objective ($\pm$80 μm, $\Delta\lambda = 400$ nm), followed by the 20x objective ($\pm$10 μm, $\Delta\lambda = 400$ nm), whereas the reflective objective exhibits less than ~2 μm of axial color shift. Since the reflective objective is expected to be free of chromatic aberration, it is possible that this modest shift is owed to refractive effects in the scan and tube lens relay and wavelength-dependent Gaussian beam divergence.

When these results are placed into context with the modeled axial PSF length of each objective [189], it is evident that efficient non-degenerate (ND) MPM is precluded by either refractive objective (**Figure 4.1(b)**). Maximally efficient ND-MPM demands minimal color shift and a smaller PSF. However, in the presence of substantial color shift, a larger PSF can compensate to improve ND overlap and hence relative non-degenerate excitation, at the tradeoff of reduced overall MPM excitation efficiency. However, the severe color shift of the refractive 10x objective overwhelms even its relatively large PSF, and the small PSF of the refractive 20x objective prevents effective ND overlap in spite of a moderate color shift. It is observed that the axial dimension of the reflective objective's PSF exceeds the expected axial shift across the 400 nm spectral range, suggesting that its ND-MPM efficiency would be superior to the refractive objectives.

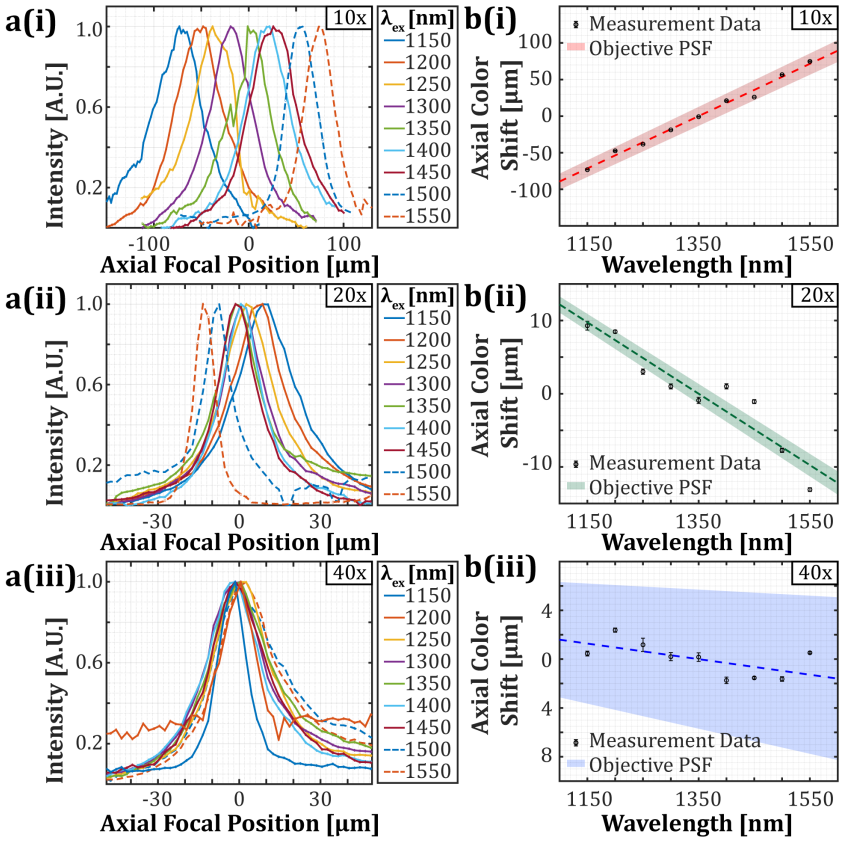

Figure 4.1: **Axial color shift measurements of refractive and reflective objectives.** (*A*) Fluorescence intensity curves versus axial focal position characterizes axial focal shift for refractive (i. 10x and ii. 20x) and reflective (iii. 40x) objectives. (*B*) Axial focal shift values versus excitation wavelength plotted against modeled axial point spread function full-width at half-maxima (shaded regions).

4.4.2. Structural-Similarity Index Measurements of Chromatic Axial Focal Shift

A byproduct of axial color shift is that imaged structures must be refocused as excitation wavelength is tuned. To confirm this effect and ensure that the previously observed axial color shift was not a possible artifact of stratified layers in the GaAsP photosensor exhibiting wavelength-dependent absorption cross sections, a monolayer of quantum dots (QD605, Thermofisher Scientific) was prepared and imaged at 50 nm wavelength increments ranging from 1150 – 1500 nm. Quantum dots were chosen

due to their brightness, photostability, and broad absorption spectrum. For each objective, a reference image was chosen from a focused slice of the λ_{ex} = 1150 nm *z*-stack and its structural similarity index measure (SSIM) was calculated relative to all other images (**Figure 4.2**) by computing correlation as a product of luminance, contrast, and structural similarity [190]. A larger SSIM score for an image indicates a higher degree of similarity to the reference image.

For the 10x refractive objective, roughly ~125 μm of axial color shift is evidenced by the SSIM scores between 1150 and 1500 nm, with the color shift being linear and consistently offset at each wavelength increment (**Figure 4.2(a)**). Calculated SSIM scores of images collected by the 20x objective reveal a similar, but muted effect with approximately ~18 μm of axial color shift across the same spectral range (**Figure 4.2(b)**). Interestingly, the direction of axial shifts in the SSIM heat maps are reversed for the two refractive objectives, indicating the lower and higher magnification objectives introduce dispersion in opposite directions. Finally, the 40x objective reveals a very slight color shift. The non-linearity of the shift suggests that it cannot be solely explained by wavelength-dependent Gaussian beam divergence, which itself is linear. In addition, the bright bands, which indicate focused regions with a high degree of image similarity, narrow as excitation wavelength increases with the 40x data. This is an unexpected result with respect to axial point spread function (PSF) length, which increases at longer excitation wavelengths. This observation highlights a critical point of clarification – the widths of these bands do not reflect direct measurements of the axial PSF length. Rather, the SSIM magnitude at each plane, and thus the apparent widths of each band, is the complement of many wavelength-dependent effects including spectral bandwidth, absorption cross section, scattering length, and n-photon power dependence, in addition, but not limited to axial PSF length.

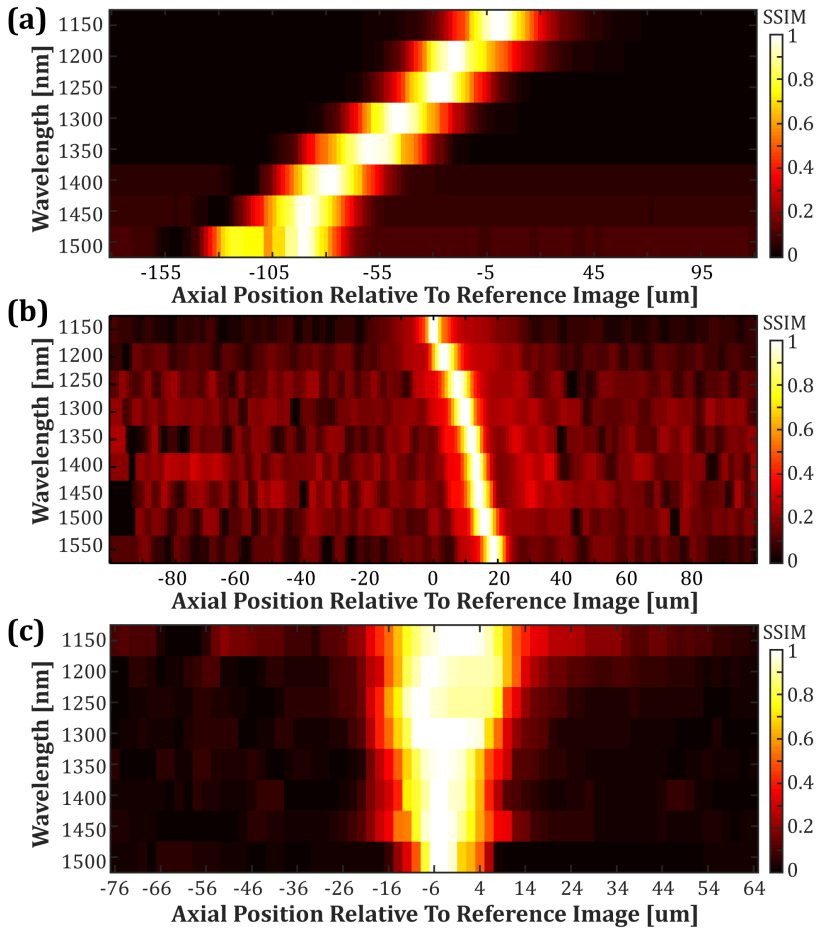

Figure 4.2: **Structural similarity index measurements of a monolayer sample imaged at distinct wavelengths.** Structural-similarity index measurements (SSIM) of individual slices from *z*-stacks recorded at discrete excitation wavelengths with (*A*) a 10x refractive objective, (*B*) a 20x refractive objective, and (*C*) a 40x reflective objective. For each objective, the SSIM scores were recorded relative to a well-focused reference image from the λ_{ex} = 1150 nm stacks.

4.4.3 Axial Focal Shift's Effects on Multi-Channel Imaging

Modern day biological microscopy studies are often highlighted by the variety and number of structures that are targeted, labeled, and imaged. Such multiplexed imaging experiments typically feature two distinct approaches: multispectral and multicolor. Emission-based multispectral imaging uses a single excitation wavelength to

simultaneously excite unique fluorescent targets that are separated by the appropriate emission filter sets. In excitation-based multicolor imaging, distinct populations of fluorophores with overlapping emission spectra can instead be resolved separately by targeting discrete populations individually using highly specific excitation wavelengths. Both are widely used techniques, along with other hybrid approaches. However, 3D imaging experiments that employ the latter excitation-based multiplexed imaging technique unveil the risk of an axial misregistration of the separate excitation channels when refractive objectives are used, especially at longer excitation wavelengths. To demonstrate this, matching regions of a fixed human brain microvascular endothelial cell monolayer sample with Alexa Fluor 488-labeled junction adhesion molecule (Alex Fluor 488-Ab-JAM) and Alexa Fluor 594-labeled occludin (Alexa Fluor 594-Ab-Occludin) were imaged with both refractive and reflective objectives (**Figure 4.3**). Alexa Fluor 488 was excited at 790 nm and detected through a 510/84 bandpass filter (FF01-510-25, Semrock), and Alexa Fluor 594 was excited at 1300 nm and detected through a 610/75 bandpass filter (HQ610/75M, Chroma Technology Corp). Due to the specific combination of excitation wavelength and emission filter used to target Alexa Fluor 594, second harmonic generation (SHG) of collagen fibers could be seen along with the occludin. 3D stacks of the cellular samples were recorded and the mean intensity of each 2D image was calculated as a function of depth to delineate the axial misregistration of the separate channels. Maximum intensity *z*-projections reveal there is no lateral shift between the separate excitation stacks and that identical regions were imaged across the 10, 20, and 40x objectives (**Figure 4.3(a-c)**). The intensity versus depth curves denote that axial misregistration with the 10x objective is significantly pronounced such that there is no evidence of cellular colocalization between the JAM and occludin structures, each occupying regions that falsely appear to be ~175 μm apart, despite the specimen

being a monolayer (**Figure 4.3(d)**). However, the misregistration caused by the 20x objective is much more subtle, mean image intensity versus depth reveals that the Alexa Fluor 594 signal is shifted ~ 10 µm relative to the Alexa Fluor 488 signal, whereas the multichannel data recorded with the reflective objective presents perfect overlap. This high magnification objective's shift is less acute than the GaAsP and QD605 results, which were evaluated at longer excitation wavelengths, suggesting that its achromat performance is improved at the shorter end of the NIR spectrum. Lastly, the 20x objective's axial shift direction is opposite to the 10x, an effect that remains consistent with prior results.

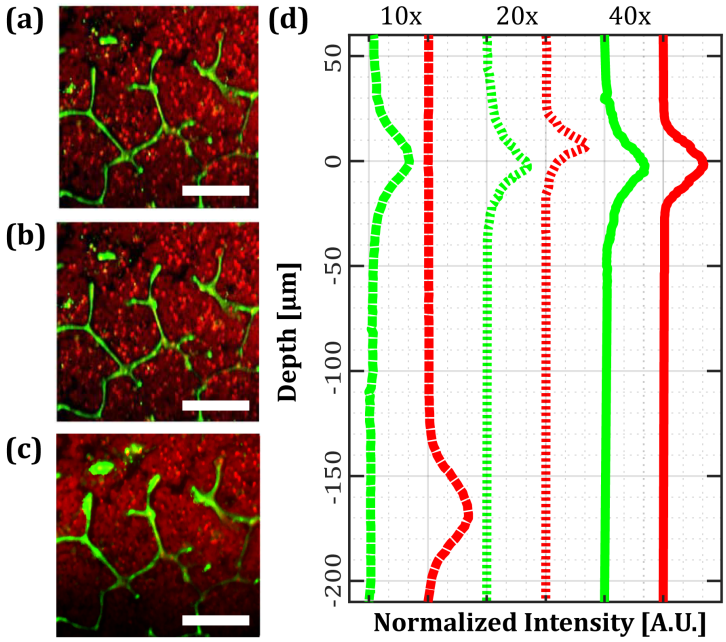

Figure 4.3: **Multicolor imaging of a cellular sample at distinct excitation wavelengths results in axial misregistration when using refractive objectives.** Transverse max intensity projections of a cellular monolayer recorded with (*A*) a 10x refractive objective, (*B*) a 20x refractive objective, and (*C*) a 40x reflective objective. (*D*) Mean image intensity versus depth for the 10x (dashed lines), 20x (finely-dashed lines), and 40x (solid lines) objectives. The green channel contains Alexa Fluor 488 signal, λ_{ex} = 790 nm, and the red channel denotes Alexa Fluor 594 signal and second harmonic generation, λ_{ex} = 1300 nm. Scale bar = 75 µm.

4.4.4 Two-Color Excitation Efficiency Comparison of Refractive and Reflective Objectives

The efficiency of non-degenerate multiphoton microscopy (ND-MPM) is directly determined, at least in part, by the precise overlap of the two synchronized laser sources' point spread functions (PSFs) in the focal plane. Results thus far suggest that the refractive objectives' axial color shift hinders accurate ND overlap relative to the reflective objective. To quantify the impact of this effect on ND-MPM efficiency, a GaAsP photosensor was simultaneously excited with the shorter and longer wavelengths of the signal and idler outputs of the NOPA, respectively (**Figure 4.4**). Idler excitation wavelength ranged from λ_1 = 1150 to 1350 nm and signal excitation wavelength was maintained at $\lambda_2 = [(515\text{ nm})^{-1} - \lambda_1^{-1}]^{-1}$ to achieve a constant virtual excitation wavelength λ_3 = 1030 nm. To evaluate ND-MPM excitation efficiency at various combinations of λ_1 and λ_2, the signal beam was aligned through an optical delay line, allowing the beam to be temporally swept through the idler without affecting spatial overlap (**Figure 4.4(a)**). The peak of the fluorescence emission as a function of delay line position is the result of precise temporal overlap of the two focused excitation pathways, the total excitation of which is given by $I_1^2 + I_2^2 + 2I_1I_2$. As the optical delay line deviates from this position, the resulting fluorescence intensity is solely a consequence of the individual D-MPM events at λ_1 and λ_2, $PSF_{D\text{-}MPM} = I_1^2 + I_2^2$, in the absence of the ND-MPM event at λ_3, given by $PSF_{ND\text{-}MPM} = 2I_1I_2$. Thus, ND-excitation efficiency can be calculated for each objective by subtracting fluorescent intensity values at a 500 fs optical delay from intensity values at precise temporal overlap to isolate the ND-MPM excitation profile, then normalizing it relative to the delayed D-MPM intensity. Since non-degenerate emission intensity is proportional to the power of each beam [62], absorbed power in the GaAsP photosensor

was measured as a voltage signal and set constant for all excitation wavelengths and each objective.

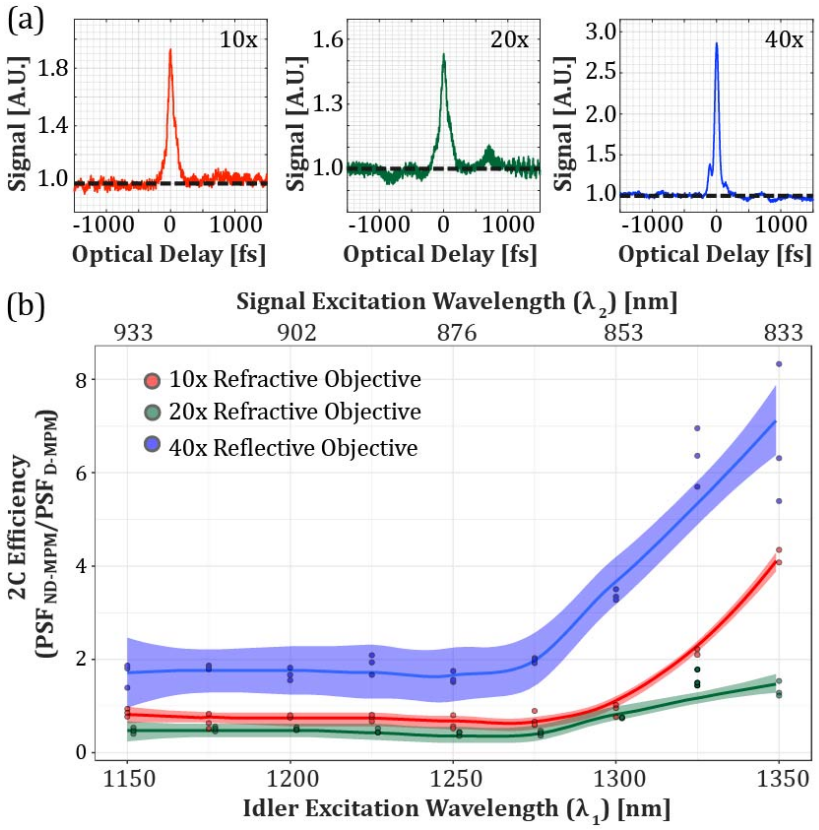

Figure 4.4: **Reflective objectives enhance non-degenerate excitation efficiency.** Fluorescence emission versus optical delay line position normalized relative to baseline degenerate excitation signal (dashed line). (b) Non-degenerate excitation efficiency comparison of the refractive and reflective objectives; scatter points denote raw data, solid lines indicate regression fits, and shaded regions demarcate corresponding 95% confidence intervals.

For all three objectives, ND efficiency remains consistently small between 1150 to 1250 nm, before a substantial increase at 1300 nm (**Figure 4.4(b)**). This suggests that the GaAsP cross section at 1030 nm is similar to the 1150 to 1250 nm or 876 to 933 nm cross sections, but quite high compared to the >1250 and <876 nm cross sections. More importantly, we observe that the ND efficiency of the 40x objective is larger than the 10x

and 20x objectives' ND efficiency at all excitation wavelength combinations, demonstrating that the improved axial overlap of the reflective objective confers enhanced properties for ND-MPM. Yet another factor that may contribute to the refractive objectives' deficient excitation efficiency is pulse broadening caused by group velocity dispersion, which was not pre-compensated for in this work. Notably, the outperformance of the reflective objective relative to the refractive objectives increases as $\Delta\lambda = \lambda_1 - \lambda_2$ widens. This suggests that an increase in the refractive objectives' axial focal shift severity with larger $\Delta\lambda$ further degrades refractive ND efficiency.

However, it remains surprising that the refractive objectives exhibit any non-degenerate excitation signal with respect to the results shown in **Figure 4.1**, which strongly indicate that there is little overlap between the ND focal profiles. This may be explained by the broad spectral bandwidth of the short pulse excitation sources, which helps maintain spectral, and therefore axial, overlap. Furthermore, due to random scatter of the ND photons and the probabilistic nature of multiphoton excitation, the likelihood of a non-degenerate excitation event remains non-zero even in cases of completely non-overlapping PSFs. This is visibly evident in the SSIM results (**Figure 4.2**), where similarity bands at different wavelengths exhibit a significant degree of overlap. This is further supported by the ND efficiency plot, which shows that the 10x objective slightly outperforms the 20x objective, possibly due to the 10x objective's enlarged PSF allowing for an expanded scattering radius. Of course, sophisticated ray tracing and modeling are needed to fully support this claim. Collectively, these experiments demonstrate that a 0.5 numerical aperture (NA) reflective objective can outperform a higher NA refractive objective for ND-MPM, despite the latter's precedence in conventional MPM. Moreover, direct comparison to a lower NA refractive objective demonstrates that reflective objectives' advantage for ND-MPM applications stems from their minimal axial focal

shift, rather than an enlarged axial PSF, although both qualities help to improve two-color overlap. Continued development in reflective objective technology to increase their NA while maintaining achromatic capabilities will undoubtedly lead to further gains in this area.

4.5 Demonstration of Two-Color and Non-Degenerate Imaging

4.5.1 Two-Color Multiphoton Excitation Can Extend Imaging Depth

To demonstrate deep imaging with two-color two-photon microscopy, an adult C57 mouse injected with 50 µl of 5% weight/volume dextran-conjugated Texas Red dye (D1830, ThermoFisher Scientific) was imaged with a synchronized pair of ytterbium fiber and diamond ultrafast laser sources. The ytterbium fiber laser is used to pump the diamond laser in order to ensure synchronization, and spatiotemporal overlap of the two sources at focus is accomplished using a combination of alignment mirrors and optical delay lines. The specimen was initially imaged using one-color two-photon (1C2P) excitation from solely the fiber laser, and power modulated from 20 mW at the dura (z = 0 µm) to 150 mW at $z \geq 400$ µm, as measured at the objective rear aperture (**Figure 4.5(a)**). An imaging depth of approximately ~800 µm was achieved before signal-to-background ratio approached a value of ~1.0. Subsequently, the fiber and diamond laser were coaligned and used to excite the Texas Red infused vasculature (**Figure 4.5(a)**). Combined power from the synchronized lasers was modulated to match the conditions from the fiber laser imaging session with a 50:50 contribution from each excitation source (e.g. 10 mW of fiber power and 10 mW of diamond power at the pial surface). Imaging depth was extended significantly by two-color two-photon (2C2P) excitation; signal-to-background ratio did not approach 1.0 until an imaging depth of approximately 950 µm. Following this imaging stack, the fiber laser was delayed in time relative to the

diamond pulses at τ = 600 fs such that non-degenerate two-photon (ND-2P) excitation would not be possible (**Figure 4.5(a)**). Instead, this condition represents simultaneous 1C2P excitation by the fiber and diamond lasers, each at half of the power used in the first imaging stack. Total imaging depth achieved here (z ~ 800 μm) was very similar to that of the fiber laser excitation volume. Please note, frame averaging, sampling speed, and all other acquisition settings were kept constant for each of the three imaging volumes, and the same region of interest was imaged each time to ensure a consistent comparison of one- and two-color excitation. Ultimately, these results demonstrate that 2C2P excitation of Texas Red at λ_1 = 1055 nm and λ_2 = 1240 nm increases imaging depth by a factor of ~20% relative to 1C2P excitation at λ_1 = 1055 nm.

To better understand these results, it is important to note the two-photon action cross section profile of the fluorophore target. Texas Red's two-photon action cross section peaks at approximately 1150 nm (**Figure 4.5(b)**), which closely matches the virtual λ_3 excitation wavelength conferred by the fiber and diamond laser combination, $2(1055^{-1} + 1240^{-1})^{-1} = 1140$ nm [81,120]. Thus, the non-degenerate excitation pathway made accessible by temporally overlapped two-color diamond and fiber imaging corresponds to an energy level where two-photon absorption by Texas Red is nearly at a maximum. This results in greater signal levels, thereby extending imaging depth. It is important to note that these results may not have been as successful with a different choice in contrast agent or a different pair of imaging wavelengths. For instance, a dye whose peak action cross section resides closer to 1055 nm may have yielded a shallower imaging depth under the 2C2P condition. With respect to Texas Red, 2C2P at λ_1 = 1140 nm and λ_2 = 1240 nm is expected to fare worse than 1C2P at λ_1 = 1140 nm. Overall, this shows that maximizing the benefits of 2C2P microscopy requires a comprehensive understanding of the available fluorophores and excitation sources. For a typical lab that

lacks the financial luxury to purchase tunable synchronized dual output sources and is confined to using standalone non-tunable lasers, 2C2P may provide the most efficient method for excitation of certain fluorophores. As illustrated here, given the limited availability of fiber and diamond lasers and Texas Red labeled vasculature, 2C2P is the most favorable excitation regime to maximize signal and extend imaging depth.

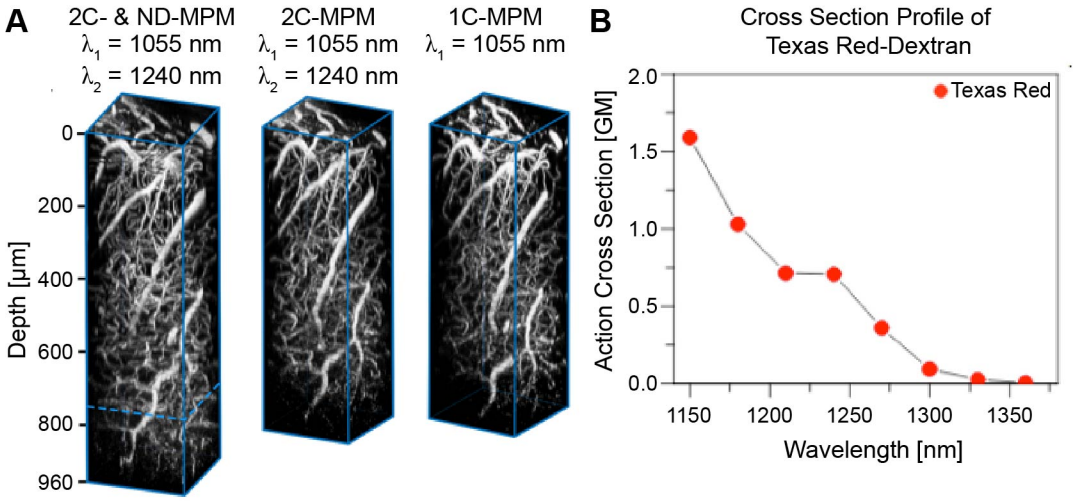

Figure 4.5: **Two-color (2C) and non-degenerate (ND) multiphoton microscopy (MPM) of Texas Red murine vasculature.** (*A*) 2C- and ND-MPM with no temporal offset extends imaging depth in C57 mouse cortex injected with Texas Red relative to temporally offset 2C imaging and one-color (1C) MPM, even when total excitation powers for each stack are held constant. (*B*) Action cross section profile of dextran conjugated Texas Red [81].

4.5.2 Two-Color Non-Degenerate Excitation Boosts Fluorescence Intensity

To demonstrate that our two-color two-photon (2C2P) system is able to produce an expected rise in fluorescent intensity, we compared signal levels using one-color (1C) 2P excitation at a degenerate excitation wavelength λ_D = 1220 nm to 2C2P excitation at a non-degenerate wavelength λ_3 = 1220 nm comprised of equal powers of λ_1 = 1150 nm and λ_2 = 1300 nm. GaAsP film was selected as the fluorescent target of interest due to its broad light absorption. When a reflective objective is used with the two-color imaging

system, we see the marked increase in signal intensity using two-color non-degenerate excitation relative to 1C2P degenerate excitation at $\lambda_D = \lambda_3 = 1220$ nm, approximately 1.8 fold (**Figure 4.6(a)**). This increase is fairly modest using the 20x refractive objective (~1.1 fold) and actually reduced using the 10x refractive objective (~0.42 fold), suggesting that the axial color shift hinders non-degenerate excitation efficiency in both cases (**Figure 4.6(b)**). This hypothesis is confirmed by plotting intensity as a function of axial position. We see that fluorescent signal peaks at the same axial position regardless of excitation wavelength for the reflective objective, whereas signal curves are substantially offset at different axial positions in the case of the refractive objectives. This offset is most severe for the 10x refractive objective, which is consistent with the drop in non-degenerate excitation efficiency we observe in that case. Revisiting the reflective objective results, we see that 2C2P signal intensity drops dramatically from 18,000 counts to 8,000 counts [A.U.] when we apply a temporal offset between the two beams; τ = 10 ps. This is explained by the loss of non-degenerate excitation at $2I_1(r)I_2(r)$, limiting signal to the point spread functions at λ_1 ($I_1^2(r)$) and λ_2 ($I_1^2(r)$). To validate this assertion, we can confirm that total signal from time-delayed 2C2P at λ_1 = 1150 nm and λ_2 = 1300 nm is equivalent to the summed signal levels of 1150 nm 1C2P excitation and 1300 1C2P excitation, which indeed it is: 7,000 + 1,000 = 8,000 [A.U.]. Ultimately, these results demonstrate a few key discoveries. First, axial color shift is eliminated by the reflective objective which results in a sharp increase of two-color non-degenerate excitation relative to direct 1C2P excitation at $\lambda_3 = \lambda_D$. Moreover, we validate that this was a true non-degenerate effect by showing a drop in signal intensity when the beams were temporally mismatched. Finally, we confirmed that 2C2P intensity with time delay is equivalent to summed 1C2P excitation at each of the direct excitation wavelengths.

We consider these results to be critical towards espousing the virtues of two-color non-degenerate multiphoton excitation and would like to more succinctly summarize these results to highlight key information.

Primary Conclusions:

1. Reflective objectives improve two-color axial overlap and thereby improve non-degenerate signal intensity relative to refractive objectives (**Figure 4.6(a)** vs **Figure 4.6(b-c)**).
2. Two-color non-degenerate mixing ($\tau \sim 0$ fs) enhances multiphoton excitation signal relative to two-color degenerate imaging ($\tau >> 0$ fs) and *can* enhance multiphoton excitation relative to one-color degenerate imaging ($\lambda_D = \lambda_3$).

Secondary Conclusions

1. Two-color non-degenerate signal ($\tau \sim 0$ fs; **Figure 4.6(a) purple**; 18k counts) exceeds one-color degenerate signal (**Figure 4.6(a) yellow**; 10k counts) when $\lambda_D = \lambda_3$.
    a. Note, this does not hold true for all fluorophores nor for all combinations of λ_1 and λ_2, but does apply in this case.
2. Two-color non-degenerate mixing ($\tau \sim 0$ fs; **Figure 4.6(a) purple**; 18k counts) enhances multiphoton excitation signal relative to degenerate two-color imaging ($\tau >> 0$ fs; **Figure 4.6(a) green**; 8k counts)
    a. This is a photophysical fact for all fluorophores and combinations of λ_1 and λ_2, unless $\sigma^{(2)}_{\lambda_{ND}} \sim 0$, in which case signal levels would be identical.
3. Degenerate two-color imaging signal ($\tau >> 0$ fs; **Figure 4.6(a) green**; 8k counts) is identical to summed one-color λ_1 signal (**Figure 4.6(a) blue**; 7k counts) and one-color λ_2 signal (**Figure 4.6(a) red**; 1k counts).

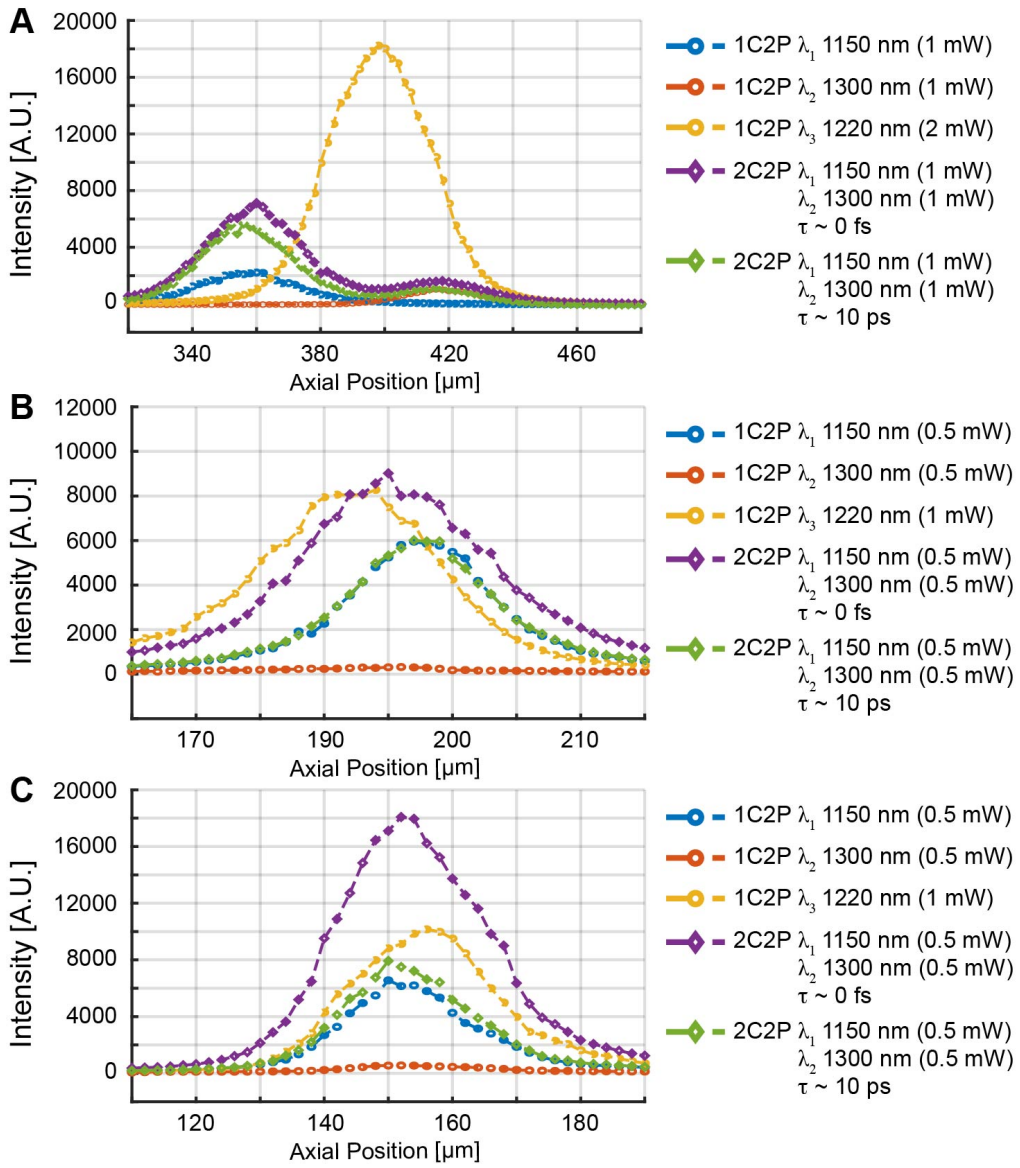

Figure 4.6: **Two-color and non-degenerate signal enhancement.** Signal intensity versus axial position for one-color two-photon (1C2P) microscopy at λ_1 = 1150 nm, λ_2 = 1300 nm, and λ_3 = 1220 nm relative to two-color two-photon (2C2P; $\tau >> 0$ fs) and 2C2P non-degenerate (ND, $\tau \sim 0$ fs) excitation at identical λ_1 and λ_2 such that the virtual non-degenerate excitation wavelength equals degenerate λ_3 using (*A*) a 10x refractive objective (MRL00102, 0.25 NA, Nikon), (*B*) a 20x refractive objective (XLUMPLFLN, 1.0 NA, Olympus), and (*C*) a 40x reflective objective (LMM-40X-P01, 0.5 NA, Thorlabs). Total excitation power for 2C2P and 1C2P at λ_3 was held constant across each condition, and degenerate 1C2P excitation power at λ_1 and λ_2 was halved.

4.5.3 Non-Degenerate Signal-to-Background Ratio Improvements

A two-color non-degenerate laser system is able to improve signal-to-background ratio (SBR) in two fairly expected ways: (1) enhancing excitation efficiency and thereby improving signal and (2) reducing background fluorescence. We have successfully demonstrated the first effect with our two-color system (**Figure 4.6**), and we note that this benefit is expected for any fluorophore with a non-negligible non-degenerate cross section at λ_3, and especially pronounced for fluorophores with relatively small degenerate cross sections at λ_1 and λ_2, ($\sigma_{ND}^{(2)}(\lambda_3) > \sigma_D^{(2)}(\lambda_1)$ and $\sigma_{ND}^{(2)}(\lambda_3) > \sigma_D^{(2)}(\lambda_2)$). However, a substantial reduction of background fluorescence depends on an atypical optical set-up, where the independent beam paths are no longer aligned collinearly, and instead in a manner that allows them to coincide only at focus in the sample plane. To better understand, we must recall that scattered photons reduce excitation efficiency, whereas ballistic photons contribute the bulk of multiphoton signal [64]. Thus, incident excitation power P_o at a depth z is subject to exponential decay that depends on the specimen's scattering mean free path l_s, such that effective excitation power at focus is described as $P(z) = P_o(e^{-z/l_s})$ [64]. By this same token, at greater depths, z, laser intensity at the surface of the sample approaches focal intensity, which results in substantial background signal that is collected indiscriminately in multiphoton microscopy [64]. To approximate fluorescence for multiphoton excitation at degenerate wavelengths $\lambda_D = \lambda_1$ or λ_2, we use the following expression where S(**r**) denotes the spatial profile of the beam:

$$\langle F_D(z,t)\rangle = \sigma_D^{(2)}(\lambda_D) I_D^2(z,t) e^{-2z/l_s} \int_{-\infty}^{\infty} S_D^2(r) dxdy \tag{4.4}$$

Meanwhile, fluorescence for non-degenerate multiphoton excitation at $\lambda_{ND} = \lambda_3$ is given by a slightly more complex expression:

$$\langle F_{ND}(z,t)\rangle = 2\sigma_{ND}^{(2)}(\lambda_{ND})I_{\lambda_1}(z,t)I_{\lambda_2}(z,t)e^{-2z/l_s}\int_{-\infty}^{\infty}S_{\lambda_1}(r)S_{\lambda_2}(r)dxdy \quad (4.5)$$

In a typical two-color excitation schematic, the degenerate and non-degenerate integral terms remain non-negligible along the optical axis, meaning that background fluorescence, $\langle F_{D,ND}(z \neq focus,t)\rangle$, can be substantial. However, using a split-beam system (**Figure 4.7(a)**), the non-degenerate integral term approaches zero at z-planes away from focus, meaning that $\langle F_{ND}(z \neq focus,t)\rangle \sim 0$. Thus, two-color, split-beam excitation of a fluorophore with negligible cross sections at λ_1 and λ_2 can result in a significant increase in SBR relative to one-color degenerate excitation at $\lambda_D = \lambda_3$. Even in the absence of a split-beam system, two-color non-degenerate excitation can help to reduce background fluorescence, since the non-degenerate axial point spread function is diminished relative to the degenerate axial point spread function as previously shown (**Figure 1.3**).

Altogether we can conclude that two-color non-degenerate imaging enhances SBR relative to one-color degenerate multiphoton imaging through two passive mechanisms, increased excitation efficiency and reduced axial point spread function, with further room for improvement using a split-beam system. Unfortunately, our research did not progress to a point where we were able to demonstrate split-beam two-color excitation, but we were able to see a substantial SBR benefit using a simpler optical set-up that relies on the two passive non-degenerate SBR enhancement mechanisms nonetheless. For this study, a 40x reflective objective (LMM-40X-P01; 0.5 NA; Thorlabs) was used to image Texas Red saturated filter paper using degenerate one-color multiphoton excitation at λ_1 = 800 nm (D-1CMP$_{800nm}$) or λ_2 = 1445 nm (D-1CMP$_{800nm}$), and non-degenerate two-color multiphoton excitation at λ_3 = 1030 nm (ND-2CMP$_{800+1445nm}$) (**Figure 4.7(b)**). In all cases, total incident excitation power P_o was

constrained to 6 mW to ensure fair comparisons of the separate image stacks. To calculate SBR, an image mask was computed at each z-plane, and mean intensity of the thresholded region was divided by mean intensity outside of the thresholded region. We find that at all depths, two-color non-degenerate excitation results in a larger SBR than either of the degenerate cases. Notably, two-color SBR peaks at a shallower depth than the either of the one-color image stacks. This might possibly reflect a diminished spatial overlap of the two excitation beams as optical path length increases due to unique, wavelength-dependent refractive interactions. On the whole, longer wavelength degenerate SBR is worse than shorter wavelength degenerate SBR, which is expected due to a reduced action cross section. However, the 1500 nm one-color SBR does overtake 800 nm one-color SBR around ~110 μm. This may reflect that Texas Red exhibits a three-photon power dependence at 1500 nm, which has inherent SBR advantages relative to two-photon excitation at greater imaging depths. Finally, it would have been prudent to include a one-color degenerate excitation comparison at 1030 nm to address the $\lambda_D = \lambda_3$ condition; alas, only one of the two non-collinear optical parametric amplifiers was operational.

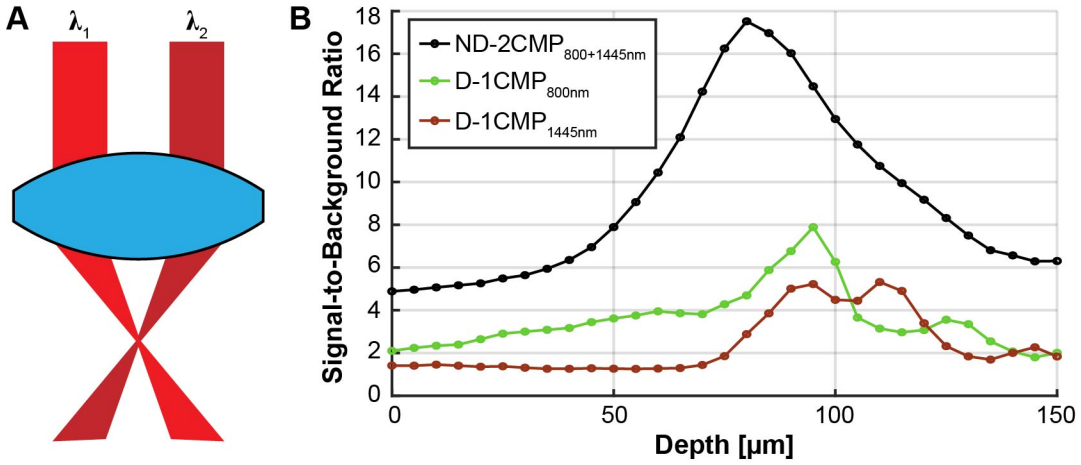

Figure 4.7: **Non-degenerate multiphoton microscopy enhances signal-to-background ratio.** (*A*) Non-degenerate two-color multiphoton (ND-2CMP) signal-to-background ratio (SBR) at λ_1 = 800 nm and λ_2 = 1445 nm, compared to degenerate one-color multiphoton (D-1CMP) SBR at those discrete wavelengths. Total excitation power is 6 mW for each condition.

In further modeling experiments using fast focused field calculations [189] we are more carefully able to predict the advantages of a split-beam system with $\lambda_1 = 1050$ nm and $\lambda_2 = 1240$ nm (**Figure 4.8**). We note that split-beam non-degenerate two-color two-photon microscopy enhances SBR relative to conventional (i.e. non split-beam) one-color two-photon microscopy at the shorter of the two excitation wavelengths (**Figure 4.8(a)**). If we compare conventional and non-degenerate two-color two-photon microscopy to one another, we immediately surmise that the split-beam system enhances SBR substantially (**Figure 4.8(b)**). However, split-beam two-color two-photon and split-beam degenerate two-color two-photon microscopy would yield a poorer resolution than short-wavelength conventional one-color two-photon microscopy, and one-color three-photon SBR is superior to all three (**Figure 4.8(a)**). Finally, a split-beam system is not advantageous with respect to SBR relative to a conventional optical set-up for two-color or degenerate two-color two-photon excitation (data not shown).

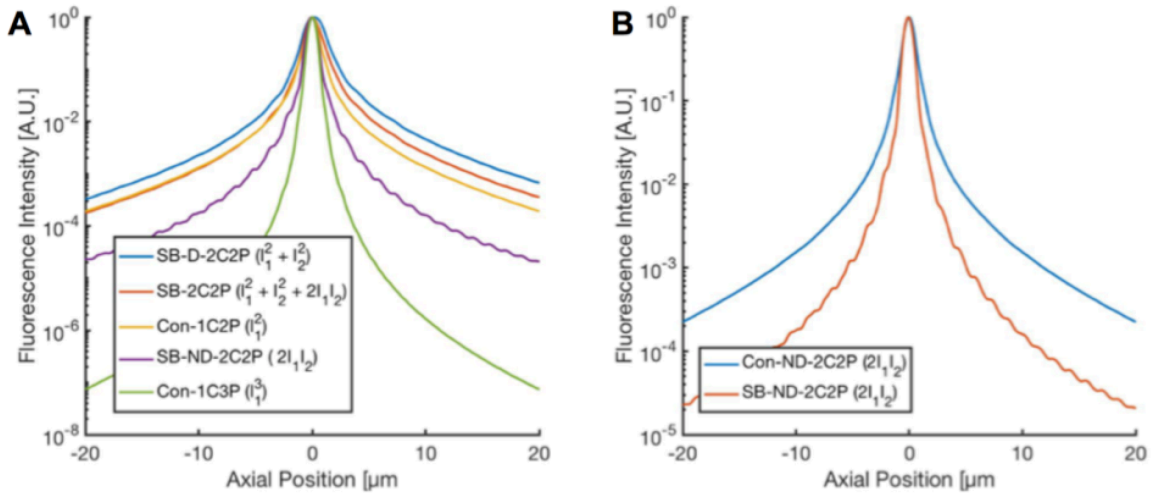

Figure 4.8: **Signal-to-background ratio using conventional or split-beam optical systems.** (*A*) Modeled fluorescence intensity versus axial position for a split-beam (SB) degenerate (D) two-color two-photon (2C2P), a SB-2C2P, a conventional (Con) one-color (1C) 2P, a SB-ND-2C2P, or a Con-1C three-photon (3P) system. (*B*) A comparison of modeled fluorescence intensity versus axial position for ND-2C2P using conventional or split-beam systems.

4.5.4 Non-Degenerate Straddling of High Absorption Excitation Bands

Indocyanine green (ICG) is a widely used organic contrast agent, most commonly recognized for its use in clinical settings and approval for human use by the U.S. Food and Drug Administration. It is also quite advantageous for multiphoton microscopy due to its longer wavelength absorption and emission. For one-photon microscopy, its excitation peak is situated around 780 nm, whereas its emission peaks at 830 nm [191]. Its peak two-photon action cross section is not well characterized, although independent studies from our lab suggest it is at or beyond 1450 nm [81]. Recall that longer near infrared wavelengths are less prone to scatter than visible light, suggesting that ICG emission is more easily collected by multiphoton microscopes in scattering thick media than conventional blue, green, or red dyes. While this same principle holds true for excitation light with respect to scatter, aqueous biological samples pose significant

hurdles in conjunction with ICG imaging with respect to absorption. To elaborate, wavelengths ranging from approximately ~1390 – 1580 nm are highly subject to water absorption; assuming typical brain tissue properties, water will absorb ≥50% of photons at a millimeter imaging depth (**Figure 4.9(a)**) [71]. Therefore, ICG maximizes neuroimaging collection efficiency, but results in poor multiphoton excitation efficiency. It was our hypothesis that we could effectively use two-color two-photon microscopy with direct excitation wavelengths at λ_1 = 1350 and λ_2 = 1600 to non-degenerately excite ICG at its presumed peak cross section near 1450 nm (λ_3 = 1464 nm).

To test this we prepared a 1 mg/ml (1.29 mM) solution of ICG (TCI0535-100MC; VWR) dissolved in double distilled water and used a 50 µl aliquot to saturate a square centimeter of filter paper positioned on a glass slide. We intentionally used water in place of saline solution as the solvent to prevent ICG aggregation [192]. This filter paper was allowed to air dry overnight in a light-tight chamber in order for water to evaporate completely without causing the ICG to photobleach. A cover-slip bottom six channel well (µ-Slide VI 0.4; Ibidi) was then sandwiched on top of the filter paper, with one of the wells positioned directly over the center of the filter paper. The relative brightness of this sample was then characterized using a non-collinear optical parametric amplifier at a tuning range of 1200 – 1600 nm at a constant excitation power of 4.5 mW. To account for the longer wavelength emission of ICG, an 830 nm bandpass filter (RT-830, Edmund Optics) was positioned in front of the wider spectral range photomultiplier tube (H7422P-50; Hamamatsu). This curve, which reflects ICG's relative brightness in the absence of water corresponds to our initial expectations that its peak cross section is situated around 1450 nm (**Figure 4.9(b)**). Our next step was to evaluate how water would diminish the delivery of excitation light and thereby reduce ICG brightness. The µSlide well was filled with a 3 mm column of water, and our imaging was repeated at a greater excitation

power through the objective (10.5 mW; MRL00102, Nikon). We find that ICG brightness peaks at 1300 nm under this condition. Specifically, it seems like the effect of water slightly diminishes 1350 nm excitation and 1600 nm excitation, while strongly suppressing 1400 - 1550 nm excitation (**Figure 4.9(b)**). This corroborates our expectations from modeling, which reveals that water absorption is substantial across this range, particularly around 1450 nm. This data suggests that, indeed, ICG is a suitable candidate for non-degenerate two-color multiphoton microscopy at 1350 nm and 1600 nm. While both of these direct excitation wavelengths are hindered by water absorption, the relative impact on direct 1450 nm excitation is much more severe. Thus, we expect ICG imaging to be much more efficient in aqueous neurophysiological environments using virtual, non-degenerate excitation at 1450 nm. Once again however, we found ourselves unable to test this hypothesis directly due to the non-operational status of one of our non-collinear optical parametric amplifiers ("Steph"), but it is our hope that this preliminary data will benefit the next generation of graduate students who work on this problem in our lab once it returns to working order.

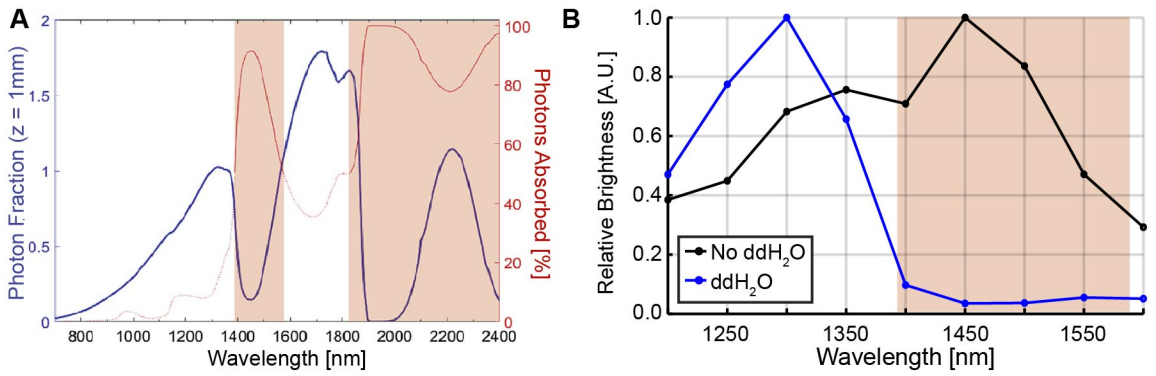

Figure 4.9: **Water absorption hinders efficient degenerate multiphoton excitation of indocyanine green.** (*A*) Modeled photon fraction at a depth of 1 mm (blue line) and percent of photons absorbed (red line) using average brain tissue optical properties [71]. Shaded red regions denote regions in which ≥ 50% of photons are absorbed. (*B*) Relative non-degenerate multiphoton brightness of indocyanine green in the absence (black) or presence (blue) of water.

4.6 Non-Degenerate Mixed Mode Super-Resolution Multiphoton Microscopy

Yet another unexplored application of non-degenerate multiphoton microscopy (ND-MPM) is its potential for imaging sub-diffraction limited neurophysiological features. Specifically, our work here will lead to the development of an advanced and unique microscopy technique that utilizes non-degenerate two-photon excitation with improved mode mixing for super-resolution imaging. This technique combines elements of fluorescence emission difference (FED) microscopy, otherwise known as switching laser mode microscopy (SLAM), with non-degenerate multiphoton excitation to approach the super-resolution capabilities of stimulated emission depletion (STED) microscopy without the risk of photodamage or photo-destruction. As previously noted, STED utilizes a doughnut shaped depletion beam that is made concentric with a Gaussian excitation beam at a slight temporal delay to confine fluorescence to a reduced focal spot. Regrettably, STED requires a high power depletion beam to achieve this effect, which

may cause thermal damage and photobleaching. FED solves this problem by alternately exciting a given specimen with a Gaussian excitation beam (TEM_{00}) and a doughnut shaped dark beam (TEM_{01}), then digitally subtracting the dark image from the excitation image to produce a ~two-fold resolution enhancement over traditional fluorescence microscopy. Specifically, the final image resolution of FED is determined by the diameter of the doughnut shaped beam's central null spot. The primary goal of our proposed super-resolution system is to produce a dark beam with a reduced central null spot to enhance the resolution of difference images beyond a mere two-fold improvement by non-degenerate mixing of spatial modes (**Figure 4.10**). This requires the spatiotemporal overlap of TEM_{00} and TEM_{01} beams at distinct wavelengths, λ_1 and λ_2. With precise synchronization, fluorescent excitation occurs at a combined wavelength $\lambda_3 = 2/(1/\lambda_1 + 1/\lambda_2)$. Recalling that the total excitation of the combined two-color beams is $(I_1(r)+I_1(r))^2 = I_1^2(r)+I_2^2(r)+2I_1(r)I_2(r)$, provided that a fluorophore of interest's cross section is negligible at λ_1 and λ_2 relative to λ_3, the dark beam excitation profile is given solely by $2I_1(r)I_2(r)$ where $I_1^2(r)$ and $I_2^2(r)$ correspond to the TEM_{00} and TEM_{01} point spread functions, respectively. Thus, the spatial product of these two modes at λ_3 results in the creation of a dark beam with a reduced central null spot. Our modeling shows that the proposed technique, non-degenerate fluorescence emission (ND-FED) microscopy, can produce sub-200 nm image resolution, which is well beyond a 150 nm resolution enhancement relative to conventional D-MPM at near infrared excitation wavelengths.

It is unclear *a priori* which polarization states for the TEM_{00} (linear or circular polarization) and TEM_{01} (vortex or azimuthal polarization) beams will confer the dark beam with the smallest central null spot for the greatest resolution enhancement. Moreover, it is unknown which polarizations (linear or circular) would produce excitation beams that minimize oversubtraction in difference imaging. In order to evaluate the

utility of the ND-FED system for sub-diffraction limited imaging, it is necessary to computationally assess and optimize its resolution enhancement capabilities. To accomplish this, virtual point spread functions (PSFs) of the incident beams modes $I_1(r)$ and $I_2(r)$ dependent on polarization, wavelength, refractive index, numerical aperture, and bandwidth at the back aperture are generated from mathematical descriptions of electromagnetic diffraction in optical systems [193]. Mode mixing is subsequently performed in MATLAB via a straightforward multiplication procedure to produce the combined excitation beam and dark beam PSFs at λ_3, $2I_1(r)I_2(r)$. Next, virtual excitation and dark images are formed by the convolution of the beam PSFs with virtual objects. Finally, the super-resolution difference image is calculated by digital subtraction, $PSF_{DIFFERENCE} = PSF_{EXCITATION} - \gamma PSF_{DARK}$, where γ is an adjustable weighting factor. By varying the polarization and wavelength of the incident beam modes given a fixed refractive index, numerical aperture, and beam diameter, this optimization identifies the ideal parameters for high-resolution ND-FED microscopy. Yet another crucial advantage of computational modeling includes an optimization of γ factors that maximize resolution enhancement and minimize over-subtraction given the size and spacing of the image features of interest. With a better sense of appropriate subtractive γ factors and the corresponding resolutions from computational simulation, we are better able to design, operate, and troubleshoot the ND-FED system during data collection. In addition, ND-FED imaging requires fluorophores with small cross sections at λ_1 and λ_2 and a large cross section λ_3. Thus, another major goal accomplished here is analysis of the brightness cross sections of popular contrast agents across a wide NIR spectral range to determine the ideal non-degenerate excitation wavelengths for each fluorophore. Ultimately, this computational modeling serves as an invaluable resource towards the development of a

well-optimized super-resolution system and helps to identify ideal fluorophore targets and appropriate excitation wavelengths for unambiguous experimental design.

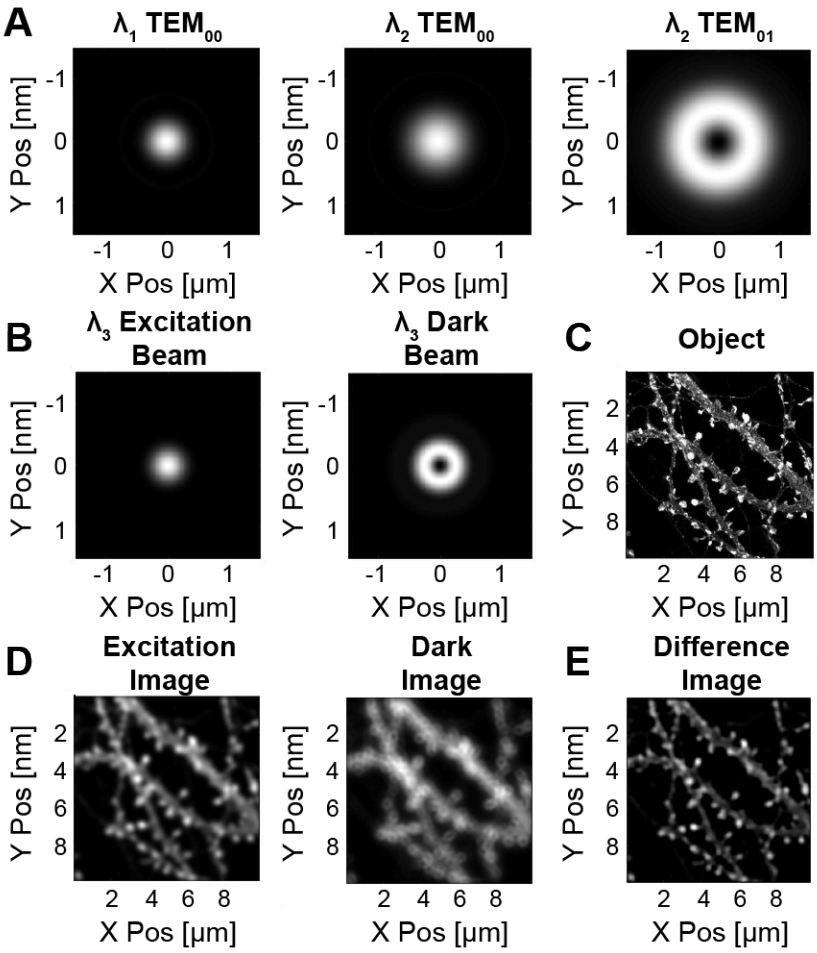

Figure 4.10: **Overview of non-degenerate fluorescence emission difference microscopy.** (*A*) Initial beam modes are non-degenerately mixed to produce (*B*) excitation and dark beams at λ_3. Beam convolution with the (*C*) virtual object generates (*D*) excitation and dark images. Weighted subtraction of the dark image from the excitation image results in a (*E*) super-resolution difference image.

4.6.1 Non-Degenerate Mode Mixing Enhances Conventional Fluorescence Emission Difference Microscopy Resolution

To assess the advantages of non-degenerate (ND) mode mixing relative to degenerate fluorescence emission difference microscopy (D-FED), both are compared where the direct degenerate excitation wavelength λ_D is equivalent to the virtual ND excitation wavelength λ_3 ($\lambda_D = \lambda_3 = 1080$ nm) (**Figure 4.11**). The first step for both processes is the generation of initial beam modes. Given the target fluorophore's peak cross section wavelength, λ_{ex}, D-FED relies on two initial TEM_{00} and TEM_{01} modes from a single excitation source at $\lambda_D = \lambda_{ex}$. In this example, circular and azimuthal polarization states were evaluated. Two-photon imaging with these individual modes results in inherent mode mixing where the excitation and dark beam PSF are solely comprised of the TEM_{00} or TEM_{01} modes, respectively. Convolution of the excitation and dark beams with an imaged object produces the excitation and dark images. Digital subtraction of the dark image from the excitation image results in a super-resolution difference image. Notably, a subtractive γ factor can be used to weight the dark image before difference imaging, where larger γ factors lead to greater resolution with the tradeoff of increased over-subtraction. This problem of over-subtraction producing negative sidebands is a well-chronicled and fundamental flaw of conventional FED [194,195], but can be mitigated by the proposed ND-FED technique (**Figure 4.12**). More specifically, we observe that in spite of the fact that D-FED may lead to a lower proportion of over-subtracted regions at a given γ factor (**Figure 4.12(d)**), ND-FED yields a lower proportion of over-subtracted pixels for a given difference image resolution (**Figure 4.12(e)**).

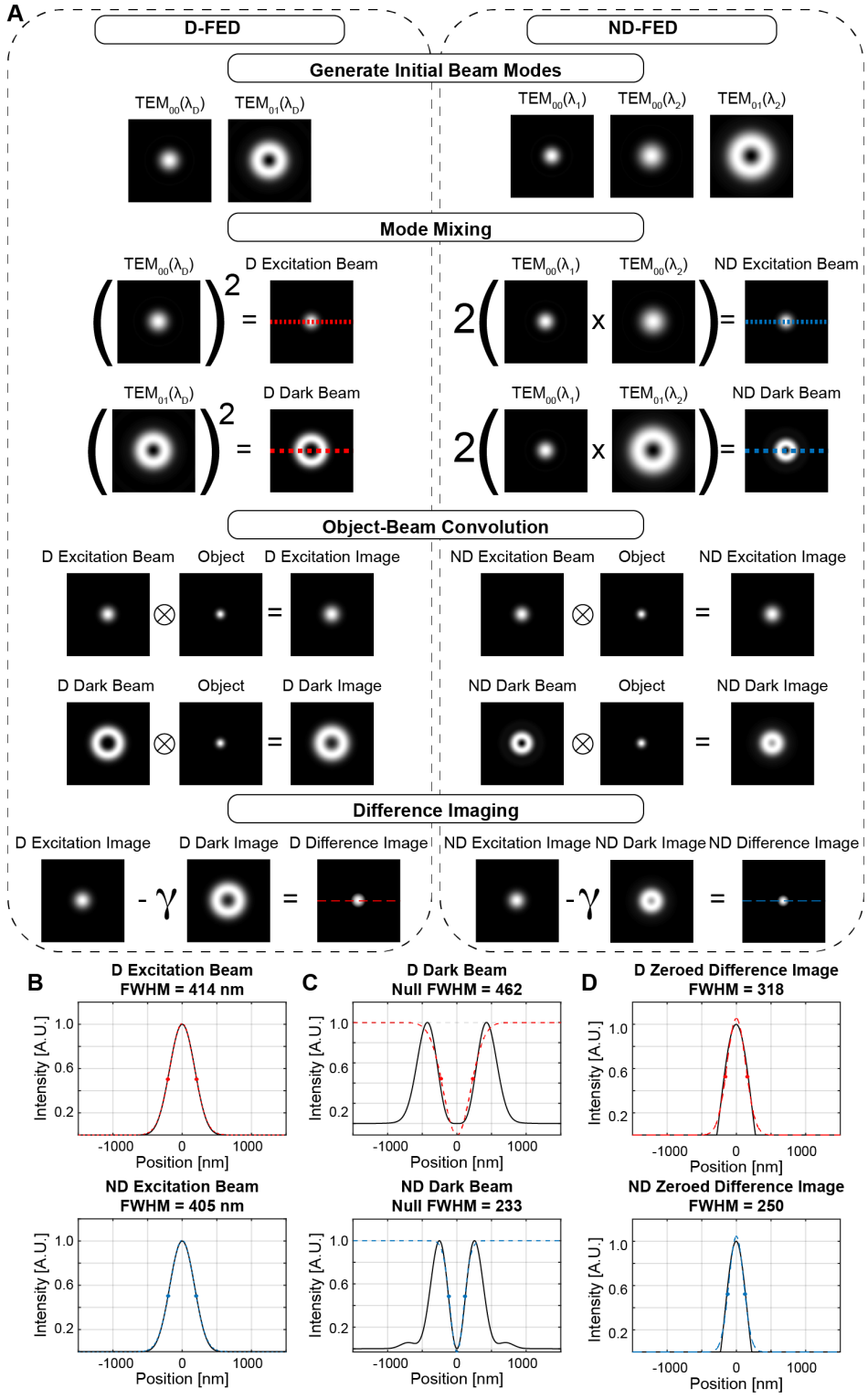

Figure 4.11: Continued on next page.

Figure 4.11: **Non-degenerate mode mixing improves the super-resolution capabilities of fluorescence emission difference microscopy.** (*A*) A comparison of degenerate (D-) and non-degenerate fluorescence emission difference (ND-FED) microscopy procedures with circular and vortex polarizations used for TEM_{00} and TEM_{01} modes, respectively. A single wavelength is selected for D-FED (λ_D = 1080 nm) and two wavelengths are selected for ND-FED (λ_1 = 900 nm, λ_2 = 1350 nm), which compound at $\lambda_3 = \lambda_D$. ND-FED employs one more initial transverse electromagnetic (TEM) mode than D-FED in the construction of the excitation and dark beams, which are independently convolved with a virtual object (FWHM = 250 nm) to generate excitation and dark images. Digital subtraction of a γ weighted dark image from the excitation image results in the super-resolution difference. TEM_{00} = circular, TEM_{01} = vortex. (*B*) D- and ND-FED excitation beam full-width at half-maxima (FWHM) are similar. (*C*) ND-FED dark beam null spots are much smaller, conferring a greater resolution enhancement. (*D*) Using the same γ factor (γ = 0.535), both D- and ND-FED result in sub-diffraction limited images, although only ND-FED manages to achieve the true size of the imaged object

Meanwhile, ND-FED requires not two, but three beam modes at two separate wavelengths from synchronized laser sources which combine at $\lambda_3 = \lambda_{ex}$. The individual component wavelengths λ_1 and λ_2 are selected to lie within a spectrum in which the fluorophore of interest's absorption cross section is negligible. Matched $TEM_{00}(\lambda_1)$ and $TEM_{00}(\lambda_2)$ mode mixing produces the ND-excitation beam, and unmatched $TEM_{00}(\lambda_1)$ and $TEM_{01}(\lambda_2)$ mode mixing produces the ND-dark beam with a greatly reduced central null spot relative to the D-dark beam. In this specific example, where λ_1 = 900 nm, λ_2 = 1350 nm, and $\lambda_D = \lambda_3$ = 1080 nm, ND mode mixing of the dark beam using circular and vortex polarization states reduces the degenerate null spot FWHM from 462 nm to 233 nm (**Figure 4.11(c)**). The remaining ND process is identical to D-FED, but results in larger resolution enhancements; sequential convolution of the beams with an object creates excitation and dark images that are used for digital subtraction to visualize sub-diffraction limited features in super-resolution. Here, a 250 nm Gaussian object was

modeled and FED was performed with a $\gamma = 0.535$, resulting in a 68 nm advantage for the ND-FED difference image relative to D-FED (**Figure 4.11(d)**).

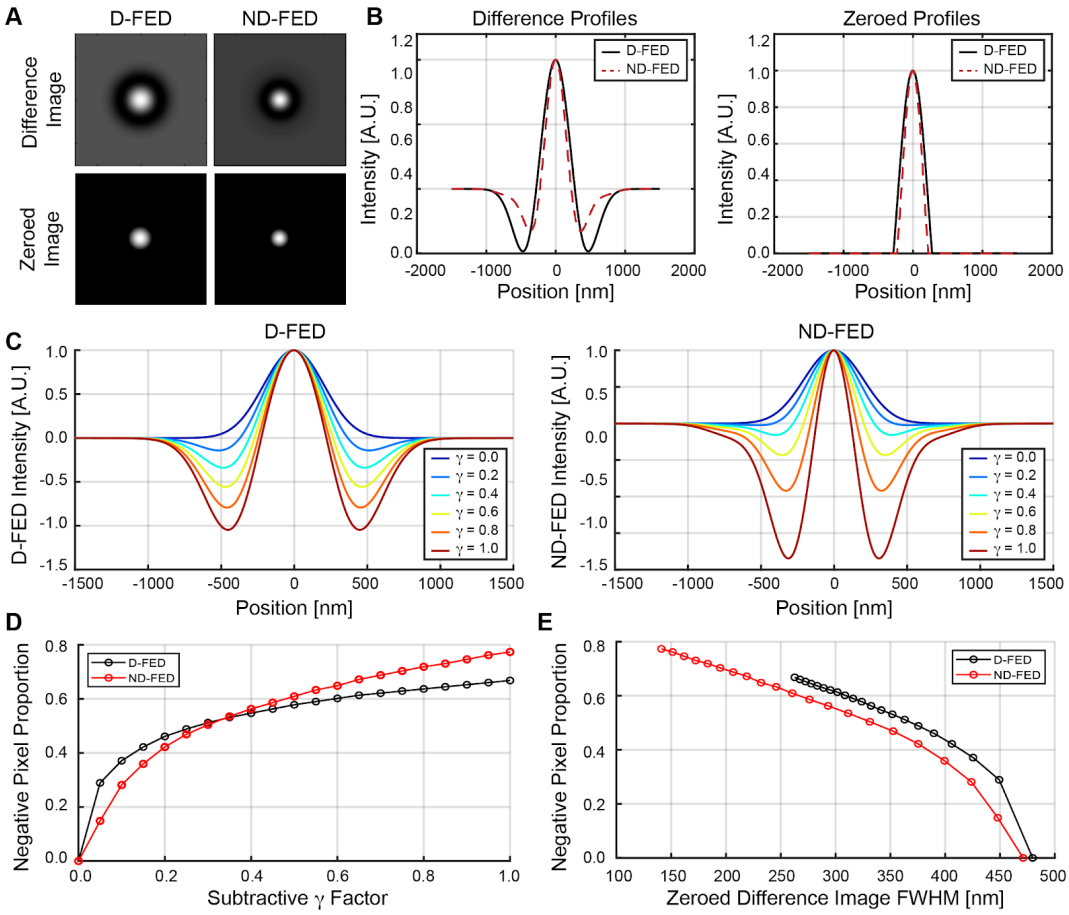

Figure 4.12: **Non-degenerate fluorescence emission difference microscopy can mitigate the extent of over-subtraction.** (*A*) Degenerate (D-) and non-degenerate fluorescence emission difference images (ND-FED) of a 250 nm object before and after zeroing negative pixel values. λ_1 = 900 nm, λ_2 = 1350 nm, λ_3 = λ_D =1080 nm, $\gamma = 0.535$, TEM_{00} = circular; TEM_{01} = vortex. (*B*) Central line profiles of the D- (*solid black*) and ND- (*dashed red*) difference (*left*) and zeroed difference (*right*) images. (*C*) Line profiles of D- (*left*) and ND-difference (*right*) images using various γ factors. (*D*) Negative pixel proportion for D- and ND-FED as a function of γ factor. (*E*) Negative pixel proportion for D- and ND-FED as a function of zeroed difference image FWHM.

4.6.2 Optimal Polarization States for Non-Degenerate Fluorescence Emission Difference Imaging

In order to fully maximize the utility of non-degenerate fluorescence emission difference (ND-FED) microscopy for sub-diffraction limited imaging, it is necessary to computationally assess and optimize its resolution enhancement capabilities. For instance, it is unclear *a priori* which TEM_{00} and TEM_{01} polarization states construct the dark beam with the smallest central null spot for most favorable resolution. To evaluate this, ND-excitation, dark, and difference beams were evaluated at wavelength combinations spanning 650 to 1350 nm, using either linear or circularly polarized TEM_{00} beams in conjunction with azimuthal or vortex TEM_{01} beams (**Figure 4.13**). Due to the anisotropic behavior of ND-FED combinations using linear polarization [177], resolution was measured in the orthogonal axis to the plane of polarization to report optimal resolution. Notably, difference beams were calculated by direct subtraction of the dark beam from the excitation beam, thereby simulating the difference image of a point source object and thus reporting on the maximum effective resolution expected for each set of wavelengths and polarization conditions characterized.

It is observed that circularly and azimuthally mode mixed dark beams' null spots are minimized relative to other TEM mode mixes for any given wavelength combination, which results in a higher-resolution difference beam (**Figure 4.13(b)**). Specifically, circular and vortex combinations' null spots are ~5-12 nm larger (**Figure 13b(ii)**) resulting in difference beams that are ~5 nm larger (**Figure 13c(ii)**). Linear and vortex or azimuthal mode mixing performs considerably worse, with null spots up to 25 nm larger (**Figure 13b(iii-iv)**) and difference images up to ~20 nm lower in resolution, depending on the wavelength combination (**Figure 13c(iii-iv)**). Notably, this study further examines potential ND-FED resolution enhancement with $TEM_{00}(\lambda_1)$ and $TEM_{01}(\lambda_2)$ dark beams in

cases where λ_1 is lower or higher energy than λ_2. It is shown that in all cases, regardless of which specific TEM modes are used, dark beam null spot diameter, and hence final difference image resolution, is minimized when λ_2, the TEM_{01} wavelength, is longer than λ_1, the TEM_{00} wavelength.

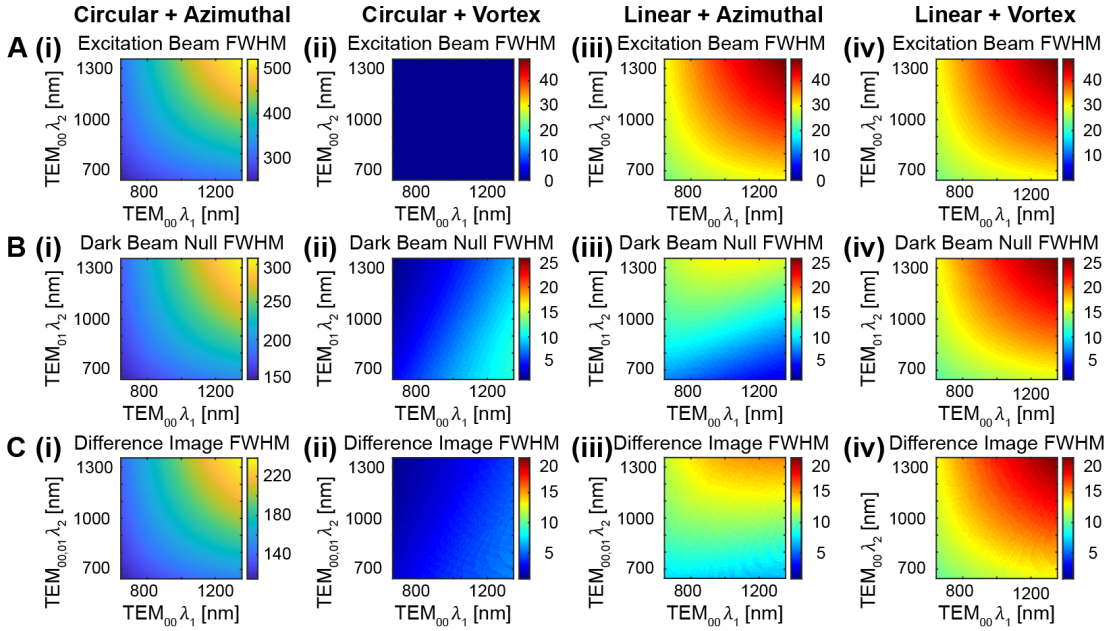

Figure 4.13: **Non-degenerate fluorescence emission difference microscopy resolution using various polarization states.** (*A*) Excitation beam full-width at half-maximum (FWHM), (*B*) dark beam null spot FWHM, (*C*) and difference image FWHM using either (*i*) circular and azimuthal, (*ii*) circular and vortex, (*iii*) linear and azimuthal, (*iv*) or linear and vortex TEM modes for non-degenerate mode mixing. Difference images were calculated by directly subtracting dark beams from excitation beams to simulate difference imaging of a point source and thereby reporting maximum effective resolution expected for each set of wavelengths and polarization conditions characterized. Scaling for (*i*) is absolute, whereas scaling for (*ii-iv*) is taken relative to the corresponding circular and azimuthal beam or image from (*i*).

4.6.3 Non-Degenerate Fluorescence Emission Difference Imaging Over-Subtraction

A shortcoming that is consistent to both degenerate and non-degenerate fluorescence emission difference (D- and ND-FED) microscopy is the possibility of over-

subtraction, where negative sidebands appear upon dark image subtraction. These negative lobes represent a potential loss of information, and an ideal ND-FED image will maximize resolution and minimize over-subtraction. Thus, we evaluated over-subtraction with respect to magnitude and proportion for all beam mode and wavelength combinations, where magnitude is defined as the mean value of negative pixels in the resulting difference image and proportion is the ratio of negative to positive value pixels after difference imaging (**Figure 4.14**). Unsurprisingly, the magnitude of over-subtraction is most severe with circular and azimuthal TEM modes, followed by circular and vortex, then linear and vortex combinations. This is a reasonable finding if one intuits that the dark beam mode combination that results in optimal resolution enhancement will also result in heavier over-subtraction. However, when we evaluate over-subtraction with respect to negative pixel proportion, we find a converse trend, where circular and azimuthal mode mixing results in a similar proportion of over-subtracted pixels to linear and azimuthal mode mixing and a significantly lower proportion relative to all other TEM mode combinations. In FED microscopy, negative pixels are conventionally zeroed out in difference images regardless of their magnitude [196], suggesting that the proportion of negative pixels is a greater concern with respect to information loss than their absolute value. Thus, we can surmise that the ideal TEM mode combination should minimize the spread of over-subtraction, but maximize the magnitude of over-subtraction, as these traits reflect well-concentrated difference imaging. This criteria identifies circular and azimuthal beam modes as an ideal set for ND-FED imaging, which corroborates the previous conclusion made by evaluating TEM polarizations solely with respect to resolution enhancement (**Figure 4.13**).

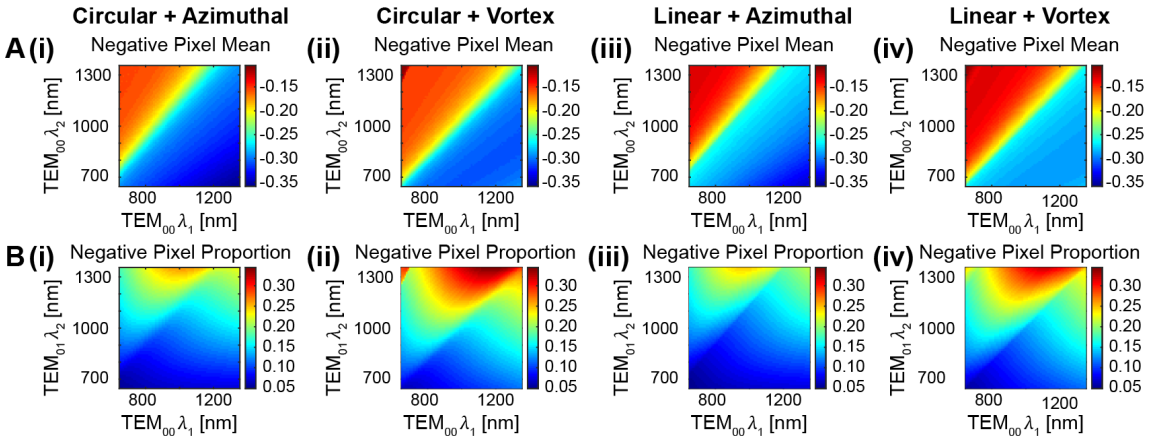

Figure 4.14: **Non-degenerate fluorescence emission difference imaging over-subtraction using various polarization states.** Over-subtraction quantified by (*A*) negative pixel mean and (*B*) negative pixel proportion using either (*i*) circular and azimuthal, (*ii*) circular and vortex, (*iii*) linear and azimuthal, (*iv*) or linear and vortex TEM modes for non-degenerate mode mixing.

4.6.4 Resolution and Over-Subtraction of Degenerate Versus Non-Degenerate Fluorescence Emission Difference Microscopy

Now that circular and azimuthal polarization states are identified as the ideal transverse electromagnetic modes (TEM) for non-degenerate fluorescence emission difference (ND-FED) microscopy, we sought to generate a direct comparison of degenerate (D-) and ND-FED imaging resolution and over-subtraction using these defined modes. D-FED was performed using $TEM_{00}(\lambda_D)$ and $TEM_{01}(\lambda_D)$ modes where λ_D = 650 - 1350 nm, and ND-FED was performed using $TEM_{00}(\lambda_1)$, $TEM_{00}(\lambda_2)$, and $TEM_{01}(\lambda_2)$ modes, where $\lambda_1 = \lambda_2$ = 650 - 1350 nm and all $\lambda_3 = 2(\lambda_1^{-1} + \lambda_2^{-1})^{-1} = \lambda_D$ combinations were directly compared to D-FED. With respect to transverse resolution, we discovered that ND-FED universally produces higher resolution images for $\lambda_3 = \lambda_D$ than D-FED regardless of which λ_1 and λ_2 wavelength combination was applied (**Figure 4.15(a)**). Specifically, ND-FED results in a ~65 nm resolution enhancement relative to D-FED at a 650 nm excitation wavelength, and widens to a ~135 nm advantage at a 1350

nm excitation wavelength. Despite this advantage, one can potentially over-subtract more heavily with ND-FED than with D-FED, although not in all cases (**Figure 4.15(b)**). This begs the question, which ND wavelength combinations minimize the severity of over-subtraction? If we segregate negative pixel proportion data into cases where $\lambda_1 > \lambda_2$ and vice versa in the construction of $TEM_{00}(\lambda_1)$ and $TEM_{01}(\lambda_2)$ non-degenerate mode mixing, we find that the final difference image contains a lower over-subtracted pixel proportion if the TEM_{00} dark beam mode wavelength is longer than the TEM_{01} wavelength (**Figure 4.15(b)**). However, it is also evident that using longer TEM_{01} wavelengths, such that $\lambda_2 > \lambda_1$ improves resolution enhancement (**Figure 4.15(a)**). To summarize, over-subtraction is minimized by longer TEM_{00} wavelengths ($\lambda_1 > \lambda_2$), whereas difference image resolution is maximized with longer TEM_{01} wavelengths ($\lambda_2 > \lambda_1$). This evidence supplements our earlier comparison of the various polarization state combinations' effects on over-subtraction (**Figure 4.14**), which lead to the conclusion that TEM mode combinations that lead to maximal difference image resolution resulted in over-subtraction over a smaller region, both of which are favorable outcomes. In contrast, these present results add that for a *selected, given* beam mode combination, longer TEM_{01} wavelengths lead to maximal difference image resolution at the cost of over-subtraction over a larger region. Ultimately, this provides valuable information for researchers who, upon selecting a certain set of beam-mode combinations, can prioritize between enhanced resolution and minimized over-subtraction, which are shown to be at odds with respect to $TEM_{00}(\lambda_1)$ and $TEM_{01}(\lambda_2)$ wavelength selection.

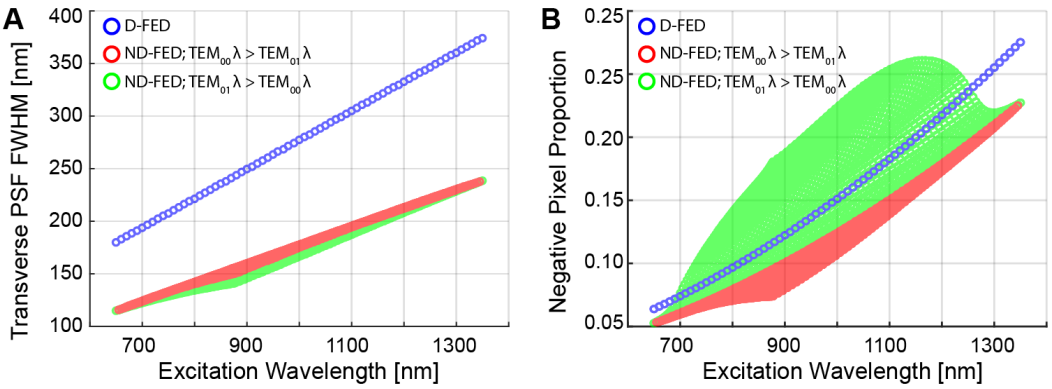

Figure 4.15: **Non-degenerate (ND) mode mixing enhances degenerate fluorescence emission difference (D-FED) image resolution and can reduce the proportion of over-subtraction.** (*A*) Transverse point spread function (PSF) full-width at half-maxima (FWHM) of FED images of point source objects as a function of excitation wavelength (λ_{ex}) for D-FED (blue, $\lambda_{ex} = \lambda_D$; the degenerate excitation wavelength) and ND-FED ($\lambda_{ex} = \lambda_3$). ND-FED FWHMs are distinguished by mode combinations of $TEM_{00}(\lambda_1)$ and $TEM_{01}(\lambda_2)$ where $\lambda_1 > \lambda_2$ (red) and $\lambda_2 > \lambda_1$ (green). (*B*) The proportion of D- and ND-FED over-subtraction, with color symbols corresponding to panel *A*.

4.6.5 Ideal Difference Imaging Gamma Weighting Factor is Object Size Dependent.

Fluorescence emission difference (FED) images are generated by digital subtraction of the dark image from the excitation image, $J_{Excitation} - \gamma J_{Dark} = J_{Difference}$, where γ is a weighting factor of the dark image. If the applied γ factor is excessively large, one can begin to over-subtract from the excitation image and generate virtual structures that are smaller than the features of the intended target. By performing circular and azimuthal mode FED modeling of virtual Gaussian objects with full-width at half-maximum (FWHM) diameters ranging from 50 to 1500 nm where $\lambda_1 = 650$ nm and $\lambda_2 = 1040$ nm, we are able to observe that the appropriate subtractive γ factor depends on the size of the object being imaged (**Figure 4.16**). The larger the object, the more easily it can be over-subtracted, even at smaller γ factors. The smaller the object, the more difficult it becomes to over-subtract; in fact, over-subtraction is precluded from object

sizes smaller than the dark beam's central null spot (i.e. point-source objects). Comparing non-degenerate (ND-) to degenerate (D-) FED ($\lambda_3 = \lambda_D = 800$ nm), we find that γ factors up to 1.0 can be used for objects up to ~150 and ~180 nm, respectively without risk of over-subtraction (**Figure 4.16(b)**). This reveals that ND-FED is incredibly valuable for visualizing smaller structures (<180 nm), which cannot be easily resolved at true size with D-FED due to its larger dark beam null spot. Notably, resolving features between ~150 - 220 nm with ND-FED requires considerable γ factor tuning. For contexts in which several targets of interest across this size distribution are imaged, multiple difference images must be produced with a range of γ factors specific to the expected size of each target. While this is certainly a drawback of ND-FED, this limitation is magnified by D-FED, which requires extensive γ tuning for objects over an even larger size distribution spanning ~180 nm - 800 nm. In contrast, ND-FED is quite robust when it comes to resolving objects between ~220 and 1500 nm using a single γ factor (0.4) without risk of over-subtraction, whereas the same statement only applies to D-FED for objects between ~800 - 1500 nm ($\gamma \sim 0.265$), a range in which super-resolution microscopy has very little to no value.

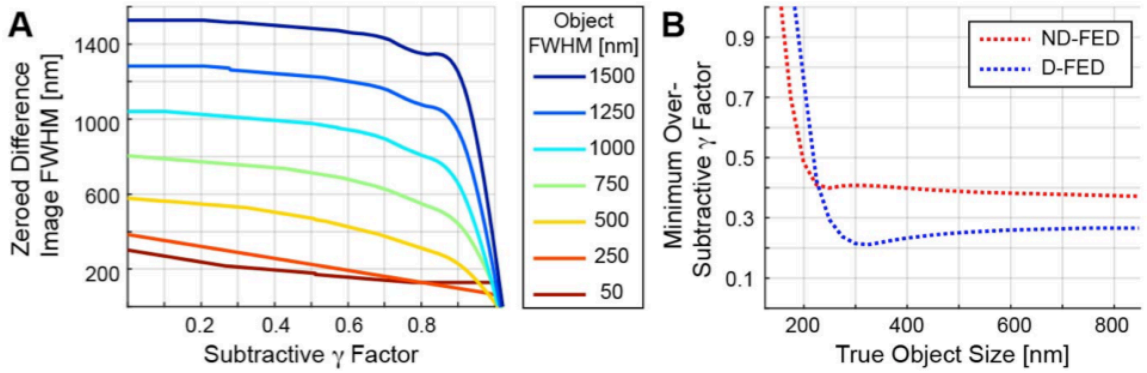

Figure 4.16: **The appropriate fluorescence emission difference imaging subtractive γ factor is object-size dependent.** (*A*) Zeroed non-degenerate fluorescence emission difference (ND-FED) microscopy difference image full-width at half-maximum (FWHM) as a function of subtractive γ factor for various size objects. (*B*) The subtractive γ factor at which a true object becomes over-subtracted (i.e. empty resolution benefits) as a function of initial, true object size.

4.6.6. Fluorophore-Specific Wavelength Combinations for Non-Degenerate Fluorescence Emission Difference Microscopy

For non-degenerate fluorescence emission difference (ND-FED) microscopy to be effective, fluorescence intensity should only appear at the virtual wavelength λ_3 where the combined beam point spread function (PSF) is given by $2I_1(r,t-\tau)I_2(r,t)$. If fluorescence is stimulated by either of the direct excitation wavelengths λ_1 or λ_2, then degenerate excitation profiles will be seen, resulting in a two-color excitation profile, $I_1^2(r,t) + I_2^2(r,t) + 2I_1(r,t-\tau)I_2(r,t)$. Two-color (2C-) FED cannot be used for super-resolution imaging due to the absence of a central null spot in the dark beam. Thus, it is imperative to first characterize the cross section profile of the fluorophore of interest and identify excitation wavelengths λ_1 and λ_2 that result in negligible degenerate cross sections relative to the non-degenerate cross section at λ_3, $\sigma_D^{(2)}(\lambda_1,\lambda_2) \ll \sigma_{ND}^{(2)}(\lambda_1,\lambda_2)$. Fainman et. al (2019) shows that if the number of molecules excited by 2C-MPM is given by:

$$N_{ex}(\boldsymbol{r},t,\tau) = \tfrac{1}{2}\sigma_D^{(2)}(\lambda_1)C(\boldsymbol{r},t)I_1^2(\boldsymbol{r},t-\tau) + \tfrac{1}{2}\sigma_D^{(2)}(\lambda_2)C(\boldsymbol{r},t)I_2^2(\boldsymbol{r},t) + \cdots$$
$$2\sigma_{ND}^{(2)}(\lambda_1,\lambda_2)C(\boldsymbol{r},t)I_1(\boldsymbol{r},t-\tau)I_2(\boldsymbol{r},t) \tag{4.6}$$

where $C(\boldsymbol{r},t)$ is the fluorophore concentration and all other terms have been previously defined, then we are able to apply a few key assumptions to arrive at an expression for time averaged fluorescent signal, $\langle F(\tau)\rangle$ [197]. Specifically, if we presume that fluorophore distribution is spatially and temporally invariant and that both excitation sources output transform limited Gaussian pulses, then paraxial beam approximation dictates:

$$\langle F(\tau)\rangle = \frac{\sqrt{\pi}C\langle P_{\lambda_1}\rangle^2\lambda_1\phi\eta\sigma_D^{(2)}(\lambda_1)}{4fc^2h^2\Gamma_{\lambda_1}} + \frac{\sqrt{\pi}C\langle P_{\lambda_2}\rangle^2\lambda_2\phi\eta\sigma_D^{(2)}(\lambda_2)}{4fc^2h^2\Gamma_{\lambda_2}} + \cdots$$
$$\frac{2\sqrt{\pi}C\langle P_{\lambda_1}\rangle\langle P_{\lambda_2}\rangle\lambda_1\,\lambda_2\phi\eta\sigma_{ND}^{(2)}(\lambda_1,\lambda_2)}{fc^2h^2\Gamma_x\sqrt{\lambda_1^2+\lambda_2^2}}\exp\left(\frac{-\tau^2}{2\Gamma_x}\right) \tag{4.7}$$

In the above expression, ϕ represents the optical system's collection efficiency, η gives the fluorophore quantum efficiency, f is the laser repetition rate, c is the speed of light, h is Planck's constant, $\langle P\rangle$ is average laser power, and Γ is the pulse's temporal standard deviation [61]. If we further assume that average laser powers at λ_1 and λ_2 are equivalent, then the ratio of non-degenerate to degenerate signal when the temporal offset of the two-color beams is $\tau = 0$ simplifies to:

$$\frac{\langle F(\tau=0)\rangle_{ND(\lambda_1,\lambda_2)}}{\langle F\rangle_{D(\lambda_1)} + \langle F\rangle_{D(\lambda_2)}} = \frac{8\Gamma_{\lambda_1}\Gamma_{\lambda_2}\lambda_1\,\lambda_2\sigma_{ND}^{(2)}(\lambda_1,\lambda_2)}{\Gamma_x\sqrt{\lambda_1^2+\lambda_2^2}\left(\Gamma_{\lambda_2}\lambda_1\sigma_D^{(2)}(\lambda_1) + \Gamma_{\lambda_1}\lambda_2\sigma_D^{(2)}(\lambda_2)\right)} \tag{4.8}$$

Therefore, to evaluate ideal ND-FED wavelength combinations for various fluorophores, we assume that all pulses are transform limited with $\Gamma_{\lambda_1} = \Gamma_{\lambda_2} = 65$ fs, where $\Gamma_x^2 = \Gamma_{\lambda_1}^2 + \Gamma_{\lambda_2}^2$, and use known degenerate absorption cross sections [129] to calculate expected ND-FED efficiency. We emphasize that ND-FED efficiency is

distinct from ND-MPM efficiency [197], which seeks to compare degenerate (D-) and ND-MPM signal where $\lambda_D = \lambda_3$, which results in a distinct expression:

$$\frac{\langle F(\tau = 0)\rangle_{ND(\lambda_1,\lambda_2)}}{\langle F\rangle_{D(\lambda_D)}} = \frac{8\langle \mathrm{P}_{\lambda_1}\rangle\langle \mathrm{P}_{\lambda_2}\rangle\lambda_1\,\lambda_2\sigma_{ND}^{(2)}(\lambda_1,\lambda_2)\Gamma_D}{\Gamma_x\langle \mathrm{P}_D\rangle^2\lambda_D\sigma_D^{(2)}(\lambda_D)\sqrt{\lambda_1^2+\lambda_2^2}} \tag{4.9}$$

Thus, we are able to use Equation 4.8 to approximate ND-FED efficiency and identify suitable 2C-excitation wavelengths for various fluorophores using action cross section data obtained from a online repository [129] (**Figure 4.17**). Please note that this data only serves as a crude approximation of relative brightness as both λ_1 and λ_2 beam profiles are assumed to be Gaussian, whereas FED mandates the use of different spatial modes. Nevertheless, these plots remain quite instructive as a visual guide to ND-FED wavelength pair selection, with brighter regions representing ideal candidates and darker portions denoting that brighter degenerate excitation profiles would hinder the efficacy of ND-FED. Individual plots of two-color action cross section profiles for $\eta\sigma_D^{(2)}(\lambda_1,\lambda_2)$and $\eta\sigma_{ND}^{(2)}(\lambda_1,\lambda_2)$ are provided in for each fluorophore for a more comprehensive overview, where $\eta\sigma_D^{(2)}(\lambda_1,\lambda_2) = \frac{1}{2}\eta\sigma_D^{(2)}(\lambda_1) + \frac{1}{2}\eta\sigma_D^{(2)}(\lambda_2)$ and $\eta\sigma_{ND}^{(2)}(\lambda_1,\lambda_2) = \eta\sigma_D^{(2)}(\lambda_3)$ (**Figure 4.17(b-d)**). Finally, a more thorough derivation is provided in Appendix II.

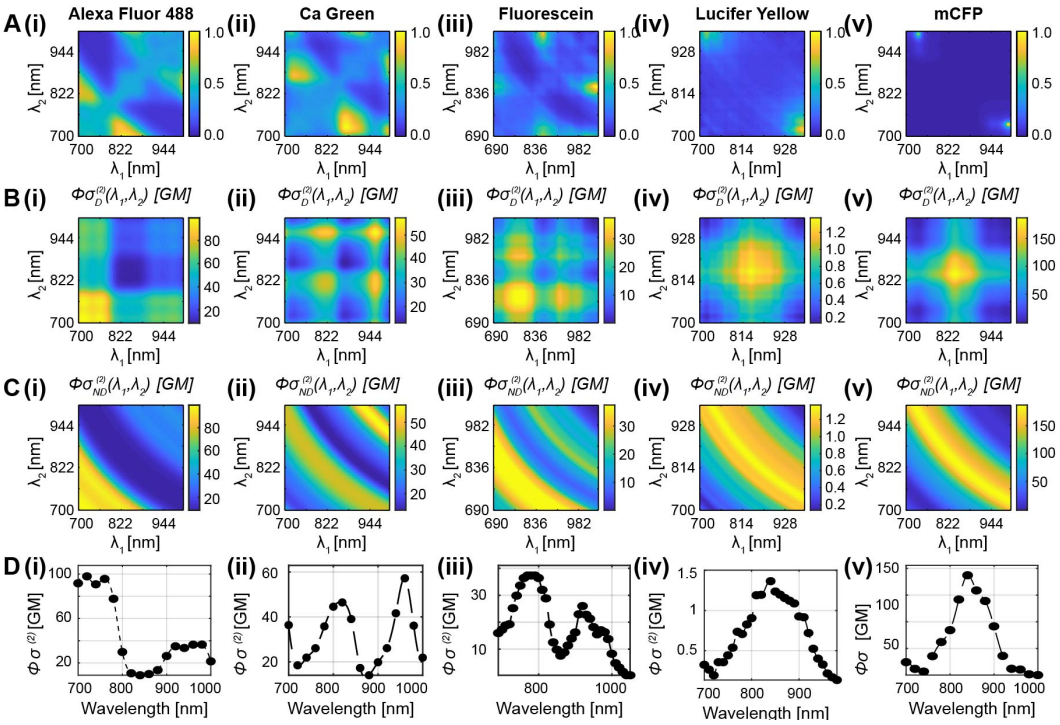

Figure 4.17: **Ideal wavelength combinations for non-degenerate fluorescence emission difference (ND-FED) microscopy are dependent on the fluorophore's cross section profile.** (*A*) Each plot indicates a unique fluorophore's normalized ND-FED efficiency, $\langle F(\tau=0)\rangle_{ND(\lambda_1,\lambda_2)}\left[\langle F\rangle_{D(\lambda_1)}+\langle F\rangle_{D(\lambda_2)}\right]^{-1}$, as a function of λ_1 and λ_2. Ideal wavelength combinations for ND-FED microscopy minimize (*B*) degenerate two-photon action cross sections (TPACs, $\eta\sigma_D^{(2)}$) and maximize (*C*) non-degenerate TPACs ($\eta\sigma_{ND}^{(2)}$). (*D*) Source data for TPACs $\left(\phi\sigma^{(2)}\right)$ [129] of (*i*) Alexa Fluor 488, (*ii*) Ca Green, (*iii*) fluorescein, (*iv*) Lucifer Yellow, and (*v*) mCFP.

4.6.7 Digital Non-Degenerate Fluorescence Emission Difference Imaging of Dendritic Spines

Neuronal architecture influences synaptic communication, and structural modifications and changes in density to dendritic spines are believed to be substrates of functional activity [162,163]. Multiphoton microscopy is commonly used to visualize neuronal and axonal protrusions at greater depths with high resolution, as well as provide

functional information through imaging of calcium dynamics [46]. In spite of this, dendritic spines, whose necks range from 70 – 300 nm in diameter, remain sub-diffraction limited, which hinders a comprehensive association of structure with cognitive function [165]. Non-degenerate fluorescence emission difference (ND-FED) microscopy may present itself as an ideal modality for *in vivo* spine imaging, due to its super-resolution capabilities and reduced need for high-power lasers. To test this, we performed a degenerate (D-) and ND-FED simulation of dendritic spines to compare the resolution benefits of the two approaches (**Figure 4.18**). A dendritic spine phantom image was used to generate a target (**Figure 4.18(a)**) for convolution with the D- and ND-excitation and dark beams (TEM_{00}, circular; TEM_{01}, azimuthal; λ_1 = 650 nm; λ_2 = 1350 nm, $\lambda_D = \lambda_3$ = 878 nm) to simulate FED microscopy (**Figure 4.18(b)**). Digital subtraction was performed at a range of γ factors (**Figure 4.18(c)**), and it is immediately apparent that structures begin to disappear at smaller γ factors using D-FED, which remains consistent with Figure 4.12(d). When we control for matching levels of information loss in the D- and ND-difference images, the measured diameter of a prominent spine is 212 and 185 nm, respectively, which reflects a greater degree of similarity to the true spine diameter in the ND image (Figure 4.18(d)). To elaborate, in this case we have identified a proportion of over-subtraction, p = 0.5, computed the appropriate ND- and D-γ factors that meet this threshold, performed FED deconvolution, and measured the corresponding spine full-width at half-maximum (FWHM) in the resulting difference images.

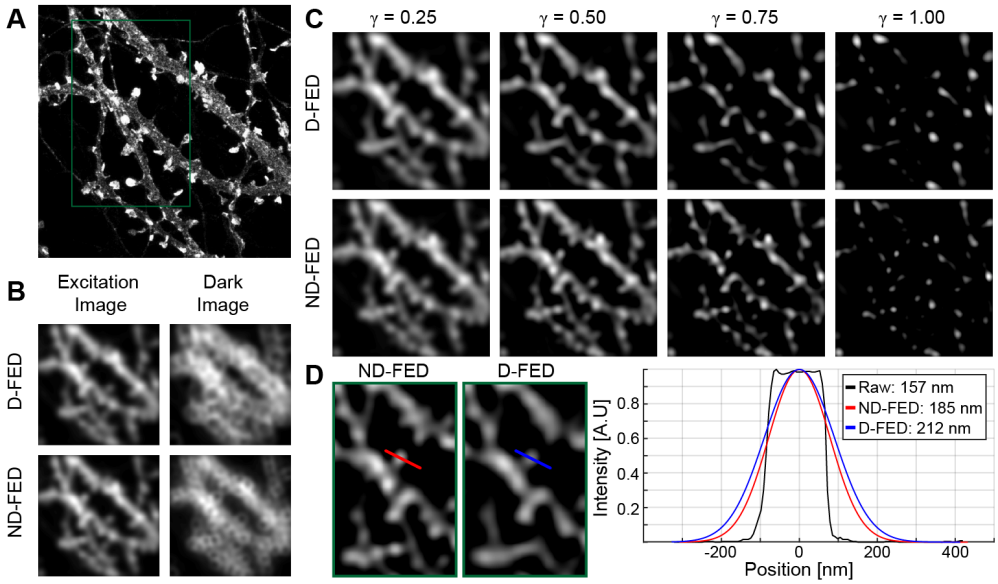

Figure 4.18: **Degenerate (D-) and non-degenerate fluorescence emission difference (ND-FED) imaging simulation of dendritic spines.** (*A*) A phantom image [198] of dendritic spines to serve as a virtual object for FED simulation. (*B*) D- and ND-FED microscopy excitation and dark images of (*A*), where λ_1 = 650 nm; λ_2 = 1350 nm, $\lambda_1 = \lambda_D$ = 878 nm; TEM_{00} = circular, TEM_{01} = azimuthal. (*C*) D- and ND-difference imaging at a range of γ factors using excitation and dark images in (*B*). (*D*) D- and ND-difference image insets from the region demarcated in (*A*) with a 50% over-subtraction level where the blue and red lines denote the location of intensity profiles plotted as normalized signal intensity relative to position.

When we perform this exercise over a broad range of values for information loss (Figure 4.19), ND-FED's advantage is even more pronounced. Direct comparison of D- and ND-FED images at the same thresholds reveals that we can more clearly resolve adjacent structures with ND-FED than D-FED, where those same structures either overlap or disappear completely. To substantiate this qualitative observation, the correlation, ρ, of object, D-, and ND-intensity profiles was computed as a function of information loss and ρ(Object Profile, ND-Profile) was found to be significantly larger than ρ(Object Profile, D-Profile). If we instead control for the final difference image resolution to compare D- and ND-FED difference images, we are able to attain the true

diameter of the spine analyzed in Figure 4.18(d) at D-γ = 0.812 and ND-γ = 0.755. In the case of the ND image, this represents a 10.87% reduction in global information loss relative to the degenerate case. This corroborates our earlier findings that ND-FED yields a lower proportion of over-subtracted pixels for a given resolution (Figure 4.12(e)). Overall, these findings directly demonstrate the utility of ND-FED for dendritic spine imaging and its unique advantage over conventional FED microscopy.

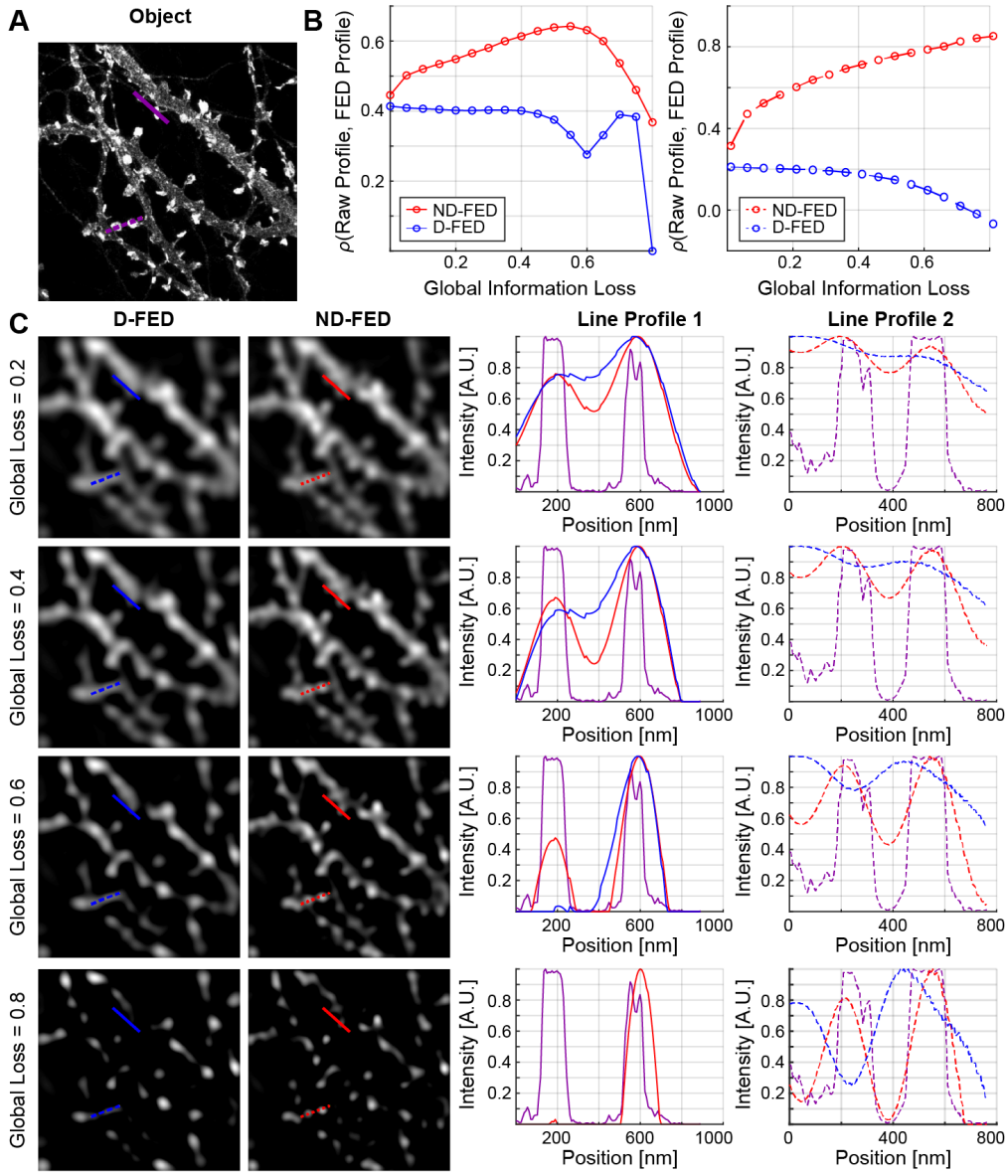

Figure 4.19: **Object and fluorescence emission difference image correlation as a function of information loss.** (*A*) Phantom dendritic spine image [198]; the positions of intensity profiles one (solid) and two (dashed) are denoted in magenta. (*B*) Correlation of raw intensity profiles with corresponding degenerate (D-, blue) and non-degenerate fluorescence emission difference (ND-FED, red) image intensity profiles one (*left*) and two (*right*) as a function of global information loss. (*C*) D-FED (*left*) and ND-FED (*second to left*) images at matching levels of information loss and their corresponding intensity profiles one (*second to right*) and two (*right*) plotted against the object intensity profiles from *A*.

4.8 Non-Degenerate Super-Resolution System Design and Evaluation

4.8.1 Evaluation of Beam-Shaping Technologies

A fundamental component to the construction of the non-degenerate super-resolution microscopy system is the integration of a beam shaping element. A few options presented themselves: a vortex phase-plate (RCP-Photonics; VPP-1C), an azimuthal polarizer (ARCoptix; Radial-Polarization Converter), or a freely programmable spatial light modulator (SLM). The first two components were already in possession of the lab, whereas the latter required some investigation. We initially referred to a publication from Bashkansky and Fatemi [199], where azimuthal and radial point spread functions were generated using a nematic SLM (Meadowlark Optics; P512 SLM). However, we found that the newer 1920 x 1152 pixel SLM was not only higher resolution, it was more compact, it had higher bit depth (12 bits vs 8 bits), and it was less expensive. Both SLMs are parallel-aligned nematic SLMs, so optically both would work the same way. Unfortunately, the Meadowlark SLM is not capable of working over the entire non-collinear optical parametric amplifier (NOPA) wavelength range – there is a 600 – 1300 nm model, and an 850 – 1650 nm model. At a larger range of wavelengths, the liquid crystal layer would be far too thick at the shorter wavelengths to support the longer wavelengths. Meadowlark also provided twisted nematic SLMS, which provide higher contrast ratio amplitude modulation at the cost of a slower response time, and are typically reserved for display applications. However, twisted nematic SLMs can't be used for pure phase modulation, whereas parallel-aligned SLMs are for more flexible. If the incident polarization is vertical and linear, the parallel configuration can be used as a phase modulator. If the incident polarization is linear and at 45 degrees to the SLM, then it acts as a polarization rotator, and a downstream analyzer can convert this polarization

rotation into amplitude modulation. However, as we began to investigate the principle and operation of parallel SLMs, it occurred to us that their function was redundant to the radial polarization converter from ARCoptix, which also produced stable radial or azimuthal modes, depending on the orientation of the device with respect to the linearly polarized input beam. Moreover, the optic is also able to rotate the orientation of linearly polarized light, just as the Meadowlark Optics SLM. While the inner workings of the radial polarization converter are a bit of a black box, our discovery that the device is a liquid crystal based polarization converter lead us to conclude that it is in fact in all likelihood a parallel aligned SLM.

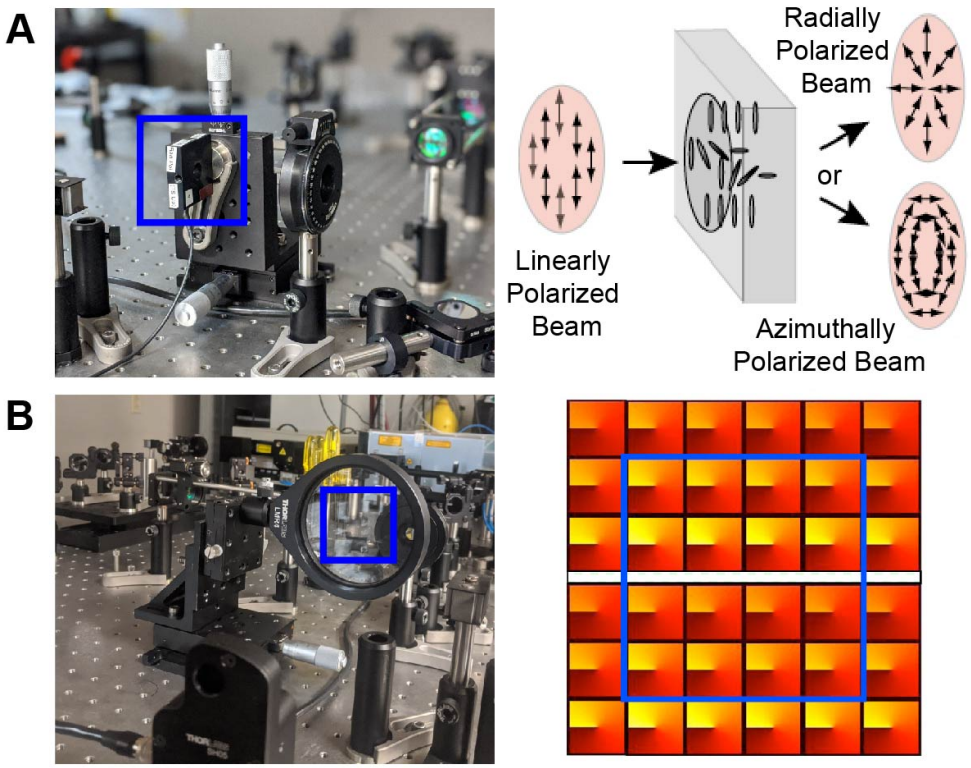

Figure 4.20: **Azimuthal and vortex polarizers.** (*A*) A radial polarization converter can transform a linearly polarized input beam into radially or azimuthally polarized beams depending on input polarization. (*B*) A vortex phase plate converts a Gaussian input into small donut-shaped beam; the appropriate grid square to use is wavelength dependent.

We proceeded to then compare azimuthal and vortex point spread functions experimentally to empirically assess their potential for resolution enhancement in a non-degenerate nanoscopy system (**Figure 4.20**). Azimuthal modes were generated using the radial polarization converter from Arcoptix and vortex modes were generated using the phase plate from RCP Photonics. Initially, five slides of $\leq$200 nm diameter nanoparticles were prepared to measure the system's point spread function: blue (Thermofisher; F8781), yellow-green (Thermofisher; F8787), red (Thermofisher; F8786), dark red (Thermofisher; F8807), and crimson (Thermofisher; F8806). As expected, point spread function measurements did not vary as a function of nanoparticle, as all were sub-diffraction limited in size. The red and dark red fluospheres were then prioritized for quantification due to their relative brightness at 1050 nm ytterbium fiber excitation. Azimuthal mode purity was found to be a strong function of the beam's linear polarization orientation relative to the converter and of the voltage applied to the liquid crystal device, and required extensive optimization and alignment. Vortex mode purity was a bit more straightforward, and only required using the correct region on the phase plate, then precise centering in the x and y axes, which was readily achieved with orthogonally mounted linear translation stages. Once each optic was fully optimized, several images of distinct beads were recorded, and image processing techniques were developed to collect radially averaged line profiles to which Gaussian profiles were fitted in order to estimate the outer and inner full-width half-maxima (FWHM) of the donut shaped point spread function. Ultimately, it was concluded that the azimuthal donut's outer FWHM was larger than the vortex donut's, whereas the azimuthal null spot's null spot FWHM was smaller than the vortex's (**Table 4.1**).

Objective	AZP		VPP	
	Outer FWHM	Null FWHM	Outer FWHM	Null FWHM
10x	2,976 ± 49 nm	1,273 ± 39.2 nm	2,818 ± 9.6 nm	1,449.6 ± 48.9 nm
20x	1457 ± 112.7 nm	574 ± 122.2 nm	1,425 ± 48.2 nm	698 ± 22.1 nm

Table 4.1: **TEM_{01} Dimensions.** Outer and null-spot full-width at half-maxima (FWHM) of azimuthally polarized (AZP) and vortex phase plate (VPP) shaped donuts, using a 10x (Nikon; MRL00102, 0.25 NA) or 20x objective (Olympus; XLUMPLFLN, 1.0 NA).

A qualitative comparison of the polarization converters clearly reveals that the vortex phase plate results in a "coffee bean" like point spread function, rather than a clean donut ring as seen with the azimuthal polarizer. It was hypothesized this might be due to the linear input polarization of the fiber laser. However, rotation of a half-wave plate positioned directly before the polarizer did not alter the orientation of the "coffee bean" lobes, nor did pre-conversion to circular polarization. It is plausible that the aberrant donut may be a result of inappropriate phase matching to the ytterbium fiber laser – the closest match on the phase plate was 1081 nm. When we compare our experimental point spread functions to our modeled point spread functions, we find some discrepancies. The null FWHM of a 20x magnification 1.0 numerical aperture objective vortex point spread function is expected to be 476 nm at 1050 nm excitation. The null FWHM of an azimuthal point spread function is expected to be 441 at the same excitation wavelength, magnification, and numerical aperture. While these numbers are not in precise agreement with our experimental values, they are reasonably close. Discrepancies may be attributed to the noisiness of the experimental point spread function images and resulting radially averaged profiles, as well as imperfect Gaussian fitting, especially with respect to the

outer FWHM. Examples of these images, processing, and fitting are shown in **Figure 4.21**.

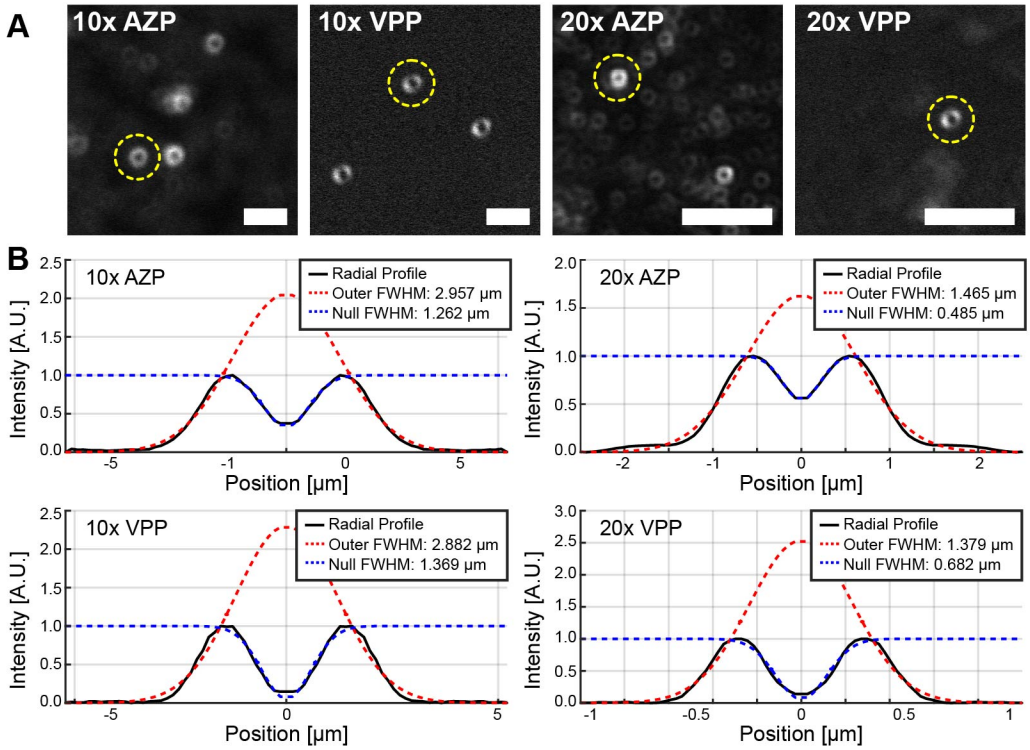

Figure 4.21: **Azimuthal and vortex point spread functions.** (*A*) Representative point spread functions using an azimuthal polarizer (AZP) or a vortex phase plate (VPP) as imaged with a 10x (Nikon; MRL00102, 0.25 NA) or 20x objective (Olympus; XLUMPLFLN, 1.0 NA). Scale bar = 10 µm; yellow circle denotes region of radial average profile corresponding to plots in *B*. (*B*) Radially averaged profiles from individual point spread functions (*black*), as well as Gaussian fits to the outer donut (*red*) and null spots (*blue*). Full-width at half-maxima (FWHM) of the Gaussian fits are provided in the legend.

4.8.2 One-Color Fluorescence Emission Difference Microscopy

As a prelude to non-degenerate fluorescence emission difference microscopy (ND-FED), we endeavored to first achieve one-color degenerate (D-) FED. A stock solution of 200 nm dark red fluospheres (Thermofisher; F8807) was sonicated for a

period of 10 minutes in order to fragment aggregated clusters and ensure that single beads were imaged. A 5 µl aliquot was then diluted into a 1.495 ml sterile saline solution, which was vortexed for 30 sec at 2,000 RPM. A 10 µl aliquot of the dilute preparation was spread out over a glass slide and sandwiched with a glass coverslip and imaged using a 0.25 numerical aperture 10x objective (Nikon; MRL00102, 0.25 NA) and a 1050 nm ytterbium fiber laser excitation laser. Initial excitation images (TEM_{00}; TEM = transverse electromagnetic mode) entailed passing the fiber laser path through a spatial filter, whereas dark images (azimuthal; TEM_{01}) required that the spatially filtered Gaussian beam was transmitted through a radial polarization converter (Arcoptix). To alternate between excitation and dark imaging, the radial polarization converter was mounted to a linear translation stage (Thorlabs; PT1). Laser power was adjusted using a reflective neutral density filter for each excitation and dark image such that the highest intensity signal in the frame was on the cusp of saturation (counts ~ 30,000 – 32,000; **Figure 4.22(a-b)**). A processing script was developed to preform digital subtraction of excitation and dark image pairs at a range of subtractive γ factors (**Figure 4.22(c-d)**). Radially averaged line profiles of individual beads were extracted and Gaussian fitting to the profiles was used to determine the full-widths at half-maxima (FWHM) of the zeroed difference image as a function of γ factor (**Figure 4.22(e)**). Each image was recorded at a 0.05 V and a 0.10 V scan size. The smaller scan size is expected to yield more accurate estimates of super-resolution FWHM due to the smaller pixel size; however, the error bars were seen to be larger. A potential explanation for this unexpected observation is that slight image shifts or sample perturbations between excitation and dark imaging results in a relatively larger misregistration at the smaller scan size.

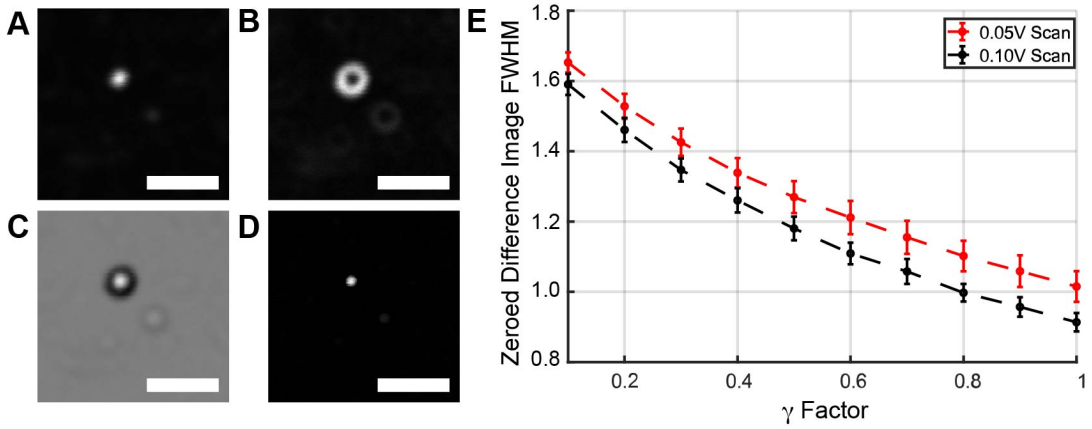

Figure 4.22: **Degenerate fluorescence emission difference microscopy.** (*A*) Excitation image of a 200 nm dark red fluosphere using a spatially filtered Gaussian 1050 nm beam (TEM_{00}). (*B*) A dark image of the same region in *A* using azimuthally polarized 1050 nm excitation (TEM_{01}). (*C*) A difference image after digital subtraction of *B* from *A*, using a subtractive γ weighting factor of 1.0. (*D*) The same image in *C*, except all negative pixel values have been coerced to zero. (*E*) Average full-width at half-maximum measurements of multiple beads as a function of gamma factor, using a 0.05 V (red) or a 1.0 V (black) scan size. All scale bars = 10 µm.

All super-resolution FWHM measurements were performed on the zeroed difference images, where negative over-subtracted pixel values were set to zero. Diffraction limited imaging at 1050 nm using this objective yields a theoretical maximum resolution of approximately ~2.56 µm. At a γ factor of 0.1 (FWHM ~ 1.6 µm), D-FED yields a ~1.6-fold resolution enhancement, and a >2.5-fold resolution enhancement using γ = 1.0 (FWHM ~1 µm). Notably, resolution measurements were not made on the raw difference image, as we can see a strong increase in negative pixel values with increasing γ values (**Figure 4.23(a-d)**) and corresponding radially averaged profiles exhibit growing side lobes as a result (**Figure 4.23(e)**).

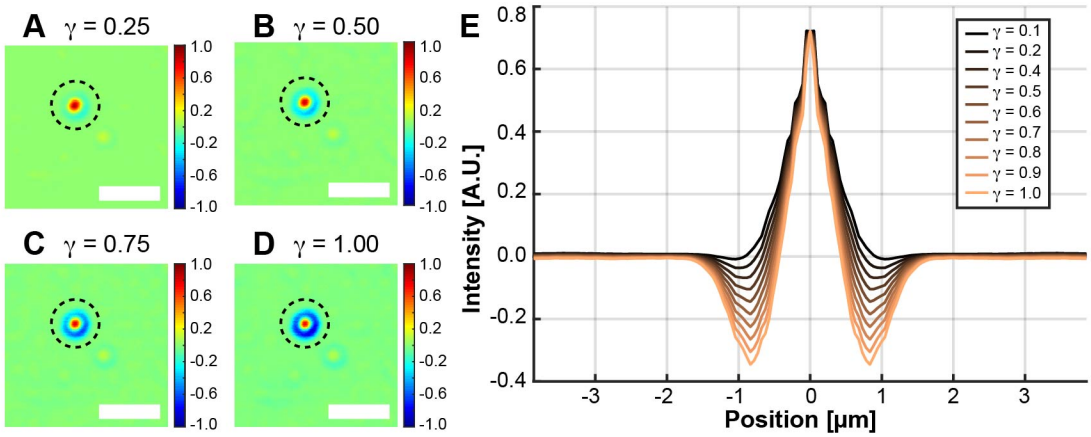

Figure 4.23: **Non-zeroed degenerate fluorescence emission difference microscopy images.** Difference images after digital subtraction using a γ weighting factor for the dark image of (*A*) 0.25, (*B*) 0.5, (*C*) 0.75, or (*D*) 1.0. (*E*) Radially averaged line profiles corresponding to the position of the dashed lines in (*A-D*) demonstrate increasing negative side lobes with increasing γ values. Scale bars = 10 μm.

4.8.3 Non-Degenerate Fluorescence Emission Difference Microscopy

To evaluate non-degenerate fluorescence emission difference (ND-FED) microscopy in comparison to degenerate (D-) FED microscopy, resolution enhancement using a two-color ytterbium fiber and diamond laser system was benchmarked relative to the independent use of either source independently. As an initial step, TEM_{00} (Gaussian) and TEM_{01} (azimuthal) profiles were recorded using both excitation sources with a 20x objective (**Figure 4.24(a)**). Multiple regions of interest of sub-diffraction limited diameter fluospheres (n > 10) were recorded and the highest quality point spread functions were used for analysis (fiber laser, n = 5; diamond laser, n = 7). In this case, high quality was defined as a well centered null spot, well-registered regions of interest across the excitation and dark images, and a lack motion artifacts in the higher resolution 0.03 V scans. These higher quality point spread functions were then averaged to construct representative point spread functions for the independent ytterbium fiber (I_1^2)

and diamond laser (I_2^2) modes to obtain critical measurements (**Figure 4.24(b-c)**). The excitation PSF at λ = 1050 nm full-width at half-maximum was smaller than the λ = 1240 nm PSF full-width at half-maximum, 682 nm versus 807 nm, as expected. Theoretical resolution limits are 640.5 nm and 756.4 nm for these two sources, respectively, which indicates that we are on the cusp of diffraction limited performance with our imaging system. The dark beam null spots were 549 nm at 1050 nm and 644 nm at 1240 nm excitation; which again reflects a greater resolution enhancement capability at shorter degenerate excitation wavelengths.

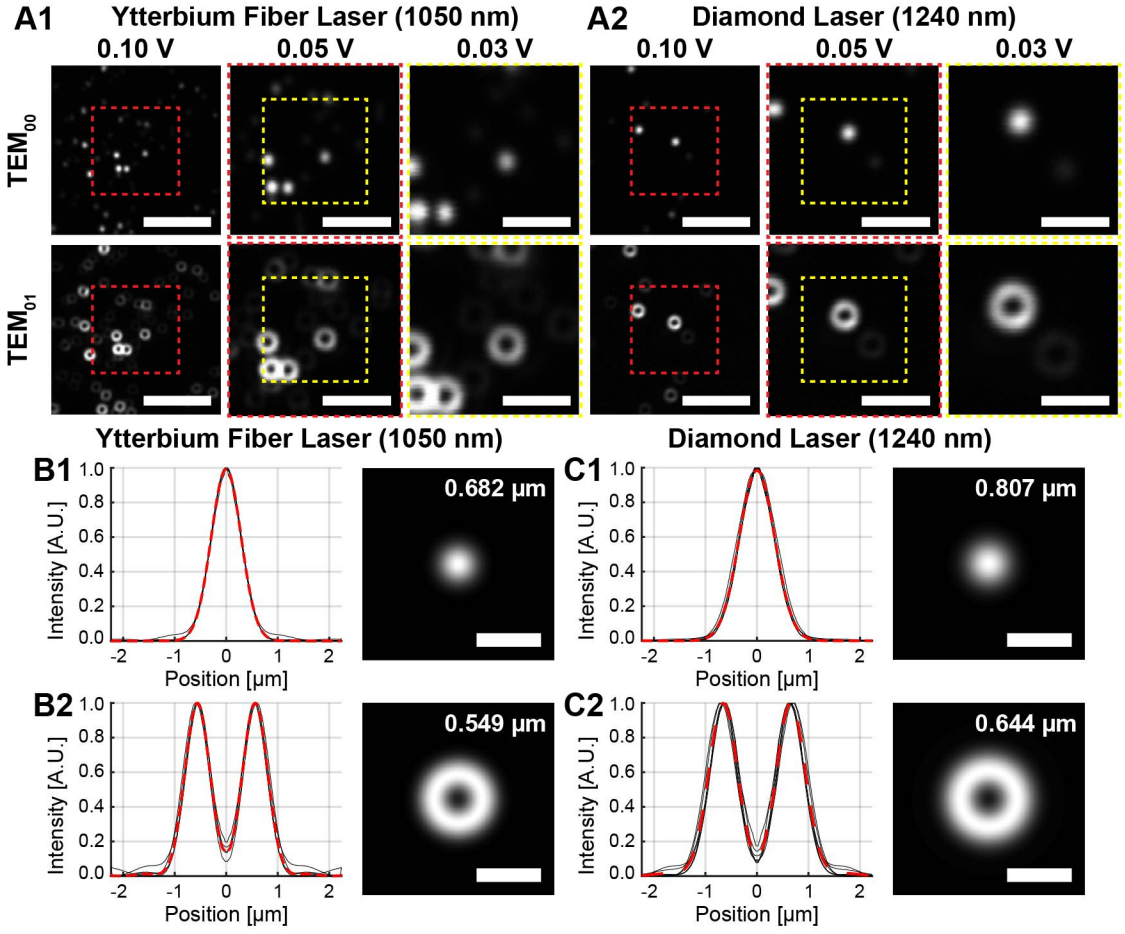

Figure 4.24: Continued on next page.

Figure 4.24: **Individual beam modes for degenerate- and non-degenerate fluorescence emission difference microscopy.** Representative regions of interest of sub-diffraction limited fluospheres at decreasing scan sizes with and without azimuthal polarization when excited by (*A1*) ytterbium fiber laser (1050 nm) or (*A2*) diamond laser (1240 nm). 0.10 V scale bar = 10 μm; 0.05 V scale bar = 5 μm; 0.03V scale bar = 3 μm. (*B1*) Individual radially averaged profiles (black) of ytterbium fiber laser TEM_{00} point spread functions (PSFs) are aggregated to construct a representative PSF profile (dashed red), shown in 2D on the right. The same process is repeated for (*B2*) ytterbium fiber laser TEM_{01} PSFs, (*C1*) diamond laser TEM_{00} PSFs, and (*C2*) diamond laser TEM_{01} PSFs. *B*-*C* Scale bars = 150 nm.

To compare ND-FED (1050 nm *and* 1240 nm) to D-FED (1050 nm *or* 1240 nm), mode mixing was performed as depicted in **Figure 4.25**. Briefly, D-FED excitation beam generation involves inherent, degenerate TEM_{00} matched mode combinations at a single wavelength, whereas ND-FED excitation beam generation requires non-degenerate TEM_{00} matched mode mixing at two discrete wavelengths. Meanwhile, D-FED dark beam generation requires inherent, degenerate TEM_{01} matched mode mixing at a single wavelength, whereas ND-FED dark beam generation requires non-degenerate *unmatched* TEM_{00} and TEM_{01} mode mixing at independent wavelengths. The ND-excitation beam FWHM was larger than the D-excitation beam at 1050 nm, but smaller than the D-excitation beam at 1240 nm. However, the ND-dark beam null spot (308 nm) was significantly smaller than either of the D-dark beam null spots (628 and 737 nm), as measured by their full-width at half-maxima.

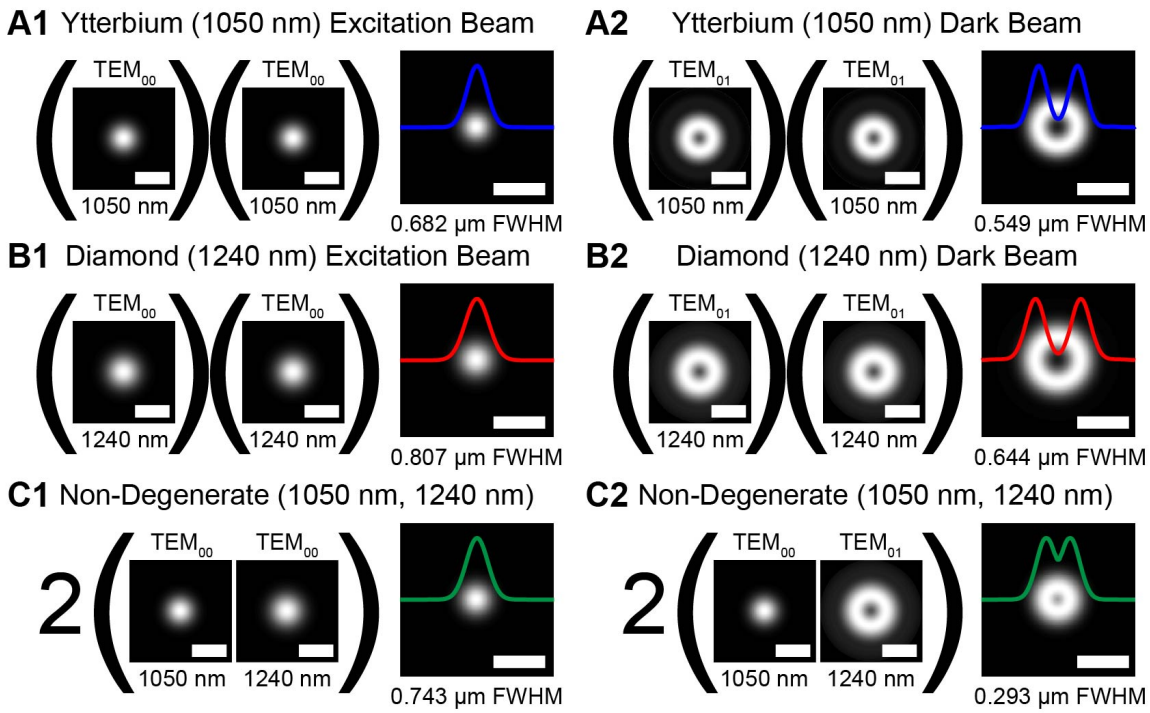

Figure 4.25: **Degenerate- and non-degenerate mode mixing for excitation and dark beam generation.** (*A*) Degenerate mode mixing with a ytterbium fiber laser (λ_{ex} = 1050 nm). (*A1*) Degenerate TEM_{00}(λ_{ex} = 1050 nm) matched mode mixing results in a 682 nm full-width at half-maximum (FWHM) excitation beam. (*A2*) Degenerate TEM_{01}(λ_{ex} = 1050 nm) matched mode mixing results in a 549 nm FWHM dark null spot. (*B*) Degenerate mode mixing with a diamond laser (λ_{ex} = 1240 nm). (*B1*) Degenerate TEM_{00}(λ_{ex} = 1240 nm) mode mixing results in a 807 nm FWHM excitation beam. (*B2*) Degenerate TEM_{01}(λ_{ex} = 1240 nm) mode mixing results in a 644 nm FWHM dark null spot. (*C*) Non-degenerate mode mixing with a ytterbium fiber laser (λ_{ex} = 1050 nm) and a diamond laser (λ_{ex} = 1240 nm). (*C1*) Non-degenerate TEM_{00}(λ_{ex} = 1050 nm, λ_{ex} = 1240 nm) matched mode mixing results in a 743 nm FWHM excitation image. (*C2*) Non-degenerate TEM_{00}(λ_{ex} = 1050 nm) and TEM_{01}(λ_{ex} = 1240 nm) unmatched mode mixing results in a 293 nm FWHM dark image. All scale bars = 1.5 μm.

ND- and D-FED imaging of different size objects with their corresponding excitation and dark beams corresponds to disparate resolution capabilities and levels of information loss (**Figure 4.26**). In this case, information loss is reported as the proportion of negative pixels after difference imaging within a 1024 x 1024 pixel frame

at a given subtractive γ factor. For a 200 nm object, we are able to resolve it at a γ factor of approximately ~0.95 using ND-FED microscopy, whereas D-FED is unable to resolve these objects at even a γ factor of 1.0 using either the ytterbium laser or the diamond laser. In fact, D-FED at 1050 nm isn't able to resolve objects less than ~350 nm at true size, and D-FED at 1240 nm isn't able to resolve objects less than ~400 nm in diameter at true size. ND-FED at a true size γ factor (i.e. the γ factor required to achieve difference image resolution at the object scale) results in less information loss than ytterbium fiber laser D-FED at comparable γ factors for 250 nm objects or greater. Meanwhile, information loss at a true size γ factor is mitigated by ND-FED relative to diamond laser D-FED for objects 400 nm or larger. Recall, that diamond laser D-FED is unable to provide sufficient difference imaging resolution for objects smaller than 400 nm, meaning that it is outrivaled by ND-FED within the resolution range where it finds any value.

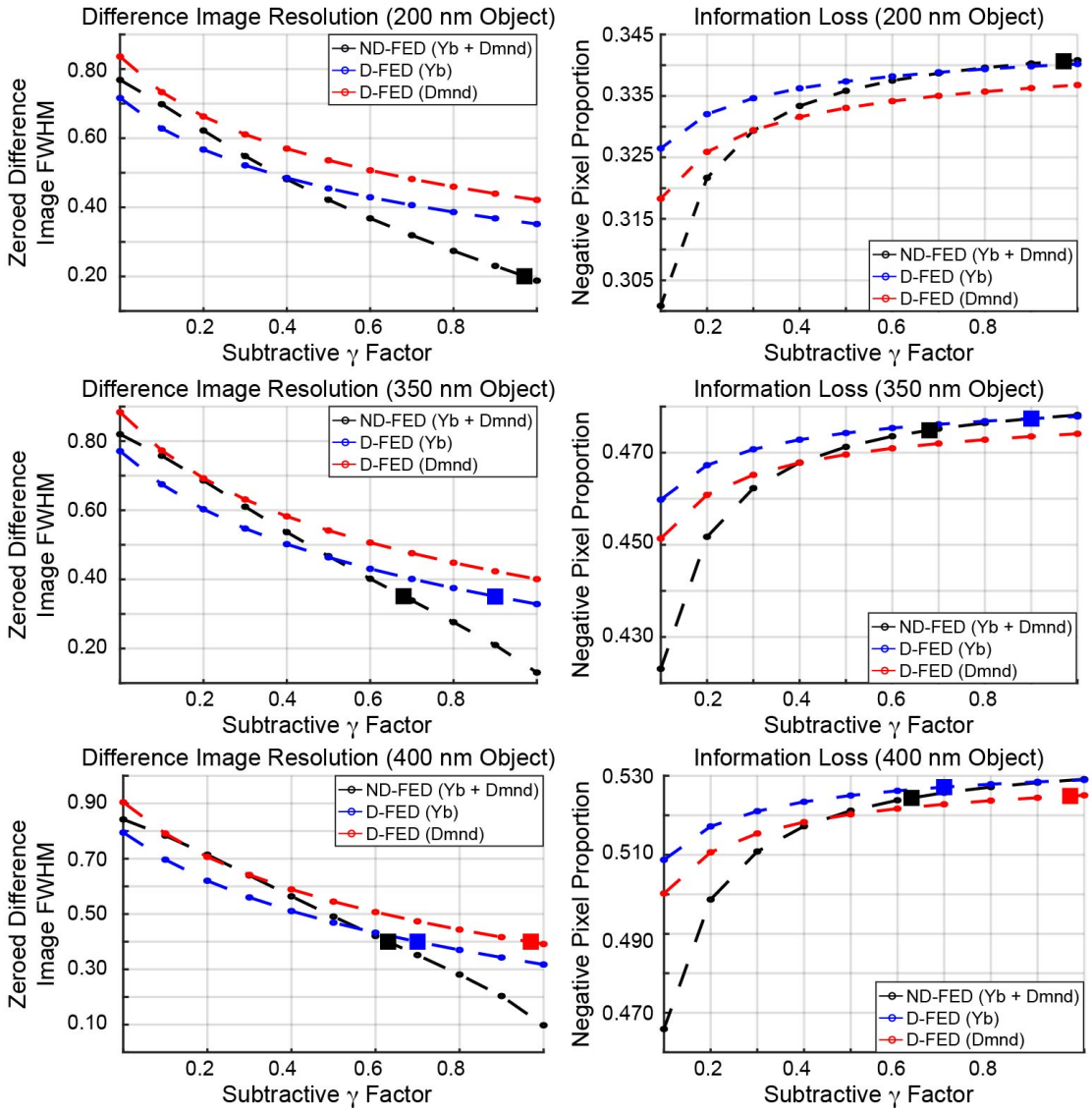

Figure 4.26: **Degenerate- (D-) versus non-degenerate (ND-) fluorescence emission difference (FED) microscopy.** D-FED versus ND-FED resolution (*left*) and information loss (*right*) as a function of subtractive γ factor for (*top*) 200 nm (*middle*) 350 nm and (*bottom*) 400 nm objects. Blue denotes D-FED at 1050 nm with an ytterbium fiber (Yb) laser, red denotes D-FED at 1240 nm with a diamond (Dmnd) laser, and black denotes ND-FED at a compound excitation wavelength of ~1137 nm. Filled squares indicate the requisite subtractive γ factor needed to achieve a difference imaging resolution matching the object size. The absence of a filled square indicates an imaging technique with insufficient resolution to visualize the given object size.

4.8.4 Non-Degenerate Fluorescence Emission Difference Microscope Design

The design and assembly of the super-resolution non-degenerate microscope underwent two iterations. A schematic of the first iteration can be seen below (**Figure 4.27**). At the time, only two excitation sources were available: a regenerative amplifier (RegA; λ_1 = 800 nm) and an optical parametric amplifier (OPA; λ_2 = 1100 - 1400 nm). Since the system only offered two outputs, and ND-FED requires three modes, two beam paths had to be split from the single OPA path. The RegA TEM_{00} line simply traversed the perimeter of the optical table before combining with the remaining modes at a dichroic mirror in a circular polarization. Meanwhile, the OPA path is first attenuated with an electro-optic modulator before being split into two arms. The first TEM_{00} arm goes through an optical delay line to enable temporal overlap with the RegA, then circularly polarized, and combined with all paths at the final dichroic mirror. The second OPA TEM_{01} arm splits off orthogonally to the first and passes through a delay line of its own. The beam is expanded with an initial telescope pair, linearly polarized with a glan-laser calcite polarizer, and then transmitted through the Arcoptix azimuthal polarization convertor. The beam is then shrunk back down to original size with a Keplerian telescope and reunited with the RegA at the dichroic mirror. The microscope can be seen in **Figure 4.27(b-c)** before and after flood damage.

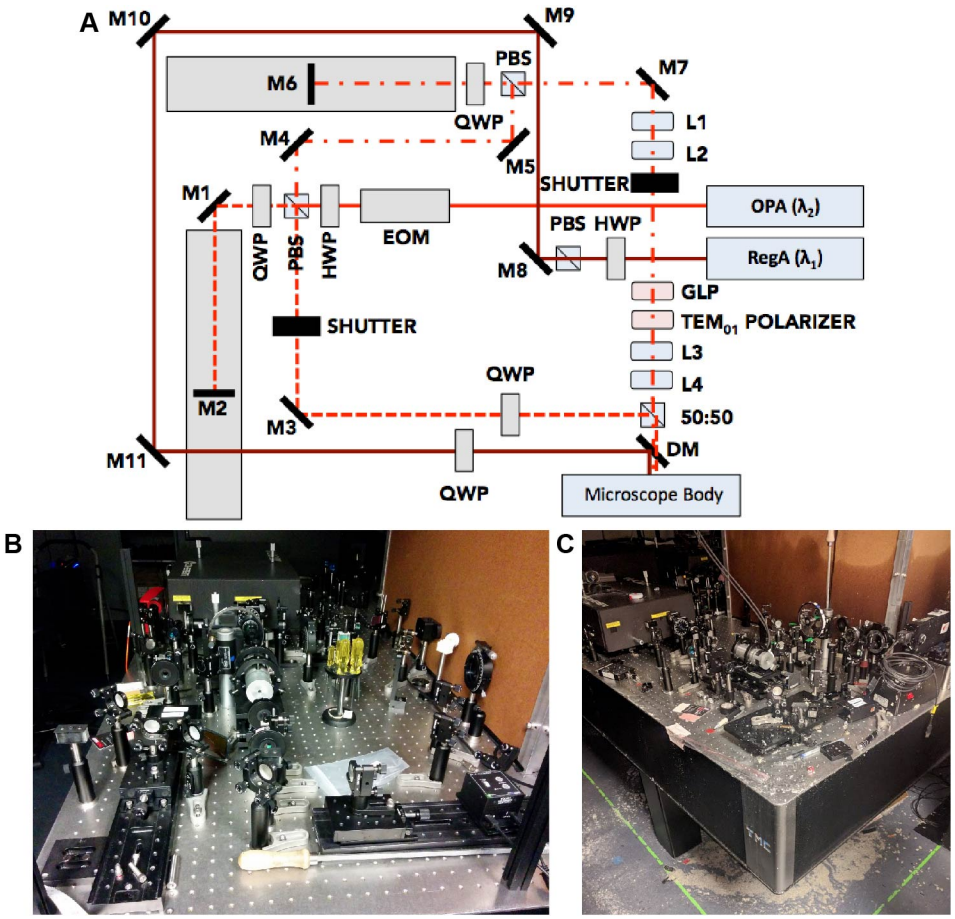

Figure 4.27: **Generation one of the non-degenerate fluorescence emission difference nanoscope.** (*A*) A schematic of the super-resolution system's first generation. OPA: optical parametric amplifier; RegA: regenerative amplifier; H/QWP: half-/quarter-waveplate; PBS: polarizing beamsplitter; M: mirror; EOM: electro-optic modulator; L: lens; GLP: glan-laser calcite polarizer; DM: dichroic mirror. Snapshots of the system (*B*) before and (*C*) after the lab flooded, which resulted in irreparable damage.

While the flood was devastating, it offered an opportunity to rebuild with the revamped non-collinear OPA (NOPA) system (**Figure 4.28**). This laser system initially consisted of a visible-infrared (VISIR) and a near-infrared (NIR) NOPA, containing three outputs in total. A refined version consisted of two VISIR NOPAs, which granted four outputs. Regardless only three of the four outputs were needed for non-degenerate

nanoscopy. While the overall microscope was similar to the pre-flood version, spatial filters were added to ensure the purity of the expected beam modes. Moreover, no individual paths needed to be split into two arms unlike its predecessor, meaning that we were able to use full output power from both lasers.

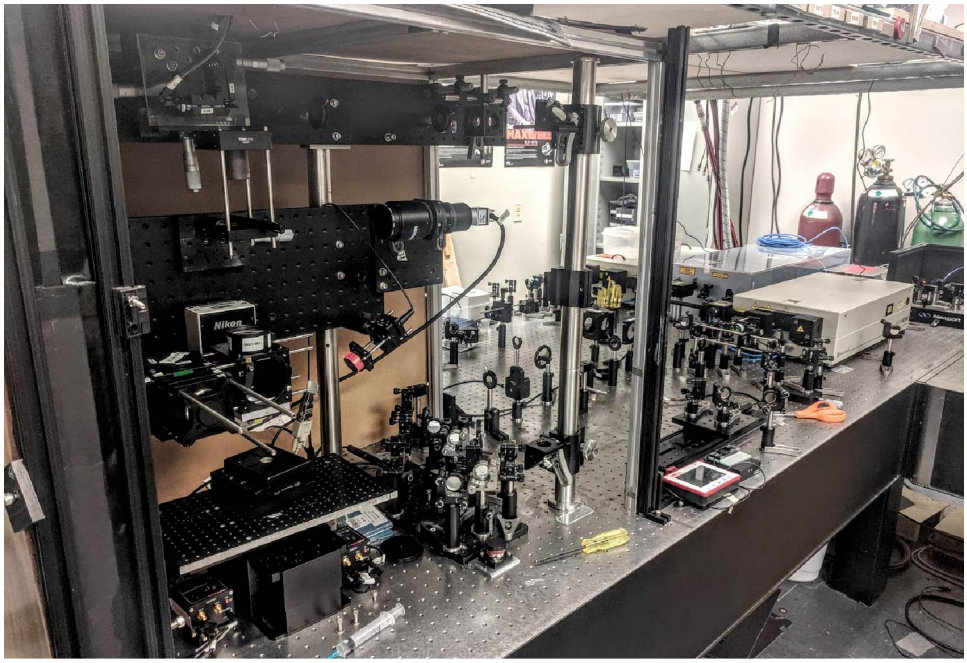

Figure 4.28: **Generation two of the non-degenerate fluorescence emission difference nanoscope.** Unlike its predecessor, generation two contained a laser output for each of the three arms of the super-resolution system.

4.9 Conclusion

The work herein represents the wide array of advantages granted by the construction of a two-color imaging system. Using synchronized excitation sources such as the Spirit-NOPAs or the ytterbium fiber and diamond laser system, we were able to demonstrate that two-color excitation has a myriad of photophysical advantages related to signal intensity and signal-to-background ratio, and that specialized non-degenerate implementations of the two-color system can yield significant resolution advantages.

Specifically, two-color non-degenerate (i.e. spatially and temporally overlapped two-color excitation) imaging with the ytterbium fiber laser and diamond laser is able to extend imaging depth relative to two-color degenerate (i.e. spatially overlapped two-color excitation) and one-color non-degenerate imaging by approximately ~20%. Through rigorous characterization of two-color, non-degenerate signal levels with a reflective objective, we were able to prove that not only do reflective objectives improve axial overlap to boost non-degenerate signal relative to refractive objectives, but that two color non-degenerate mixing ($\tau \sim 0$ fs) universally enhances multiphoton excitation relative to two-color degenerate excitation ($\tau > 0$ fs) for fluorophores with a non-degenerate cross section $\sigma_{\lambda_D}^{(2)} > 0$. We also provide evidence that in some cases, two-color non-degenerate signal exceeds one-color degenerate signal when $\lambda_D = \lambda_3$.

Finally, we distinguish that the primary advantage of two-color non-degenerate multiphoton excitation (i.e. $I_1^2 + I_2^2 + 2I_1I_2$) is an increase in signal intensity whereas non-degenerate multiphoton excitation alone (i.e. $2I_1I_2$) has a unique advantage in its inherent resolution benefits. Building off this premise, we establish the framework for a novel super-resolution imaging method termed non-degenerate fluorescence emission difference microscopy (ND-FED). We are able to demonstrate that ND-FED has substantial resolution benefits over degenerate (D-) FED, which is a strong function of the specific transverse electromagnetic (TEM) modes, excitation wavelengths, and subtractive γ factor. For instance, comparing D-FED and ND-FED using circular and vortex polarizations where λ_D = 1080 nm and two wavelengths are selected for ND-FED (λ_1 = 900 nm, λ_2 = 1350 nm) which compound at $\lambda_3 = \lambda_D$; ND-FED improves resolution by ~68 nm when γ = 0.535. We acknowledge that a broad limitation of FED is the ability to oversubtract structures and yield missing information, and demonstrate that ND-FED mitigates the extent of over-subtraction relative to FED for a given resolution scale.

Moreover, we provide guidance to researchers that circular and azimuthal polarizations are appropriate choices for ND-FED beam modes with respect to both resolution and information loss. In this same context, we show the nuanced subtleties of ND-FED, illustrating that reversing two-color excitation wavelengths between TEM_{00} and TEM_{01} poses distinct tradeoffs with respect to resolution enhancement and information loss for a given set of polarizations. In addition, we navigate perhaps the biggest complexity of FED, which is identifying an appropriate γ factor. We provide evidence to show that γ factor influences resolution scale, and needs to be increased for finer resolution, at the detriment of over-subtracting larger objects in the super-resolution difference image. Despite this shortcoming of FED, we are able to show that ND-FED γ selection is significantly more constant with respect to resolution scale than D-FED, limiting the negative consequences of this shortcoming for non-degenerate implementations. Finally, we are able to provide a guide to two-color wavelength pair selection for ND-FED for five specific fluorophores given their cross section profiles. Ultimately, we believe that we have rigorously characterized the benefits and criteria for ND-FED and, more broadly, two-color multiphoton microscopy. It is our hope that this will lay a strong foundation for future work and adoption of some of these techniques as the availability of synchronized, tunable lasers increases and this technology becomes more ubiquitous in academic and commercial laboratories.

Appendix I: Fluorophore Cross Section Determination

Please note, two- and three-photon cross section formulations are derived from equations established in Cheng et al. (2014) [118]. Any conclusions regarding these expressions and their units stem from theoretical foundations in their work. We begin with time-averaged fluorescence signal $\langle F^{(n)}(t)\rangle$, which is given by:

$$\langle F^{(n)}(t)\rangle = \frac{1}{n}\frac{g_p^{(n)}}{(f\tau)^{n-1}}\phi\eta\sigma_n C n_0 \frac{a_n (NA)^{2n-4}\langle P(t)\rangle^n}{8\pi^{3-n}\lambda^{2n-3}} \tag{I.1}$$

The definition and categorization (i.e. known or unknown) of each term is given below.

Known Constant Terms	
f	laser repetition rate [s^{-1}]
C	fluorophore concentration $\left[\left(\frac{mol}{L}\right)\left(\frac{6.022\times10^{23}}{mol}\right)\left(\frac{L}{1000cm^3}\right) = cm^{-3}\right]$
n_0	refractive index [unitless]
a_n	constant term [a_2 = 64; a_3 =28.1; a_4 = 18.3; unitless]
NA	numerical aperture
$\langle P(t)\rangle$	incident power $\left[W\frac{\lambda}{hc} = \frac{J}{s}\frac{m}{Js\frac{m}{s}} = \frac{photons}{s}\right]$
λ	wavelength [cm]
Unknown Variable Terms Attained Through Metrology	
$\langle F^{(n)}(t)\rangle$	Time-averaged fluorescence photon flux [photons/sec]
n	n^{th}-order excitation [unitless]
$g_p^{(n)}$	n^{th}-order temporal coherence of the excitation source [Gaussian temporal profile pules: $g_p^{(2)} = 0.664$, $g_p^{(3)} = 0.51$, $g_p^{(4)} = 0.415$; hyperbolic-secant-squared pulse: $g_p^{(2)} = 0.587$, $g_p^{(3)} = 0.413$, $g_p^{(4)} = 0.312$; unitless]
τ	pulse width [variable, s]
ϕ	system collection efficiency [unitless]
η	fluorescence quantum efficiency [unitless]
σ_n	n-photon absorption cross section [2P = $\frac{cm^4 s}{photons}$; 3P = $\frac{cm^6 s^2}{photons^2}$]

Table I.1: **Cross section equation terms.** Fluorophore cross section determination requires known constant terms as well as variables that must be measured directly.

Equation **I.1** can be used to derive two-, three-, and four-photon excitation in thick samples, and our primary metric of interest is the absorption cross section, σ_n, or the action cross section, $\eta\sigma_n$.

$$\eta\sigma_n = \frac{\langle F^{(n)}(t)\rangle (f\tau)^{n-1} 8\pi^{3-n}\lambda^{2n-3}}{g_p^{(n)} C n_0 a_n (NA)^{2n-4}\langle P(t)\rangle^n}\frac{n}{\phi} \tag{I.2}$$

For the sake of this research, we will limit ourselves to a two-photon and three-photon action cross section derivation. The two-photon action cross section, by definition exhibits a two-photon power dependence. Thus, we can fill in all necessary terms as needed.

$$\eta\sigma_2 = \frac{\langle F^{(2)}(t)\rangle (f\tau) 8\pi\lambda}{0.664 C n_0 64\langle P(t)\rangle^2}\frac{2}{\phi} \tag{I.3}$$

$$\eta\sigma_2 = \frac{\langle F^{(2)}(t)\rangle (f\tau)\lambda}{C n_0\langle P(t)\rangle^2}\frac{0.377\pi}{\phi} \tag{I.4}$$

It follows that the dimensions of two-photon action cross sections are $cm^4 \cdot s \cdot photon^{-1}$.

$$\eta\sigma_2 = \frac{photon \cdot s^{-1} \cdot s^{-1} \cdot s \cdot cm}{cm^{-3}(photon \cdot s^{-1})^2} = \frac{photon \cdot s^{-1} \cdot cm^4}{photon^2 \cdot s^{-2}} = \frac{cm^4 \cdot s}{photon} \tag{I.5}$$

We repeat this process for the three-photon action cross section, $\eta\sigma_n^3$.

$$\eta\sigma_3 = \frac{\langle F^{(3)}(t)\rangle (f\tau)^2 8\lambda^3}{0.51 C n_0 28.1 (NA)^2\langle P(t)\rangle^3}\frac{3}{\phi} \tag{I.6}$$

$$\eta\sigma_3 = \frac{\langle F^{(3)}(t)\rangle (f\tau)^2\lambda^3}{C n_0 (NA)^2\langle P(t)\rangle^3}\frac{1.674}{\phi} \tag{I.7}$$

The dimensions of the three-photon action cross section are then $cm^6 \cdot s^2 \cdot photon^{-2}$.

$$\eta\sigma_3 = \frac{photon \cdot s^{-1} \cdot s^{-2} \cdot s^2 \cdot cm^3}{cm^{-3} \cdot photon^3 \cdot s^{-3}} = \frac{cm^3 \cdot s^2}{cm^{-3} \cdot photon^2} = \frac{cm^6 \cdot s^2}{photon^2} \tag{I.8}$$

This unit comparison of the two- and three-photon action cross sections exposes a fundamental flaw of comparing relative fluorophore brightness. Since the underlying

units differ across the different excitation regimes, it is difficult to compare the brightness of shorter wavelength excitable dyes to fluorophores with cross sections further out in the near infrared that are far more likely to exhibit a three-photon power dependence.

Appendix II: Non-Degenerate Excitation Efficiency

The final expression for non-degenerate fluorescence emission difference (ND-FED) efficiency hinges on foundational work established in Sadegh et al. (2019) [197]. Note our final derived expression is unique from the one documented in this manuscript, which instead compares the ratio of ND fluorescence to D- fluorescence at matching excitation wavelengths, $\lambda_D = \lambda_3$. But please be aware that all initial equations and assumptions are taken directly from this work. We first establish that the combined signal from a two-color two-photon imaging system where both beams are of equal intensities and are temporally delayed by an offset τ is given by:

$$N_{ex}(\boldsymbol{r},t,\tau) = \tfrac{1}{2}\sigma_D^{(2)}(\lambda_1)C(\boldsymbol{r},t)I_1^2(\boldsymbol{r},t-\tau) + \tfrac{1}{2}\sigma_D^{(2)}(\lambda_2)C(\boldsymbol{r},t)I_2^2(\boldsymbol{r},t) + 2\sigma_{ND}^{(2)}(\lambda_1,\lambda_2)C(\boldsymbol{r},t)I_1(\boldsymbol{r},t-\tau)I_2(\boldsymbol{r},t) \quad \text{(II.1)}$$

If we next assume each of the two-color beams is a Gaussian pulse and use a paraxial approximation for their cross-sections, we are able to parse the spatial (S) and temporal (T) components of their profiles independently.

$$I_1(\boldsymbol{r},t,\tau) = S(\boldsymbol{r};\lambda_1)T(t-\tau;\lambda_1)$$
$$I_2(\boldsymbol{r},t,\tau) = S(\boldsymbol{r};\lambda_2)T(t-\tau;\lambda_2) \quad \text{(II.2)}$$

The spatial and temporal components can be furthered decomposed into:

$$T(t;\lambda) = I_0^{(\lambda)}\exp\left(\frac{-t^2}{2\Gamma_\lambda^2}\right) \quad \text{(II.3)}$$

$$S(\boldsymbol{r};\lambda) = \left[\frac{w_0(\lambda)}{w(z;\lambda)}\right]^2 \exp\left[-2\left(\frac{r}{w(z;\lambda)}\right)^2\right] \quad \text{(II.4)}$$

From hereon, we assume each pulse is transform-limited with a temporal standard deviation Γ_λ with an intensity $I_0^{(\lambda)}$. Gaussian optics tell us that:

$$w^2(z;\lambda) = w_0^2(\lambda)\left[1+\left(\frac{z}{z_0(\lambda)}\right)^2\right] \quad \text{(II.5)}$$

$$z_0(\lambda) = \frac{\pi w_0^2(\lambda)}{\lambda} \tag{II.6}$$

$$w_0(\lambda) = \frac{\lambda}{\pi NA} \tag{II.7}$$

Where $w_0(\lambda)$ is the wavelength-dependent beam waist, $z_0(\lambda)$ is the Rayleigh length (i.e. the distance across which the beam waist radius increases by a factor of $\sqrt{2}$), and NA is numerical aperture. We combine this information into expression II.1, again parsing the spatial and temporal components separately. It is important to note that we have also assumed that fluorophore distribution is spatially and temporally constant, allowing us to move the concentration term outside of the integrals.

$$\begin{aligned} N_{ex}(\boldsymbol{r}, t, \tau) = {} & \tfrac{1}{2}\sigma_D^{(2)}(\lambda_1) C T^2(t - \tau; \lambda_1) \int_V [S(\boldsymbol{r}; \lambda_1)]^2 \, dV \\ & + \tfrac{1}{2}\sigma_D^{(2)}(\lambda_2) C T^2(t; \lambda_2) \int_V [S(\boldsymbol{r}; \lambda_2)]^2 \, dV \\ & + 2\sigma_{ND}^{(2)}(\lambda_1, \lambda_2) C T(t - \tau, \lambda_1) T(t, \lambda_2) \int_V [S(\boldsymbol{r}; \lambda_1)][S(\boldsymbol{r}; \lambda_2)] \, dV \end{aligned} \tag{II.8}$$

The shading in the above expression denotes factors that we believe were omitted in Sadegh et al.'s publication. If we proceed under the assumption that the beam point spread functions are much smaller than the fluorescent target, and that the system NA is common to both paths, the multi-beam spatial term is given by:

$$\int_V [S(\boldsymbol{r}; \lambda_1)][S(\boldsymbol{r}; \lambda_2)] \, dV = \frac{\lambda_1^2 \, \lambda_2^2}{2\sqrt{2}\pi NA^4 \sqrt{\lambda_1^2 + \lambda_2^2}} \tag{II.9}$$

In the case where $\lambda_1 = \lambda_2$, this further simplifies to:

$$\int_V [S(\boldsymbol{r}; \lambda_1)][S(\boldsymbol{r}; \lambda_2)] \, dV = \frac{\lambda^3}{4\pi NA^4} \tag{II.10}$$

Xu and Webb et al. (1996) provide the basis for relating fluorescence photon flux to the number of excited molecules, where ϕ is collection efficiency and η is quantum yield [127].

$$F(t,\tau) = \phi\eta N_{ex}(t,\tau) \tag{II.11}$$

If we substitute Equations II.8 and II.9 into Equation II.11, we arrive at the following.

$$\begin{aligned} F(t,\tau) =& \frac{\phi\eta\sigma_D^{(2)}(\lambda_1)C\lambda_1^3T^2(t-\tau;\lambda_1)}{8\pi NA^4} \\ &+ \frac{\phi\eta\sigma_D^{(2)}(\lambda_2)C\lambda_2^3T^2(t;\lambda_2)}{8\pi NA^4} \\ &+ \frac{\phi\eta\sigma_{ND}^{(2)}(\lambda_1,\lambda_2)C\lambda_1^2\,\lambda_2^2T(t-\tau;\lambda_1)T(t;\lambda_2)}{\sqrt{2}\pi NA^4\sqrt{\lambda_1^2+\lambda_2^2}} \end{aligned} \tag{II.12}$$

We note, that our formulation of II.12 is identical to Sadegh et al., which indicates that we were correct in retaining the coefficients in II.8. Next, the ultimate measured photomultiplier tube signal is non-instantaneous, which means the time average of the previous equation must still be calculated. The time overlap integral is:

$$\langle T(t-\tau,\lambda_1)T(t;\lambda_2)\rangle = f\int_{-1/2f}^{1/2f} T(t'-\tau;\lambda_1)T(t';\lambda_2)dt' \tag{II.13}$$

Where f is the laser repetition rate. If the temporal bandwidth and delay time is much smaller than the temporal pulse separation and delay time is negligible, as is the case for high-repetition rate lasers, the integration can be given over an infinite period.

$$\int_{-1/2f}^{1/2f} T(t'-\tau;\lambda_1)T(t';\lambda_2)dt' \approx \int_{-\infty}^{\infty} T(t'-\tau;\lambda_1)T(t';\lambda_2)dt' \tag{II.14}$$

Substitution of Equation II.3 into II.14 shows that this time overlap integral is simply the convolution of two Gaussians, which can be computed using the convolution theorem:

$$h * g = \Im^{-1}\{\Im\{h\}\cdot\Im\{g\}\} \tag{II.15}$$

Thus:

$$\int_{-\infty}^{\infty} I_0^{(\lambda_1)} I_0^{(\lambda_2)} \exp\left(\frac{-(t-\tau)^2}{2\Gamma_{\lambda_1}^2}\right) \exp\left(\frac{-t'^2}{2\Gamma_{\lambda_2}^2}\right) dt = \sqrt{2\pi}\, I_0^{(\lambda_1)} I_0^{(\lambda_2)} \frac{\Gamma_{\lambda_1}\Gamma_{\lambda_2}}{\Gamma_x} \exp\left(\frac{-\tau^2}{2\Gamma_x}\right) \tag{II.16}$$

$\Gamma_x^2 = \Gamma_{\lambda_1}^2 + \Gamma_{\lambda_2}^2$ is the convolution's standard deviation. In the degenerate case where $\lambda_1 = \lambda_2$, $\Gamma_{\lambda_1}^2 = \Gamma_{\lambda_2}^2$, $I_0^{(\lambda_1)} = I_0^{(\lambda_2)}$, and $\tau = 0$, this expression simplifies to $\pi I_0^2 \Gamma$. Finally, we redefine fluorescence over time using time-averaged laser power (mW).

$$\langle P_\lambda \rangle = I_T E_\lambda f \tag{II.17}$$

In this case, I_T is the total photon flux at focus, and E_λ is simply photon energy $hc\lambda^{-1}$.

$$I_t = \int\int\int_{-\infty}^{\infty} I_\lambda(x,y,t)dxdydt = I_0^{(\lambda)} \sqrt{\pi^3/2}\Gamma_\lambda w_0^2 \tag{II.18}$$

If we use Equation II.7, we describe laser photon flux using the expression:

$$I_0^{(\lambda)} = \frac{2\lambda\langle P_\lambda \rangle}{\pi\sqrt{2\pi}\Gamma_\lambda chf w_0^2} = \frac{\sqrt{2\pi}NA^2\langle P_\lambda \rangle}{\Gamma_\lambda chf\lambda} \tag{II.19}$$

Therefore, our time averaged fluorescence by combining Equations II.12, II.16 (including the degenerate case), and II.19 is:

$$\begin{aligned}\langle F(t,\tau)\rangle = &\frac{\pi C \left\langle P_{\lambda_1}\right\rangle^2 \lambda_1 \phi\eta\sigma_D^{(2)}(\lambda_1)}{4f^2c^2h^2\Gamma_{\lambda_1}} \\ &+ \frac{\pi C \left\langle P_{\lambda_2}\right\rangle^2 \lambda_2 \phi\eta\sigma_D^{(2)}(\lambda_2)}{4f^2c^2h^2\Gamma_{\lambda_2}} \\ &+ \frac{2\sqrt{\pi}C\langle P_{\lambda_1}\rangle\langle P_{\lambda_2}\rangle\lambda_1\lambda_2\phi\eta\sigma_{ND}^{(2)}(\lambda_1,\lambda_2)}{f^2c^2h^2\Gamma_x\sqrt{\lambda_1^2+\lambda_2^2}} \exp\left(\frac{-\tau^2}{2\Gamma_x}\right)\end{aligned} \tag{II.20}$$

Again, we arrive at slightly different expressions from Sadegh et al., denoted in shading. The authors go on to derive an expression for non-degenerate two-photon excited fluorescence relative to degenerate fluorescence where λ_1 and λ_2 compound at $\lambda_3 = \lambda_D$.

$$\frac{\langle F(\tau=0)\rangle_{ND(\lambda_1,\lambda_2)}}{\langle F\rangle_{D(\lambda_D)}} \tag{II.21}$$

However, we are interested in comparing non-degenerate to degenerate signal contributions when performing non-degenerate two-photon imaging.

$$\frac{\langle F(\tau = 0)\rangle_{ND(\lambda_1,\lambda_2)}}{\langle F\rangle_{D(\lambda_1)} + \langle F\rangle_{D(\lambda_2)}} \tag{II.22}$$

If we assume that $\langle P_{\lambda_1}\rangle^2 = \langle P_{\lambda_2}\rangle^2$:

$$\langle F\rangle_{D(\lambda_1)} + \langle F\rangle_{D(\lambda_2)} = \frac{\pi C \langle P\rangle^2 \phi\eta}{4f^2c^2h^2}\left(\frac{\Gamma_{\lambda_2}\lambda_1\sigma_D^{(2)}(\lambda_1) + \Gamma_{\lambda_1}\lambda_2\sigma_D^{(2)}(\lambda_2)}{\Gamma_{\lambda_1}\Gamma_{\lambda_2}}\right) \tag{II.23}$$

Therefore:

$$\frac{\langle F(\tau = 0)\rangle_{ND(\lambda_1,\lambda_2)}}{\langle F\rangle_{D(\lambda_1)} + \langle F\rangle_{D(\lambda_2)}} = \frac{8\sqrt{\pi}\Gamma_{\lambda_1}\Gamma_{\lambda_2}\lambda_1\,\lambda_2\sigma_{ND}^{(2)}(\lambda_1,\lambda_2)}{\pi\Gamma_x\sqrt{\lambda_1^2+\lambda_2^2}\left(\Gamma_{\lambda_2}\lambda_1\sigma_D^{(2)}(\lambda_1) + \Gamma_{\lambda_1}\lambda_2\sigma_D^{(2)}(\lambda_2)\right)} \tag{II.24}$$

If we relied on the published formulation of II.20 to perform this calculation, we'd omit the shaded π factor in the denominator.

References

1. N. J. Sofroniew, D. Flickinger, J. King, and K. Svoboda, "A large field of view two-photon mesoscope with subcellular resolution for in vivo imaging.," Elife **5**, (2016).

2. M. B. Ahrens, M. B. Orger, D. N. Robson, J. M. Li, and P. J. Keller, "Whole-brain functional imaging at cellular resolution using light-sheet microscopy," Nat. Methods **10**(5), 413–420 (2013).

3. E. Tal, D. Oron, and Y. Silberberg, "Improved depth resolution in video-rate line-scanning multiphoton microscopy using temporal focusing," Opt. Lett. **30**(13), 1686 (2005).

4. Y. Shao, W. Qin, H. Liu, J. Qu, X. Peng, H. Niu, and B. Z. Gao, "Ultrafast, large-field multiphoton microscopy based on an acousto-optic deflector and a spatial light modulator," Opt. Lett. **37**(13), 2532 (2012).

5. T. A. Klar, S. Jakobs, M. Dyba, A. Egner, and S. W. Hell, "Fluorescence microscopy with diffraction resolution barrier broken by stimulated emission," Proc. Natl. Acad. Sci. U. S. A. **97**(15), 8206–8210 (2000).

6. W. Denk, J. H. Strickler, W. W. Webb, N. Series, and N. Apr, "Two-photon laser scanning fluorescence microscopy," Science (80-.). **248**(4951), 73–76 (2007).

7. J. N. D. Kerr and W. Denk, "Imaging in vivo: watching the brain in action," Nat. Rev. Neurosci. **9**(3), 195–205 (2008).

8. R. Yuste, F. Lanni, and A. Konnerth, *Imaging Neurons : A Laboratory Manual* (Cold Spring Harbor Laboratory Press, 2000).

9. K. E. Sorra and K. M. Harris, "Overview on the structure, composition, function, development, and plasticity of hippocampal dendritic spines," Hippocampus **10**(5), 501–511 (2000).

10. K. M. Harris, "Structure, development, and plasticity of dendritic spines," Curr. Opin. Neurobiol. **9**(3), 343–348 (1999).

11. K. M. Harris, F. E. Jensen, and B. Tsao, "Three-dimensional structure of dendritic spines and synapses in rat hippocampus (CA1) at postnatal day 15 and adult ages: implications for the maturation of synaptic physiology and long-term potentiation.," J. Neurosci. **12**(7), 2685–705 (1992).

12. K. M. Harris, J. C. Fiala, and L. Ostroff, "Structural changes at dendritic spine synapses during long-term potentiation," Philos. Trans. R. Soc. London. Ser. B

Biol. Sci. **358**(1432), 745–748 (2003).

13. E. A. Susaki, K. Tainaka, D. Perrin, F. Kishino, T. Tawara, T. M. Watanabe, C. Yokoyama, H. Onoe, M. Eguchi, S. Yamaguchi, T. Abe, H. Kiyonari, Y. Shimizu, A. Miyawaki, H. Yokota, and H. R. Ueda, "Whole-brain imaging with single-cell resolution using chemical cocktails and computational analysis," Cell **157**(3), 726–739 (2014).

14. J. L. Schroeder, M. Bakalar, T. J. Pohida, and R. S. Balaban, "Rapid overlapping-volume acquisition and reconstruction (ROVAR): automated 3D tiling for high-resolution, large field-of-view optical microscopy," J. Microsc. **243**(1), 103–110 (2011).

15. S. K. Chow, H. Hakozaki, D. L. Price, N. A. B. MacLean, T. J. Deerinck, J. C. Bouwer, M. E. Martone, S. T. Peltier, and M. H. Ellisman, "Automated microscopy system for mosaic acquisition and processing," J. Microsc. **222**(2), 76–84 (2006).

16. B. E. Losavio, Y. Liang, A. Santamaría-Pang, I. A. Kakadiaris, C. M. Colbert, and P. Saggau, "Live neuron morphology automatically reconstructed from multiphoton and confocal imaging data," J. Neurophysiol. **100**(4), 2422–2429 (2008).

17. K. Kanemaru, H. Sekiya, M. Xu, K. Satoh, N. Kitajima, K. Yoshida, Y. Okubo, T. Sasaki, S. Moritoh, H. Hasuwa, M. Mimura, K. Horikawa, K. Matsui, T. Nagai, M. Iino, and K. F. Tanaka, "In vivo visualization of subtle, transient, and local activity of astrocytes using an ultrasensitive Ca2+ indicator," Cell Rep. **8**(1), 311–318 (2014).

18. J. Sword, T. Masuda, D. Croom, and S. A. Kirov, "Evolution of neuronal and astroglial disruption in the peri-contusional cortex of mice revealed by in vivo two-photon imaging," Brain **136**(5), 1446–1461 (2013).

19. W. C. Lemon and P. J. Keller, "Live imaging of nervous system development and function using light-sheet microscopy," Mol. Reprod. Dev. **82**(7–8), 605–618 (2015).

20. T. Bast and J. Feldon, "Hippocampal modulation of sensorimotor processes," Prog. Neurobiol. **70**(4), 319–345 (2003).

21. J. Radulovic and N. C. Tronson, "Molecular specificity of multiple hippocampal processes governing fear extinction," Rev. Neurosci. **21**(1), 1–18 (2010).

22. J. L. C. Lee, B. J. Everitt, and K. L. Thomas, "Independent cellular processes for

hippocampal memory consolidation and reconsolidation.," Science **304**(5672), 839–43 (2004).

23. M. G. M. Velasco and M. J. Levene, "In vivo two-photon microscopy of the hippocampus using glass plugs," Biomed. Opt. Express **5**(6), 1700 (2014).

24. D. A. Dombeck, C. D. Harvey, L. Tian, L. L. Looger, and D. W. Tank, "Functional imaging of hippocampal place cells at cellular resolution during virtual navigation," Nat. Neurosci. **13**(11), 1433–1440 (2010).

25. T. A. Murray and M. J. Levene, "Singlet gradient index lens for deep in vivo multiphoton microscopy," J. Biomed. Opt. **17**(2), 021106 (2012).

26. W. Denk, K. R. Delaney, A. Gelperin, D. Kleinfeld, B. W. Strowbridge, D. W. Tank, and R. Yuste, "Anatomical and functional imaging of neurons using 2-photon laser scanning microscopy," J. Neurosci. Methods **54**(2), 151–162 (1994).

27. Z. F. Mainen, M. Maletic-Savatic, S. . Shi, Y. Hayashi, R. Malinow, and K. Svoboda, "Two-photon imaging in living brain slices," Methods **18**(2), 231–239 (1999).

28. P. C. Lauterber, "Image formation by induced local interactions : examples employing nuclear magnetic resonance," Nature **246**, 469 (1974).

29. N. Barrie Smith and A. Webb, *Introduction to Medical Imaging: Physics, Engineering and Clinical Applications* (Cambridge University Press, 2010).

30. S. Vreemann, A. Rodriguez-Ruiz, D. Nickel, L. Heacock, L. Appelman, J. Van Zelst, N. Karssemeijer, E. Weiland, M. Maas, L. Moy, B. Kiefer, and R. M. Mann, "Compressed sensing for breast MRI: Resolving the trade-off between spatial and temporal resolution," Invest. Radiol. **52**(10), 574–582 (2017).

31. L. M. Hamberg, G. J. Hunter, E. F. Halpern, B. Hoop, G. S. Gazelle, and G. L. Wolf, "Quantitative high-resolution measurement of cerebrovascular physiology with slip-ring CT.," AJNR. Am. J. Neuroradiol. **17**(4), 639–50 (1996).

32. L. Li, L. Zhu, C. Ma, L. Lin, J. Yao, L. Wang, K. Maslov, R. Zhang, W. Chen, J. Shi, and L. V. Wang, "Single-impulse panoramic photoacoustic computed tomography of small-animal whole-body dynamics at high spatiotemporal resolution," Nat. Biomed. Eng. **1**(5), 0071 (2017).

33. I. Nasrallah and J. Dubroff, "An overview of PET neuroimaging," Semin. Nucl. Med. **43**(6), 449–461 (2013).

34. T. Skotland, "Molecular imaging: challenges of bringing imaging of intracellular

targets into common clinical use," Contrast Media Mol. Imaging **7**(1), 1–6 (2012).

35. C. Errico, J. Pierre, S. Pezet, Y. Desailly, Z. Lenkei, O. Couture, and M. Tanter, "Ultrafast ultrasound localization microscopy for deep super-resolution vascular imaging," Nature **527**(7579), 499–502 (2015).

36. J. C. Fiala and K. M. Harris, *Dendrites: Dendrite Structure*, 1st ed. (Oxford University Press, 1999).

37. A. Despopoulos and S. Silbernagl, *Color Atlas of Physiology*, 6th ed. (Thieme, 2003).

38. B. R. Masters, P. T. So, and E. Gratton, "Multiphoton excitation fluorescence microscopy and spectroscopy of in vivo human skin," Biophys. J. **72**(6), 2405–2412 (1997).

39. K. P. Quinn, G. V. Sridharan, R. S. Hayden, D. L. Kaplan, K. Lee, and I. Georgakoudi, "Quantitative metabolic imaging using endogenous fluorescence to detect stem cell differentiation," Sci. Rep. **3**(1), 3432 (2013).

40. C. M. Rovainen, T. A. Woolsey, N. C. Blocher, D. B. Wang, and O. F. Robinson, "Blood flow in single surface arterioles and venules on the mouse somatosensory cortex measured with videomicroscopy, fluorescent dextrans, nonoccluding fluorescent beads, and computer-assisted image analysis.," J. Cereb. Blood Flow Metab. **13**(3), 359–71 (1993).

41. D. Kleinfeld, P. P. Mitra, F. Helmchen, and W. Denk, "Fluctuations and stimulus-induced changes in blood flow observed in individual capillaries in layers 2 through 4 of rat neocortex.," Proc. Natl. Acad. Sci. U. S. A. **95**(26), 15741–6 (1998).

42. W. G. Sheridan, R. H. Lowndes, and H. L. Young, "Intraoperative tissue oximetry in the human gastrointestinal tract," Am. J. Surg. **159**(3), 314–319 (1990).

43. A. D. Estrada, "High-resolution measurement of dissolved oxygen concentration in vivo using two-photon microscopy," The University of Texas at Austin (2011).

44. J. R. Lakowicz, *Principles of Fluorescence Spectroscopy*, Third Edition (Springer, 2013).

45. O. S. Finikova, A. Y. Lebedev, A. Aprelev, T. Troxler, F. Gao, C. Garnacho, S. Muro, R. M. Hochstrasser, and S. A. Vinogradov, "Oxygen microscopy by two-photon-excited phosphorescence," ChemPhysChem **9**(12), 1673–1679 (2008).

46. D. R. Miller, J. W. Jarrett, A. M. Hassan, and A. K. Dunn, "Deep tissue imaging

with multiphoton fluorescence microscopy," Curr. Opin. Biomed. Eng. **4**, 32–39 (2017).

47. L. L. Looger and O. Griesbeck, "Genetically encoded neural activity indicators," Curr. Opin. Neurobiol. **22**(1), 18–23 (2012).

48. B. L. Sabatini, T. G. Oertner, and K. Svoboda, "The life cycle of Ca2+ ions in dendritic spines," Neuron **33**(3), 439–452 (2002).

49. L. Tian, S. A. Hires, T. Mao, D. Huber, M. E. Chiappe, S. H. Chalasani, L. Petreanu, J. Akerboom, S. A. McKinney, E. R. Schreiter, C. I. Bargmann, V. Jayaraman, K. Svoboda, and L. L. Looger, "Imaging neural activity in worms, flies and mice with improved GCaMP calcium indicators," Nat. Methods **6**(12), 875–881 (2009).

50. J. Akerboom, T.-W. Chen, T. J. Wardill, L. Tian, J. S. Marvin, S. Mutlu, N. C. Calderón, F. Esposti, B. G. Borghuis, X. R. Sun, A. Gordus, M. B. Orger, R. Portugues, F. Engert, J. J. Macklin, A. Filosa, A. Aggarwal, R. A. Kerr, R. Takagi, S. Kracun, E. Shigetomi, B. S. Khakh, H. Baier, L. Lagnado, S. S.-H. Wang, C. I. Bargmann, B. E. Kimmel, V. Jayaraman, K. Svoboda, D. S. Kim, E. R. Schreiter, and L. L. Looger, "Optimization of a GCaMP calcium indicator for neural activity imaging.," J. Neurosci. **32**(40), 13819–40 (2012).

51. J. Nakai, M. Ohkura, and K. Imoto, "A high signal-to-noise Ca2+ probe composed of a single green fluorescent protein," Nat. Biotechnol. **19**(2), 137–141 (2001).

52. T.-W. Chen, T. J. Wardill, Y. Sun, S. R. Pulver, S. L. Renninger, A. Baohan, E. R. Schreiter, R. A. Kerr, M. B. Orger, V. Jayaraman, L. L. Looger, K. Svoboda, and D. S. Kim, "Ultrasensitive fluorescent proteins for imaging neuronal activity," Nature **499**(7458), 295–300 (2013).

53. D. G. Ouzounov, T. Wang, M. Wang, D. D. Feng, N. G. Horton, J. C. Cruz-Hernández, Y.-T. Cheng, J. Reimer, A. S. Tolias, N. Nishimura, and C. Xu, "In vivo three-photon imaging of activity of GCaMP6-labeled neurons deep in intact mouse brain," Nat. Methods **14**(4), 388–390 (2017).

54. J. Frangioni, "In vivo near-infrared fluorescence imaging," Curr. Opin. Chem. Biol. **7**(5), 626–634 (2003).

55. K. Lee, S. Choi, C. Yang, H.-C. Wu, and J. Yu, "Autofluorescence generation and elimination: a lesson from glutaraldehyde," Chem. Commun. **49**(29), 3028 (2013).

56. N. G. Horton, K. Wang, D. Kobat, C. G. Clark, F. W. Wise, C. B. Schaffer, and C. Xu, "In vivo three-photon microscopy of subcortical structures within an intact

mouse brain," Nat. Photonics **7**(3), 205–209 (2013).

57. M. Wang, C. Wu, D. Sinefeld, B. Li, F. Xia, and C. Xu, "Comparing the effective attenuation lengths for long wavelength in vivo imaging of the mouse brain," Biomed. Opt. Express **9**(8), 3534 (2018).

58. F. Helmchen and W. Denk, "Deep tissue two-photon microscopy," Nat. Methods **2**(12), 932–940 (2005).

59. D. Fu, T. Ye, T. E. Matthews, G. Yurtsever, and W. S. Warren, "Two-color, two-photon, and excited-state absorption microscopy," J. Biomed. Opt. **12**(5), 054004 (2007).

60. M.-H. Yang, M. Abashin, P. A. Saisan, P. Tian, C. G. L. Ferri, A. Devor, and Y. Fainman, "Non-degenerate 2-photon excitation in scattering medium for fluorescence microscopy," Opt. Express **24**(26), 30173 (2016).

61. S. Sadegh, M.-H. Yang, C. G. L. Ferri, M. Thunemann, P. A. Saisan, Z. Wei, E. A. Rodriguez, S. R. Adams, K. Kiliç, D. A. Boas, S. Sakadžić, A. Devor, Y. Fainman, S. Sakadžić, A. Devor, A. Devor, A. Devor, A. Devor, Y. Fainman, and Y. Fainman, "Efficient non-degenerate two-photon excitation for fluorescence microscopy," Opt. Express **27**(20), 28022 (2019).

62. M.-H. Yang, M. Abashin, P. A. Saisan, A. Devor, and Y. Fainman, "Non-degenerate multiphoton microscopy for deep brain imaging," in *Optics and the Brain* (Optical Society of America, 2015), p. BrW3B.6.

63. C. Stringari, L. Abdeladim, G. Malkinson, P. Mahou, X. Solinas, I. Lamarre, S. Brizion, J.-B. Galey, W. Supatto, R. Legouis, A.-M. Pena, and E. Beaurepaire, "Multicolor two-photon imaging of endogenous fluorophores in living tissues by wavelength mixing," Sci. Rep. **7**(1), 3792 (2017).

64. D. Kobat, G. Zhu, and C. Xu, "Background reduction with two-color two-beam multiphoton excitation," in *Biomedical Optics* (OSA, 2008), p. BMF6.

65. N. Ji, J. Freeman, and S. L. Smith, "Technologies for imaging neural activity in large volumes," Nat. Neurosci. **19**(9), 1154–1164 (2016).

66. K. H. Kim, C. Buehler, and P. T. C. So, "High-speed, two-photon scanning microscope," Appl. Opt. **38**(28), 6004 (1999).

67. N. Ji, H. Shroff, H. Zhong, and E. Betzig, "Advances in the speed and resolution of light microscopy," Curr. Opin. Neurobiol. **18**(6), 605–616 (2008).

68. W. Zheng, Y. Wu, P. Winter, R. Fischer, D. D. Nogare, A. Hong, C. McCormick,

R. Christensen, W. P. Dempsey, D. B. Arnold, J. Zimmerberg, A. Chitnis, J. Sellers, C. Waterman, and H. Shroff, "Adaptive optics improves multiphoton super-resolution imaging," Nat. Methods **14**(9), 869–872 (2017).

69. H. MacMahon, C. J. Vyborny, C. E. Metz, K. Doi, V. Sabeti, and S. L. Solomon, "Digital radiography of subtle pulmonary abnormalities: an ROC study of the effect of pixel size on observer performance.," Radiology **158**(1), 21–26 (2014).

70. E. H. Stelzer, "Contrast, resolution, pixelation, dynamic range and signal-to-noise ratio: fundamental limits to resolution in fluorescence light microscopy," J. Microsc. **189**(1), 15–24 (1998).

71. D. R. Miller, J. W. Jarrett, A. M. Hassan, and A. K. Dunn, "Deep tissue imaging with multiphoton fluorescence microscopy," Curr. Opin. Biomed. Eng. **4**, 32–39 (2017).

72. P. J. Drew, A. Y. Shih, J. D. Driscoll, P. M. Knutsen, P. Blinder, D. Davalos, K. Akassoglou, P. S. Tsai, and D. Kleinfeld, "Chronic optical access through a polished and reinforced thinned skull," Nat. Methods **7**(12), 981–984 (2010).

73. A. Y. Shih, C. Mateo, P. J. Drew, P. S. Tsai, and D. Kleinfeld, "A polished and reinforced thinned-skull window for long-term imaging of the mouse brain.," J. Vis. Exp. (61), (2012).

74. A. Holtmaat, T. Bonhoeffer, D. K. Chow, J. Chuckowree, V. De Paola, S. B. Hofer, M. Hübener, T. Keck, G. Knott, W.-C. A. Lee, R. Mostany, T. D. Mrsic-Flogel, E. Nedivi, C. Portera-Cailliau, K. Svoboda, J. T. Trachtenberg, and L. Wilbrecht, "Long-term, high-resolution imaging in the mouse neocortex through a chronic cranial window," Nat. Protoc. **4**(8), 1128–1144 (2009).

75. C. Heo, H. Park, Y.-T. Kim, E. Baeg, Y. H. Kim, S.-G. Kim, and M. Suh, "A soft, transparent, freely accessible cranial window for chronic imaging and electrophysiology," Sci. Rep. **6**(1), 27818 (2016).

76. T. H. Chia and M. J. Levene, "Microprisms for in vivo multilayer cortical imaging," J. Neurophysiol. **102**(2), 1310–1314 (2009).

77. M. Andermann, N. Gilfoy, G. Goldey, and R. Sachdev, "Chronic cellular imaging of entire cortical columns in awake mice using microprisms," Elsevier (n.d.).

78. J. C. Jung, A. D. Mehta, E. Aksay, R. Stepnoski, and M. J. Schnitzer, "In vivo mammalian brain imaging using one- and two-photon fluorescence microendoscopy," J. Neurophysiol. **92**(5), 3121–3133 (2004).

79. M. J. Levene, D. A. Dombeck, R. M. Williams, J. Skoch, G. A. Hickey, K. A.

Kasischke, R. P. Molloy, M. Ingelsson, E. A. Stern, J. Klucken, B. J. Bacskai, W. R. Zipfel, B. T. Hyman, and W. W. Webb, "In vivo multiphoton microscopy of deep tissue with gradient index lenses," in A. Periasamy and P. T. C. So, eds. (International Society for Optics and Photonics, 2004), **5323**, p. 291.

80. D. Kobat, N. G. Horton, and C. Xu, "In vivo two-photon microscopy to 1.6-mm depth in mouse cortex," J. Biomed. Opt. **16**(10), 106014 (2011).

81. D. R. Miller, A. M. Hassan, J. W. Jarrett, F. A. Medina, E. P. Perillo, K. Hagan, S. M. Shams Kazmi, T. A. Clark, C. T. Sullender, T. A. Jones, B. V. Zemelman, and A. K. Dunn, "In vivo multiphoton imaging of a diverse array of fluorophores to investigate deep neurovascular structure," Biomed. Opt. Express **8**(7), 3470 (2017).

82. D. G. Ouzounov, T. Wang, M. Wang, D. D. Feng, N. G. Horton, J. C. Cruz-Hernández, Y.-T. Cheng, J. Reimer, A. S. Tolias, N. Nishimura, and C. Xu, "In vivo three-photon imaging of activity of GCaMP6-labeled neurons deep in intact mouse brain," Nat. Methods **14**(4), 388–390 (2017).

83. T. Wang, D. G. Ouzounov, M. Wang, and C. Xu, "Quantitative comparison of two-photon and three-photon activity imaging of GCaMP6s-labeled neurons in vivo in the mouse brain," in *Optics InfoBase Conference Papers* (OSA, 2017), **Part F76-B**, p. BrM4B.4.

84. N. G. Horton, K. Wang, D. Kobat, C. G. Clark, F. W. Wise, C. B. Schaffer, and C. Xu, "In vivo three-photon microscopy of subcortical structures within an intact mouse brain," Nat. Photonics **7**(3), 205–209 (2013).

85. RP Photonics Encyclopedia, "Time–bandwidth Product," https://www.rp-photonics.com/time_bandwidth_product.html.

86. H. M. Kim and B. R. Cho, "Small-molecule two-photon probes for bioimaging applications," Chem. Rev. **115**(11), 5014–5055 (2015).

87. U. Resch-Genger, M. Grabolle, S. Cavaliere-Jaricot, R. Nitschke, and T. Nann, "Quantum dots versus organic dyes as fluorescent labels," Nat. Methods **5**(9), 763–775 (2008).

88. N. C. Shaner, P. A. Steinbach, and R. Y. Tsien, "A guide to choosing fluorescent proteins," Nat. Methods **2**(12), 905–909 (2005).

89. D. Shcherbo, C. S. Murphy, G. V. Ermakova, E. A. Solovieva, T. V. Chepurnykh, A. S. Shcheglov, V. V. Verkhusha, V. Z. Pletnev, K. L. Hazelwood, P. M. Roche, S. Lukyanov, A. G. Zaraisky, M. W. Davidson, and D. M. Chudakov, "Far-red

fluorescent tags for protein imaging in living tissues," Biochem. J. **418**(3), 567–574 (2009).

90. R. Bianchi, A. Teijeira, S. T. Proulx, A. J. Christiansen, C. D. Seidel, T. Rülicke, T. Mäkinen, R. Hägerling, C. Halin, and M. Detmar, "A transgenic Prox1-Cre-tdTomato reporter mouse for lymphatic vessel research," PLoS One **10**(4), e0122976 (2015).

91. S. J. Kuhlman and Z. J. Huang, "High-resolution labeling and functional manipulation of specific neuron types in mouse brain by Cre-activated viral gene expression," PLoS One **3**(4), e2005 (2008).

92. S. E. Schindler, J. G. McCall, P. Yan, K. L. Hyrc, M. Li, C. L. Tucker, J. M. Lee, M. R. Bruchas, and M. I. Diamond, "Photo-activatable Cre recombinase regulates gene expression in vivo," Sci. Rep. **5**, (2015).

93. Q. Chen, Z. Zeng, and Z. Hu, "Optogenetics in neuroscience: What we gain from studies in mammals," Neurosci. Bull. **28**(4), 423–434 (2012).

94. S. Hammad, A. Othman, C. Meyer, A. Telfah, J. Lambert, B. Dewidar, J. Werle, Z. C. Nwosu, A. Mahli, C. Dormann, Y. Gao, K. Gould, M. Han, X. Yuan, M. Gogiashvili, R. Hergenröder, C. Hellerbrand, M. Thomas, M. P. Ebert, S. Amasheh, J. G. Hengstler, and S. Dooley, "Confounding influence of tamoxifen in mouse models of Cre recombinase-induced gene activity or modulation," Arch. Toxicol. **92**(8), 2549–2561 (2018).

95. D. R. Larson, "Water-soluble quantum dots for multiphoton fluorescence imaging in vivo," Science (80-.). **300**(5624), 1434–1436 (2003).

96. I. L. Medintz, H. T. Uyeda, E. R. Goldman, and H. Mattoussi, "Quantum dot bioconjugates for imaging, labelling and sensing," Nat. Mater. **4**(6), 435–446 (2005).

97. C. Wu and D. T. Chiu, "Highly fluorescent semiconducting polymer dots for biology and medicine," Angew. Chemie Int. Ed. **52**(11), 3086–3109 (2013).

98. C. Wu, C. Szymanski, Z. Cain, and J. McNeill, "Conjugated Polymer Dots for Multiphoton Fluorescence Imaging," J. Am. Chem. Soc. **129**(43), 12904–12905 (2007).

99. J. Pecher, J. Huber, M. Winterhalder, A. Zumbusch, and S. Mecking, "Tailor-made conjugated polymer nanoparticles for multicolor and multiphoton cell imaging," Biomacromolecules **11**(10), 2776–2780 (2010).

100. C. Xu and W. R. Zipfel, "Multiphoton excitation of fluorescent probes," Cold

Spring Harb. Protoc. **2015**(3), 250–258 (2015).

101. M. Drobizhev, N. S. Makarov, S. E. Tillo, T. E. Hughes, and A. Rebane, "Two-photon absorption properties of fluorescent proteins," Nat. Methods **8**(5), 393–399 (2011).

102. J. Mütze, V. Iyer, J. J. Macklin, J. Colonell, B. Karsh, Z. Petrasek, P. Schwille, L. L. Looger, L. D. Lavis, and T. D. Harris, "Excitation spectra and brightness optimization of two-photon excited probes," (2012).

103. M. Kauert, P. C. Stoller, M. Frenz, and J. Ri?ka, "Absolute measurement of molecular two-photon absorption cross-sections using a fluorescence saturation technique," Opt. Express **14**(18), 8434 (2006).

104. D. A. Oulianov, I. V. Tomov, A. S. Dvornikov, and P. M. Rentzepis, "Observations on the measurement of two-photon absorption cross-section," Opt. Commun. **191**(3–6), 235–243 (2001).

105. P. Tian and W. S. Warren, "Ultrafast measurement of two-photon absorption by loss modulation," Opt. Lett. **27**(18), 1634 (2002).

106. P. Sengupta, J. Balaji, S. Banerjee, R. Philip, G. Ravindra Kumar, and S. Maiti, "Sensitive measurement of absolute two-photon absorption cross sections," J. Chem. Phys. **112**(21), 9201–9205 (2000).

107. R. Kapoor, C. S. Friend, and A. Patra, "Two-photon-excited absolute emission cross-sectional measurements calibrated with a luminance meter," J. Opt. Soc. Am. B **20**(7), 1550 (2003).

108. D. Siegfried, U. Resch-Genger, and O. S. Wolfbeis, *Near-Infrared Dyes for High Technology Applications* (Springer Netherlands, 2012).

109. S. A. Soper and Q. L. Mattingly, "Steady-state and picosecond laser fluorescence studies of nonradiative pathways in tricarbocyanine dyes: Implications to the design of near-IR fluorochromes with high fluorescence efficiencies," J. Am. Chem. SOC **116**, 3144–3152 (1994).

110. S. A. Soper, H. L. Nutter, R. A. Keller, L. M. Davis, and E. B. Shera, "The photophysical constants of several fluorescent dyes pertaining to ultrasensitive fluorescence spectroscopy," Photochem. Photobiol. **57**(s1), 972–977 (1993).

111. A. M. Derfus, W. C. W. Chan, and S. N. Bhatia, "Probing the cytotoxicity of semiconductor quantum dots," Nano Lett. **4**(1), 11–18 (2004).

112. C. Kirchner, T. Liedl, S. Kudera, T. Pellegrino, A. M. Javier, H. E. Gaub, S.

Stölzle, N. Fertig, and W. J. Parak, "Cytotoxicity of colloidal CdSe and CdSe/ZnS nanoparticles," Nano Lett. **5**(2), 331–338 (2004).

113. R. Hardman, "A toxicologic review of quantum dots: toxicity depends on physicochemical and environmental factors.," Environ. Health Perspect. **114**(2), 165–72 (2006).

114. M. Massey, M. Wu, E. M. Conroy, and W. R. Algar, "Mind your P's and Q's: the coming of age of semiconducting polymer dots and semiconductor quantum dots in biological applications," Curr. Opin. Biotechnol. **34**, 30–40 (2015).

115. M. A. Albota, C. Xu, and W. W. Webb, "Two-photon fluorescence excitation cross sections of biomolecular probes from 690 to 960 nm," Appl. Opt. **37**(31), 7352 (1998).

116. C. Wu, S. J. Hansen, Q. Hou, J. Yu, M. Zeigler, Y. Jin, D. R. Burnham, J. D. McNeill, J. M. Olson, and D. T. Chiu, "Design of highly emissive polymer dot bioconjugates for in vivo tumor targeting," Angew. Chemie Int. Ed. **50**(15), 3430–3434 (2011).

117. R. Dickie, R. M. Bachoo, M. A. Rupnick, S. M. Dallabrida, G. M. DeLoid, J. Lai, R. A. DePinho, and R. A. Rogers, "Three-dimensional visualization of microvessel architecture of whole-mount tissue by confocal microscopy," Microvasc. Res. **72**(1–2), 20–26 (2006).

118. L.-C. Cheng, N. G. Horton, K. Wang, S.-J. Chen, and C. Xu, "Measurements of multiphoton action cross sections for multiphoton microscopy," Biomed. Opt. Express **5**(10), 3427 (2014).

119. S. M. S. Kazmi, A. J. Salvaggio, A. D. Estrada, M. A. Hemati, N. K. Shaydyuk, E. Roussakis, T. A. Jones, S. A. Vinogradov, and A. K. Dunn, "Three-dimensional mapping of oxygen tension in cortical arterioles before and after occlusion," Biomed. Opt. Express **4**(7), 1061 (2013).

120. E. P. Perillo, J. W. Jarrett, Y.-L. Liu, A. Hassan, D. C. Fernée, J. R. Goldak, A. Bonteanu, D. J. Spence, H.-C. Yeh, and A. K. Dunn, "Two-color multiphoton in vivo imaging with a femtosecond diamond Raman laser," Light Sci. Appl. **6**(11), (2017).

121. A. D. Estrada, A. Ponticorvo, T. N. Ford, and A. K. Dunn, "Microvascular oxygen quantification using two-photon microscopy," Opt. Lett. **33**(10), 1038 (2008).

122. E. B. Brown, R. B. Campbell, Y. Tsuzuki, L. Xu, P. Carmeliet, D. Fukumura, and R. Jain, "In vivo measurement of gene expression, angiogenesis and physiological

function in tumors using multiphoton laser scanning microscopy," Nat. Med. **7**(7), (2001).

123. L. Y. Lee, S. L. Ong, J. Y. Hu, W. J. Ng, Y. Feng, X. Tan, and S. W. Wong, "Use of semiconductor quantum dots for photostable immunofluorescence labeling of Cryptosporidium parvum.," Appl. Environ. Microbiol. **70**(10), 5732–6 (2004).

124. J. Pecher and S. Mecking, "Nanoparticles of conjugated polymers," Chem. Rev. **110**(10), 6260–6279 (2010).

125. A. Kaeser and A. P. H. J. Schenning, "Fluorescent nanoparticles based on self-assembled π-conjugated systems," Adv. Mater. **22**(28), 2985–2997 (2010).

126. S. L. Jacques, "Optical properties of biological tissues: a review," Phys. Med. Biol. **58**(11), R37–R61 (2013).

127. C. Xu and W. W. Webb, "Measurement of two-photon excitation cross sections of molecular fluorophores with data from 690 to 1050 nm," J. Opt. Soc. Am. **13**(3), 481–491 (1996).

128. C. Xu and F. W. Wise, "Recent advances in fibre lasers for nonlinear microscopy," Nat. Photonics **7**(11), 875–882 (2013).

129. W. R. Zipfel, "http://www.drbio.cornell.edu/cross_sections.html," (2018).

130. E. P. Perillo, J. E. McCracken, D. C. Fernée, J. R. Goldak, F. A. Medina, D. R. Miller, H.-C. Yeh, and A. K. Dunn, "Deep in vivo two-photon microscopy with a low cost custom built mode-locked 1060 nm fiber laser," Biomed. Opt. Express **7**(2), 324 (2016).

131. P. J. Drew, P. Blinder, G. Cauwenberghs, A. Y. Shih, and D. Kleinfeld, "Rapid determination of particle velocity from space-time images using the Radon transform," J. Comput. Neurosci. **29**(1–2), 5–11 (2010).

132. C. J. Schrandt, S. S. Kazmi, T. A. Jones, and A. K. Dunn, "Chronic monitoring of vascular progression after ischemic stroke using multiexposure speckle imaging and two-photon fluorescence microscopy," J. Cereb. Blood Flow Metab. **35**(6), 933–942 (2015).

133. W. Sun, F. Ye, M. E. Gallina, J. Yu, C. Wu, and D. T. Chiu, "Lyophilization of semiconducting polymer dot bioconjugates," Anal. Chem. **85**(9), 4316–4320 (2013).

134. M. Albota, D. Beljonne, J.-L. Brédas, J. E. Ehrlich, J.-Y. Fu, A. A. Heikal, S. E. Hess, T. Kogej, M. D. Levin, S. R. Marder, D. McCord-Maughon, J. W. Perry, H.

Röckel, M. Rumi, G. Subramaniam, W. W. Webb, X.-L. Wu, and C. Xu, "Design of organic molecules with large two-photon absorption cross sections," Science (80-.). **281**(5383), (1998).

135. Z. Hashim, P. Howes, and M. Green, "Luminescent quantum-dot-sized conjugated polymernanoparticles—nanoparticle formation in a miniemulsion system," J. Mater. Chem. **21**(6), 1797–1803 (2011).

136. The Jackson Laboratory, "JAX Mice Strain - C57BL/6J," https://www.jax.org/jax-mice-and-services/strain-data-sheet-pages/body-weight-chart-000664.

137. M. Oheim, E. Beaurepaire, E. Chaigneau, J. Mertz, and S. Charpak, "Two-photon microscopy in brain tissue: Parameters influencing the imaging depth," J. Neurosci. Methods **111**(1), 29–37 (2001).

138. R. G. Nunes, P. Jezzard, and S. Clare, "Investigations on the efficiency of cardiac-gated methods for the acquisition of diffusion-weighted images," J. Magn. Reson. **177**(1), 102–110 (2005).

139. J. R. Bumstead, J. J. Park, I. A. Rosen, A. W. Kraft, P. W. Wright, M. D. Reisman, D. C. Côté, and J. P. Culver, "Designing a large field-of-view two-photon microscope using optical invariant analysis," Neurophotonics **5**(02), 1 (2018).

140. N. Ji, J. Freeman, and S. L. Smith, "Technologies for imaging neural activity in large volumes," Nat. Neurosci. **19**(9), 1154–1164 (2016).

141. A. Negrean and H. D. Mansvelder, "Optimal lens design and use in laser-scanning microscopy," Biomed. Opt. Express **5**(5), 1588 (2014).

142. R. Salomé, Y. Kremer, S. Dieudonné, J.-F. Léger, O. Krichevsky, C. Wyart, D. Chatenay, and L. Bourdieu, "Ultrafast random-access scanning in two-photon microscopy using acousto-optic deflectors," J. Neurosci. Methods **154**(1–2), 161–174 (2006).

143. G. Duemani Reddy, K. Kelleher, R. Fink, and P. Saggau, "Three-dimensional random access multiphoton microscopy for functional imaging of neuronal activity," Nat. Neurosci. **11**(6), 713–720 (2008).

144. K. M. N. S. Nadella, H. Roš, C. Baragli, V. A. Griffiths, G. Konstantinou, T. Koimtzis, G. J. Evans, P. A. Kirkby, and R. A. Silver, "Random-access scanning microscopy for 3D imaging in awake behaving animals," Nat. Methods **13**(12), 1001–1004 (2016).

145. E. J. Botcherby, R. Juškaitis, M. J. Booth, and T. Wilson, "An optical technique for remote focusing in microscopy," Opt. Commun. **281**(4), 880–887 (2008).

146. P. Rupprecht, A. Prendergast, C. Wyart, and R. W. Friedrich, "Remote z-scanning with a macroscopic voice coil motor for fast 3D multiphoton laser scanning microscopy," Biomed. Opt. Express **7**(5), 1656 (2016).

147. P. Mahou, J. Vermot, E. Beaurepaire, and W. Supatto, "Multicolor two-photon light-sheet microscopy," Nat. Methods **11**(6), 600–601 (2014).

148. J. Huisken, J. Swoger, F. Del Bene, J. Wittbrodt, and E. H. K. Stelzer, "Optical sectioning deep inside live embryos by selective plane illumination microscopy," Science (80-.). **305**(5686), 1007–1009 (2004).

149. M. B. Bouchard, V. Voleti, C. S. Mendes, C. Lacefield, W. B. Grueber, R. S. Mann, R. M. Bruno, and E. M. C. Hillman, "Swept confocally-aligned planar excitation (SCAPE) microscopy for high-speed volumetric imaging of behaving organisms," Nat. Photonics **9**(2), 113–119 (2015).

150. H. Yu, P. T. galwaduge, V. Voleti, K. Patel, W. Li, M. A. Shaik, and E. M. Hillman, "Two-photon swept confocally aligned planar excitation microscopy (2P-SCAPE)," in *Optics in the Life Sciences Congress* (OSA, 2017), p. NW4C.3.

151. V. Voleti, M. B. Bouchard, C. Lacefield, R. Bruno, and E. M. C. Hillman, "Fast, volumetric imaging of in vivo mouse brain with swept confocally aligned planar excitation (SCAPE) microscopy," in *Optics in the Life Sciences* (OSA, 2015), p. BrM2B.3.

152. G. Katona, G. Szalay, P. Maák, A. Kaszás, M. Veress, D. Hillier, B. Chiovini, E. S. Vizi, B. Roska, and B. Rózsa, "Fast two-photon in vivo imaging with three-dimensional random-access scanning in large tissue volumes," Nat. Methods **9**(2), 201–208 (2012).

153. I. Veilleux, J. A. Spencer, D. P. Biss, D. Cote, and C. P. Lin, "In vivo cell tracking with video rate multimodality laser scanning microscopy," IEEE J. Sel. Top. Quantum Electron. **14**(1), 10–18 (2008).

154. V. Iyer, B. E. Losavio, and P. Saggau, "Compensation of spatial and temporal dispersion for acousto-optic multiphoton laser-scanning microscopy," J. Biomed. Opt. **8**(3), 460 (2003).

155. M. N. Sweeney, "Polygon scanners revisited," in L. Beiser and S. F. Sagan, eds. (International Society for Optics and Photonics, 1997), **3131**, pp. 65–76.

156. A. M. Packer, L. E. Russell, H. W. P. Dalgleish, and M. Häusser, "Simultaneous all-optical manipulation and recording of neural circuit activity with cellular resolution in vivo," Nat. Methods **12**(2), 140–146 (2015).

157. P. S. Tsai, J. P. Kaufhold, P. Blinder, B. Friedman, P. J. Drew, H. J. Karten, P. D. Lyden, and D. Kleinfeld, "Correlations of neuronal and microvascular densities in murine cortex revealed by direct counting and colocalization of nuclei and vessels," J. Neurosci. **29**(46), (2009).

158. H. J. Karten, "Process flow diagram for automated identification and segmentation of vascular subvolumes," https://www.researchgate.net/figure/Process-flow-diagram-for-automated-identification-and-segmentation-of-vascular_fig3_38099026.

159. T. Zhang, "Some sharp performance bounds for least squares regression with L 1 regularization," Ann. Stat. **37**(5), 2109–2144 (2009).

160. I. Guyon and A. Elisseeff, "An introduction to variable and feature selection," J. Mach. Learn. Res. 1157–1182 (2003).

161. A. Mittal, A. K. Moorthy, and A. C. Bovik, "Blind/referenceless image spatial quality evaluator," in *Conference Record - Asilomar Conference on Signals, Systems and Computers* (2011), pp. 723–727.

162. K. M. Harris and R. J. Weinberg, "Ultrastructure of synapses in the mammalian brain.," Cold Spring Harb. Perspect. Biol. **4**(5), a005587 (2012).

163. M. Nedergaard, B. Ransom, and S. A. Goldman, "New roles for astrocytes: Redefining the functional architecture of the brain," Trends Neurosci. **26**(10), 523–530 (2003).

164. J. N. D. Kerr and W. Denk, "Imaging in vivo: watching the brain in action," Nat. Rev. Neurosci. **9**(3), 195–205 (2008).

165. K. M. Harris and S. B. Kater, "Dendritic spines: cellular specializations imparting both stability and flexibility to synaptic function," Annu. Rev. Neurosci. **17**(1), 341–371 (1994).

166. K. M. Harris and J. K. Stevens, "Dendritic spines of CA 1 pyramidal cells in the rat hippocampus: serial electron microscopy with reference to their biophysical characteristics.," J. Neurosci. **9**(8), 2982–97 (1989).

167. K. L. McDonald and M. Auer, "High-pressure freezing, cellular tomography, and structural cell biology," Biotechniques **41**(2), 137–143 (2006).

168. K. I. Willig, B. Harke, R. Medda, and S. W. Hell, "STED microscopy with continuous wave beams," Nat. Methods **4**(11), 915–918 (2007).

169. S. W. Hell and J. Wichmann, "Breaking the diffraction resolution limit by

stimulated emission: stimulated-emission-depletion fluorescence microscopy," Opt. Lett. **19**(11), 780 (1994).

170. M. J. Rust, M. Bates, and X. Zhuang, "Sub-diffraction-limit imaging by stochastic optical reconstruction microscopy (STORM)," Nat. Methods **3**(10), 793–796 (2006).

171. X. Zhuang, "Nano-imaging with STORM," Nat. Photonics **3**(7), 365 (2009).

172. E. Betzig, "Imaging intracellular fluorescent proteins at nanometer resolution," Science (80-.). **313**(5793), 1642–1645 (2006).

173. B. Huang, M. Bates, and X. Zhuang, "Super-resolution fluorescence microscopy," Annu. Rev. Biochem. **78**(1), 993–1016 (2009).

174. C. Kuang, S. Li, W. Liu, X. Hao, Z. Gu, Y. Wang, J. G.-S. reports, and undefined 2013, "Breaking the diffraction barrier using fluorescence emission difference microscopy," nature.com (n.d.).

175. G. Vicidomini, G. Moneron, K. Y. Han, V. Westphal, H. Ta, M. Reuss, J. Engelhardt, C. Eggeling, and S. W. Hell, "Sharper low-power STED nanoscopy by time gating," Nat. Methods **8**(7), 571–573 (2011).

176. P. Bethge, R. Chéreau, E. Avignone, G. Marsicano, and U. V. Nägerl, "Two-photon excitation STED microscopy in two colors in acute brain slices," Biophys. J. **104**(4), 778–785 (2013).

177. H. Dehez, M. Piché, and Y. De Koninck, "Resolution and contrast enhancement in laser scanning microscopy using dark beam imaging," Opt. Express **21**(13), 15912 (2013).

178. M. P. Gordon, T. Ha, and P. R. Selvin, "Single-molecule high-resolution imaging with photobleaching," Proc. Natl. Acad. Sci. U. S. A. **101**(17), 6462–6465 (2004).

179. K. A. Lidke, B. Rieger, T. M. Jovin, and R. Heintzmann, "Superresolution by localization of quantum dots using blinking statistics," Opt. Express **13**(18), 7052 (2005).

180. T. Pfeiffer, S. Poll, S. Bancelin, J. Angibaud, V. V. G. K. Inavalli, K. Keppler, M. Mittag, M. Fuhrmann, and U. V. Nägerl, "Chronic 2P-STED imaging reveals high turnover of dendritic spines in the hippocampus in vivo," Elife **7**, (2018).

181. P. Bianchini, C. Peres, M. Oneto, S. Galiani, G. Vicidomini, and A. Diaspro, "STED nanoscopy: a glimpse into the future," Cell Tissue Res. **360**(1), 143–150 (2015).

182. W. Wang, G. Zhao, C. Kuang, L. Xu, S. Liu, S. Sun, P. Shentu, Y. (Michael) Yang, Y. Xu, and X. Liu, "Integrated dual-color stimulated emission depletion (STED) microscopy and fluorescence emission difference (FED) microscopy," Opt. Commun. **423**, 167–174 (2018).

183. S. Sadegh, M.-H. Yang, C. G. Ferri, M. Thunemann, P. A. Saisan, E. A. Rodriquez, S. R. Adams, S. A. Vinogradov, Y. Fainman, and A. Devor, "In vivo brain imaging with non-degenerate 2-photon microscopy," in *Optics and the Brain* (Optical Society of America, 2018), p. BF3C.2.

184. J. Jiang, D. Zhang, S. Walker, C. Gu, Y. Ke, W. H. Yung, and S. Chen, "Fast 3-D temporal focusing microscopy using an electrically tunable lens," Opt. Express **23**(19), 24362 (2015).

185. H. Wang, X. Yang, Y. Liu, B. Jiang, and Q. Luo, "Reflection-mode optical-resolution photoacoustic microscopy based on a reflective objective," Opt. Express **21**(20), 24210 (2013).

186. B. Amirsolaimani, B. Cromey, N. Peyghambarian, and K. Kieu, "All-reflective multiphoton microscope," Opt. Express **25**(19), 23399 (2017).

187. D. R. Miller, "Extending the depth limit of multiphoton microscopy for in vivo brain imaging," (2016).

188. J. P. Zinter and M. J. Levene, "Maximizing fluorescence collection efficiency in multiphoton microscopy," Opt. Express **19**(16), 15348 (2011).

189. M. Leutenegger, R. Rao, R. A. Leitgeb, and T. Lasser, "Fast focus field calculations," Opt. Express **14**(23), 11277 (2006).

190. Z. Wang, A. C. Bovik, H. R. Sheikh, and E. P. Simoncelli, "Image quality assessment: From error visibility to structural similarity," IEEE Trans. Image Process. **13**(4), 600–612 (2004).

191. K. Murari, Y. Zhang, S. Li, Y. Chen, M.-J. Li, and X. Li, "Compensation-free, all-fiber-optic, two-photon endomicroscopy at 155 μm," Opt. Lett. **36**(7), 1299 (2011).

192. T. Desmettre, J. M. Devoisselle, and S. Mordon, "Fluorescence properties and metabolic features of indocyanine green (ICG) as related to angiography," Surv. Ophthalmol. **45**(1), 15–27 (2000).

193. L. Novotny and B. Hecht, *Principles of Nano-Optics* (Cambridge university press, 2006).

194. N. Wang and T. Kobayashi, "Polarization modulation for fluorescence emission

difference microscopy," Opt. Express **23**(10), 13704 (2015).

195. Z. Rong, C. Kuang, Y. Fang, G. Zhao, Y. Xu, and X. Liu, "Super-resolution microscopy based on fluorescence emission difference of cylindrical vector beams," Opt. Commun. **354**, 71–78 (2015).

196. H. Dehez, M. Piché, and Y. De Koninck, "Resolution and contrast enhancement in laser scanning microscopy using dark beam imaging," Opt. Express **21**(13), 15912 (2013).

197. S. Sadegh, M.-H. Yang, C. G. L. Ferri, M. Thunemann, P. A. Saisan, A. Devor, and Y. Fainman, "Measurement of the relative non-degenerate two-photon absorption cross-section for fluorescence microscopy," Opt. Express **27**(6), 8335 (2019).

198. Leica Microsystems, "Restless Receptors: New Insights Into the Dynamic Organization of Synapses," https://www.leica-microsystems.com/company/news/news-details/article/restless-receptors-new-insights-into-the-dynamic-organization-of-synapses/.

199. M. Bashkansky, D. Park, and F. K. Fatemi, "Azimuthally and radially polarized light with a nematic SLM," Opt. Express **18**(1), 212 (2010).